

LMU

LUDWIG-
MAXIMILIANS-
UNIVERSITÄT
MÜNCHEN

DYNAMIC EARTHQUAKE RUPTURES IN THE PRESENCE OF MATERIAL DISCONTINUITIES

DISSERTATION
DER FAKULTÄT FÜR GEOWISSENSCHAFTEN
DER LUDWIG-MAXIMILIANS-UNIVERSITÄT MÜNCHEN

GILBERT BJÖRN BRIETZKE

MÜNCHEN,
15. SEPTEMBER 2008



**Dynamic Earthquake Ruptures
in the Presence of Material Discontinuities**

Dissertation

von Gilbert Björn Brietzke

zur Erlangung des akademischen Grades

Doktor der Naturwissenschaften

an der Fakultät für Geowissenschaften

der Ludwig-Maximilians-Universität München



vorgelegt in München am 15. September 2008

Referees

Erstgutachter:

Prof. Dr. Heiner Igel

Department für Geo- und Umweltwissenschaften

Ludwig-Maximilians-Universität München

Theresienstraße 41

80333 München

✉ igel@geophysik.uni-muenchen.de

☎ +49 89 2180 4204

Zweitgutachter:

Prof. Dr. Matthias Holschneider

Universität Potsdam

Institut für Mathematik

Postfach 60 15 53

14415 Potsdam

✉ hols@math.uni-potsdam.de

☎ +49 331 977 1500 / 1663

Tag der mündlichen Prüfung: 2. März 2009

Summary

A general feature of tectonic faults is the juxtaposition of materials with dissimilar elastic properties in a variety of contexts and scales. Normal and reverse faults offset vertical stratifications, large strike-slip faults displace different crustal blocks, oceanic and continental crusts at subduction interfaces, and oceanic transforms juxtapose rocks of different ages. Bimaterial interfaces associated with rock damage are present with various degrees of sharpness in typical fault zone structures, and failure along a bimaterial interface can be effective even on microscopic scale of grain boundaries.

A first order representation of a geological fault for seismic events is a frictional interface embedded in an elastic body. This study focusses on dynamic effects in the presence of material discontinuities altering dynamics of failure and dynamic rupture propagation on frictional interfaces. When the medium surrounding a fault is heterogeneous, the symmetry of stress is broken up and perturbations of normal stress introduces additional instability potentially generating additional propagation modes of rupture.

This study presents three specific numerical investigations of the aforementioned rupture phenomena associated with material contrasts at the fault. A first numerical study (a) investigates 2-D in-plane ruptures in a model consisting of two different half-spaces separated by a low-velocity layer and possible simultaneous slip along multiple faults. This study shows that bimaterial frictional interfaces are attractive trajectories of rupture propagation, and ruptures tend to migrate to material interfaces and becoming self-sustained slip pulses for wide ranges of conditions. In a second numerical study (b), the propagation of a purely material contrast driven rupture mode, that is associated with the so-called Weertman or Adams-unstable pulse, is shown to exist also in the general 3-D case, where there is a mixing of in-plane and anti-plane modes, the bimaterial mechanism acting in the in-plane direction only. Finally, in a further numerical investigation (c) it is demonstrated, that the rupture dynamics and ground motion can be significantly influenced by bimaterial mechanisms of rupture propagation for ranges of parameters. The model studied here comprises heterogeneous initial shear stress on a slip-weakening frictional interfaces separating two dissimilar elastic bodies, a free surface. The discussion focusses on the diversity of existing rupture propagation modes and ground motion.

The investigated models and obtained results are motivated and discussed in the context of complementary numerical investigations, theoretical studies of stability analysis, seismological

observations of earthquakes and aftershock sequences, geological observations of fault zone structures, tomographic studies, and geodetic observations.

Contents

Preliminaries	iii
Title	iii
Referees	iv
Summary	vii
Contents	ix
1 Introduction	1
1.1 Motivation	1
1.2 Goal of the Study	4
1.3 Structure of the Thesis	4
2 Earthquake Source Model	7
2.1 Fault-zone and Rupture Dynamics	7
2.1.1 Fault-zone Structure	7
2.1.2 Fault Constitutive Behavior	10
2.1.3 Crack and Pulse-like Rupture	13
2.2 Fault as a Frictional Interface	14
2.2.1 Elastodynamic Equations	14
2.2.2 Fault Jump Conditions	15
2.2.3 Numerical Implementation	15
2.3 Bimaterial Interface	16
2.3.1 A Bimaterial Fault - a Common Feature	16
2.3.2 Bimaterial Mechanics	18
2.3.3 Ill-posedness	19
3 Rupture Migration to Material Interfaces	23
3.1 Introduction	25
3.2 Methods and Model Setup	28
3.2.1 Finite-Difference Method and Fault Model	28

3.2.2	Nucleation Procedure	30
3.3	Initial Results and Choice of Model Parameters	31
3.3.1	Influence of Viscosity	31
3.3.2	Effects of Multiple Faults	33
3.3.3	Prakash-Clifton Friction	35
3.3.4	Choice of Parameters for Subsequent Simulations	36
3.4	Results on Rupture Migration	39
3.4.1	Two-fault System	39
3.4.2	A Nine-fault System	40
3.5	Discussion and Conclusions	45
4	Bimaterial Interface in 3D	51
4.1	Introduction	52
4.2	Ill-posedness, and Numerical Convergence	52
4.3	Physical Model, Nucleation, Numerical Implementation	55
4.4	Results	56
4.5	Discussion	58
5	Bimaterial Dynamics and Ground Motion	61
5.1	Introduction	63
5.2	Model Setup	64
5.2.1	Heterogeneous Stress and Nucleation	64
5.2.2	Friction and Regularization	64
5.2.3	Numerical Method	65
5.3	Results	66
5.3.1	Example 1	69
5.3.2	Example 2	77
5.3.3	Example 3	86
5.3.4	Example 4	97
5.3.5	General Stable Features	106
5.3.6	Results of 300 Simulation Pairs	106
5.3.7	Summary of Results	110
5.4	Discussion	111
5.5	Conclusion	115
6	Discussion, Conclusion and Future Work	117
6.1	Discussion and Conclusion	117
6.2	Future Work	119
	Appendices	123

A	Finite Difference Approximations	123
A.1	Elastic Wave Propagation	123
A.1.1	Time Derivatives	123
A.1.2	Space Derivatives	123
A.1.3	Wave Equations	125
A.2	Fault Interface: Traction-at-Split-Nodes (TSN)	126
A.2.1	Fault Plane Slip Velocity and Shear Traction	126
A.2.2	Split Stress Components	128
A.2.3	Verification of TSN-implementation	130
A.3	Fault Interface: Stress Glut Method (SGM)	135
A.3.1	Description of the Stress Glut Method & Implementation	135
A.3.2	Verification of the SGM-Implementation	137
B	Definitions	141
B.1	Slip, Slip Velocity, Peak Slip Velocity	141
B.2	Rupture Propagation Velocity	141
B.3	Seismic Moment and Moment Magnitude	142
B.4	Peak Ground Velocity and Peak Ground Acceleration	143
B.5	Weertman Pulse or Adams' Steady State Pulse	143
B.6	Generalized Rayleigh Velocity	144
	Acknowledgement	145
	Bibliography	147

Chapter 1

Introduction

1.1 Motivation

As a consequence of continental plate movement, most likely driven by viscous flow of material in the Earth's mantle, the Earth's crust accommodates tectonic strain and therefore elastic strain energy. This energy can either be released slowly by creep and viscous flow, or it can be released abruptly and rapidly, in this case, a part of it is transferred into non-elastic deformation and transformed in dissipative processes when breaking crustal materials and during frictional sliding, while another part of the energy is radiated through elastic waves reaching even remote places far away from the source. Such a rapidly and abruptly happening seismic event is called earthquake.

Earthquakes and their radiated ground motion pose a serious natural hazard in many parts of the world. Six of the most fatal earthquakes during the past five years – the magnitude 7.9 China 2008, magnitude 8.0 Peru 2007, magnitude 6.3 Indonesia 2006, magnitude 7.6 Pakistan 2005, magnitude 9.1 Sumatra 2004, magnitude 6.6 Iran 2003 earthquakes – caused, altogether, more than 420000 fatalities and an even larger number of injured. Injuries and diseases, structural damage, damage of crop and infrastructure put another large number of people into misery, harm and/or economic ruin. Beyond its cruel effect on individuals and society within it has economically a large impact world wide due to globalization of commerce and required spread of risk. Hence, it is of huge interest world wide to rise the endeavors in research to better understand the dynamics of the earth's crust, the dynamics of earthquakes, its structural response, and to develop forecast models in order to prevent humanitarian catastrophes, minimize damage and risk in future times.

One of the major goals of today's seismology is the estimation of time histories of the ground motion at specific locations after a hypothetical earthquake rupture on a particular fault or system of faults. These histories (earthquake scenario) can be used to model the response of infrastructure and constructions in order to improve the resistance of structures to damage from ground shaking or to evaluate potential seismic hazard.

Estimating earthquake ground motions requires a detailed description of the kinematic source, the slip history between opposite sides of the fault during the earthquake rupture process, and of the medium through which the seismic waves propagate from the fault to the site of interest. Variations of material properties and stress in the crust occur over a wide range of spatial scales, from the small-scale variety of minerals in a rock to the large-scale variety of geologic units on the continental scale, affecting both earthquake source and transmitting medium of the seismic waves. The dynamics of faults also incorporate a wide range of time scales from geological times of thousands of years to fractions of seconds during an individual earthquake. Earthquakes nucleate when the slip between the two sides of a fault accelerates in a spontaneously growing patch. The acceleration and deceleration of the propagating rupture due to variations and evolution of stress and strength generates seismic waves over a broad frequency range. The emitted seismic waves are refracted and reflected by horizontal and lateral seismic boundaries in the crust due to variations of rock type and composition, fractures, and fluid pressure. Man-made structures have natural frequencies of vibration between about 0.1 and 20 Hz; and variations in seismic velocity and density on a scale of tens of meters to kilometers have to be considered for accurate shaking estimates, focussing or scattering effects lead to focusing or dispersion or diffusion of ground motion and can affect building response. The large ranges of temporal and spatial scales and the large number of degrees of freedom involved in the earthquake faulting process pose a challenging problem which cannot yet be solved without rigorous simplifications on the involved scales and/or processes.

Principally various types of sources can generate seismic waves (explosions, rapid phase transformations, etc.). However, the source of interest in geological faulting is mostly the one involving a surface, the fault-plane, across which shear motion develops. Such a source comprises a discontinuity of displacement as a function of time (slip history). For the case the slip history on the fault plane is known, the motion throughout the medium is deterministic and the ground motion at the surface in a region of interest can be calculated when a sufficiently accurate model of elastic parameters is available. This provides the possibility to characterize what may be learned from far-field and/or near-field observation about the kinematics of motion at an earthquake source. It is also the basis of the kinematic source inverse process, that is calculating slip history on a fault from seismometer recordings. The key source parameters in such kinematic models are: fault area, rupture velocity, permanent slip, and rise time. The physical processes occurring in the source region are not described in such a model. In order to learn about the physical mechanisms that are responsible for the resulting source kinematics, stress-dependent material properties have to be taken into account such that strength, material failure, friction, and stress evolve consistently. In such models the kinematic spreading of the rupture over the fault-plane is spontaneous and is a solution of a non-linear problem.

Seismic wave propagation can be described to a large portion by the relationship between the gradient of the stress and acceleration and the relationship of stress and strain (Hooke's

law). In the source region of an earthquake, Hooke's law fails and needs to be replaced by other expressions that relate stress and deformation of the material within that source region. The non-elastic processes can often be simplified to a model of a surface of weakness, the fault-plane, which has the potential to rupture during an individual event. Stress can rise in the region of the source due to tectonic processes over mostly long time ranges prior to a significant event. Frictional resistance governing the fault is limited, and when exceeded failure and slip begin. Pre-existing fault-surfaces are likely reused over many earthquake cycles since they are weaker than the strength of intact material and therefore efficient failure surfaces as long as the orientation of the fault is efficient with respect to the shear loading.

In theoretical seismology the frictional shearing stress between two faces of a fault surface is thought to be proportional to normal stress. In order to generate stick-slip behavior it is necessary that frictional resistance falls from a static value of friction at the onset of slip to a lower value when sliding. How exactly does the failure take place is the topic of ongoing research: for instance, ductile behavior of the material, non-linear stress-strain relation during nucleation, stress and time-scale dependence of the nucleation, temporal evolution of the weakening of a fault during a seismic event, etc.. In order to effectively excite a reduction of frictional shear resistance, it is also plausibly possible, that changes of normal stress in addition to a change in friction coefficient during rupture propagation takes place for various reasons (e.g., non-planar fault geometries (kinked or curved fault), free surface reflections at normal, reverse, and dipping strike-slip faults). A simple but effective example for a mechanism causing changes in normal stress is the presence of material discontinuities in the source region, which are known to exist on different spatial scales, and various levels of sharpness. Other sources of normal stress perturbations on the fault can be non-planar fault geometries (kinked or curved fault), and/or free surface reflections at normal, reverse, and dipping strike-slip faults.

Properties of friction, shear resistance, evolution of sliding surfaces and related topics are subject of laboratory experiments since a long time. A prevalent outcome of such experiments are empirical laws of frictional evolution. Nowadays approximate solutions to the dynamic rupture problem are obtainable due to the combination of today's computer processing power and numerical concepts. Therefore the empirical laws for friction have been (and can be) successfully applied to model spontaneous rupture propagation reproducing characteristic features of seismological and laboratory observations. However, many involved parameters of these models are poorly constrained. This is originated by a large discrepancy between the scales of many relevant physical parameters in laboratory experiments and natural geological fault systems. Therefore numerous numerical simulations have to be performed usually in order to graze significant ranges of parameters and parameter combinations, even in the case of relatively simple models, to capture the wide range of system behavior and response.

Despite this success of self-consistency of many empirical friction laws, still a major problem is that the governing physical mechanisms are poorly understood and/or the parameters

of these mechanisms are poorly constraint and physically interpretable. Therefore additional theoretical concepts as well as additional laboratory experiments have to be invented to pursue future research in this challenging field.

1.2 Goal of the Study

The study presented here focuses on the aspect of the influence of material contrasts (contrasts in elastic parameters) on fault dynamics and ground motion. As mentioned before, such material discontinuities may allow for a reduction of shear resistance due to variations of normal stress in addition to potential loss in shear strength due to frictional weakening mechanisms. The study presented here shows, that (a) bimaterial frictional interfaces are attractive trajectories of rupture propagation, (b) propagation modes specific to in-plane shear along bimaterial interfaces exist also in the 3D-case of mixed in-plane and anti-plane modes, and (c) that the rupture dynamics and therefore the ground motion can be significantly influenced by the bimaterial mechanism during rupture propagation. The interpretation of the results and phrasing of the conclusions presented here tries to reflect and incorporate a broad range of additionally available knowledge from other studies that is excluded by the limits and simplifications of the studied model.

1.3 Structure of the Thesis

Chapter 1 introduces and motivates the topic, and presents the structure of the thesis.

Chapter 2 gives an overview of representative fault-zone structures and decisive physical processes in these structures in order to motivate a simplified model of a frictional surface embedded in an elastic medium as a meaningful model of earthquake faulting. The discussion reveals potentials and limits of these models. Specifically, section 2 discusses representative fault-zone structure from field observations, the constitutive behavior of such fault structure, modes of rupture propagation, section 2.2 describes the model of a fault as a frictional interface, and its governing equations and numerical implementations (their details given in the appendices A). Section 2.3 discusses the complications of rupture dynamics specific to bimaterial interfaces.

Chapter 3 presents a numerical parameter-space study of 2-D in-plane ruptures in a model consisting of two different half-spaces separated by a low-velocity layer and possible simultaneous slip along multiple faults. Ruptures are nucleated by a bilateral expanding stress drop in a limited source region, and may continue to propagate spontaneously (or not) along one or several faults. A general result of the study is that ruptures tend to migrate to the material interfaces and become self-sustained wrinkle-like pulses for wide ranges of conditions, supporting the hypothesis that bimaterial interfaces are attractive trajectories of failure for realistic earthquake

sources. This chapter presents the study of Brietzke and Ben-Zion (2006) in a slightly modified form.

Chapter 4 presents a numerical study of dynamic rupture propagation on a plane in a model consisting of two different elastic half spaces connected via a planar frictional interface governed by regularized Coulomb friction. Here it is shown how a purely material contrast driven rupture pulse can mature also in the 3D case due to perturbations of normal stress. This chapter presents the study of Brietzke et al. (2007) in a slightly modified form.

Chapter 5 presents a numerical investigation of dynamic ruptures on a bimaterial interface in 3D with regularized slip-weakening friction and a heterogeneous initial shear stress. The model includes a free surface and therefore allows for discussion of rupture dynamics as well as the resulting strong ground motion. Effects introduced by the material contrast are separated by running simulations twice, the orientation of the bimaterial setup being switched for the individual orientations. The study demonstrates, that for many parameter sets the dynamics of rupture propagation are significantly influenced by the material discontinuity during rupture propagation. Therefore the differences between both material contrast orientations in ground motion can be very large even when distribution of final slip are very similar, the moment magnitude essential identical. This chapter presents the study of Brietzke et al. (2009) in a slightly modified form.

Chapter 6 presents overall conclusions of the presented study, addresses open questions, and accordingly highlights potential near future studies in this line of research.

Chapter 2

Earthquake Source Model

2.1 Fault-zone and Rupture Dynamics

2.1.1 Fault-zone Structure

The structure of fault-zones has been the focus of many investigations to improve knowledge of micro-scale processes, fault zone rheology and dynamic weakening processes. It has been found that coseismic slip on mature faults is often localized within 1 - 5 mm inside an ultracataclasite core of cm to meter scale. A zone of highly fractured and/or granulated material with large porosity is often surrounding the fault core with up to hundreds of meters thickness: the damage zone.

Evidence for such a model has been collected from the Punchbowl fault by Chester and Chester (1998) (see Figure 2.1 taken from (Chester and Chester, 1998)), the San Gabriel fault by Chester et al. (1993), the Median Tectonic Line by Wibberley and Shimamoto (2002), the Nojima fault Lockner et al. (1999), as well as from other observations summarized in Sibson (2003), Ben-Zion and Sammis (2003) and Biegel and Sammis (2004), Shipton et al. (2006) (see Figure 2.2 taken from Shipton et al. (2006)). According to these observations slip is generally accommodated along a single nearly planar surface. The width and the complexity of fault zones inferred from the analysis of surface ruptures depend on the faulting mechanism (i.e., whether reverse, normal, strike-slip or oblique), and free surface effects (e.g. induced by a sedimentary cover)(Rice and Cocco, 2006).

The geological observations of fault zones presented above raise several important issues which have to be addressed in order to understand the mechanical properties of faults as well as the dynamic weakening processes occurring during earthquakes.

In the absence of any mechanism to rapidly reduce strength at the onset of slip (weakening), the temperature increase caused by a meter of slip within a few millimeters thick slipping zone would be larger than 1000°C. Such a change in temperature should lead to melting and formation of pseudotachylytes as well as an increased heat outflow along the fault (Rice and Cocco,

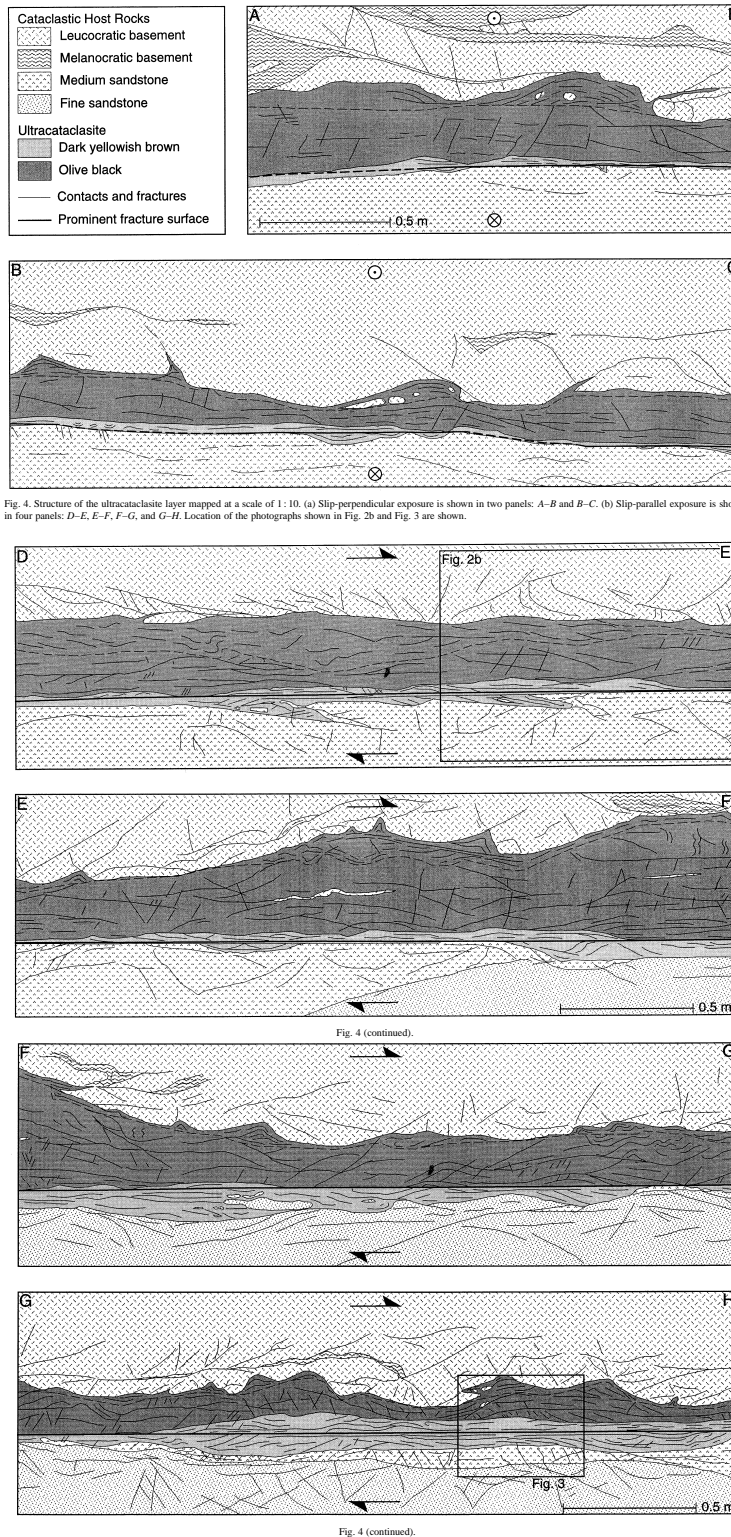


FIGURE 2.1: Evidence for localization of coseismic slip on a narrow zone of 1 - 5 mm inside an ultracataclasite core at the Punchbowl fault (taken from Chester and Chester (1998)).

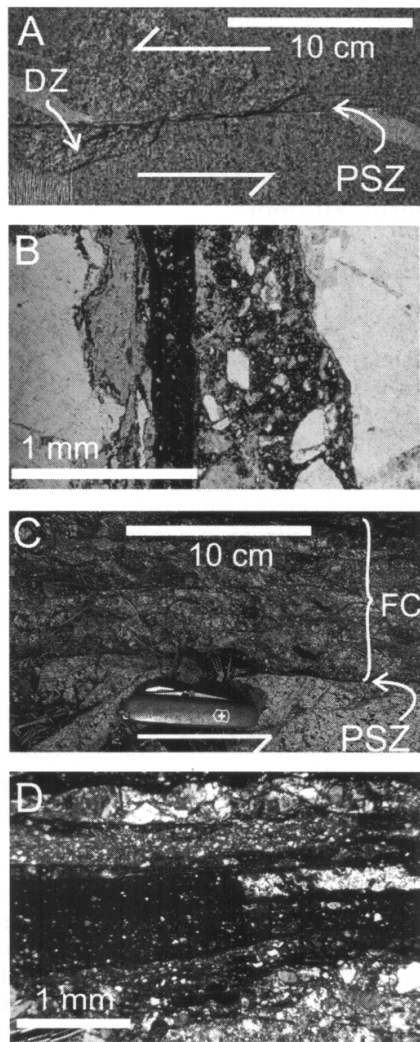


Figure 1. a) Small fault from Bear Creek, Sierra Nevada, with slip of ~ 20 cm. This fault nucleated on a cooling joint filled with chlorite, epidote, and quartz. b) Photomicrograph from a fault in Bear Creek, Sierra Nevada, with ~ 60cm slip exhibiting a narrow cataclastic PSZ within a 5 mm thick fault zone. c) PSZ with ~ 80 m slip from King's Canyon, Sierra Nevada, localized along the edge of the fault core. d) Photomicrograph of a PSZ from the Gemini fault with 100 m of total slip. Dark fine-grained material is chlorite muscovite foliated gouge with quartz fragments in the matrix.

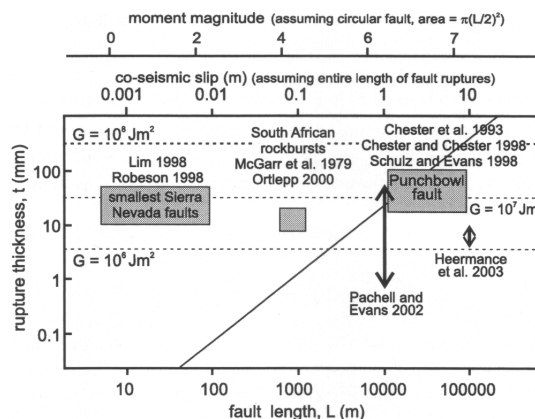


Figure 2. Fault length vs. PSZ thickness. Field data for thickness of the PSZ are represented by arrows where a range of PSZ thicknesses exist for a single fault, and by boxes where a range of PSZ thicknesses were measured on a range of fault lengths. If we assume the entire length of the observed faults slipped in an earthquake the maximum coseismic slip is calculated using the scaling of fault length and slip from *Scholz* [2002]. Moment magnitudes for these earthquakes are calculated from *Wells and Coppersmith* [1994]. The lines show maximum PSZ thickness as a function of seismic slip calculated from equation 3 using values for S , γ and ρ from the text and assuming that E_{disp}/A is equivalent to G . The solid line uses the empirical relation between G and earthquake size from *Abercrombie and Rice* [2005]. The dotted lines are for constant labeled values of G .

FIGURE 2.2: Left panel: evidence for localization of coseismic slip at a fault at Bear Creek, Sierra Nevada (after Shipton et al. (2006)). Right panel: parameter range for the localization of slip (as thickness of the principle slip zone (PSZ)) in dependence of earthquake magnitude, co-seismic slip and fault length (after Shipton et al. (2006))

2006). Melts with low viscosity can lubricate and thus weaken faults (Sibson, 1975; Spray, 1993; Brodsky and Kanamori, 2001; Kanamori and Brodsky, 2001). However, the scarcity of melts, pseudotachylytes and the lack of increased heat flow along faults (e.g., heat flow paradox at the San Andreas Fault (SAF)) suggests that dynamic fault weakening must happen, and weakening mechanisms other than melt lubrication play an important role in earthquake faulting (Sibson, 2003).

2.1.2 Fault Constitutive Behavior for Predictive Earthquake Models

For the usage of experimental and theoretical results in predictive large scale fault rupture models simplification without the loss of essential features is necessary. Accordingly a main result that is relevant to characterizing dynamic fault weakening during an earthquake is the evolution of traction on the fault.

Weakening during earthquake rupture propagation is usually represented by a drop in traction with increasing slip (see Figure 2.3), resulting in the well known slip-weakening model. Constitutive laws with a consistent behavior can have different physical processes as origin (Cocco and Bizzarri, 2002). Reduction of shear stress during dynamic rupture propagation occurs within a finite zone behind the tip of the crack called the cohesive zone (Barenblatt, 1959; Ida, 1972; Palmer and Rice, 1973), also called process zone, breakdown zone by others (e.g., Ben-Zion, 2003). Traction variation with slip is common to any constitutive relation proposed to model rupture propagation, but the shape of the slip weakening curve differs among various constitutive formulations. The constitutive laws proposed in the literature can be grouped in

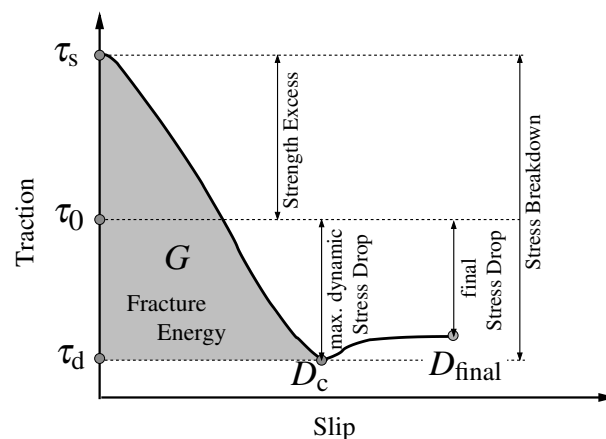


FIGURE 2.3: Schematic slip dependent weakening at a point on the fault. Traction increases from its initial value τ_0 to the upper yield stress, here τ_s , when slip starts, stress drops.

two main classes: slip-dependent (Andrews, 1976a,b; Ohnaka and Yamashita, 1989) and rate- and state-dependent laws (Dieterich, 1979; Runia, 1983). The former assumes that friction is a function of the fault slip only, while the latter implies that the friction is a function of slip veloc-

ity and state variables. The slip weakening model has been widely used as a constitutive relation to model dynamic rupture with theoretical and numerical approaches (Andrews, 1976a,b), its advantages are simplicity and prescription of traction evolution. In a simple triangular form often used in numerical calculations the slip weakening model can be written as follows:

$$f_{\text{sw}} = \begin{cases} f_s - (f_s - f_d) \frac{D}{D_c} & \text{for } D < D_c \\ f_d & \text{for } D \geq D_c \end{cases} \quad (2.1)$$

with f_s static friction coefficient, f_d dynamic friction coefficient, and D_c characteristic slip-weakening distance. Dependence of traction on slip has been observed in dynamic laboratory experiments (e.g., Ohnaka and Yamashita, 1989). With the initial stress τ_0 , the yield stress $\tau_s = f_s \sigma_n$, the kinetic friction level $\tau_d = f_d \sigma_n$ the slip-weakening law (equation 2.1) exhibits the traction vs. slip evolution curve as shown in Figure 2.4. The size of the cohesive zone in the

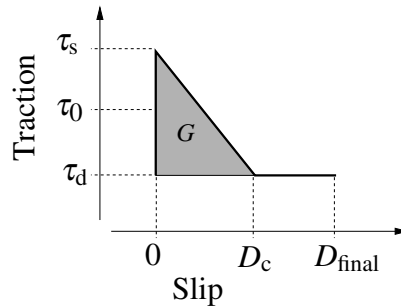


FIGURE 2.4: Traction evolution as a function of slip with a simple triangular slip-weakening model. τ_0 being the initial stress, $\tau_s = f_s \sigma_n$ the yield stress, and $\tau_d = f_d \sigma_n$ the kinetic friction level.

slip-weakening formulation is $X_c = c\mu D_c / [\sigma_n (f_s - f_d)]$ with dimensionless constant c of order 2-3 and rigidity μ . Laboratory values of D_c depend on the roughness of the sliding surface and possible existence of gouge (Marone, 1998, and references therein). Laboratory experiments (e.g., Li, 1987; Ohnaka, 2003), give estimates on its value in the range of $(10^{-6} - 5 \times 10^{-4})$ m. With $f_s - f_d = 0.05$ and a representative ratio for the seismogenic zone $\mu / \sigma_n = 300$ implies values of X_c in the range (0.01-10) m. However, seismological observations give estimates of $D_c = 0.01 - 4$ m (Mikumo et al., 2003).

In rate- and state-dependent friction laws the dependency of the friction coefficient is on slip velocity, and history (represented by state variables), and normal stress. In a classical form of rate- and state-dependent friction, with a single state variable and no dependency of the friction coefficient on normal stress, the friction coefficient can be written as:

$$f = f_0 + a \ln \left(\frac{V}{V_0} \right) + b \ln \left(\frac{V_0 \Theta}{L} \right), \quad (2.2)$$

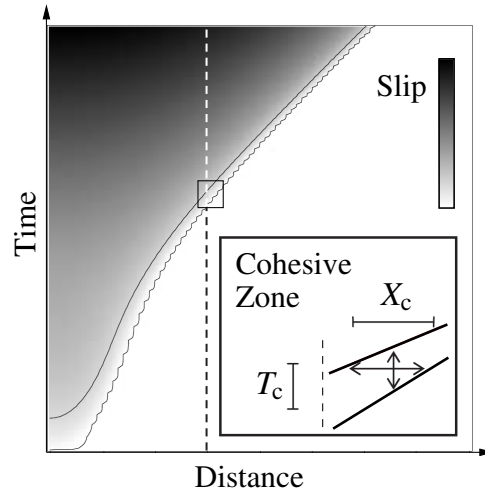


FIGURE 2.5: Schematic spatio-temporal evolution of slip obtained by a numerical experiment of spontaneous dynamic propagation on a 2-D fault (modified after (Cocco et al., 2004)) with slip weakening (equation 2.1). The cohesive or breakdown zone is defined as the region shear stress degradation from the upper yield stress to the kinetic friction level. Note that the spatial dimension of the cohesive or breakdown zone X_c is different from the critical slip weakening distance D_c .

with the evolution equation of the state-variable Θ :

$$\dot{\Theta} = 1 - \frac{V\Theta}{L}, \quad (2.3)$$

where f_0 is a nominal friction coefficient, V and V_0 are current and reference values of sliding velocity, a and b are material properties (e.g., Scholz, 1998).

The characteristic length scale parameters of these two constitutive formulations are the slip weakening distance D_c , the slip required for traction to drop to its residual value, and the parameter L , the characteristic length for the renewal of a population of contacts along the sliding surface. These two length scale parameters are different although it is possible to associate slip weakening and rate- and state-constitutive parameters in situations of rapid increase in slip velocity, like at a propagating rupture front (Cocco and Bizzarri, 2002; Bizzarri and Cocco, 2003).

While the slip-weakening formulation allows for modeling of dynamic propagation of rupture, the rate- and state-constitutive laws allow the definition of different frictional regimes: the modeling of rupture nucleation (Lapusta and Zheng, 2000, and references therein), dynamic rupture propagation (e.g., Bizzarri et al., 2001) as well as fault restrengthening during the interseismic period (e.g., Cocco et al., 2004); therefore, it has been used to simulate repeated seismic cycles (e.g., Lapusta and Zheng, 2000; Hori et al., 2004). Slip-weakening is a characteristic behavior of rate- and state-friction.

Theoretical constitutive modeling of weakening by thermal pressurization (Bizzarri and

Cocco, 2006a,b), as well as seismic attempts to look at the scaling of fracture energy with slip in an earthquake (Abercrombie and Rice, 2005; Rice et al., 2005; Tinti et al., 2005), suggest that the effective slip-weakening law might have a multiscale character not envisioned in the classical formulations of slip weakening. That multiscale character means that discernible weakening continues, at an ever diminishing rate with slip, out to large slips of the order of meters. Such response, when fitted to classical linear slip-weakening models has led instead to the interpretation that D_c depends on the slip in an earthquake $D_c = D_c(D_{\text{final}})$ (e.g., Ohnaka, 2003; Fukuyama and Mikumo, 2007).

2.1.3 Crack and Pulse-like Rupture

Seismological observations show that slip duration at a point can be relatively short compared to the duration of the entire rupture event (Heaton, 1990). A mechanism of such a healing of slip may be a feature of the constitutive relation. A possible interpretation is the association of healing of slip with strong heterogeneity of stress or strength on the fault plane (Beroza and Mikumo, 1996; Day et al., 1998). Another interpretation associates healing with strong rate-weakening in the constitutive relation (Cochard and Madariaga, 1996; Beeler and Tullis, 1996; Zheng and Rice, 1998; Nielsen and Carlson, 2000). If the healing of slip is caused by the constitutive relation, a fast restrengthening occurs immediately after the dynamic weakening, whereas if strength or stress heterogeneity controls slip duration, the stress remains near to or slightly below (dynamic overshoot) the kinetic friction level. A sketch for those two traction evolutions is shown in Figure 2.6. In the presence of a material discontinuity across the fault, the

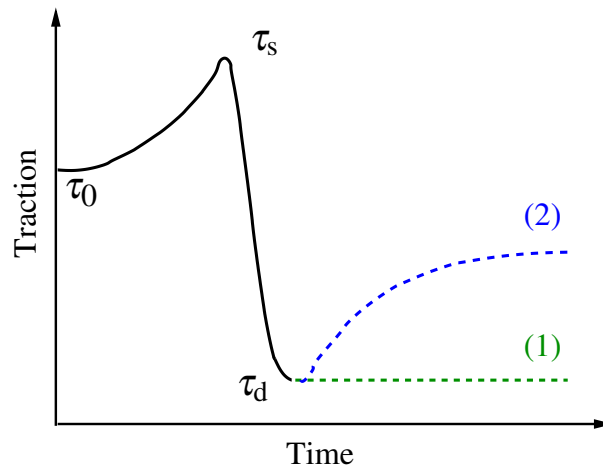


FIGURE 2.6: Schematic traction evolution at a point on the fault: dynamic traction increases from its initial value τ_0 to the upper yield stress τ_s and drops to the kinetic friction level τ_d . In evolution (1) slip occurs at a constant kinetic friction level, while for case (2) a fast restrengthening causes the healing of slip.

difference in elastic properties on the two sides of the fault plane can asymmetrically contribute

to healing (Weertman, 1980; Andrews and Ben-Zion, 1997). Other possibilities of induced healing are, e.g. abrupt cessation of a weakening mechanism by hydraulic cracking (Sibson, 1973), or abrupt increase of frictional resistance with the earliest phases of melting (Tsutsumi and Shimamoto, 1997; Hirose and Shimamoto, 2005). The understanding of what controls slip duration during real earthquakes is relevant to estimating frictional heating, radiated seismic energy, and the earthquake energy balance.

2.2 Fault as a Frictional Interface in an Elastic Medium

Since field observations indicate that slip of individual events on mature crustal faults occurs essentially within a very narrow zone of shear, the idealization of the earthquake source rupture as a dynamically running shear crack on a frictional interface embedded in a linearly elastic continuum is widely accepted as a useful approximation of coseismic fault evolution that allows for exploring dynamic behavior of spontaneous rupture propagation (e.g., Kostrov, 1964, 1966; Andrews, 1976a,b; Das and Aki, 1977; Day, 1982a,b; Fukuyama and Madariaga, 1998; Harris and Day, 1999; Dalguer et al., 2001). Since the frictional interface introduces a non-linear coupling of stress and strain as described by the governing constitutive law, the problem then can be seen as a partial differential equation with a non-linear boundary condition. There are no analytical solutions to such a system, and finding solutions requires computationally intensive numerical procedures to achieve approximate solutions. As discussed later, for the case that the interface separates two half spaces of different elastic properties (bimaterial case), grid independent numerical solutions are even harder to achieve than in the homogeneous case because the physical problem is extremely unstable (Weertman, 1980; Adams, 1998).

2.2.1 Elastodynamic Equations

Since an idealized earthquake fault can be seen as a mathematical plane with a governing friction law, that is embedded in a linear elastic medium, the system has to comply with the equations of motions. With ρ the density, \mathbf{v} the velocity vector, $\boldsymbol{\sigma}$ the stress-tensor, $\mathbf{c} = c_{ijkl}$ the elasticity tensor, $\dot{\boldsymbol{\epsilon}} = \dot{\epsilon}_{kl}$ the strain-rate tensor, the equations of motion in a three dimensional linear elastic anisotropic media without sources can be formulated in the following compact form:

$$\partial_t \mathbf{v} = \rho^{-1} \nabla \boldsymbol{\sigma}, \quad (2.4)$$

$$\partial_t \boldsymbol{\sigma} = \mathbf{c} \dot{\boldsymbol{\epsilon}}. \quad (2.5)$$

In the isotropic case the elastic tensor \mathbf{c} reduces to two independent elastic constant λ and μ and equation 2.5 can be written as

$$\partial_t \boldsymbol{\sigma} = \lambda (\nabla \cdot \mathbf{v}) \boldsymbol{\delta} + \mu (\nabla \mathbf{v} + \mathbf{v} \nabla), \quad (2.6)$$

with $\boldsymbol{\delta} = \delta_{ij}$ the Kronecker delta.

2.2.2 Fault Jump Conditions

Shear strength on a frictional interface is the frictional strength. As discussed in section 2.1.2 frictional strength evolves according to some specified friction law, and may (or may not) depend on many variables or parameters:

$$\dot{\tau}^s = \sigma_n^{\text{eff}} f(D, V, t, \theta, \gamma, \dots), \quad (2.7)$$

with σ_n^{eff} the effective normal stress, and f the friction coefficient, which, in general, can be a function of slip $D = |\mathbf{D}|$, slip velocity $V = |\mathbf{V}|$, time t and evolutionary variable of state θ and/or other mechanical or thermal variables or parameters γ . The frictional sliding on an interface is then governed by the fault velocity discontinuity (boundary) conditions in the following two equations:

$$\tau^s - |\boldsymbol{\tau}| \geq 0, \quad (2.8)$$

meaning that the amplitude of shear traction $\tau = |\boldsymbol{\tau}|$ on the interface cannot exceed the shear or frictional strength, and

$$\tau^s \mathbf{V} - \boldsymbol{\tau} |\mathbf{V}| = 0, \quad (2.9)$$

stipulating that any nonzero velocity discontinuity \mathbf{V} (vector of differential velocity or slip velocity) will be opposed by an antiparallel traction $\boldsymbol{\tau}$ with its amplitude equal to the frictional strength τ^s .

2.2.3 Numerical Implementation

Different numerical implementations have been developed until recently to solve the set of differential equations and boundary conditions given above (equations 2.4, 2.6, 2.7, 2.9). Although finite-differences are the most simple discretization approach, they have been proven to be efficient for many scientific problems and frictional boundary implementations for finite-differences have been developed and used since decades (e.g., Andrews, 1973, 1976a,b; Day, 1982a,b; Madariaga et al., 1998; Andrews, 1999) and adopted or improved in recent developments (e.g., Dalguer and Day, 2007a). Three different formulations are used later on: in chapter 3, a traction-at-split-node formulation as introduced by Andrews (1973), in chapter 4, a formulation introduced by Andrews (1999) (for details see appendix A.3), and in chapter 5, a

formulation introduced by Dalguer and Day (2007a) (see appendix A.2 for details).

The coding of the numerical schemes is done using the programming language Fortran. The language standards used comprise mostly the Fortran 95 standard, with a few Fortran 2003 language features that are already supported by recent compiler versions (ifort 10.1, gfortran 4.2), and a few other extensions which are generally available in most computing environments. The Fortran-code is parallelized using the Message Passing Interface (MPI), and can run on large parallel supercomputers such as the HLRB II of the Leibniz-Rechenzentrum (LRZ) in Munich. The software developed here is designed for a massive parallel environment and has been tested on up to 512 computational nodes using about 1 terra byte distributed memory (Brietzke et al., 2004). In principle it should be capable of even handling thousands of processes with several terra byte distributed memory for even larger computations of larger and/or more accurate models. The code can also run with a small model setup as a single process on a single processor, however, the MPI-library with a Fortran 90 interface must be present during compilation or execution. In addition to its dependence on the MPI-library, the program can optionally produce simple graphics output (exporting eps- and/or png-files). The graphics option is based on the fortran graphics subroutine library PGPLOT, developed by Pearson (1995-2002). For the case the graphics option is used, the number of MPI-processes and therefore the total size of a simulation is limited depending on the architecture of the used computer.

2.3 Bimaterial Interface

2.3.1 A Bimaterial Fault - a Common Feature

The juxtaposition of materials with dissimilar elastic properties is a general feature of tectonic faults in a variety of contexts and scales. Oceanic and continental crusts are brought into contact by subduction interfaces, normal and reverse faults offset vertical stratifications, and large strike-slip faults displace different crustal blocks and oceanic transforms juxtapose rocks of different ages. At the scale of the inner architecture of a fault zone, bimaterial interfaces associated with rock damage are present with various degrees of sharpness. An illustrating example for juxtaposition along a strike-slip fault is given in Figure 2.7. Failure along a bimaterial interface can also be relevant at the microscopic scale where grain boundaries are potential fracture surfaces and in the context of glacial quakes with slip at the interface between ice and rock. Moreover, bimaterial rupture is a prevalent mode of failure in composite engineering materials: impact-induced delamination of composite laminates, decohesion of adhesive joints in bonded structures, particle debonding in reinforced elastomers, fibre/matrix debonding and pull-out in fibre-reinforced materials, delamination of thin-film/substrate interfaces, etc.

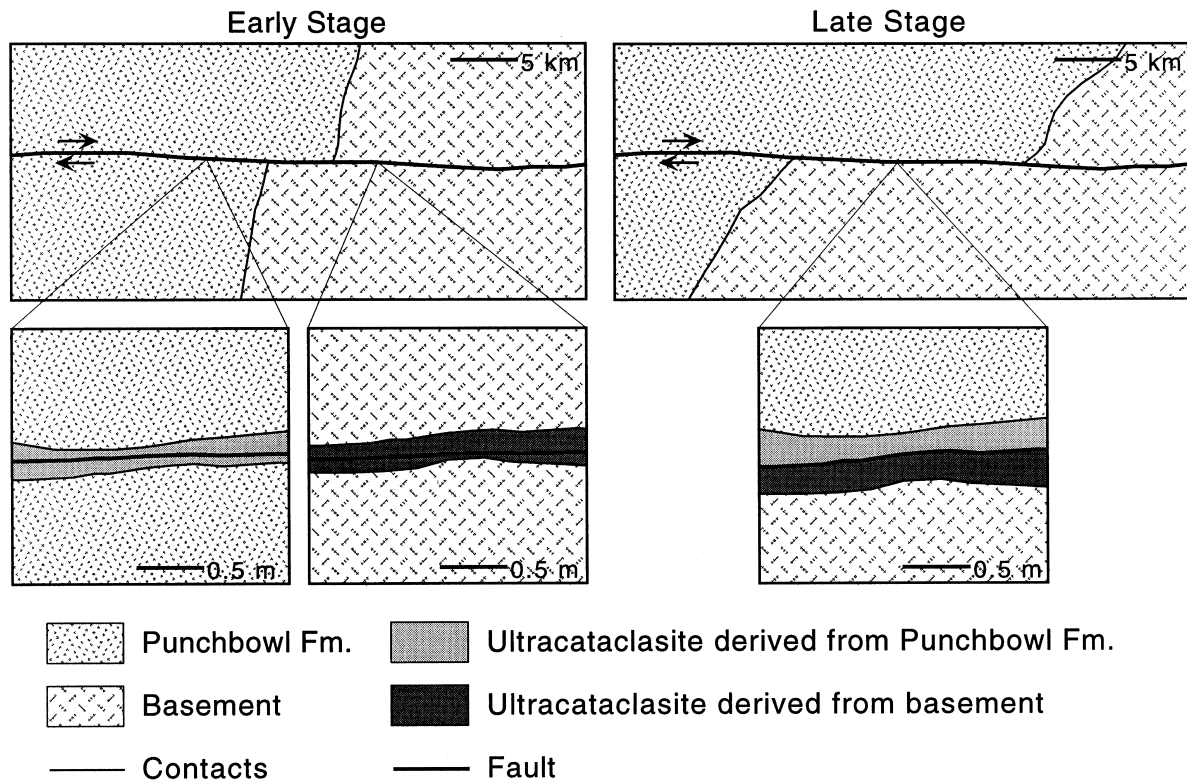


Fig. 6. Schematic illustrating a simple model for the formation and juxtaposition of the dark yellowish-brown and olive-black ultracataclasites. During the early stages of faulting some segments of the fault were wholly contained in the Punchbowl Formation or in the basement. In these segments the ultracataclasite is derived from a single host rock type. At late stages of faulting, after large displacement on the fault, the Punchbowl Formation and the basement are juxtaposed. Translation of the brown and black ultracataclasites with the host rock places the ultracataclasite in contact.

FIGURE 2.7: Evidence for juxtaposition of materials with dissimilar elastic properties at the Punchbowl fault (taken from Chester and Chester (1998)).

2.3.2 Bimaterial Mechanics

On an interface between identical materials with Coulomb friction (constant friction coefficient) and initial stress below frictional strength, any event nucleated, no matter how forcefully it is initiated in the nucleation zone, will ultimately die due to the lack of dynamic reduction in frictional strength. Therefore, the reduction of frictional strength $\tau^s = \sigma_n^{\text{eff}} f$ is caused by the reduction of friction coefficient f from static to dynamic values (Brace and Byerlee, 1966) (see equation 2.7) in traditional earthquake models. Later it has been suggested that a reduction of normal stress σ_n^{eff} during spatially nonuniform slip on a bimaterial interface might also be responsible for dynamic weakening of faults during earthquakes (Weertman, 1980). It has been found that in the case of a constant friction coefficient and existing generalized Rayleigh wave speed (see appendix B.6 for details), there exists a steady state propagating slip pulse solution (Adams, 1998; Rice, 1997). The existence of such a pulse has been suggested before by Weertman (1980). This pulse is often referred to as the Weertman pulse or the Adams' steady state pulse (see appendix B.5 for details).

With dissimilar materials one would ideally wish to use Coulomb friction, to study the instability due to material contrast independently from other, more classical sources of instabilities (e.g., slip- or rate-dependent friction). It has been mentioned by Ben-Zion (2001) that in-plane ruptures on planar bimaterial interfaces have remarkable dynamic properties that may be relevant to many different issues of basic and applied science in general. In contrary to the dissension on whether or not the effect is important in earthquakes, it is well established theoretically that frictional sliding with constant friction coefficient f (Coulomb friction) between elastic solids with different elastic properties is unstable for a wide range of material pairs and friction coefficients characteristic of natural faults (Renardy, 1992; Adams, 1995; Ranjith and Rice, 2001). For the case that the contrast of wave-speeds across the fault is less than about 30%, an interfacial wave known as the generalized Rayleigh wave exists for frictionless contact and no opening (Weertman, 1963; Achenbach and Epstein, 1967). The range of the velocity contrast across the San Andreas and other large faults is estimated to be about up to 30%, with values of 5 - 20% often reported (Feng and McEvilly, 1983; Eberhart-Phillips and Michael, 1998; Tanimoto and Prindle Sheldrake, 2002; Fuis et al., 2003).

An interface without friction generates two generalized Rayleigh waves when perturbed. These propagate in opposite directions with a subshear propagation velocity and are concatenated with changes in normal stress that is tensile in one direction and compressive in the antipodal direction. When an arbitrarily small amount of friction is added, shear and normal tractions on the interface become coupled and the wave associated with tensile change of normal stress becomes unstable, while the wave associated with compressive change of normal stress is damped and therefore stabilized the (Ranjith and Rice, 2001).

Andrews and Ben-Zion (1997); Ben-Zion and Andrews (1998) generated pulses of slip caused by such a bimaterial induced instability. One property of these pulses is that they typ-

ically propagate unilaterally away from a localized nucleation region. Friction coefficient was taken constant $f = \text{const}$, and the remote loading ratio of shear to effective normal stress on the fault was less than f but nevertheless the pulses could propagate in a self-sustaining manner after the instability was triggered by a transient decrease in effective normal stress in a limited space-time region of elliptical shape. Due to the tensional motion during the passage of such a pulse of slip Andrews and Ben-Zion (1997) characterized the pulse by the analogon of a wrinkle in a carpet. Therefore the unidirectional self-sustaining pulse on a bimaterial interface associated with the theoretical prediction of Weertman (1980) is often called wrinkle-like slip pulse. Harris and Day (1997) modeled slip on a bimaterial interface with a drop of the friction coefficient f from static to dynamic values with increasing slip. In their simulations ruptures started bilaterally and the bimaterial effect revealed by introducing asymmetry in rupture propagation velocity as well as the amplitude of slip velocities at the tip of the crack. While many studies focus on the pure dynamic bimaterial effect Harris and Day (1997) allowed for a mixing of frictional and bimaterial induced instabilities, and therefore address the question of whether or not the bimaterial weakening effect is important during earthquakes. Andrews and Harris (2005) tried to address this issue invoking considerable debate lately, with some authors arguing that bimaterial weakening effects are important during earthquakes (e.g., Ben-Zion, 2006a,b), while others claim they are not (e.g., Andrews and Harris, 2005; Harris and Day, 2005). Recent more elaborate studies unsurprisingly indicate that the influence of the dynamic bimaterial effect on earthquake dynamics can depend on the choice of the physical model and corresponding parameters which are often not well constraint (Ampuero and Ben-Zion, 2008; Dunham and Rice, 2008). Hence, a definite and comprehensive answer on whether the bimaterial mechanism is important in earthquake source dynamics cannot be given. On the contrary, strong and clear statements have been made by Andrews and Harris (2005); Harris and Day (2005) on the basis of very limited calculations.

2.3.3 Ill-posedness, Regularization and Numerical Convergence

It has been shown by Renardy (1992); Martins and Simões (1995) for the particular case of an elastic solid sliding against a rigid body and by Adams (1995) for the general case of two elastic bodies that sliding at a planar bimaterial interface under Coulomb friction does not possess any solution. Ranjith and Rice (2001) showed that sliding between dissimilar materials at constant f is ill-posed. Both, the elastic response and the friction law do not contain characteristic length or time scales and therefore the growth rate of unstable Fourier modes is proportional to their wavenumber. This prevents the construction of a general solution from superposition of modes since the growth rate of the highest wavenumber modes is unbounded. A connection between the existence of the generalized Rayleigh wave and the ill-posed nature of the problem has been found (Ranjith and Rice, 2001): when the material pair is such that the generalized Rayleigh wave speed is defined, the problem is ill-posed for any value of the friction coefficient, whereas,

when it is not defined, the problem remains ill-posed for values of the friction coefficient larger than a critical value. As a consequence numerical solutions with Coulomb friction (constant friction coefficient $f = \text{const.}$) do not converge with refinement of the numerical mesh. A regularization of the problem can be achieved when the response of normal and shear stress are non-instantaneous, hence a scale of time or displacement is introduced over which shear traction $\tau = f\sigma$ evolves after a change of normal stress σ (Ranjith and Rice, 2001). Friction with a piecewise constant friction (e.g., slip-weakening friction) does not provide regularization.

In experiments of high-speed sliding a non-instantaneous response of traction was found (Prakash and Clifton, 1993; Prakash, 1998). While other experiments at slower slip speeds provide an instantaneous coupling of the evolution (e.g., Linker and Dieterich, 1992; Richardson and Marone, 1999; Boettcher and Marone, 2004; Hong and Marone, 2005).

The cases studied by (Andrews and Ben-Zion, 1997) have been repeated and extended by Cochard and Rice (2000) using a regularized Coulomb friction. Cochard and Rice (2000) discussed and numerically demonstrated the ill-posedness of the problem with constant friction and achieved convergent solutions with regularization of the problem. The results of the regularized problem achieved by Cochard and Rice (2000) demonstrated that some features (e.g., rupture propagation velocity, unilateral propagation, self-amplification) were similar to the original, unregularized ones and can therefore be called stable features. However, other features (e.g., pulse-splitting) were grid-dependend artifacts of the ill-posed problem. The regularization procedure described above does not stabilize any modes, but instead forces the growth rate to asymptotically vanish with decreasing wavelength. To stabilize the self-amplifying behavior other mechanism have to be introduced or allowed, e.g., divergence might be mitigated by permitting fault opening instead of permitting normal stresses to become tensile (Dalguer and Day, 2007a), or plastic deformation of the medium (Ben-Zion and Shi, 2005). Recent laboratory experiments confirmed many of the phenomena described in the earlier numerical studies (Xia et al., 2005). In particular, the laboratory ruptures took the form of bilaterally expanding cracks like in Harris and Day (1997), whose tips traveled at different speeds as in Cochard and Rice (2000). The findings of Ranjith and Rice (2001) have been summarized in a table by Cochard and Rice (2000), which can be seen in Figure 2.8.

		20% contrast; c_{GR} defined	30% contrast; c_{GR} not defined
		0	0
		$f_{crit} \approx 0.22$	$f_{crit1} \approx 0.15$ $f_{crit2} \approx 1.75$
		$+\infty$	$+\infty$
Coulomb law	Modal analysis	Unstable modes, R independent of k $V_{prop} \approx +c_{GR}$ $V_{prop} \approx +c_{GR}$ and/or $ V_{prop} \gtrsim P_{slow} (V_{prop} < 0)$	Stable modes Unstable modes, R independent of k $V_{prop} \approx +S_{slow}$ $V_{prop} \approx +S_{slow}$ and/or $ V_{prop} \gtrsim P_{slow} (V_{prop} < 0)$
	Realistic cases	Ill posed: no convergence through grid size reduction	Well posed; only dying pulses Ill posed: no convergence through grid size reduction
Modified Prakash-Clifton law	Modal analysis	Unstable modes V_{prop} (weak) function of k R function of k	Stable modes Unstable modes V_{prop} (weak) function of k for $k < k_{crit1}$ for $k < k_{crit2}$ ($k_{crit2} > k_{crit1}$)
	Realistic cases	Regularization of ill-posedness at large k Self-sustained pulses may propagate at $V_r \lesssim +c_{GR}$ $V_r \lesssim +c_{GR}$ and/or $V_r \approx -P_{slow}$	Well posed; only dying pulses Regularization of ill-posedness Self-sustained pulses may propagate at $V_r \approx +S_{slow}$ $V_r \approx +S_{slow}$ and/or $V_r \approx -P_{slow}$

Figure 12. Summary of results, with link to *Ranjith and Rice* [2000] modal analysis. R is normalized growth rate (see Figure 2); k is mode number; V_{prop} is propagation velocity of harmonic modes; V_r is propagation velocity of pulses in simulations like reported here. Sign of propagation velocities refers to the direction of propagation, plus being that of the direction of slip in the more compliant medium, minus being the opposite direction. Note the closeness between the theoretical V_{prop} for the Coulomb law and the numerically observed V_r for simulations that have been made possible through the regularization with the Prakash-Clifton law.

FIGURE 2.8: Table showing propagation modes at a bimaterial interface with Coulomb friction and regularized Coulomb friction (modified Prakash-Clifton friction) in theoretical modal analysis and numerical calculations (Cochard and Rice, 2000).

Motivation for Coming Chapter

Many studies (e.g., Andrews and Ben-Zion, 1997; Ben-Zion and Andrews, 1998; Cochard and Rice, 2000; Ben-Zion and Shi, 2005, and references therein) addressed the question of what are the properties and behavior of the wrinkle-like slip pulse? However, one shortcoming of all previous theoretical and numerical works on this topic is that the path of rupture propagation was prescribed rather than being allowed to develop spontaneously. This is very important for resolving whether the remarkable dynamic phenomena associated with rupture along material interfaces occur only for a (perhaps small) subset of ruptures with hypocenters at the interface, or whether they also tend to occur in the more general case of hypocenters in a volume surrounding material interfaces. Chapter 3 “Examining Tendencies of In-plane Rupture to Migrate to Material Interfaces” (after Brietzke and Ben-Zion, 2006) presents a systematic parameter-space study in a clearly-defined theoretical context. The model comprises possible simultaneous slip along multiple 2D in-plane faults with Coulomb friction within a structure of a low velocity zone embedded in-between two different elastic materials.

Chapter 3

Examining Tendencies of In-plane Rupture to Migrate to Material Interfaces

This chapter presents the work of Brietzke and Ben-Zion (2006) in a slightly modified form.

Gilbert B. Brietzke¹, Yehuda Ben-Zion²

¹ Department für Geo- und Umweltwissenschaften, Sektion Geophysik, Ludwig-Maximilians-Universität München, Theresienstrasse 41, 80333 München, Germany.

² Department of Earth Sciences, University of Southern California, Los Angeles, CA 90089-0740, USA.

Summary

We perform a numerical parameter-space study of two-dimensional in-plane ruptures in a model consisting of two different half spaces separated by a low velocity layer and possible simultaneous slip along multiple faults. Ruptures are nucleated by a bilateral expanding stress drop in a limited source region, and may continue to propagate spontaneously (or not) along one or several faults. Most calculations are done for purely elastic media and faults governed by Coulomb friction, but some simulations employ Prakash-Clifton friction and Kelvin-Voigt viscosity. The faults, two of which are material interfaces, are situated equidistant and parallel to each other. Using different nucleation locations, different initial stress, different velocity contrasts, different frictional fault separations, different widths of a low velocity zone, and different number of faults, we examine the range of conditions for which ruptures migrate to other faults and continue to propagate in a self-sustaining manner. The model produces diverse migration and propagation phenomena represented by several phase diagrams. However, a general result of the study is that ruptures tend to migrate to the material interfaces and become self-sustained wrinkle-like pulses for wide ranges of conditions. The wrinkle-like pulses propagate along each material interface unilaterally in the direction of motion on the

more compliant side of the interface (referred to as the "positive" direction). The existence of a large number of faults produces, like viscosity, distributed deformation that reduces the divergent behavior of the wrinkle-like pulses. In many cases, ruptures migrate to the interface with the stronger contrast and propagate unilaterally in the positive direction associated with that interface and the overall contrast across the fault zone. In smaller number of cases, ruptures migrate to the interface with the weaker contrast and propagate unilaterally in the opposite positive direction associated with that interface. For various parameter combinations, self-sustained unilateral pulses travel simultaneously, in the two opposite positive directions, along the interfaces on the opposite sides of the low velocity layer. A low resolution imaging of these ruptures would lead to an inference on bilateral propagation. The M6, September 2004, Parkfield California earthquake may provide a natural example of such a case.

Keywords: dynamic rupture, material interfaces, fault-zone structure, friction, rupture migration, numerical simulations.

3.1 Introduction

Active faulting over geological times brings into contact materials that were originally separated and are thus likely to have different elastic properties. In some cases, large faults nucleate and grow along a pre-existing suture that separates different lithologies. Recent geological mapping in the structure of several large strike slip fault zones indicates that the principal slip zones of large earthquakes are localized along interfaces that separate rock units with considerably different properties (Dor et al., 2006b,a). The slip zones in lab experiments that include material interfaces (e.g., due to the presence of a gouge layer) also tend to localized along such interfaces. Contrasts of elastic properties across large faults have been imaged by seismic reflection and refraction studies (e.g., Fuis et al., 2001, 2003; Lutter et al., 2004), body and coda wave tomography (e.g., Eberhart-Phillips and Michael, 1998; Magistrale and Sanders, 1995; Shapiro et al., 2005), modeling of geodetic data (Le Pichon et al., 2005) and analysis of head waves that refract along material interfaces in the fault zone structure (Ben-Zion and Malin, 1991; Ben-Zion et al., 1992; McGuire and Ben-Zion, 2005). Estimates of the seismic velocity contrasts across the San Andreas and other large faults range from a few percent to more than 30%, depending on the geographical location and resolution of the employed imaging method. In addition, the faulting process produces in the top few km of the crust localized belts of damaged fault zone rocks that act as trapping structures for seismic waves (e.g., Ben-Zion et al., 2003; Peng et al., 2003; Fohrmann et al., 2004; Lewis et al., 2005) and are also manifested by fault-related anisotropy (e.g., Zhang and Schwartz, 1994; Peng and Ben-Zion, 2004). In some cases, the opposite sides of a fault are separated by a layer (sliver) of rock with faster velocity than one or both sides of the fault. This holds, e.g., for a portion of the Bear valley section of the San Andreas fault (McGuire and Ben-Zion, 2005).

There are fundamental differences between properties of dynamic ruptures on faults that do or do not separate different elastic solids. On a planar fault between solids with identical elastic properties, there is no coupling between slip and changes of normal traction. On the other hand, mode II (in-plane) rupture along a material interface generates local changes of normal stress that are proportional to the spatial derivative of slip Weertman (1980); Adams (1995); Ben-Zion (2001); Ranjith and Rice (2001). This produces dynamic dilation at the tip that propagates in the direction of slip on the more compliant side of the fault (referred to below as the "positive" direction) and dynamic compression at the tip propagating in the opposite direction (referred to as the "negative" direction). The magnitudes of these effects increase with the rupture velocity and the degree of velocity contrast across the fault, up to about 30-40% contrast beyond which the generalized Rayleigh wave speed C_{GR} does not exist (e.g., Weertman, 1980; Ben-Zion and Andrews, 1998; Ben-Zion, 2001). In addition, the dynamic changes of normal stress increase with propagation distance along the material interface due to a dynamic instability (Adams, 1995, 1998) that produces a continual transfer of energy to shorter wavelengths during rupture propagation. The Adams (1995; 1998) instability reduces dynamically the physical length

scales such as the width of the rupture pulse or the crack-tip region with high slip-velocity. This leads to a grid-size dependency in simulations with purely elastic materials and instantaneous Coulomb-like relation between the frictional strength and normal stress (e.g., Cochard and Rice, 2000; Ranjith and Rice, 2001; Ben-Zion and Huang, 2002). The Adams instability can be regularized using a Prakash-Clifton friction law (Prakash and Clifton, 1993; Prakash, 1998) with a gradual response to changes of normal stress (Cochard and Rice, 2000; Ben-Zion and Huang, 2002), using artificial viscosity that damps short wavelength features (S. Day, personal comm., 2003), incorporation of plastic yielding off the fault (Ben-Zion and Shi, 2005), and other mechanisms that suppress the development of small scale aspects of the response (e.g., Ben-Zion, 2001). However, the inclusion of any such ingredient changes the physical problem that is being solved and increases the number of model parameters.

Previous analytical and numerical parameter-space studies indicate (Weertman, 1980; Adams, 1995; Andrews and Ben-Zion, 1997; Ben-Zion and Andrews, 1998; Ben-Zion and Huang, 2002; Cochard and Rice, 2000; Ranjith and Rice, 2001; Shi and Ben-Zion, 2006) that mode II rupture along a material interface with slip-independent friction can propagate in a self-sustaining manner, for ranges of frictional parameters, material contrasts, and stress/strength heterogeneities, as a unidirectional "wrinkle-like" pulse that propagates in the positive direction with a speed close to C_{GR} . Adams (2001), Ranjith and Rice (2001) and Cochard and Rice (2000) showed that slip pulses with a velocity near that of the slower P wave can also propagate along a material interface in the negative direction. However, these pulses are considerably weaker than the primary wrinkle-like pulses in the positive direction and are unlikely to evolve to self-sustaining ruptures. Characteristic features of the wrinkle-like pulse include: 1) strong correlation between variations of normal stress and slip, 2) strongly asymmetric motion across the fault, 3) self-sharpening with propagation distance, and 4) preferred direction of rupture propagation. Cochard and Rice (2000) and Ranjith and Rice (2001) suggested that the regularized Prakash-Clifton friction law can suppress the divergent behavior associated with feature (3). However, subsequent calculations for large propagation distance (Ben-Zion and Huang, 2002) and analytical work (Adda-Bedia and Ben Amar, 2003) showed that the divergent behavior persists even with the Prakash-Clifton friction. Ben-Zion and Huang (2002) found that the parameters of the regularized Prakash-Clifton friction law have to be fine-tuned to produce (with a fixed set of material properties) apparent stability for a given propagation distance, rendering that friction law unsuitable for a systematic parameter-space study.

Numerical simulations of rupture along a material interface governed by slip-weakening friction produced results that depend strongly on the nucleation procedure. The employed procedures belong generally to the following two classes (Ben-Zion, 2006a,b). Class (I) is associated with relatively small and strong nucleation phases mimicking the initiation of a cascade-type process by a failure of a strong asperity (e.g., Andrews and Ben-Zion, 1997). Such cases generate for wide ranges of frictional and material contrast conditions ruptures that

evolve with sufficient propagation distance to wrinkle-like pulses similar to those generated with slip-independent friction (Shi and Ben-Zion, 2006). Class (II) studies with slip-weakening friction involves relatively large nucleation phases mimicking the final stage of a quasi-static growth of a slip patch to a critical size needed to produce macroscopic dynamic instability in a homogenous medium. The associated critical patch size scales in laboratory experiments with the largest wavelength of the roughness characterizing the sliding surfaces (e.g., Ohnaka, 1996). Such cases generate bilateral cracks with a wrinkle-like pulse superposed at the tip propagating in the positive direction (e.g., Harris and Day, 1997). The superposed wrinkle-like pulse produces higher slip velocity near the tip propagating in the positive direction than at the other rupture front. Recent simulations with fine resolution of sharp dynamical features generated (Rubin and Ampuero, 2007) very prominent asymmetry of slip velocities at the opposite rupture fronts. In those calculations, the strong asymmetry of slip velocities at the opposite crack tips can not manifest itself into macroscopic rupture asymmetry. However, incorporating in the simulations rate-dependent friction compatible with experiments of rock friction at high slip rates (e.g., Tsutsumi and Shimamoto, 1997; Di Toro et al., 2004) is expected to produce larger stress drop in the positive direction, leading to asymmetric rupture with larger energy release in the positive direction (Ben-Zion, 2006b). This expectation should be tested in a future work.

On polished man-made interfaces, having roughness only over very short wavelengths, dynamic instabilities are likely to be initiated by nucleation phases of class (II). On large fractal-like surfaces, however, class (I) may be realized first since the required critical patch of class (II) is essentially the size of the entire surface. On realistic natural surfaces with roughness over broad bandwidth, a nucleation phase of class (II) in a small spatial domain may trigger a stronger nucleation phase of class (I). The same may hold for other types of strength heterogeneities. These cases are likely to excite on a material interface the wrinkle-like mode of rupture Ben-Zion (2006b). Clarifying the ability of different nucleation phases to excite different modes of rupture, and the relation of the various proposed nucleation mechanisms to natural faulting, are important topics for continuing theoretical and observational studies. Here we simply note that rupture on a material interface tends to evolve, for realistic classes of nucleation mechanisms and constitutive laws, to a wrinkle-like pulse with properties similar to those associated with the simple Coulomb friction.

One shortcoming of all previous works in this topic is that the path of rupture propagation was prescribed rather than being allowed to develop spontaneously. While material interfaces are mechanically efficient failure surfaces due to the dynamic reduction of normal stress in the positive direction, it is not clear for which conditions ruptures that start in the bulk would migrate on their own to material interfaces. We test in a well defined model with a typical fault-zone velocity structure how unstable slip on multiple possible faults localize as a pure material contrast effect. Resolution of this issue is important to clarifying whether the remarkable dynamic phenomena associated with rupture along material interfaces occur only for a (perhaps

small) subset of ruptures with hypocenters at the interface, or whether they also tend to occur in the more general case of hypocenters in a volume surrounding material interfaces. In the present paper we address this issue by performing a numerical parameter-space study in a model having a compliant layer between two different elastic blocks and a number of possible rupture planes, two of which are material interfaces. Ruptures are nucleated in different positions within the compliant layer or in the surrounding blocks and we examine the conditions (velocity structure, initial stress, assumed rheology) for which ruptures migrate spontaneously to a material interface.

The results of Ben-Zion and Huang (2002) and Shi and Ben-Zion (2006), and persistence of features (1)-(4) of the wrinkle-like pulse in simulations with Coulomb, Prakash-Clifton, and slip-weakening friction laws, and the foregoing discussed indicate that the simple Coulomb friction provides a useful constitutive law for exploring general tendencies associated with rupture along a material interface. Given the complexity of the problem and large number of possible parameters, most simulations of this work employ the simple Coulomb friction and purely elastic materials. Some simulations are performed with Kelvin-Voigt viscosity in the bulk or the regularized Prakash-Clifton friction on faults.

The results show that ruptures tend to migrate spontaneously to the material interfaces and continue to propagate there in a self-sustaining manner for broad ranges of conditions. In some cases, ruptures migrate simultaneously to the material interfaces on the opposite sides of the low velocity layer and propagate along both interfaces in the two (opposite) positive directions, creating together an apparent bilateral rupture. In other cases, ruptures propagate in the positive direction along the interface with weaker material contrast, which is the opposite preferred direction associated with the overall contrast across the fault. Low resolution imaging of such cases may be interpreted erroneously as violating the prediction of a preferred propagation direction along a material interface.

3.2 Methods and Model Setup

3.2.1 Finite-Difference Method and Fault Model

We perform 2D numerical simulations of in-plane rupture in a model (Fig. 3.1) consisting of two different half spaces separated by a fault zone layer, which is the medium with lowest seismic velocity, and a number of possible rupture planes. As noted by Ben-Zion (2006a), the 2D in-plane calculations may be understood to represent ruptures that already saturated the seismogenic zone of a strike-slip fault and continue to propagate as in-plane ruptures. Modeling the initial transient regime, where small earthquakes grow as mixed in-plane and anti-plane ruptures, requires 3-D calculations. Some results associated with this transient mixed-mode regime can be found in Harris and Day (2005).

The simulations employ a version of the code used by Andrews and Ben-Zion (1997), Ben-Zion and Andrews (1998) and Ben-Zion and Huang (2002) that can account for simultaneous rupture on multiple faults. The calculations are based on a staggered velocity-stress finite-difference formulation of the governing elastodynamic equations on a triangular grid. Frictional sliding on a set of predetermined possible rupture planes is calculated using the traction at split-node sliding logic described by Andrews (1973). If the ratio of the x - and y -traction components exceeds the static coefficient of friction on a fault, slip begins and continues until the slip velocity tends to change sign. The frictional strength is proportional to the compressive normal stress and most calculations employ a constant coefficient of friction (i.e., Coulomb friction). The set of possible fault planes are defined along the space dimension (the x coordinate) parallel to the material interfaces, which are two possible rupture plane. The other faults are situated equidistantly to each other across the material interfaces, so that each medium has a number of possible rupture planes.

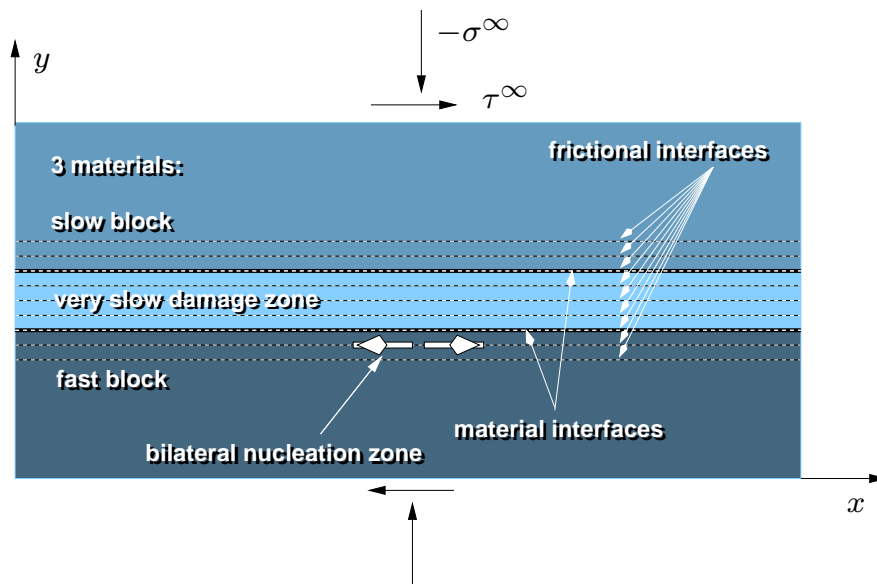


FIGURE 3.1: A sketch of the general model setup in this study, consisting of three materials and multiple parallel frictional interfaces.

In principle the number of faults that can be defined in our code is limited by the number of grid-points along one dimension. However, in most of our calculations the number of frictional interfaces is fixed to nine faults: four faults outside the fault zone layer (two on each side), three faults inside the fault zone layer, and two faults on the material interfaces. We use the following different fault-separations $y_{fs} = 7$ m, 14 m, 21 m. The width of the fault zone layer is coupled to the fault separation as $4y_{fs} = y_{vl}$, so $y_{vl} = 28$ m, 56 m, 84 m.

The initial shear stress varies between 64 MPa and 72 MPa and the nucleation locations are $y_{\text{nuc}} = \{\text{fault 1, fault 2, \dots, fault 9}\}$. In all cases we use the following two sets of velocity contrasts: $\Delta v_1 = \{v_{s_2}/v_{s_1}, v_{s_3}/v_{s_1}\} = \{0.85, 0.94\}$ and $\Delta v_2 = \{v_{s_2}/v_{s_1}, v_{s_3}/v_{s_1}\} = \{0.75, 0.90\}$. The range of the investigated parameters is summarized in table 3.1.

parameter	symbol	value range	unit
friction coefficient	f	0.75	1
initial shear stress	τ^∞	64 ... 72	MPa
initial normal stress	σ^∞	100	MPa
grid-spacing	Δx	0.5	m
propagation distance	x_{pd}	$\approx -850 \dots +850$	m
fault separation	y_{fs}	7, 14, 21	m
width of fault zone layer	y_{lvl}	28, 56, 84	m
width of nucleating pulse	w_{nuc}	≤ 20	m
total size of nucleation zone	\varnothing_{nuc}	120	m
nucleation locations	y_{nuc}	fault 1 ... fault 9	1
number of materials	n_{mat}	1 ... 3	1
density $n_{\text{mat}} = 1$	ρ_1	3333.3	kg/m ³
density $n_{\text{mat}} = 2$	ρ_2	2666.7 ... 2898.5	kg/m ³
density $n_{\text{mat}} = 3$	ρ_3	3030.3 ... 3144.7	kg/m ³
s-wave velocity $n_{\text{mat}} = 1$	v_{s_1}	3000.0	m/s
s-wave velocity $n_{\text{mat}} = 2$	v_{s_2}	2400.0 ... 2608.7	m/s
s-wave velocity $n_{\text{mat}} = 3$	v_{s_3}	2727.3 ... 2830.2	m/s
p-wave velocity $n_{\text{mat}} = 1$	v_{p_1}	5196.2	m/s
p-wave velocity $n_{\text{mat}} = 2$	v_{p_2}	4156.9 ... 4518.4	m/s
p-wave velocity $n_{\text{mat}} = 3$	v_{p_3}	4723.8 ... 4902.0	m/s
nucleation velocity	v_{nuc}	2394 ... 2549	m/s

TABLE 3.1: Range of simulation parameters.

We ensure that all results shown in this study are free of artificial reflections or wrap around from the model boundaries by always choosing the model big enough for the investigated time interval.

3.2.2 Nucleation Procedure

To prevent a bias for rupture propagation direction by the nucleation procedure, we nucleate each event bilaterally and symmetrically by increasing the fluid pressure in two limited space-time regions. This generalizes the nucleation procedure of Andrews and Ben-Zion (1997) of a traveling drop of normal stress to the symmetrically expanding case, i.e. two drops of normal stress that propagate within the nucleation region in the opposite directions. Using a syntax similar to the one of Andrews and Ben-Zion (1997), the coordinates for the two pulses traveling in the opposite directions are $\xi = (|x| - v_{\text{nuc}}t)/a$, $\eta = (|x| + v_{\text{nuc}}t)/b - \eta_0$, $\eta_0 = \sqrt{a^2 + b^2}/b$,

and the boundary of the two sources are the ellipses $1 - \xi^2 - \eta^2 = 0$. Within the two elliptical sources, the fluid pressure is given as $P_f = P_0 (1 - \xi^2 - \eta^2)^2$, while outside those regions it is zero. The width of the pulse and the overall size of the nucleation zone are denoted as $w_{\text{nuc}} \leq 2a$ and $\varnothing_{\text{nuc}} = 2b$.

Rupture along a material interface tends to propagate at the generalized Rayleigh wave speed C_{GR} , which maximizes the interaction between in-plane slip and dynamic changes of normal stress (e.g., Weertman, 1980; Ben-Zion, 2001; Ranjith and Rice, 2001). The generalized Rayleigh wave is a phase that propagates along a material discontinuity interface and reduces to the regular Rayleigh wave when the two materials are the same (Weertman, 1963; Achenbach and Epstein, 1967). To have a smooth transition from the initiation procedure and continuing propagation, the nucleation velocity v_{nuc} in our study is taken to be close to C_{GR} of the strongest material contrast. We tested the sensitivity of the model response to different nucleation velocities and found that with nucleation velocities substantially less than C_{GR} , self-sustaining pulses on the interfaces always start traveling with a speed close to the generalized Rayleigh velocity. Additional results related to this issue can be found in Shi and Ben-Zion (2006). Since the main focus of the study is to examine migration patterns of ruptures, we conduct a large number of simulations in which the nucleation zone, dictating the initial rupture position, is varied systematically across the structure.

3.3 Initial Results and Choice of Model Parameters

3.3.1 Influence of Viscosity

In this section we perform calculations that incorporate Kelvin-Voigt Viscosity, whose mechanical analogue is a system of a dash-pot and a spring in parallel (Figure 3.2). Our goal is not to provide a complete regularization of the problem but rather to illustrate the effects of viscosity.

The incorporation of viscosity introduces a length scale into the problem that can stabilize the Adams (1995) instability. Harris and Day (1997) simulated ruptures along a material interface governed by a slip-weakening friction in a model consisting of a low velocity layer between two half spaces. Although their calculations incorporated viscosity to reduce numerical oscillations, they encountered numerical difficulties associated with grid size dependency. As discussed by Ben-Zion (2001), however, a viscosity associated with exponential attenuation with amplitude larger than a value determined by the Adams (1995) instability, can regularize the problem. This was confirmed by S. Day (personal comm., 2003).

The stress-strain relation of a Kelvin-Voigt visco-elastic body in 2D can be written as: $\boldsymbol{\sigma} = 2c\boldsymbol{\varepsilon} + C2c\dot{\boldsymbol{\varepsilon}}\Delta x/v_p$ with $c = ((\lambda + 2\mu, \lambda, 0), (\lambda, \lambda + 2\mu, 0), (0, 0, \mu))$, $\boldsymbol{\sigma} = (\sigma_{xx}, \sigma_{yy}, \sigma_{xy})$, $\boldsymbol{\varepsilon} = (\varepsilon_{xx}, \varepsilon_{yy}, \varepsilon_{xy})$, and C being a non-dimensional viscosity parameter defined in Andrews (1973). Identifying $\eta = Cc\Delta x/v_p$ as the Kelvin-Voigt viscosity, the governing equation becomes $\boldsymbol{\sigma} =$

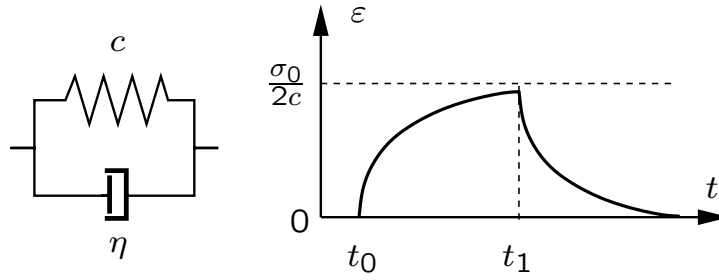


FIGURE 3.2: The response of Kelvin-Voigt viscosity in a model consisting of a spring and a dash-pot in parallel. The viscosity introduces non-instantaneous gradual evolution of stress and strain. The graph shows the response of to a constant applied stress $\sigma(t) = \sigma_0$ for $t_0 < t < t_1$, and abruptly released stress $\sigma(t_1) \leq \sigma_0$.

$2c\epsilon + 2\eta\dot{\epsilon}$. The ordinary differential equation of a dash-pot and a spring in parallel $\sigma = 2c\epsilon + 2\eta\dot{\epsilon}$ has the well known analytical solution $\epsilon = (\int 1/2\eta^{-1}\sigma e^{\frac{t}{\eta}} dt + const.)e^{-\frac{t}{\eta}}$.

We eliminate the grid-dependency of the viscosity by dividing η by Δx , so η in our study becomes $\eta = Cc/v_p$ and the formerly non-dimensional parameter C has in our study the dimension of length-scale. With the above implementation we can achieve some regularization of the Adams (1995) instability, as shown below in the context of a model configuration with a single material interface (Fig. 3.3). However, the existence of viscous deformation changes additional aspects of the dynamics, since it leads to energy dissipation in the bulk. Unfortunately, this requires changes of other parameters, such as the initial shear stress or frictional strength, to obtain the same reference solution. Nevertheless, for a given rupture propagation distance and a fixed set of model parameters (e.g., material contrast, pre-stress, friction coefficient, etc.) one can find a value of the Kelvin-Voigt viscosity such that the results collapse with several grid refinements to the same solution. This is illustrated in Figure 3.4 where the normal-stress, shear-stress and slip-velocity are seen to converge to the same solution with grid-refinement at the distance of investigation ($x = 100$ m).

In cases where the wrinkle-like rupture pulse is self-amplifying (Ben-Zion and Andrews, 1998; Ben-Zion and Huang, 2002), this convergence is limited due to the growing instability beyond a certain propagation distance. However, increasing the viscous component of deformation can always suppress the self-amplification and lead to dying rupture pulses only. The existence of either self-amplifying or dying pulses, and required fine-tuning for a given propagation distance, is similar to the behavior encountered with material interface governed by the Prakash-Clifton friction (Ben-Zion and Huang, 2002). Exploratory calculations for sets of cases with Coulomb frictional interfaces in the general model configuration of Figure 3.1 show that general aspects of the solution (self-sharpening, approximate rupture velocity, overall tendencies of rupture migration) are the same with and without viscosity in the bulk. To reduce the

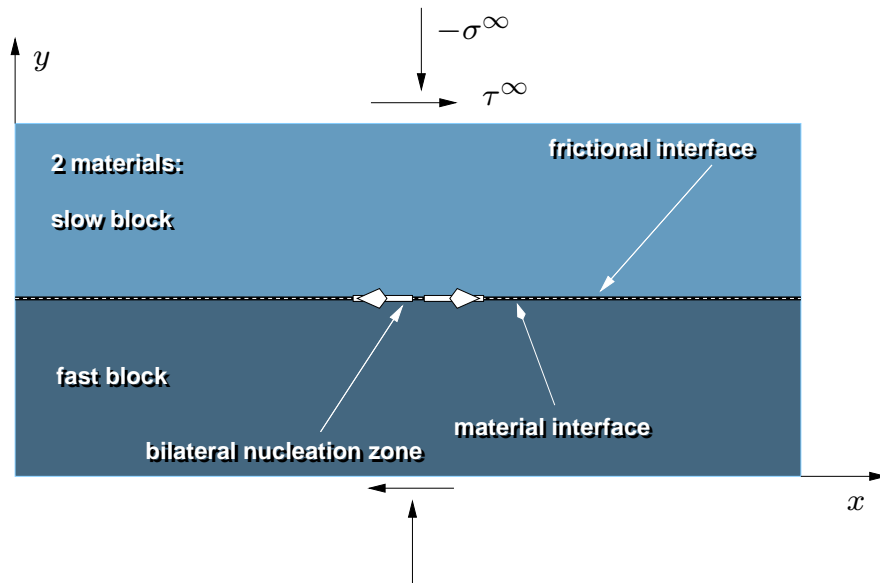


FIGURE 3.3: A model configuration with a single material interface governed by Coulomb friction used in calculations with Kelvin-Voigt viscosity in the bulk.

number of parameters, we use in most subsequent calculations Coulomb frictional interfaces without viscosity in the bulk. Since the calculations have grid-size dependency, we focus only on general tendencies and relative (rather than absolute) amplitudes of effects.

3.3.2 Effects of Multiple Faults

For most of our simulations we use a fixed amount of 9 equidistant parallel faults. The simultaneous sliding on multiple faults produces distributed slip that mimics viscosity in the bulk and leads to a weaker rupture behavior. This is illustrated here with results for three simulations with 9, 17 and 33 parallel faults (Figure 3.5). Each frictional interface has a Coulomb friction coefficient of 0.75 and initial stress components $\tau^\infty = 70$ MPa, $\sigma^\infty = 100$ MPa. As in all our simulations with multiple faults, each frictional surface is able to rupture spontaneously, independently of the neighboring faults. Figure 3.5 shows how the number of faults affects the rupture ability to migrate between the different interfaces and propagate along the material interfaces in a self-sustaining manner. In general, as the number of faults increases, the likelihood of ruptures to migrate and develop self-sustaining pulses decreases due to dissipation of elastic strain energy associated with the slip on the multiple faults. This is similar to the influence of the Kelvin-Voigt viscosity, which also leads to energy dissipation and suppresses the ability of ruptures to develop to self-sustaining pulses. A model configuration with 9 faults (Figure 3.5 top) produces two rupture pulses traveling in the opposite positive directions along

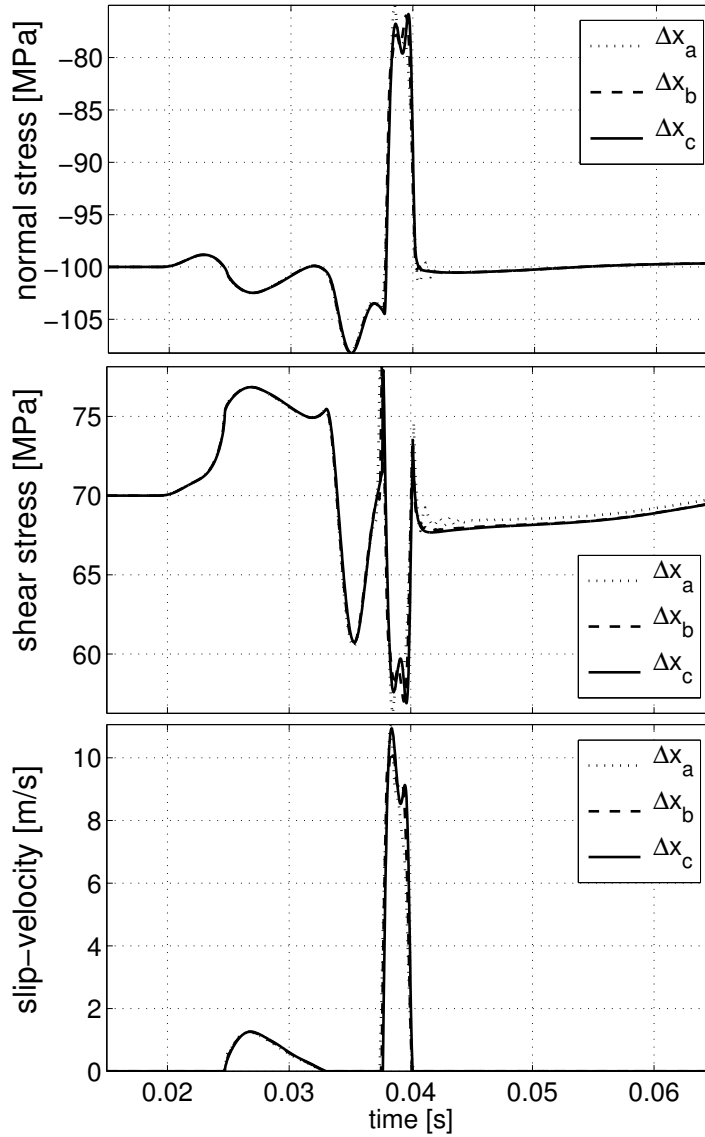


FIGURE 3.4: Results for three different grid-spacing denoted by indices a, b and c for a Coulomb frictional fault surrounded by a Kelvin-Voigt visco-elastic media. Shown are normal-stress (top) shear-stress (center) and slip-velocity (bottom) as a function of time at a point 100 m away from the nucleation location. The simulation results converge to the same solution with grid-refinement. For cases where rupture pulse is self-amplifying this convergence is limited to a certain propagation distance. The material parameters are densities $\rho_1 = 3333.3 \text{ kg/m}^3$, $\rho_2 = 2898.5 \text{ kg/m}^3$, s-wave velocities $v_{s1} = 3000.0 \text{ m/s}$, $v_{s2} = 2608.7 \text{ m/s}$, p-wave velocities, $v_{p1} = 5196.2 \text{ m/s}$, $v_{p2} = 4518.4 \text{ m/s}$, non-dimensional viscosity $c_1 = c_2 = 0.04$, and initial conditions $\tau_0 = 70 \text{ MPa}$, $\sigma_0 = 100 \text{ MPa}$. The grid parameters are $\Delta x_a = 1 \text{ m}$, $\Delta x_b = 0.5 \text{ m}$, $\Delta x_c = 0.25 \text{ m}$, $\Delta t_a = 0.133 \text{ ms}$, $\Delta t_b = 0.0667 \text{ ms}$, $\Delta t_c = 0.0334 \text{ ms}$, and the nucleation velocity $v_{\text{nuc}} = 2549.0 \text{ m/s}$.

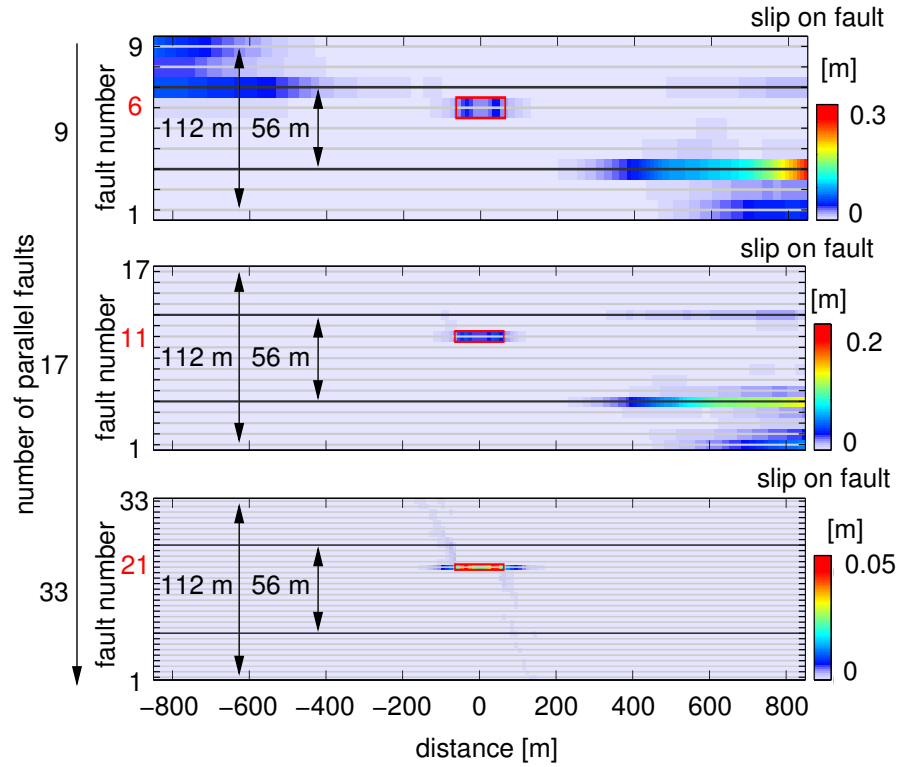


FIGURE 3.5: Final slip distribution in simulations having 9, 17 and 33 faults. The material properties, initial conditions, physical dimensions of the model space and nucleation zone (red box within the fault zone layer) are identical in all cases. Increasing number of possible rupture surfaces leads to more distributed deformation and reduces the ability of the rupture pulse to propagate in a self-sustained manner. These effects are similar to what is produced by incorporation of viscosity.

the two material interfaces. We note that such a case would be seen in a low resolution imaging as a bilateral rupture. Keeping all the model parameters the same but increasing the number of possible faults to 17 (Figure 3.5 center) produces only a single rupture pulse propagating in the positive direction on the stronger material contrast. A system with 33 faults (Figure 3.5 bottom) does not produce self-sustaining rupture pulses due to the dissipation of the initial stored elastic strain energy at the multiple faults.

3.3.3 Prakash-Clifton Friction

In this section we present example results with purely elastic media and frictional sliding governed by the Prakash-Clifton friction (Prakash and Clifton, 1993; Prakash, 1998) with a gradual response to changes of normal stress (Figure 3.6). A simplified version of the Prakash-Clifton friction that can regularize (Cochard and Rice, 2000; Ranjith and Rice, 2001; Ben-Zion and Huang, 2002) the grid-size dependency associated with the Adams (1995) instability can be expressed as $\dot{\tau}_{xy}^s = -(|V| + V^*) (\tau_{xy}^s - f \max(0, -\sigma_{yy})) / L$, where τ_{xy}^s is the frictional strength,

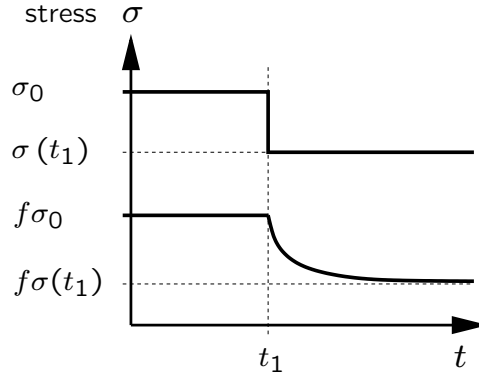


FIGURE 3.6: A characteristic response of the Prakash-Clifton friction law. A normal stress $\sigma = \sigma_0$ for $t < t_1$ changing abruptly to $\sigma = \sigma(t_1)$ for $t \geq t_1$ causes a gradual evolution of the shear strength towards the corresponding Coulomb strength $\tau^s(t_\infty) = f\sigma(t_1)$.

V is the slip-velocity, f is the friction coefficient, V^* is a characteristic slip-velocity for friction evolution and L is a corresponding characteristic slip distance. Figure 3.7 demonstrates the migration of slipping patches between nine parallel faults, two of which are bimaterial interfaces with different material contrast. In the shown snapshots of fault-parallel velocity the rupture is nucleated on the middle fault and migrates to the bimaterial interfaces (solid lines). Figure 3.8 shows migration patterns associated with different nucleation positions (red rectangles) across a fault zone structure having three materials and nine possible faults (Figure 3.1). Each panel gives the spatial distribution of the maximum slip-velocity in a given simulation. The employed conditions are material contrast Δv_2 , initial shear stress $\tau^\infty = 70$ MPa, fault separation $y_{fs} = 21$ m, characteristic slip-distance $L = 0.003$ m, and characteristic slip-velocity $V^* = 1$ m/s. In this and other calculated examples, self-sustained pulses are produced for nucleation locations that are within or at the boundaries of the low velocity fault zone layer. The ruptures tend to migrate spontaneously to the material interfaces (fault 3 or fault 7) and become there self-sustained wrinkle-like pulses. Both material interfaces act as attractors for the ruptures, which become wrinkle-like pulses in the (opposite) positive directions associated with the local velocity contrasts across the fault zone layer, and can produce jointly apparent bilateral ruptures. The general aspects of the migration and propagation patterns of ruptures are similar to those that are produced with the classical Coulomb friction (Figure 3.5 and section 4).

3.3.4 Choice of Parameters for Subsequent Simulations

As discussed in the previous sections, the use of the Prakash-Clifton friction and Kelvin-Voigt viscosity can regularize the grid-size dependency associated with the Adams (1995) instability by suppressing the development of sharp dynamical features. However, the parameters of both the Prakash-Clifton friction and Kelvin-Voigt viscosity have to be fine-tuned to provide apparent

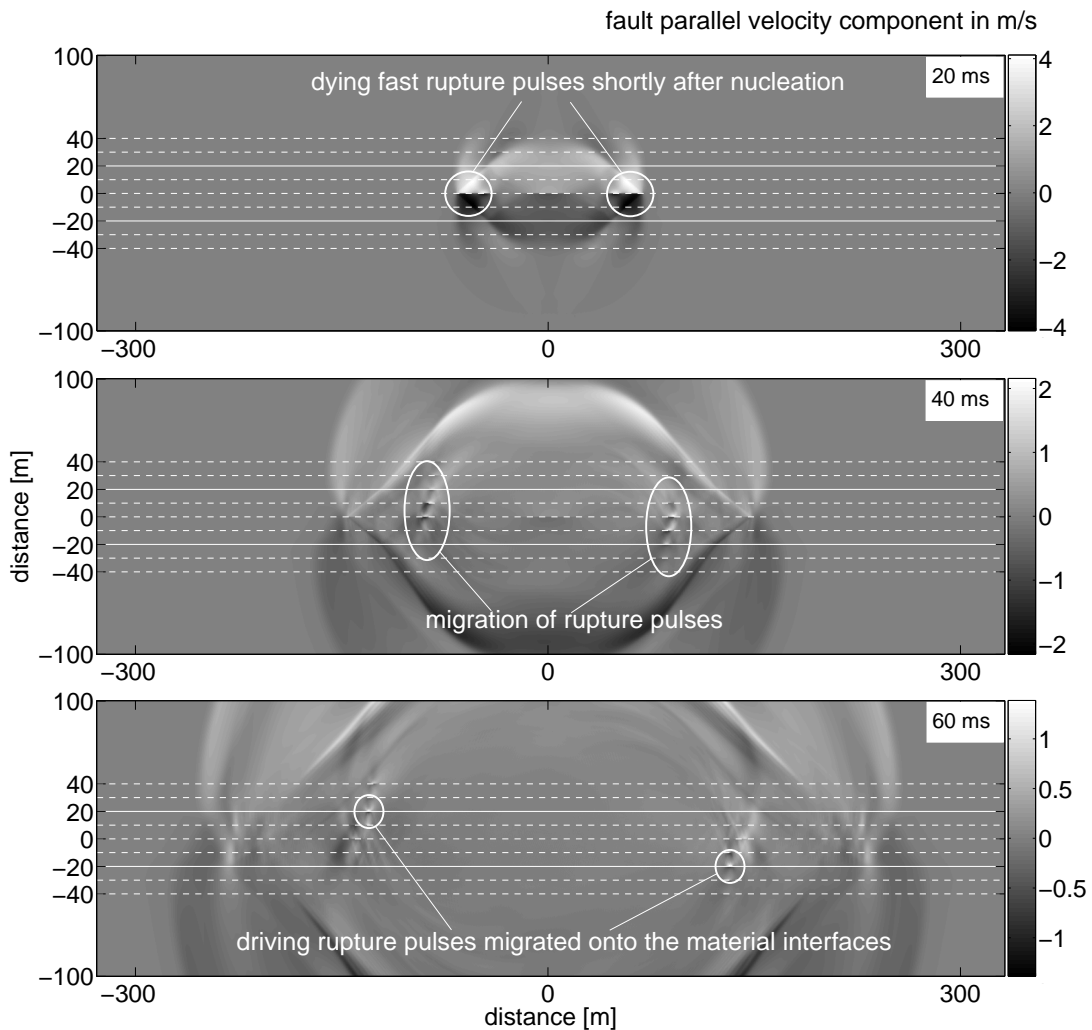


FIGURE 3.7: Snapshots of the fault-parallel velocity component at three instances in time visualizing the migration of ruptures from the central fault onto the faults at the material discontinuities located at $y = \pm 20$ m fault-normal distance (Brietzke et al., 2004). The bimaterial interfaces are marked by the solid lines.

stability over a given propagation distance (for a fixed set of model parameters). This renders the use of the Prakash-Clifton friction and viscosity unsuitable for the present work, where the main focus is to examine systematically tendencies of rupture migration for different cases of velocity models and multiple parallel faults. Simulations with material interfaces governed by Coulomb friction and purely elastic media are subjected to grid-size dependency. However, as pointed out by Ben-Zion (2001) and illustrated by Ben-Zion and Huang (2002) and above, such results can be used to obtain a general understanding of rupture behavior by performing a careful comparative study. In the next section we use a model with three purely elastic materials and Coulomb frictional interfaces, and examine the overall large-scale properties of ruptures for various cases of velocity contrasts, initial shear stress and fault separation.

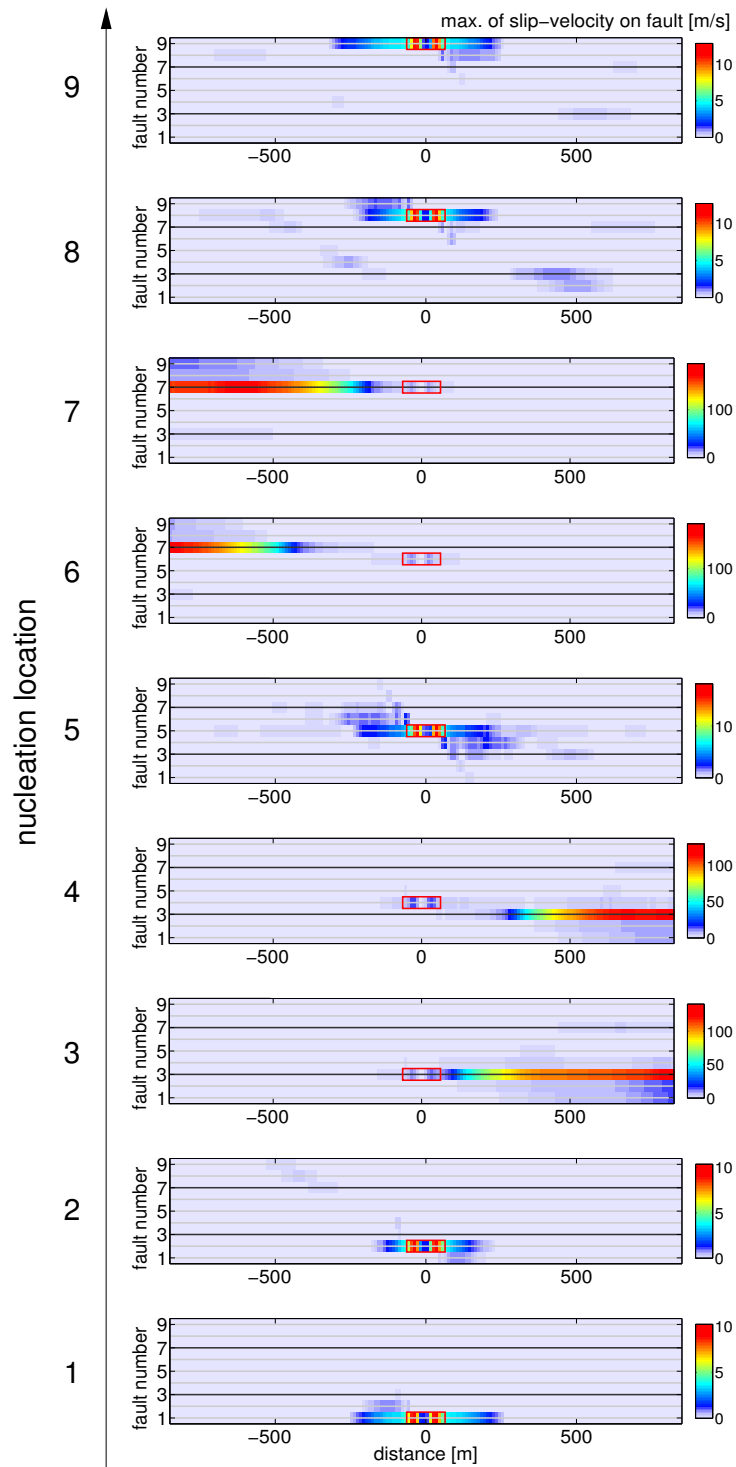


FIGURE 3.8: Distributions of maximum slip-velocity in nine simulations with the regularized Prakash-Clifton friction and different nucleation locations (red rectangles). The panels illustrate common patterns of rupture migration across the fault zone structure. The results are similar to those generated with Coulomb friction.

3.4 Results on Rupture Migration

The parameter-space associated with a model consisting of nine Coulomb frictional faults and three elastic materials (Figure 3.1) is quite complex. For this reason we first investigate in section 3.4.1 a model of three materials and two frictional interfaces only. Results associated with the more general case of nine faults are discussed in section 3.4.2. When a rupture pulse propagates throughout the analyzed model region (850 m from nucleation), we refer to the initiated rupture as self-sustained. We distinguish between triggered rupture on parallel faults and migrated self-sustained rupture pulses by examining the maximum amplitude of slip-velocity on the faults. A triggered rupture has much smaller slip-velocity than that of the self-sustained rupture, although the amount of triggered slip close to the driving fault can be high.

3.4.1 Two-fault System

Here we consider the response of a model with three elastic media and two Coulomb frictional faults located on the two material interfaces. This is an extension of the studies of Ben-Zion and Huang (2002) and Harris and Day (1997) on the influence of a low velocity fault zone layer on rupture dynamics. In contrast to those previous studies, our model allows simultaneous sliding on both sides of the low velocity layer.

We use the set of material contrasts $\Delta v1 = \{v_{s2}/v_{s1}, v_{s3}/v_{s1}\} = \{0.85, 0.94\}$. These are realistic contrasts for natural faults and in the range for which C_{GR} exists (Weertman, 1963; Achenbach and Epstein, 1967; Ben-Zion, 2001; Ranjith and Rice, 2001). In such cases an increase of velocity contrast leads to an increase in the strength of the wrinkle-like pulse on the material interface (Ben-Zion and Andrews, 1998; Ben-Zion and Huang, 2002). The friction coefficient is $f_c = 0.75$, the initial normal stress is $\sigma_0 = 100$ MPa and the initial shear stress is $\tau_0 = 70$ MPa. The nucleation procedure is as described in section 3.2.2 and is applied to both faults in two sets of simulations. Below we discuss results of twelve simulations associated with six different widths of the low velocity layer: $y_{|v|} = 1.75$ m, 3.5 m, 7 m, 14 m, 28 m, 56 m, and two different nucleation locations (fault 1 associated with the stronger contrast, and fault 2 associated with the lesser contrast).

Figure 3.9 shows the maximum slip-velocities on the two faults for the twelve simulations. The slip velocities are unrealistically high since the calculations are done for purely elastic media. An incorporation of plastic yielding off the fault (Ben-Zion and Shi, 2005) or viscous component of deformation (section 3) will limit the slip velocities and stabilize the divergent behavior of the wrinkle-like pulses. The results exhibit the following competing effects: (i) A low velocity layer with width on the order of the nucleation size makes it easier for ruptures to migrate from one fault to the other. (ii) When the width of the low-velocity layer becomes considerably smaller, the overall material contrast of the two surrounding half spaces dominates. In this case the fault on the weaker material contrast cannot sustain dynamic ruptures, while the

fault on the stronger material contrast has a pulse with reduced strength. In some such cases, a small amount of slip on the interface with the weaker contrast suppresses the development of self-sustained slip on the other interface. (iii) Once the width of the low-velocity layer becomes large enough, each material contrast between a bounding medium and the low-velocity layer acts like a single material interface, and the existence of the other frictional material interface has little effect.

The differences in amplitude and the dying vs. amplifying behavior in all simulations are consistent with the competing effects (i)-(iii) above. As examples, for a very narrow low-velocity layer $y_{lv} = 1.75$ m (Figure 3.9a), the opposing influences of the two material contrasts inhibit rupture propagation on both faults. The overall contrast of 6% between the two half spaces would in general support rupture propagation on a single fault (e.g., Ben-Zion and Huang, 2002; Shi and Ben-Zion, 2006). However, in the simulated case with simultaneous sliding on two faults, self-sustaining rupture does not propagate even on fault 1 having a 15% material contrast. Comparing the results for the two different nucleation locations (fault 1 (top), fault 2 (bottom) of $y_{lv} = 7$ m (Figure 3.9c), we see that nucleating on fault 2 can initiate dynamically propagating rupture on fault 1, but nucleating on fault 1 cannot initiate dynamically propagating rupture on fault 2. This is consistent with the fact that fault 2 is a weaker material contrast and (as already mentioned) we are in the range in which the instability increases with increasing contrast. Comparing cases of nucleating on fault 1 for widths of the low-velocity layer of $y_{lv} = 7$ m and $y_{lv} = 14$ m (Figure 3.9c,d), it is seen that for $y_{lv} = 14$ m there are stronger ruptures, propagating in the (opposite) positive direction on both faults, than for $y_{lv} = 7$ m. Comparing the amplitudes of the triggered slip-velocity in Figure 3.9e top/bottom and 3.9f top/bottom, it is seen that the amplitude of triggered motion is smaller for the wider low-velocity layer.

3.4.2 A Nine-fault System

In this section we examine the combined effects of sliding on many parallel faults, discussed previously in section 3.3.2, and the competing effects associated with properties of the low velocity layer discussed in section 3.4.1. The complexity of the system with three media and nine faults produces a high richness of dynamic phenomena. To obtain a general understanding of overall properties of dynamic ruptures in this model we performed a large number (over 250) of simulations. Since it is not practical to show the results of all cases, we plot and discuss below details of several simulation examples and then summarize the key results of all the cases in section 3.4.2

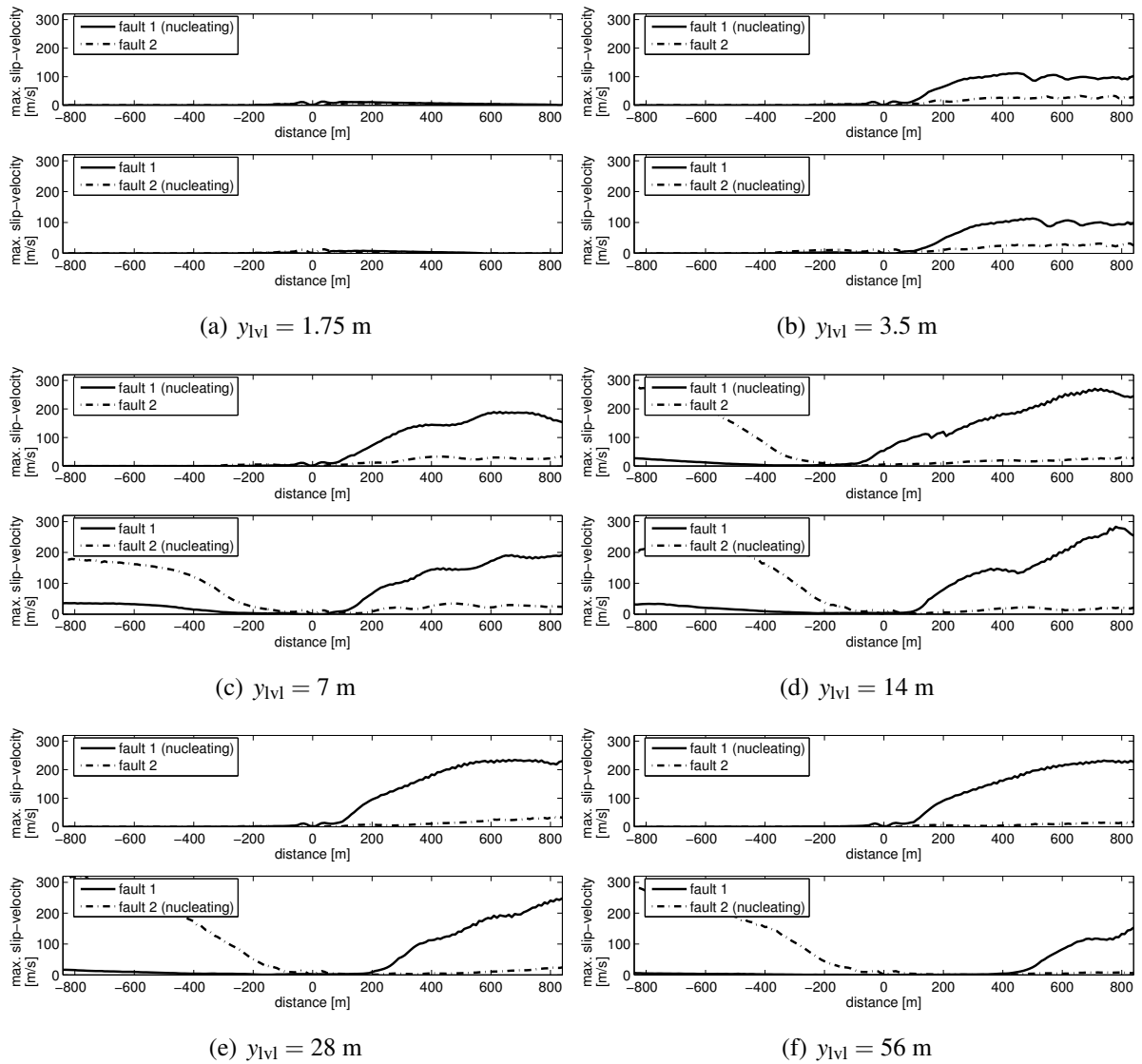


FIGURE 3.9: Slip-velocity on the two faults for each of the twelve simulations associated with two different nucleation locations $y_{nuc} = \{\text{fault 1, fault 2}\}$ and six different width of the low-velocity layer $y_{lv} = 1.75, 3.5, 7, 14, 28, 56$ m. Fault 1 is associated with the stronger material contrast. For $y_{lv} = 1.75$ m (Figure 3.9a) the initiated rupture pulse is decaying for both nucleation locations. For $y_{lv} = 3.5$ m (Figure 3.9b) both nucleation locations produce self-sustaining ruptures on fault 1 in the positive direction, and only triggered slip is produced on fault 2 in the opposite positive direction. This case is classified as rupture migration, overall unilateral event. For $y_{lv} = 7$ m (Figure 3.9c) self-sustained pulses propagate on both faults for nucleation location 2 (classified as migration of rupture, overall bilateral event) but only on fault 1 for nucleation location 1 (overall unilateral event). For $y_{lv} = 14$ m (Figure 3.9d) self-sustained pulses exist on both faults for both nucleation locations (rupture migration, overall bilateral event). For $y_{lv} = 28$ m (Figure 3.9e) nucleation on fault 1 leads to a self-sustained pulse on fault 1 and triggered slip on fault 2 (overall unilateral event), while nucleation on fault 2 produces self-sustained pulses on both faults (migration fault ruptures, overall bilateral event). For $y_{lv} = 56$ m (Figure 3.9f) the results are similar to the case with $y_{lv} = 28$ m (Figure 3.9e). In all cases (b-f) with a self-sustained pulse, the primary pulses produce triggered (but not self-sustained) slip on the opposite side of the low velocity layer.

Simulation Examples

Fixing all simulation parameters other than the nucleation location (fault 1, fault 2, ... , fault 9), we get a set of nine simulations for which we show results in Figure 3.10. The set of employed model parameters are marked in Figure 3.11c. Starting from the nucleation region on a given fault (marked by a red rectangular), the slip may migrate to the neighboring faults. In the examples shown in Figure 3.10, self-sustained pulses are produced for the nucleation locations fault 3 to fault 7 that are within or at the boundaries of the low velocity fault zone layer. The self-sustained pulses always localize on fault 3 or fault 7, which are the faults located on the material interfaces. For nucleation location on fault 3 associated with the stronger velocity contrast, the initiated rupture produces a self-sustained slip pulse that propagates on that fault in the positive direction. When the nucleation is on fault 4, the pulse migrates onto fault 3 and propagates there in a self-sustaining manner in the positive direction. When nucleating on fault 5, the rupture migrates onto both material interfaces (stronger velocity contrast on fault 3 and weaker contrast on fault 7). Both rupture pulses propagate in a self-sustained manner in the two opposite positive directions associated with the velocity contrast and sense of loading. As mentioned earlier, a low resolution "macroscopic" view of this and other such simulated cases would label the events as bilateral ruptures. When the nucleation is on fault 6, the initiated rupture migrates onto fault 7 and continues to propagate there in a self-sustaining manner. Nucleation on fault 7 produces a self-sustained rupture on that material interfaces, along with migration onto fault 3 and propagation there with the opposite preferred direction. In the investigated time-window, no migration of rupture pulses that led to self-sustained propagation are observed for nucleation locations on fault 1, fault 2, fault 8 and fault 9. The discussed features are summarized in Figure 3.11c, along with the main results of many other cases.

Overview of Nine-fault System Simulations

Figure 3.11 summarizes the main results of 252 simulations with three elastic media and nine Coulomb frictional faults. The figure consists of six phase-diagrams associated with different values of initial shear stress, nucleation location, fault separation, and velocity contrast. Each symbol (cross, arrow or double arrow) specifies the overall macroscopic behavior of rupture in a simulation associated with a given parameters set. The main features and implications of the simulated results are discussed in the next section.

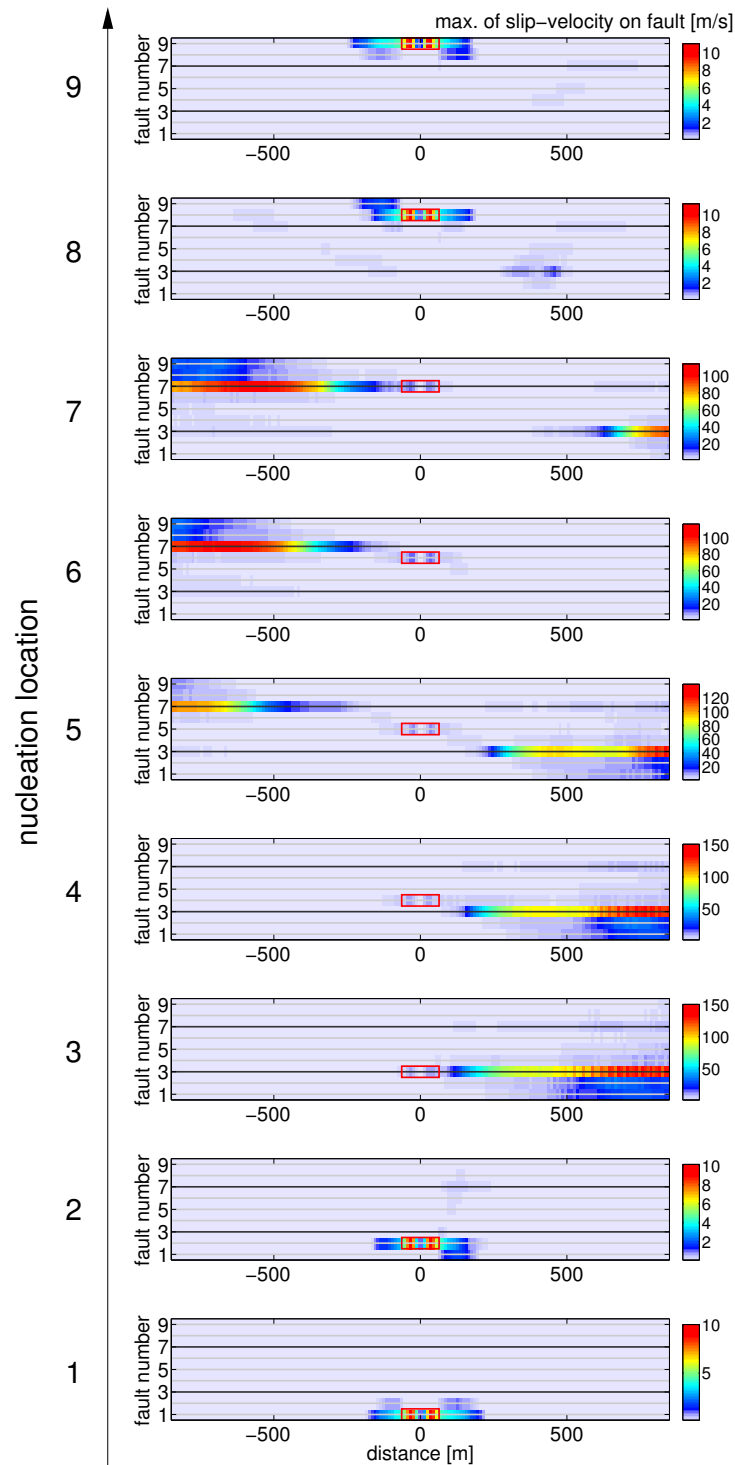


FIGURE 3.10: Results of nine simulations with fixed model parameters and nine different nucleation locations. The maximum slip-velocities at equidistantly spaced points on the fault-profiles are shown as color plots (note the different scales). The nucleation regions are marked by red rectangles and self-sustained rupture pulses are produced for nucleation locations along faults 3-7. The self-sustained ruptures propagate in the positive directions associated with the material contrasts on the opposite sides of the low velocity layer.

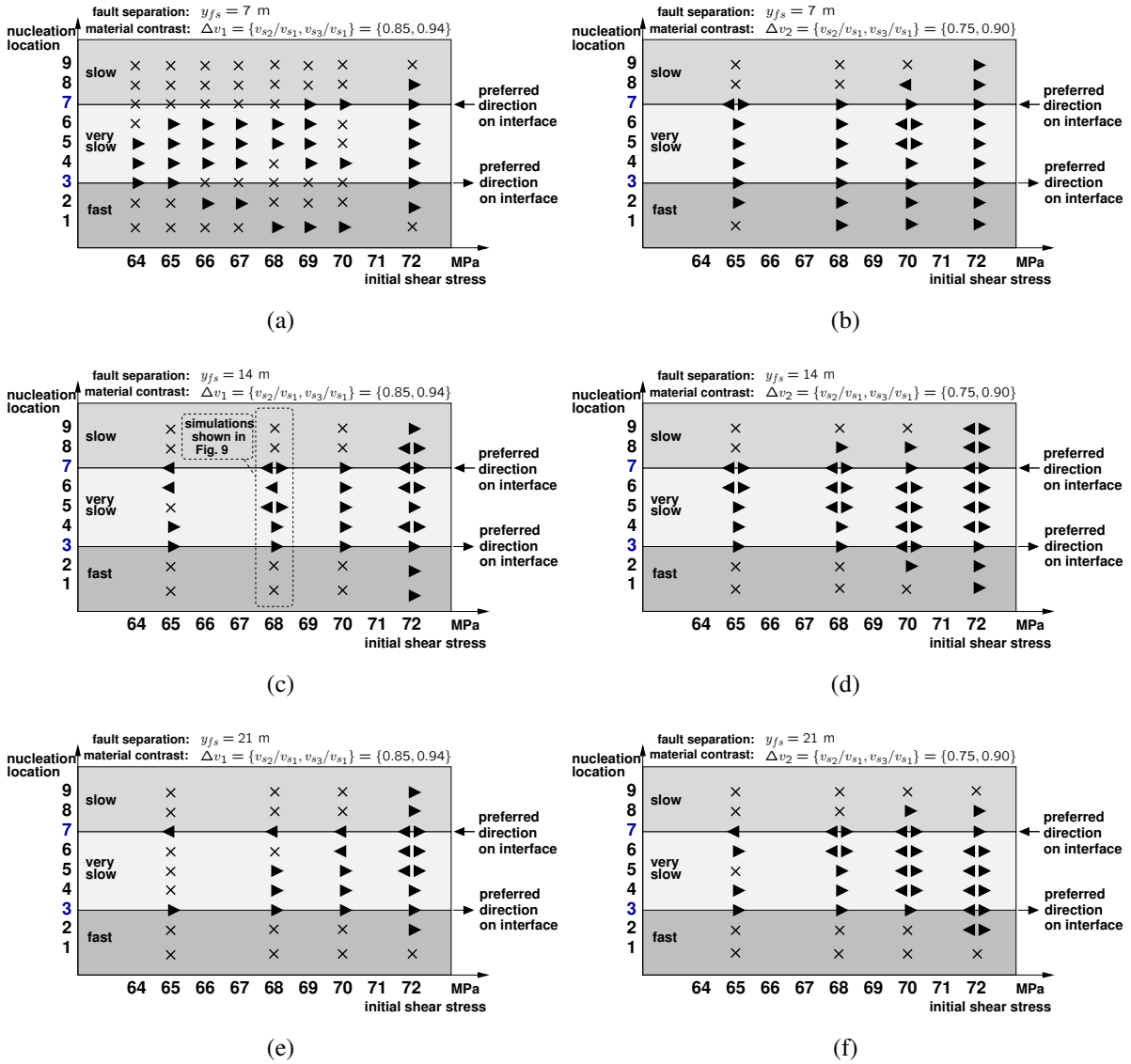


FIGURE 3.11: Main properties of rupture behavior in 252 simulations with three elastic materials and nine parallel faults governed by Coulomb friction. The diagrams show the initial shear stress on the x -axes and the location of nucleation in terms of fault numbering on the y -axes. The result of each simulation is reduced to four symbols: An arrow to the right means generation of a self-sustained pulse traveling on fault number 3 (associated with the stronger material contrast v_{s2}/v_{s1}) in the positive (right) direction. An arrow to the left denotes a self-sustained pulse on fault number 7 (associated with the weaker material contrast v_{s3}/v_{s2}) travelling in the positive (left) direction. A double arrow means two self-sustained pulses propagating on both material interfaces in the opposite positive directions (i.e., generation of apparent bilateral rupture). A cross is shown when no self-sustained pulses were generated. The set of employed velocity contrasts are: $\Delta v_1 = \{v_{s2}/v_{s1}, v_{s3}/v_{s1}\} = \{0.85, 0.94\}$ and $\Delta v_2 = \{v_{s2}/v_{s1}, v_{s3}/v_{s1}\} = \{0.75, 0.90\}$. Panels (a-f) correspond to the following parameter sets: (a) $\Delta v_1, y_{fs} = 7$ m; (b) $\Delta v_2, y_{fs} = 7$ m; (c) $\Delta v_1, y_{fs} = 14$ m; (d) $\Delta v_2, y_{fs} = 14$ m; (e) $\Delta v_1, y_{fs} = 21$ m; (f) $\Delta v_2, y_{fs} = 21$ m

3.5 Discussion and Conclusions

We performed a large numerical parameter-space study of two-dimensional in-plane ruptures in a structure consisting of 3 media and possible simultaneous slip on multiple frictional faults, two of which are material interfaces. Some cases with Kelvin-Voigt viscosity in the bulk and Prakash-Clifton friction on the material interfaces were used to explore effects of those rheologies and choose parameters for a systematic study of tendencies of rupture migration in a structure with purely elastic media and Coulomb frictional faults. Our model with two faults (among several others) on the boundaries of a low velocity layer has two opposite positive propagation directions of wrinkle-like pulses. With the employed right-lateral loading, the positive direction of rupture propagation on the fault between the low velocity layer and the faster bounding block (fault 3) is to the right, while the positive direction on the fault (number 7) between the low velocity layer and the slower bounding block is to the left.

The main results of our study are as follows:

Migration of dynamic ruptures: A general observation of this study is that ruptures that are nucleated in the bulk tend to migrate spontaneously to the material interfaces associated with faults number 3 and 7. The ruptures continue to propagate in the positive directions on those faults in a self-sustained manner for a large number of parameter combinations (see Figure 3.11). As might be expected, more cases of ruptures propagating to the right on the stronger velocity contrast fault 3 are produced, compared to ruptures propagating to the left on the weaker velocity contrast fault 7.

Apparent bilateral rupture due to low velocity layer: When the low velocity layer is not too thin, many sets of parameters produce simultaneous propagation of unilateral rupture pulses on faults 3 and 7 in the opposite positive directions (see e.g. Figure 3.10: nucleation location 5, and Figure 3.11). From a distant low resolution perspective, such ruptures would look like bilateral events. For a model with very thin or no low-velocity layer, the model produces only single unilateral ruptures, in agreement with the analytical solution of Weertman (1980) and previous numerical simulations (e.g., Ben-Zion and Huang, 2002; Shi and Ben-Zion, 2006).

In a structure with three media, the eventual rupture plane is not necessarily the one with the largest material contrast: Depending on the nucleation location, ruptures can migrate onto either material interface. Rupture migration to the fault with the weaker velocity contrast (fault 7 in our model), can lead to self-sustained pulses that propagate unilaterally in the positive direction of that interface. Such examples can be seen, e.g., in Figure 3.11c and e. Since this direction is opposite to that associated with the overall velocity contrast across the bounding half-spaces, a low resolution view would lead to the erroneous conclusion that the rupture propagated in the opposite (negative) direction from that predicted for the wrinkle-like pulse.

Many parallel faults lead to "effective viscous" behavior: The existence of multiple faults dissipates elastic strain energy and reduces the divergent behavior of the wrinkle-like pulses. As the number of faults increases the deformation become more distributed and the model response

becomes similar to that of a viscous material. In contrast, self-sustained rupture pulses, leading to effective brittle behavior, are associated with localization of the energy change on a small number of faults (in our case material interfaces).

Higher initial stress favors rupture migration and self-sustained pulses: Increasing initial stress leads in general to a higher likelihood that nucleated ruptures will migrate to the two material interfaces. With higher initial stress, such migrated ruptures have overall also a higher likelihood of becoming self-sustained pulses. Nevertheless, in some cases the latter does not hold. Specifically, when a relatively thin low velocity layer has a relatively large number of faults (in our parameter-space 7 m fault separation, 28 m-wide layer), the effectiveness of migration and generation of self-sustained ruptures reduces for a range of increasing initial shear stress (see Figure 3.11a). This is probably produced by higher dissipation of strain energy in such cases due to simultaneous low-level slip on several faults. However, increasing the initial shear stress further toward the shear strength always produces self-sustained ruptures on the material interfaces.

Wider fault separation, easier generation of self-sustained pulses: When the faults separation increases, once a rupture can migrate onto one of the material interfaces it is more likely to become self-sustained. This can be understood in terms of the features discussed above, since larger fault separation makes it more difficult for the energy to be transferred to one of the neighboring faults.

Nucleation on slower side leads to stronger migration onto the interface: Using always the same nucleation procedure as described in section 3.2.2, we found that ruptures that were initiated on the slower side of the material contrast could more often succeed in migrating onto the material interface. This is intuitive since a slower wave propagation velocity leads to higher wave amplitudes (e.g., as for fault-zone trapped waves or waves in sedimentary basins). This is also manifested in Figure 3.11 where it is seen that more self-sustained ruptures are generated by nucleation locations within the low-velocity layer than from outside the layer.

Nucleation closer to the material interface can lead to less migration: In some cases we observe that ruptures nucleated close to a material interface could not migrate onto the material interface, while ruptures nucleated at some larger distance could (see, e.g., Figure 3.11a for initial shear stress of 68 MPa). This is related to the fact that the radiation pattern of the shear waves has a nodal plane on the continuation of the rupture. Increasing the strength of the nucleation procedure, e.g., by increasing the source size or stress drop, would produce migration also in such cases.

The results may have important implications to a number of issues of earthquake and fault physics associated with large structures that have well-developed material interfaces. The common spontaneous migration of ruptures to the material interfaces implies that the dynamic phenomena associated with the wrinkle-like pulses are not limited to the set of hypocenters located directly on the material interfaces. The migration of ruptures to material interfaces provides

a mechanism for a positive feedback between structure and rupture properties that can lead to progressive regularization of geometrical heterogeneities with cumulative slip and suppression of dynamic branching from large fault zone structures (Ben-Zion and Andrews, 1998). The dynamic reduction of normal stress at the tip propagating along a material interfaces in the positive direction (e.g., Figure 3.4) increases the mechanical efficiency of such ruptures, and has fundamental implications for the effective constitutive laws and energy partition in structures with material interfaces.

The simulations provide a simple explanation for recent observations and inferences on rupture propagation directions along sections of the San Andreas fault (SAF). Rubin and Gillard (2000) relocated earthquakes in the Bear Valley section of the SAF and found that the number of immediate aftershocks near the edges of prior ruptures to the NW is more than double the number to the SE. They interpreted this asymmetry as resulting from the dynamic changes of normal stress associated with the material contrast across the SAF. Our results explain the ability of ruptures to propagate in both directions, with an elevated probability for propagation in the positive direction of the overall contrast across the fault (which is the same direction associated with ruptures on the stronger velocity contrast between the fault zone layer and the stiffer half space). McGuire (2004) inverted directly seismic data for rupture directivity of two small (M 2.7) earthquakes on the Bear valley section of the SAF. One of these earthquakes had clear unilateral rupture propagation to the SE, as predicted by the overall material contrast across the SAF, while the other had overall bilateral "macroscopic" properties.

Dor et al. (2006b,a) performed multi-signal multi-scale geological mapping in the structure of several faults of the San Andreas system in southern California. Their results show strong asymmetry of rock damage across the faults, compatible with a preferred propagation direction and related generation of damage asymmetry across a bimaterial interface (Ben-Zion and Shi, 2005). Similar asymmetric damage zones, which correlate with the velocity structure as predicted for wrinkle-like ruptures, were observed in seismic imaging studies using fault zone trapped and head waves at sections of the San Andreas and San Jacinto faults Lewis et al. (2005, 2007). The possible relation between the observed asymmetric rock damage and preferred propagation direction of earthquake ruptures is supported by our general result that ruptures tend to migrate to material interfaces and become self-sustained wrinkle like pulses for wide range of conditions.

The Parkfield region of the SAF resembles overall the model configuration of Figure 3.1, with two large faults - the main SAF and the Southwest Fracture Zone - separated by 1.5 km wide deformation/damage zone (e.g., Rymer et al., 2006). As noted by Ben-Zion (2006b), both faults are highly active on the scales of small to moderate events, and the M 6 2004 Parkfield event along with many of its aftershocks appear to be located on the Southwest Fracture Zone rather than the main SAF. Rymer et al. (2006) found that the surface fractures generated by the M 6 2004 event are concentrated on the SW side of the Southwest Fracture Zone and on

the NE side of the SAF. These observations and near-fault seismic data (Shakal et al., 2005) suggest that the M6 2004 Parkfield event consisted of two separate pulses, one propagating on the Southwest Fracture Zone to the SE and the other propagating on the SAF to the NW. In that case, both pulses propagated (as occurred commonly in our simulations) in the two positive directions associated with the SAF and Southwest Fracture Zone. This should be clarified in future observational analysis of the structure and rupture properties associated with the M6 2004 Parkfield event.

Harris and Day (2005) concluded from inferred propagation directions of several earthquakes on the Parkfield sections of the SAF that the prediction of a preferred rupture propagation direction does not hold for natural faults. The simulated richness of propagation behavior in our model with two blocks separated by a low velocity layer highlights the lack of decisive information in the results considered by Harris and Day (2005). More generally, our results emphasize the need to base tests of a preferred propagation direction along a material interface (and other features of wrinkle-like pulses) on detailed high-resolution observations associated with large data sets.

The calculations of this work were done for situations (in-plane strain, slip-independent friction) chosen to focus on effects associated with the assumed structure (many possible faults in a 3-media configuration) and dynamic changes of normal stress along material interfaces. The generality of the results should be tested in future simulations incorporating additional levels of realism in the assumed structure (e.g., dimensionality) and rheology (e.g., slip- and rate-dependent friction).

Motivation for Coming Chapter

The previous chapter 3 “Examining Tendencies of In-plane Rupture to Migrate to Material Interfaces” (after Brietzke and Ben-Zion, 2006) showed that for significant ranges of parameters, bimaterial interfaces are efficient surfaces of failure in a velocity structure that is, in a simplified form, characteristic for mature earthquake faults. Another open question is whether or not a bimaterial specific unilateral propagation mode of rupture on a 2D in-plane fault model, the Weertman pulse (or wrinkle like slip pulse), is persistent also in the 3D case where in-plane and anti-plane propagation modes are mixed. There is no previous study analyzing the wrinkle-mode of rupture in 3D in an appropriate way. In the following chapter 4 “Dynamic Ruptures along Bimaterial Interfaces in 3D” (after Brietzke et al., 2007) it is demonstrated that the wrinkle-like slip pulse can persist in the general 3D-case.

Chapter 4

Dynamic Ruptures along Bimaterial Interfaces in 3D

This chapter presents the work of Brietzke et al. (2007) in a slightly modified form.

Gilbert B. Brietzke¹, Alain Cochard², and Heiner Igel¹

¹ Department für Geo- und Umweltwissenschaften, Sektion Geophysik, Ludwig-Maximilians-Universität München, Theresienstrasse 41, 80333 München, Germany.

² École et Observatoire des Sciences de la Terre, 5 rue René Descartes, 67084 Strasbourg Cedex, France.

Abstract

We perform numerical simulations of dynamic rupture propagation on a plane in a model consisting of two different elastic half spaces connected via a planar frictional interface governed by regularized Coulomb friction. Therefore, ruptures in this study are purely driven by the presence of a material contrast. Ruptures are nucleated on the fault using a circular symmetric expanding increase of pore-pressure in a limited source region. We show how a wrinkle-like rupture pulse can mature also in the 3D case where we have a mixing of in-plane and anti-plane modes, the instability specific of a bimaterial interface acting only for the in-plane mode. The pulse develops inside a cone-shaped region with its axis aligned with the direction of displacement in the softer material, its tip being at the nucleation region.

Keywords: dynamic rupture, bimaterial interface, numerical simulation.

4.1 Introduction

Geological faults with a long slip history are likely to bring into contact materials with different elastic properties. Contrasts of elastic properties across large faults have been imaged by seismic reflection and refraction studies (e.g., Lutter et al., 2004), body and coda wave tomography (e.g., Eberhart-Phillips and Michael, 1998), modeling of geodetic data (e.g., Le Pichon et al., 2005), geologic mapping (Dor et al., 2006a,b), and analysis of head waves that refract along material interfaces in the fault zone structure (e.g., McGuire and Ben-Zion, 2005). The range of the velocity contrast across the San Andreas and other large faults is estimated to be about up to 30%, with values of 5-20% often reported. A fault surrounded by identical materials on both sides cannot become unstable when the governing friction law has a single, constant coefficient of friction. However, an interface separating materials of different elastic properties can become unstable even under this condition (Weertman, 1980). How much earthquake ruptures are influenced by such material contrasts has been under debate recently (Andrews and Harris, 2005; Harris and Day, 2005; Ben-Zion, 2006a,b). The model of rupture propagation along a bimaterial interface with a single, constant friction coefficient evidently excludes the weakening behavior of friction during sliding and is unrealistic in this respect. Nevertheless, it is also believed that simple weakening models of friction and their parameters do not have a clean physical basis and additional physical knowledge has to be developed to come to physically consistent models (Rice and Cocco, 2006). Destabilization of slip on a bimaterial interface is only present in the 2D in-plane case and it is not present in the 2D anti-plane case. It has been mentioned by Ben-Zion and Andrews (1998) that the results of bimaterial driven 2D in-plane rupture simulations might be modified considerably in cases of 3D rupture propagation. Harris and Day (2005) show results of dynamic rupture calculations in 3D with slip-weakening and Kelvin-Voigt viscosity in the bulk. However, (1) it is not yet clear that the Kelvin-Voigt viscosity does regularize ill-posedness, and (2) we wish to isolate the bimaterial instability from that coming from the intrinsic frictional weakening. Therefore the problem of a rupture along a bimaterial interface in 3D still needs examination.

4.2 Ill-posedness, and Numerical Convergence

The model consists of two elastic halfspaces of different elastic properties which are coupled by a frictional interface (see Figure 4.1). A frictional interface governed by Coulomb friction in a homogeneous medium with a uniform initial stress along the fault less than the frictional strength never becomes unstable no matter how forcefully an event is initiated in the nucleation zone. As mentioned above, in order to study unstable slip on a bimaterial interface independently from other sources of instability (e.g., slip- or rate-dependent friction) one would therefore ideally wish to use Coulomb friction (constant friction coefficient). However, sliding along

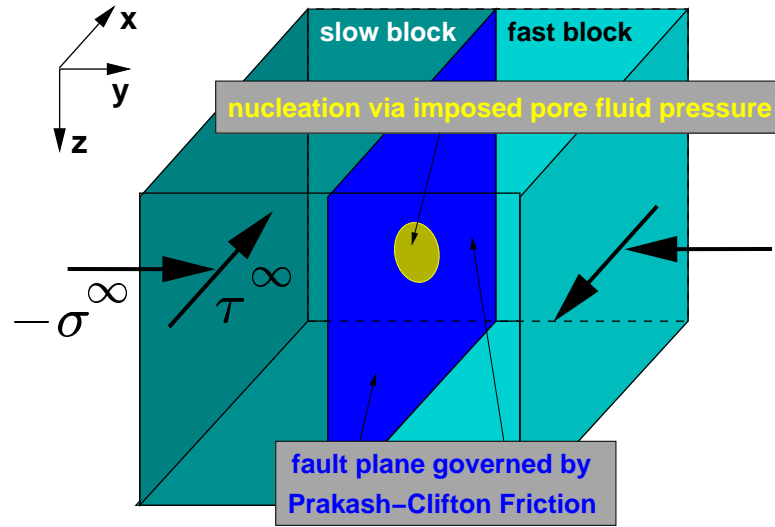


FIGURE 4.1: Sketch of the model setup: a frictional interface embedded in-between two elastic half-spaces with dissimilar elastic properties.

a planar bimaterial interface under Coulomb friction is often not well-posed (Adams, 1995; Ranjith and Rice, 2001), and there is a connection between the ill-posedness of the problem and the existence of the generalized Rayleigh wave (Ranjith and Rice, 2001). A summarizing table is given in Cochard and Rice (2000). The source of ill-posedness has been studied by Adams (1995) and is referred to as the Adams instability (Cochard and Rice, 2000). In this study we use an experimentally based constitutive law in its simplified form (Cochard and Rice, 2000, and references therein) with its characteristic differential equation for the shear strength τ_1^s given by:

$$\dot{\tau}_1^s = -\frac{|V| + V^*}{L} [\tau_1^s - f \max(0, -\tau_2)], \quad (4.1)$$

with slip velocity V , characteristic slip velocity V^* , characteristic length L , and friction coefficient f letting the shear stress τ_1 to respond gradually rather than instantaneously to an abrupt change of normal stress τ_2 . It has been shown by Ranjith and Rice (2001) to regularize the previously discussed ill-posedness. Classical slip-weakening or rate- and state-dependent constitutive laws with strength proportional to local normal stress do not provide a regularization (Cochard and Rice, 2000).

Even in the well-posed regime it is numerically challenging to resolve a wrinkle-like rupture pulse travelling along a bimaterial interface, because of the above mentioned intrinsic instability of such an interface (Cochard and Rice, 2000; Ben-Zion and Huang, 2002). To test the numerical results for their physical plausibility we strive for converging results of grid-refined simulations. In Figure 4.2 we show converging results achieved with the finite-difference method used in this study (details in section 4.3) for three levels of grid refinement ($\Delta x = 0.5, 0.25, 0.125$ m). Because of the huge computational expense we cannot accomplish further refinements or larger

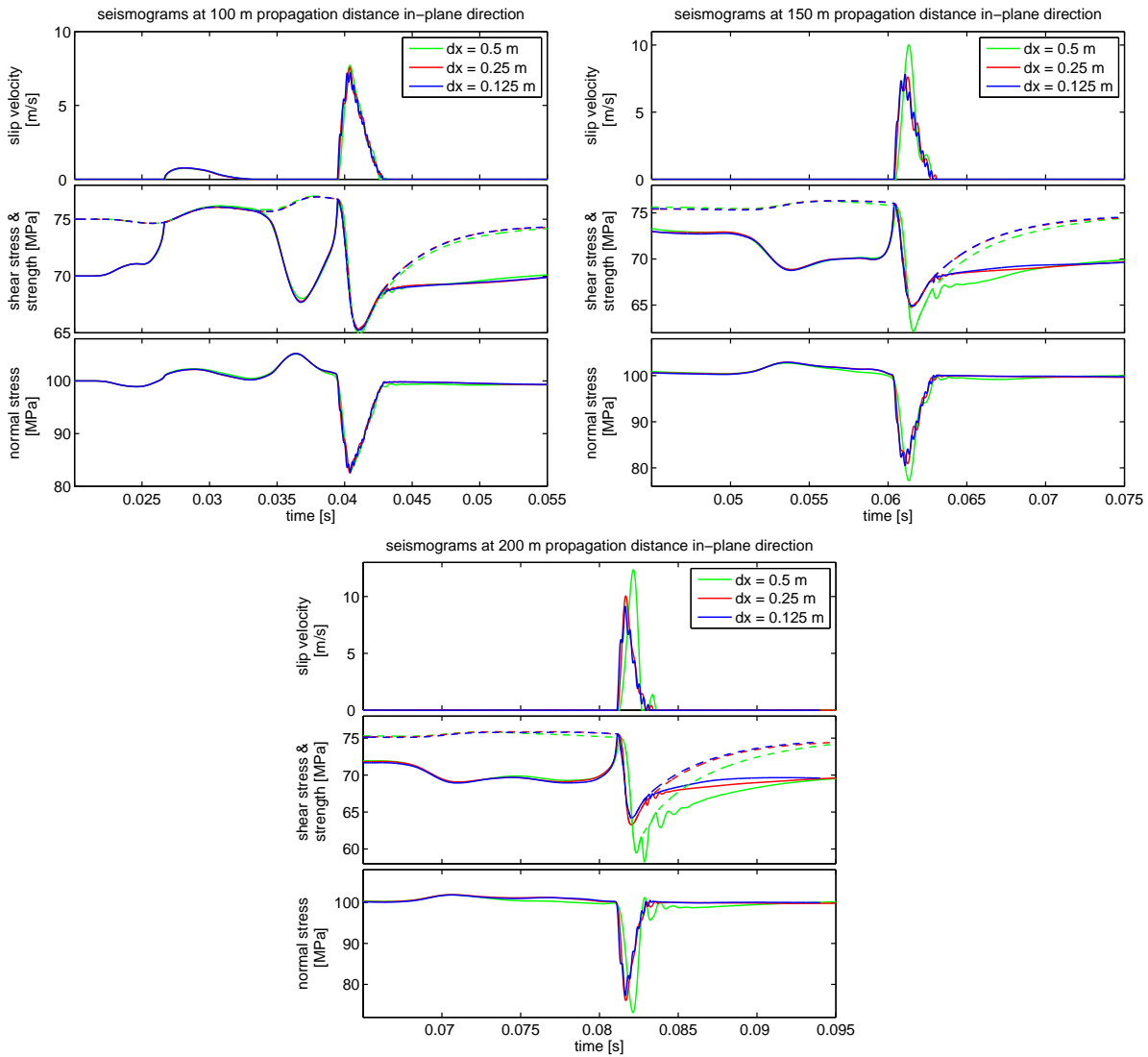


FIGURE 4.2: Slip velocity, shear-stress, friction, and normal stress at three stations at 100 m (top left), 150 m (top right), and 200 m (bottom) propagation distance along the in-plane direction for the parameter case shown in table 4.1. For the shown propagation distances, a resolution of $\Delta x = 0.25$ m provides already good convergence, since the results of the next refinement with $\Delta x = 0.125$ m basically shows the same solution.

propagation distances at the same time. The top panel shows slip velocity as a function of time at three different points ($x_{pd} = 100$ m, 150 m, 200 m) along the in-plane direction on the fault. At about 0.03 s we see a slip pulse that corresponds to what is labeled ‘supershear’ in Figure 4.3 – it has already totally disappeared at 150 m away from the nucleation. Thus, as in 2D, the main feature is the so called Weertman pulse (e.g., Andrews and Ben-Zion, 1997), appearing in all three stations. For the least refined grid (green curve) we can see numerical noise, especially for the station at 200 m propagation distance. The corresponding features can also be seen in the bottom panel which shows normal stress. We can see that suitable convergence is achieved

for $\Delta x = 0.25$ m.

4.3 Physical Model, Nucleation, Numerical Implementation

The model consists of two elastic halfspaces of different elastic properties which are coupled by a frictional interface (see Figure 4.1). We use a standard 4th-order staggered-grid finite-difference technique for solving the elastic wave equations inside the elastic medium which has been described by various authors (e.g., Igel et al., 1995; Graves, 1996). Frictional sliding is numerically included via the stress-glut method which has been introduced by Andrews (1999). Following earlier studies (e.g., Andrews and Ben-Zion, 1997; Cochard and Rice, 2000) we do not allow the fault to open while we set shear strength to zero when normal stress becomes tensile. To keep the simulations clean from artificial reflections caused by the finiteness of the numerical implementation of the model we use perfectly matched layers (Marcinkovich and Olsen, 2003) of appropriate width on all sides of the modelspace. Although Ampuero and Dahlen (2005) show that the elastic constants on a material discontinuity are ambiguous, we found that we could achieve the best duplication of results of Cochard and Rice (2000) using the harmonic mean for the elastic $c_{av} = 2c_1c_2/(c_1 + c_2)$ constants and the arithmetic mean for the density $\rho_{av} = (\rho_1 + \rho_2)/2$, as has been suggested elsewhere (e.g., Wu and Chen, 2003), for points on the material boundary.

We nucleate each event in a circular symmetric way by increasing the fluid pressure in a limited space-time region. We thus prevent a propagation direction that is privileged by the nucleation procedure. Our procedure is similar to the one used by Brietzke and Ben-Zion (2006). In 3D it is a spatially ring-shaped nucleation pulse with the spatial width a , expanding at the nucleation velocity v_{nuc} until the maximum radius b , which can be expressed using the geometric variables

$$\begin{aligned}\xi &= (|r| - v_{nuc}t)/a, \\ \eta &= (|r| + v_{nuc}t)/b - (\sqrt{a^2 + b^2}/b),\end{aligned}\tag{4.2}$$

, with radius $|r| = \sqrt{y^2 + z^2}$. Within the source, the fluid pressure is given as

$$P_f = P_0 (1 - \xi^2 - \eta^2)^2,\tag{4.3}$$

while outside this region it is zero. To make our study comparable to other numerical studies (Cochard and Rice, 2000; Ben-Zion and Huang, 2002; Ben-Zion and Shi, 2005) we use parameters that are similar to the ones used in those studies. The range of the investigated parameters is summarized in table 4.1.

parameter	value or value range
numerical method	finite-differences
grid type	staggered cartesian grid
grid-spacing Δx	0.5 m, 0.25 m, 0.125 m
maximum grid size $n_x \times n_y \times n_z$	$500 \times 3200 \times 3200$
density material 1 ρ_1	3333.3 kg/m^3
wave velocities material 1 v_{s1}, v_{p1}	3000.0, 5196.2 m/s
density material 2 ρ_2	2777.7 kg/m^3
wave velocities material 2 v_{s2}, v_{p2}	2500.0, 4330.1 m/s
size of the fault model $y \times z$	$1580 \times 1580 = 2496400 \text{ m}^2$
type of friction	simplified Prakash-Clifton
friction coefficient f	0.75
characteristic slip velocity V^*	1 m/s
characteristic length L	4 mm
initial shear stress τ^∞	70 MPa
initial normal stress σ^∞	100 MPa
size of nucleation zone $\phi_{\text{nuc}} = 2b$	120 m
nucleation velocity v_{nuc}	2475 m/s
nucleation pulse width a	10 m

TABLE 4.1: Range of simulation parameters

4.4 Results

Snapshots of slip velocity on the fault at three instances in time are shown in Figure 4.3 for $\Delta x = 0.25 \text{ m}$. The nucleation initiates rupture phases in the subshear as well as the supershear range. The supershear part of the rupture dies out for the shown parameter set in all directions. In the in-plane direction and some time-dependent angle the subshear rupture phase develops towards a self-amplifying wrinkle-like pulse in the positive direction (direction of displacement in the softer material), and it dies out in the opposite (negative) direction. This self-amplifying wrinkle-like pulse travels at about the generalized Rayleigh velocity within a limited region of slip that has the shape of a fraction of a circle. Therefore the propagation velocity of this pulse is constant in all directions where it exists. In the anti-plane direction the pulse symmetrically dies out for all propagation velocities. Although this might look trivial knowing the corresponding 2D cases, where we have the development of a unilateral rupture-pulse in the positive direction of the in-plane case, and dying rupture pulses in the anti-plane case, we want to emphasize that this result cannot be deduced trivially from the separate 2D cases.

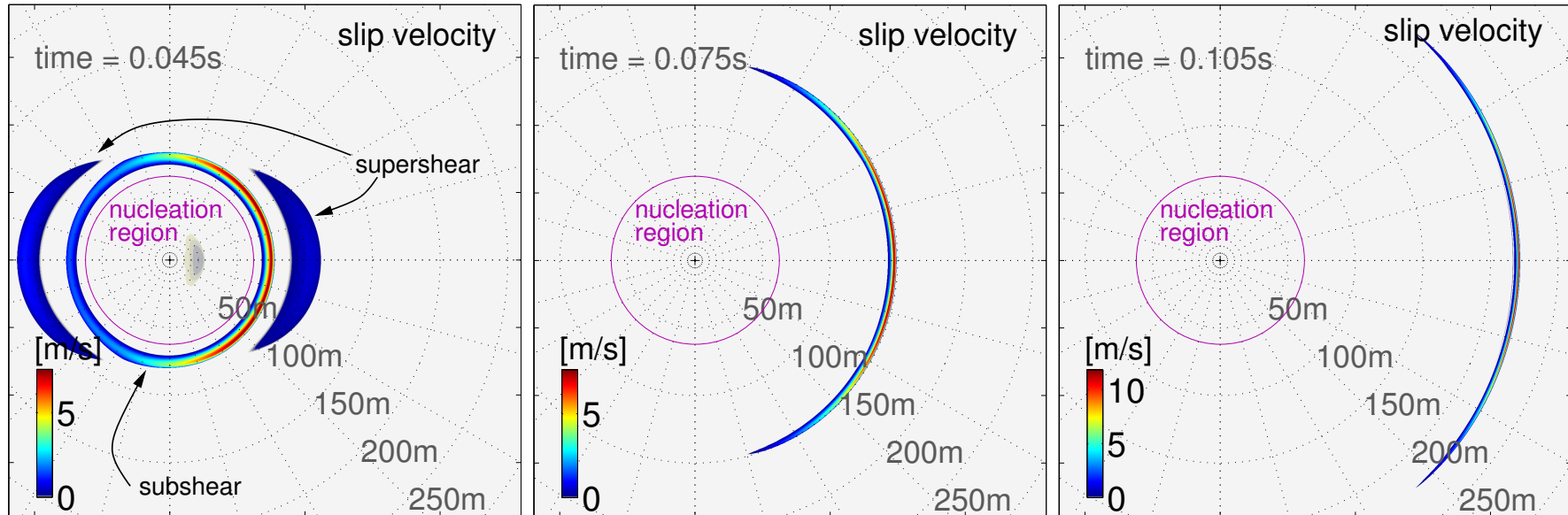


FIGURE 4.3: Snapshots of the slip velocity on the fault-plane at three instances in time for the same parameters as in Figure 4.2. The nucleation takes place inside the pink circle ($\mathcal{O}_{\text{nuc}} = 2b = 120$ m). The left panel shows slip velocity shortly after the nucleation. Two supershear half-moon shaped rupture phases, and a subshear rupture phase traveling at about the generalized Rayleigh velocity in all directions (see left panel) are initiated. The subshear rupture phase develops towards a self-amplifying wrinkle-like pulse within a cone around the positive in-plane direction, it dies out in the negative in-plane as well as in the anti-plane directions (see middle/right panel).

The snapshots show how a self-amplifying, purely material-contrast driven wrinkle-like rupture pulse can appear also in the 3D case. We found that the allowance of rake rotation in the 3D case does not change the results qualitatively (in a few simulations, not shown here, we found that the self-amplification is stronger for the cases for which we prohibited rake-rotation).

In order to investigate how the pulse evolves after some larger propagation distance we performed a 3D simulation with a coarse numerical grid ($\Delta x = 0.5$ m) allowing us to enlarge the propagation distance to $x_{pd} = 1$ km. The resulting slip-distribution after 475 ms is shown in Figure 4.4. The buldge of slip on the rightmost part shows a very small disturbance ($< 4\%$ of the total slip) propagating ahead of the main pulse at the same velocity, and which originates at a propagation distances of about 400 m. The non-circular rupture front in Figure 4.4 also indicates a transition at the edge, the rupture propagation velocity being slightly smaller there.

Our results show that for adequate parameters a wrinkle-mode of rupture that is purely driven by the decrease in normal stress during slip and its positive feedback (amplification) can exist also in the 3D case. However, in 3D it appears that the wrinkle-like rupture pulse degenerates possibly faster than in 2D towards a potentially unrealistic state with a huge slip-acceleration and very small width of the pulse (sharpening).

4.5 Discussion

The problem of rupture on a bimaterial interface is numerically extremely challenging because of the highly unstable physical mechanism associated with it (compared to, e.g., the classical slip-weakening instability). Using finite-difference calculations we show that a self-sustained pulse can exist under the simplified Prakash-Clifton law also in 3D. Such a pulse travels inside a cone with a time-dependent angle on the fault plane around the positive in-plane direction. How robust are the results of this study? Based on our experience in 2D and the very limited experience in 3D, we found that there exists ranges of parameters, e.g., regarding the nucleation procedure or a too low level of initial stress, for which self-sustained pulses have not been observed. Nevertheless we are confident that self-sustained propagation occurs in at least some significant neighborhood of the present parameters. However, a full parameter space study remains to be done, even in 2D.

Based on very few numerical simulations of rupture propagation along a bimaterial interface governed by slip-weakening friction (Andrews and Harris, 2005) state that this phenomenon of the wrinkle-like pulse is not important for realistic earthquake rupture. In contrast, it has been under debate recently what is a realistic and physically consistent earthquake model. Additional physical knowledge has to be developed (Rice and Cocco, 2006) to narrow the involved uncertainties and to evaluate physically more consistent, more realistic models of earthquake rupture; off-fault energy dissipation due to plastic strain, visco-elasticity, melt lubrication, thermal pressurization are just examples of what could be taken into account. Also, in the presented simu-

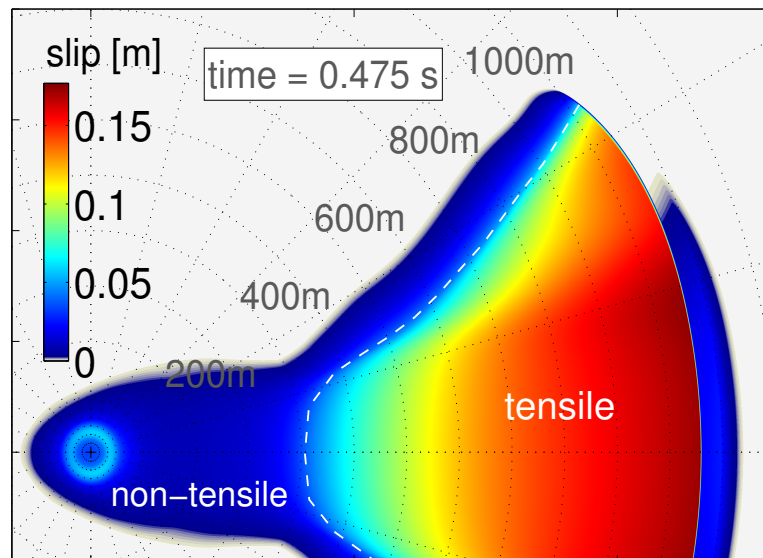


FIGURE 4.4: Distribution of slip after 475 ms simulation time. After passing the nucleation region at $r_{pd} < 60$ m the pulse travels through a transitional area of relatively stable pulse propagation (compare with Figure 4.3) until it becomes clearly self-sustained.

lations of self-sustaining pulses, normal stress becomes strongly tensile after some propagation distance. This suggests that the consequences of allowing fault opening should be investigated in future studies of 2D and 3D dynamic rupture propagation along bimaterial interfaces. Our study has the clearly defined conceptual limit of a purely material driven effect. The results of recent studies on bimaterial interfaces bring in complementary insights (e.g., Rudnicki and Rice, 2006; Shi and Ben-Zion, 2006; Brietzke and Ben-Zion, 2006; Rubin and Ampuero, 2007). There are indeed good examples for which the bimaterial mechanism seems to be necessary to properly interpret the observations: Rubin and Gillard (2000) observed asymmetric alongstrike distribution of aftershocks on the San Andreas fault, and Dor et al. (2006b) observed asymmetric rock damage across faults of the San Andreas system.

In order to address the question of whether or not the wrinkle-like slip pulse (or, more generally, the bimaterial mechanism) is relevant in existing earthquake rupture mechanisms, a much wider range of models and parameter combinations would need to be tested, owing to the aforementioned uncertainties in our knowledge of source physics. The strong self-sharpening behavior of the wrinkle-like rupture pulse suggests that, with increasing propagation distance, it degenerates towards unrealistically large slip velocities (as already noted by Ben-Zion and Huang (2002) in 2D), and perhaps vanishes as a consequence of pulse thinning, this latter aspect obviously deserving a deeper investigation.

Motivation for Coming Chapter

The preceding chapter contributed to the first question of what are the properties of the wrinkle-like propagating Weertman pulse. Until recently only few studies (Harris and Day, 1997; Andrews and Harris, 2005; Harris and Day, 2005) addressed the second question on whether or not the bimaterial mechanism is important in realistic earthquake dynamics. Andrews and Harris (2005) (AH) and Harris and Day (2005) provoked considerable debate (Ben-Zion, 2006a,b). More recently other studies have contributed to the puzzling second question (e.g., Shi and Ben-Zion, 2006; Rubin and Ampuero, 2007; Dunham and Rice, 2008; Ampuero and Ben-Zion, 2008; Brietzke et al., 2009) with the consensus that there is indication that for certain ranges of parameters (type of friction, frictional parameters, heterogeneity of stress, asperities, poroelastic parameters, level of average initial stress etc.) the material contrast across a frictional interface can become significant for natural earthquakes. A shortcoming of AH is that their study is very limited in several aspects. AH back their hypothesis “The wrinkle-like slip pulse is not important in earthquake dynamics” with three simulations only, two of which are too coarse to study the addressed phenomenon (Andrews and Harris, 2005, paragraph 20: “These calculations are too coarse to resolve the wrinkle-like slip pulse well. If the calculations were repeated with a smaller grid interval, we would expect to see a narrower slip pulse with a greater tensile change of normal stress in the case of favored propagation direction. Achieving adequate resolution in 3D would require a great deal of computing power, so a calculation with fine resolution is done in 2D.”), the third one being 2D only. Their model incorporate simultaneously multiple ingredients, pretending to be “realistic”, but the dimensionality of the parameter-space is very high, the results are based on very small number of simulations, and the conclusion is phrased in very strong and general terms. Therefore their conclusion is highly questionable at best. The following chapter 5 “Importance of Bimaterial Interfaces for Earthquake Dynamics and Strong Ground Motion” (after Brietzke et al., 2009) extends the limited parameter set of AH with more than 300 parameter sets of a similar 3D model with a three-times finer numerical resolution. The study shows that for many situations the bimaterial mechanism is significantly altering rupture dynamics and strongly affecting the radiated ground motion at the surface.

Chapter 5

Importance of Bimaterial Interfaces for Earthquake Dynamics and Strong Ground Motion

This chapter presents the work of Brietzke et al. (2009) in a slightly modified form.

Gilbert B. Brietzke¹, Alain Cochard², and Heiner Igel¹

¹ Department für Geo- und Umweltwissenschaften, Sektion Geophysik, Ludwig-Maximilians-Universität München, Theresienstrasse 41, 80333 München, Germany.

² École et Observatoire des Sciences de la Terre, 5 rue René Descartes, 67084 Strasbourg Cedex, France.

Summary

We perform a numerical investigation of dynamic ruptures on a bimaterial interface in 3D with regularized slip-weakening friction and a heterogeneous initial shear stress, and discuss the resulting strong ground motion. To separate effects introduced by the material contrast we perform pairs of simulations with opposite material orientations as it has been done by Andrews and Harris (2005). We show that for many parameter sets the dynamics of rupture propagation are significantly influenced by the broken symmetry due to the material discontinuity during rupture propagation. The resulting slip histories of two events with reversed orientations of the material contrast can deviate such that the emanating waves lead to large differences in peak ground motion (PGV & PGA) even when slip-distribution of the individual events are very similar and therefore their moment magnitudes are basically identical. We also show that the wrinkle-like slip pulse specific to the bimaterial mechanism can be nucleated naturally from an initially crack-like mode of rupture when the initial stress allows for large propagation distances. Once such a pulse has been nucleated it travels at a dominant propagation speed

close to the generalized Rayleigh velocity. The dynamic weakening of the fault due to the normal stress alteration during slip allows nucleating ruptures to overcome asperities of low initial shear stress in the preferred direction, which is the direction of slip on the seismically slower side of the fault. In such situations the orientation of the material contrast determines rupture extent and therefore the size of the earthquake, potentially by orders of magnitude.

Keywords: dynamic rupture, bimaterial interface, ground motion, numerical simulation.

5.1 Introduction

Large faults with a long slip history often separate rocks of dissimilar elastic properties. It has been reported that such bimaterial interfaces exhibit remarkable dynamic properties in the 2D in-plane case that may be relevant to many issues of earthquake rupture dynamics (Ben-Zion and Andrews, 1998). The existence of a pulse mode of rupture, travelling unilaterally along a bimaterial interface at the generalized Rayleigh velocity v_{gr} into the direction of displacement in the more compliant side, has been predicted by a theoretical analysis of Weertman (1980). Andrews and Ben-Zion (1997) confirmed the existence of such wrinkle-like pulse-mode of rupture in numerical calculations. Many aspects of the wrinkle-mode of rupture and sliding along a bimaterial interface have been clarified by various studies (e.g., Adams, 1995; Cochard and Rice, 2000; Ranjith and Rice, 2001). In the 2D in-plane case, slip along a bimaterial interface generates dynamic changes of normal stress, modifying the local fault strength which, in principle, can generate a unilateral wrinkle-like pulse. This mechanism is neither present in the homogeneous case nor the 2D anti-plane case. It has been shown by Cochard and Rice (2000) that there exists also a bimaterial driven pulse in the opposite direction (direction of displacement in the stiffer side) travelling at the p-wave velocity of the softer side, v_p^{slow} . A propagation mode at the slower p-wave velocity has been identified by Harris and Day (1997) from a simple model of failure induced slip of a single-point asperity on a friction-free fault. Effects of a low velocity fault-zone structure and multiple fault surfaces have been studied by others (e.g. Harris and Day, 1997; Ben-Zion and Huang, 2002; Brietzke and Ben-Zion, 2006). Theoretical and numerical calculations with rate-dependent friction indicate the bimaterial mechanism to be important for earthquake rupture for ranges of parameters leading to macroscopic and statistical asymmetry of rupture properties while being suppressed for others (e.g., Ampuero and Ben-Zion, 2008). It has been shown that the wrinkle-like rupture pulse can persist also in the 3D case where there is a mixing of the in-plane and anti-plane cases (Brietzke et al., 2007).

There are good examples for which the bimaterial mechanism seems to be necessary to properly interpret the observations: asymmetric along strike distribution of aftershocks (Rubin and Gillard, 2000; Rubin and Ampuero, 2007), asymmetric rock damage across faults of the San Andreas system (Dor et al., 2006a), and geomorphologic asymmetry across the rupture zones of the North Anatolian fault (Dor et al., 2008) have been reported. The uncertainty in the basic physical concepts involved and the constraints of their parameter ranges make it difficult to come to definite conclusions, and indeed the relevance of this mechanism for natural faulting has also been a subject of controversy recently (e.g., Andrews and Harris, 2005; Ben-Zion, 2006a).

Here we present results of a numerical investigation of dynamic ruptures with regularized slip-weakening friction on a bimaterial interface with a heterogeneous initial shear stress load in 3D with a free surface. A heterogeneous stress distribution on a bimaterial interface has been used before by Andrews and Harris (2005) for the 3D-case and by Ampuero and Ben-Zion

(2008) for the in-plane 2D-case.

5.2 Model Setup

We numerically simulate dynamic rupture propagation on a planar fault with regularized slip-weakening friction separating two blocks of dissimilar elastic materials (20% contrast). A sketch of the model is shown in Figure 5.1. We introduce Λ as a symbol for the Weertman pulse since slip along a bimaterial interface can in principle generate unilateral wrinkle-like Weertman pulses with a unidirectional propagation (Weertman, 1980). This direction is often referred to as the *preferred* direction of a bimaterial interface, despite the possible existence of an opposing pulse at v_p^{slow} . We identify the orientation of the material contrast in our simulations by specifying the propagation direction of the mentioned Weertman pulse using Λ_R and Λ_L , subscripts R and L meaning propagation to the right-hand side and to left-hand side, respectively.

5.2.1 Heterogeneous Stress and Nucleation

We use a heterogeneous initial shear stress with random phase and amplitude proportional to the reciprocal wavenumber ($1/k$). Mai and Beroza (2002) find that slip on a fault plane satisfies $D \propto 1/k^{1+H_D}$ with an associated Hurst exponent H_D within the interval of $H_D = [0.5, 1.0]$. For the associated stress field τ_0 the corresponding interval for the Hurst exponent is $H_\tau = [-0.5, 0.0]$. We use $\tau_0 \propto 1/k^{1+H_\tau}$ with $H_\tau = 0$ which corresponds to the upper limit of the range proposed by Mai and Beroza (2002). This value has also been used by Andrews and Harris (2005) and therefore allows for a direct comparison with their results. The distribution is tapered towards zero for wavenumbers close to the Nyquist wavenumber k_{Ny} of our coarsest numerical grid with $\Delta x = 200$ m. The resulting initial shear stress is arbitrarily scaled, and it is smoothly tapered towards the free surface and the model boundaries. We nucleate each event by elevating the initial stress by 15% in a circular patch of 1 km radius around the overall peak-stress of the random distribution.

5.2.2 Friction and Regularization

Sliding along a planar bimaterial interface has been shown to be often ill-posed (Adams, 1995; Ranjith and Rice, 2001; Cochard and Rice, 2000). Regularization is achieved using an experimentally based constitutive law (Prakash and Clifton, 1993; Prakash, 1998) in combination with classical slip-weakening dependence of friction coefficient (note that slip-weakening alone does not provide regularization – see Cochard and Rice (2000, page 25,897)). Shear stress τ in such a system responds gradually to changes in normal stress σ_n . The characteristic differential

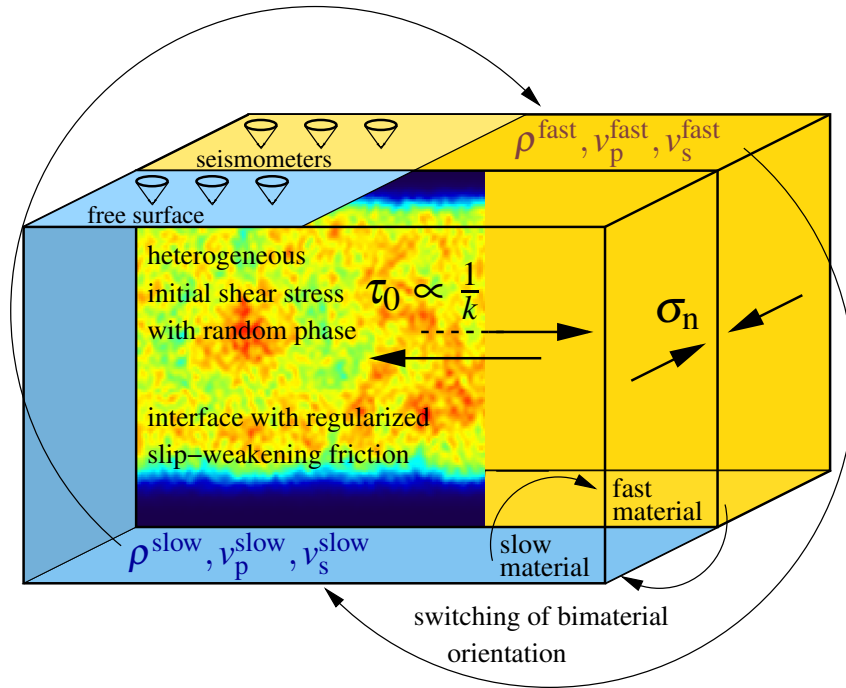


FIGURE 5.1: Sketch of the physical model: bimaterial frictional interface with regularized slip-weakening friction and heterogeneous stress. Each set of parameters is simulated twice, with the material contrast orientation being switched for the second simulation.

equation for the shear strength τ^s is given by:

$$\dot{\tau}^s = -\frac{|V| + V^*}{L} [\tau^s - f_{\text{sw}} \max(0, -\sigma_n)] , \quad (5.1)$$

with slip velocity V , characteristic slip velocity V^* , characteristic length L , and friction coefficient f_{sw} . With this regularized friction law, results in principle converge with grid size reduction (see Cochard and Rice (2000)). We use a slip-weakening friction coefficient given by:

$$f_{\text{sw}} = \begin{cases} f_s - (f_s - f_d) D/D_c, & \text{for } D < D_c \\ f_d, & \text{for } D \geq D_c . \end{cases} \quad (5.2)$$

5.2.3 Numerical Method

We use a second-order finite-difference formulation in a staggered grid with traction-at-split-nodes for the implementation of the frictional interface as it has been introduced by Dalguer and Day (2007a). In order to suppress artificial reflection originated by the finiteness of the numerical model, we use perfectly matched layers (PML) on all sides of the model except for the side representing the free surface. The PML technique has been adapted to velocity-stress formulations of the elastodynamic wave equations by Collino and Tsogka (2001) in 2D, and

shown to work efficiently in the velocity-stress staggered-grid finite-difference scheme used in this study by Marcinkovich and Olsen (2003). The free surface is implemented using a simple stress-imaging technique at the free surface (Levander, 1988).

5.3 Results

It has been shown by Andrews and Harris (2005) that for a pair of simulations with reversed material orientation (Λ_R , Λ_L) the resulting slip distribution on the fault may be very similar. Andrews and Harris (2005) also mentioned that the wrinkle-like pulse they observed in their 2D calculations might have an important effect on the radiated ground motion. Since they have not been able to resolve the wrinkle-like pulse in their 3D calculations due to computational limits, they could not evaluate its effect on the ground motion, which is the main goal of our study.

We tested for more than 300 pairs of simulations the influence of the bimaterial mechanism on rupture propagation and final slip as well as on the resulting ground motion. Within this set of simulations we changed initial shear stress (τ_0) and frictional parameters (f_d , f_s , D_c , L).

We discuss our simulations by showing results of four representative examples in sections 5.3.1, 5.3.2, 5.3.3, 5.3.4. Each set of parameters is simulated once, and then once again with the material contrast orientation being switched. Each such simulation pair of these four sets of parameters features certain effects which can thus be related to the presence of the material contrast. The more than 300 pairs of simulations exhibit mixtures of the effects presented in the four representative examples, sometimes less, sometimes more pronounced; those are summarized in section 5.3.6.

For characterization of the initial level of shear stress we use the strength excess parameter S , which is defined as:

$$S = \frac{\tau_s - \tau_0^{\text{av}}}{\tau_0^{\text{av}} - \tau_d}, \quad (5.3)$$

with τ_0^{av} the average initial shear stress in the non-tapered region.

In order to evaluate differences of final slip we define values for the dissimilarity of final slip and peak slip velocity (see equation B.2) on the fault:

$$\delta D = \frac{\sum_{i=1}^N |D_i^{\Lambda_R} - D_i^{\Lambda_L}|}{\frac{1}{2} \left(\sum_{i=1}^N D_i^{\Lambda_R} + \sum_{i=1}^N D_i^{\Lambda_L} \right)}, \quad \delta V_{\text{max}} = \frac{\sum_{i=1}^N |V_{\text{max}_i}^{\Lambda_R} - V_{\text{max}_i}^{\Lambda_L}|}{\frac{1}{2} \left(\sum_{i=1}^N V_{\text{max}_i}^{\Lambda_R} + \sum_{i=1}^N V_{\text{max}_i}^{\Lambda_L} \right)}, \quad (5.4)$$

with N the number of fault elements.

We will look at seismograms and their amplitude spectra at the free surface. All seismograms we will show are low-pass filtered at 2 Hz. Using a grid-spacing of $\Delta x = 100$ m this means

that for the slowest wave-speed of $v_s^{\text{slow}} = 2917$ m/s we have a grid-resolution of 15 points per smallest unfiltered wavelength of 1500 m.

In order to evaluate the effects on the radiated ground motion on the surface we show maps of peak ground velocity (PGV) and peak ground acceleration (PGA) (see equations B.6) and their relative differences with respect to both material orientations (δPGV and δPGA) which are normalized by the average of the value for both orientations PGV^{Λ_R} and PGV^{Λ_L} ; they are local parameters at point j of the surface:

$$\delta\text{PGV}_j = \frac{\left| \text{PGV}_j^{\Lambda_R} - \text{PGV}_j^{\Lambda_L} \right|}{\frac{1}{2} \left(\text{PGV}_j^{\Lambda_R} + \text{PGV}_j^{\Lambda_L} \right)}, \quad \delta\text{PGA}_j = \frac{\left| \text{PGA}_j^{\Lambda_R} - \text{PGA}_j^{\Lambda_L} \right|}{\frac{1}{2} \left(\text{PGA}_j^{\Lambda_R} + \text{PGA}_j^{\Lambda_L} \right)}, \quad (5.5)$$

with superscript Λ_R and Λ_L labeling the ground motions of the simulations with its Weertman pulse related preferred directions to the right and left, respectively.

The ranges of parameters of our simulations are summarized in table 5.1.

In order to identify robust features we decrease the numerical grid-spacing in selected parameter cases. In those cases we do not modify the original random realization but interpolate the initial shear stress to the refined grid-spacing.

In the following we discuss stable features present in our 300 pairs of simulations (including the four example cases). Ideally, one should quantify the results in a statistical sense, but we have not enough individual realizations to do so.

In section 5.3.1 we discuss an example where final slip on the fault is very similar for both orientations of a simulation pair (Λ_L , Λ_R), but the ground motion differs a lot. In section 5.3.2 we discuss an example where final slip on the fault and moment magnitude (definition given in section B.3) differ a lot between both orientations of a simulation pair (Λ_L , Λ_R), resulting in huge differences in ground motion. In section 5.3.3 we discuss an example where at first a superimposed, finally a distinct wrinkle-like pulse of slip is generated for one material contrast orientation (Λ_R), letting the rupture front propagate essentially at the generalized Rayleigh velocity, while no such pulse is generated for the reversed setup (Λ_L). Here the difference of final slip and moment magnitude is moderate, while the difference in ground motion is large. In section 5.3.4 we discuss an example where we have the generation of a supershear rupture front propagating to one side, a subshear rupture front to the opposite direction for both material contrast orientations (Λ_L , Λ_R). This example demonstrates how supershear propagation can be supported or prevented depending on the orientation of the material contrast, and how a secondary pulse of rupture can travel behind the supershear rupture front travelling at the generalized Rayleigh velocity.

TABLE 5.1: Range of Tested Parameters

parameter	value or value range
numerical method	finite-differences
grid type	staggered Cartesian grid
grid-spacing Δx	100 m
size of physical domain	20 km \times 44 km \times 20 km
density fast material ρ^{fast}	2900.0 kg/m ³
wave velocities fast material $v_s^{\text{fast}}, v_p^{\text{fast}}$	3500.0, 6000.0 m /s
density slow material ρ^{slow}	2416.7 kg/m ³
wave velocities slow material $v_s^{\text{slow}}, v_p^{\text{slow}}$	2916.7, 5000.0 m /s
size of the fault model $y \times z$	44 km \times 20 km = 880 km ²
type of friction	regularized slip-weakening
static friction coefficient f_s	0.8 ... 0.75
dynamic friction coefficient f_d	0.4 ... 0.7
characteristic slip velocity V^*	1 m/s
characteristic length L	0.1, ... , 0.2 m
critical slip distance D_c	0.1, ... , 0.3 m
initial shear stress τ_0	(20...80),(26...80),(40...80) MPa (40...80),(53...80),(60...80) MPa
inverse strength excess S^{-1}	0...1.2
initial normal stress σ_{n_0}	100 MPa
size of nucleation zone \odot_{nuc}	2 km
initial shear stress of nucleation patch	+15%
resulting moment magnitudes M_W	5.3-7.2

5.3.1 Example 1

Here we discuss an example where final slip on the fault is very similar for both orientations of the simulation pair (Λ_L , Λ_R), while the ground motion differs substantially.

The parameters are summarized in table 5.1. Here $L = 0.2$ m, $D_c = 0.3$ m, $f_s = 0.8$, $f_d = 0.5$, initial shear stress varies randomly between 40 and 80 MPa (tapered to zero towards the edges), inverse of strength excess $S^{-1} = 0.4$, $\Delta x = 100$ m.

In Figure 5.2 we show the distribution of initial shear stress for example 1. The initial shear stress is the same for both simulations with reversed orientation of the material contrast. The rupture is nucleated at about 11.5 km down dip and 24 km along strike by an instantaneously overstressed patch ($\phi_{\text{nuc}} = 2$ km around the peak value of initial stress) visible in dark-red color.

The distributions of final slip D for the pair of simulations with switched material orientation (top, Λ_L & bottom, Λ_R) are displayed in Figure 5.3. There is considerable visual similarity. We calculate the correlation coefficient of final slip $C_{D^{\Lambda_R}, D^{\Lambda_L}} = 0.99$, the slip dissimilarity value $\delta D = 9\%$ (equation (5.4)), and the moment magnitudes M_W for both events $M_W^{\Lambda_R} = M_W^{\Lambda_L} = 6.91$, which show that distributions of final slip in this example are indeed very similar. After 10 s already 96% of total final slip in the Λ_R -case and 100% of total final slip in the Λ_L -case are accumulated, so the duration of both events are also comparable.

Slip history on the fault is illustrated in Figure 5.4 with distributions of slip velocity at four instances in time for both material contrast orientations (Λ_L , Λ_R). One can recognize that in this specific example rupture propagates faster to its preferred direction in both cases (Λ_L , Λ_R). Also the amplitudes of slip velocity at the tip of the crack differ between the two simulations with reversed material contrast orientations. Hence, despite the similarity of final slip (see Figure 5.3) rupture history on the fault is significantly altered when switching materials. This becomes more obvious in Figure 5.5 showing distributions of peak slip velocity V_{max} on the fault (top, Λ_L & bottom, Λ_R , equation. The correlation coefficient for both distributions of peak

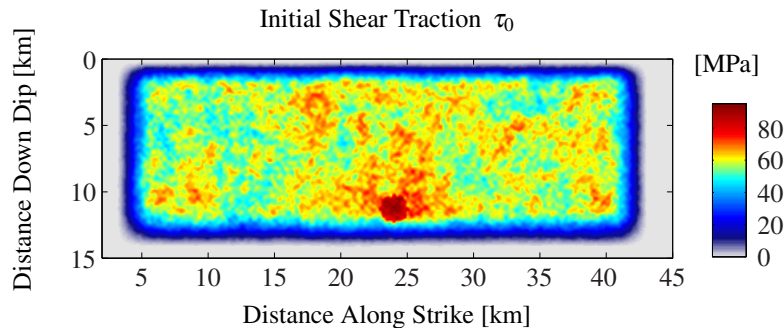


FIGURE 5.2: Initial shear stress for example 1. The shear stress distribution is identical for the two simulations with reversed bimaterial orientations $\tau_0^{\Lambda_R} = \tau_0^{\Lambda_L} = \tau_0$. The overstressed patch is visible at about 11.5 km down dip and 24 km along strike.

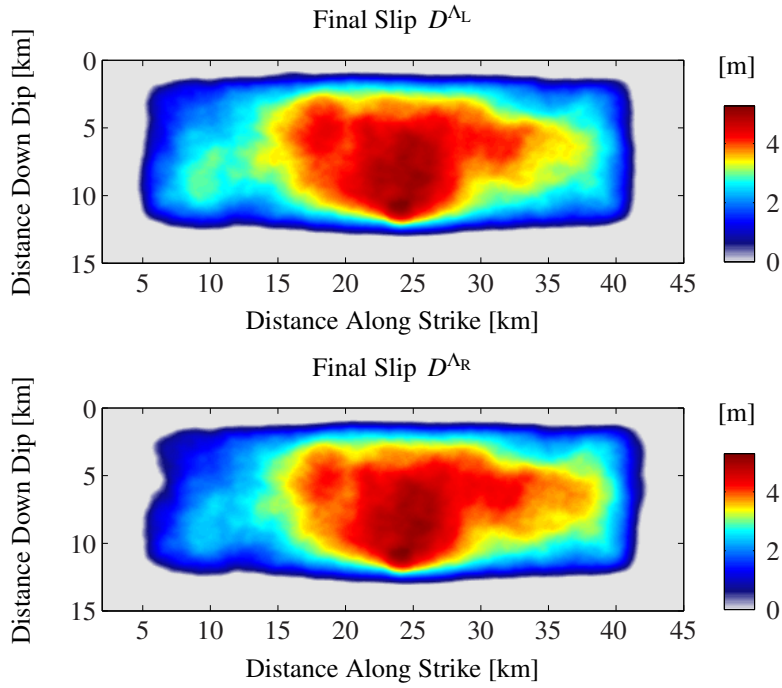


FIGURE 5.3: Distributions of final slip for both material orientations (top, Λ_L & bottom, Λ_R) of example 1. The correlation coefficient for both distributions of slip is $C_{D^{\Lambda_R}, D^{\Lambda_L}} = 0.99$, slip dissimilarity value, as defined in equation (5.4), $\delta D = 9\%$, and the moment magnitudes are identical: $M_W^{\Lambda_R} = M_W^{\Lambda_L} = 6.91$.

slip velocity is $C_{V_{\max}^{\Lambda_R}, V_{\max}^{\Lambda_L}} = 0.72$, the dissimilarity value of the peak slip velocity distributions $\delta V_{\max} = 14\%$ (equation (5.4)).

The results presented in Figures 5.2, 5.4, 5.5 show that the rupture history on the fault is controlled both by the distribution of initial shear stress and the bimaterial mechanism. Since the distribution of peak slip velocity of Λ_L and Λ_R (Figure 5.5) as well as the snapshots of slip velocity for both cases (Figure 5.4) would be identical with no material contrast, we infer that the bimaterial effect contributes significantly to the slip history on the fault.

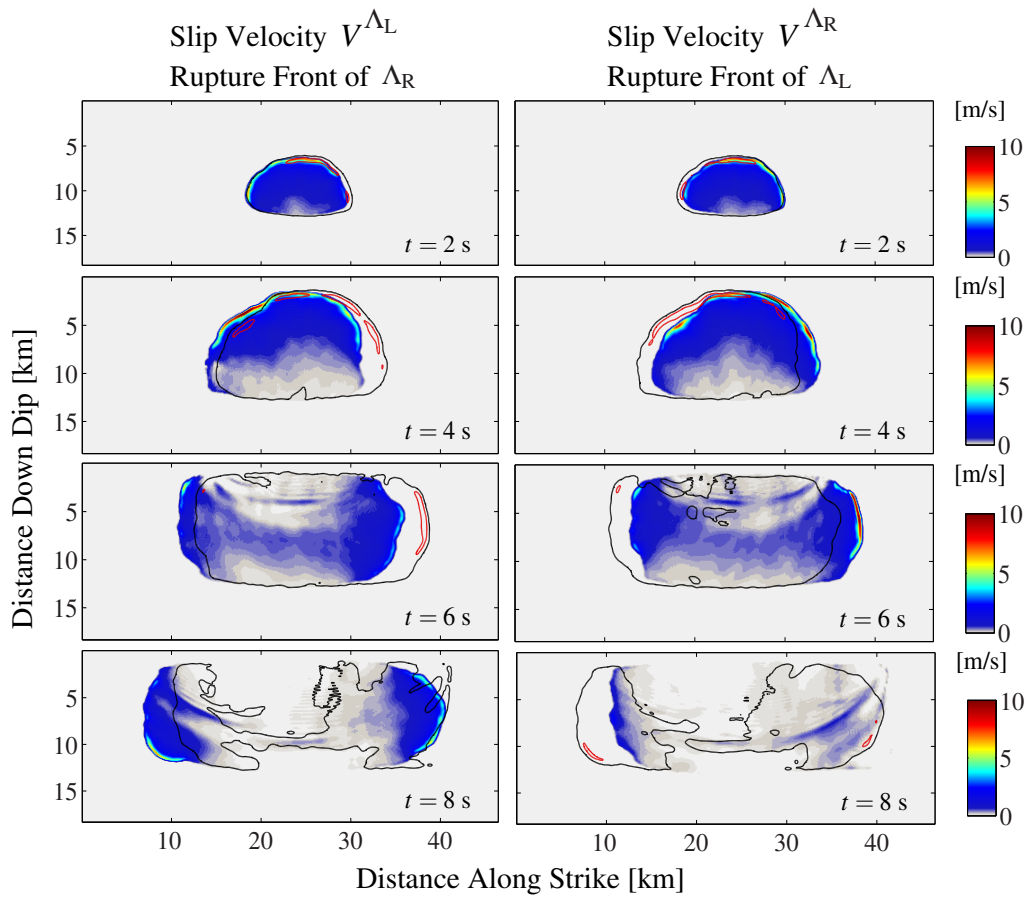


FIGURE 5.4: Time evolution of the rupture for example 1, showing snapshots of slip velocity for four instances in time for both material orientations (left panel, Λ_L , and right panel, Λ_R). In order to better identify differences between both panels, the red and back lines on each panel correspond to the other panel (reversed orientation); the black contour marks the rupture front (of the reversed orientation), the red one shows regions of high slip velocity (of the reversed orientation). In both cases the rupture is enhanced (higher amplitude and larger propagation velocity) in the preferred direction.

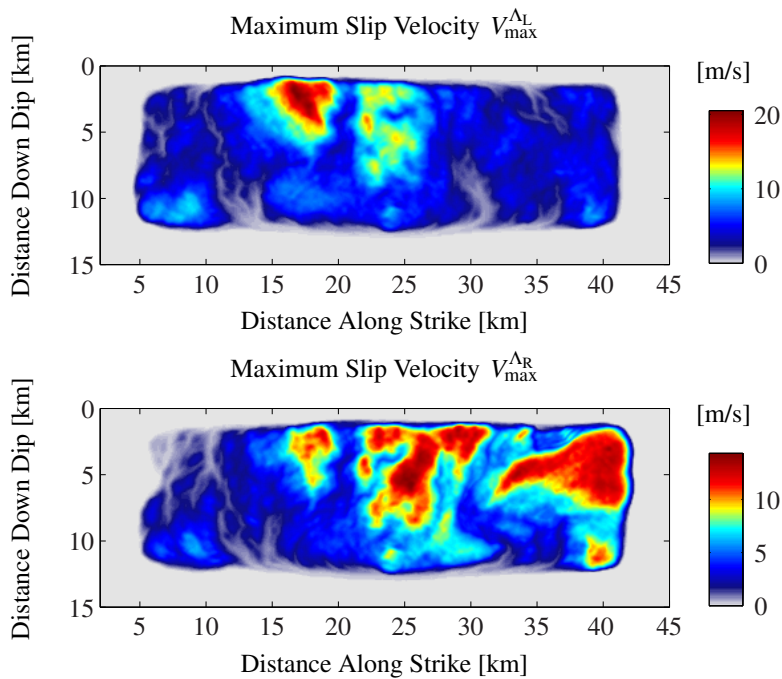


FIGURE 5.5: Distributions of peak slip velocity for both material orientations (top, Λ_L & bottom, Λ_R) of example 1. A region with a peak slip velocity of about $V_{\max}^{\Lambda_L} = 20$ m/s can be identified at around 17 km along strike and 2.5 km down dip in the Λ_L -case which corresponds to an initially high stressed region. In the Λ_R -case mainly two patches of high peak slip velocity can be identified at around 25 km along strike and 5 km down dip, its value being $V_{\max}^{\Lambda_R} = 14$ m/s, and at around 40 km along strike and 5 km down dip, with a value of about $V_{\max}^{\Lambda_R} = 13$ m/s.

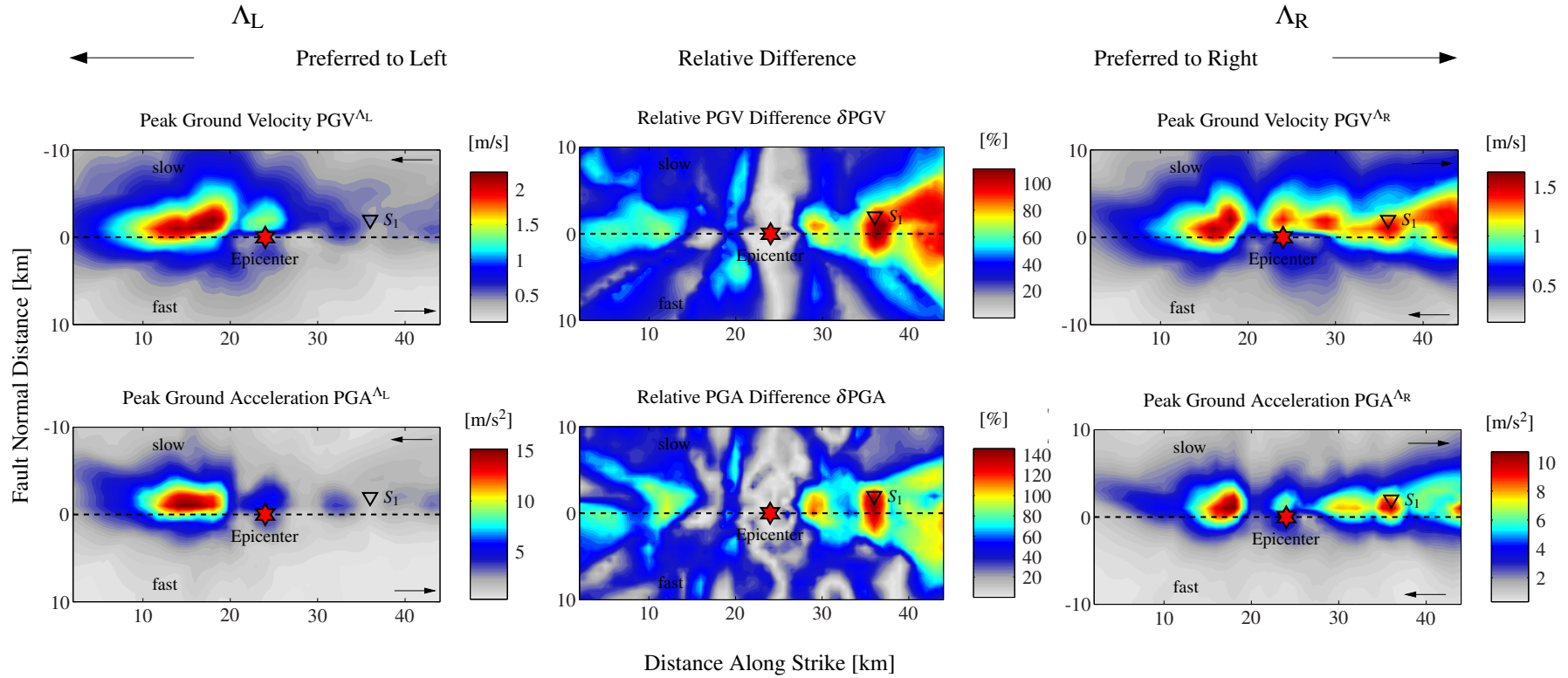


FIGURE 5.6: Peak ground motion maps of example 1 for both material contrast orientations (Λ_L , Λ_R). The epicenter is marked by the red star, the location of a virtual seismometer S_1 is marked by a black triangle, its seismograms being shown in Figure 5.7. Note that for the Λ_L -case the fault-normal axis is reversed for easier comparison, hence the slower side is always at the top for all six panels.

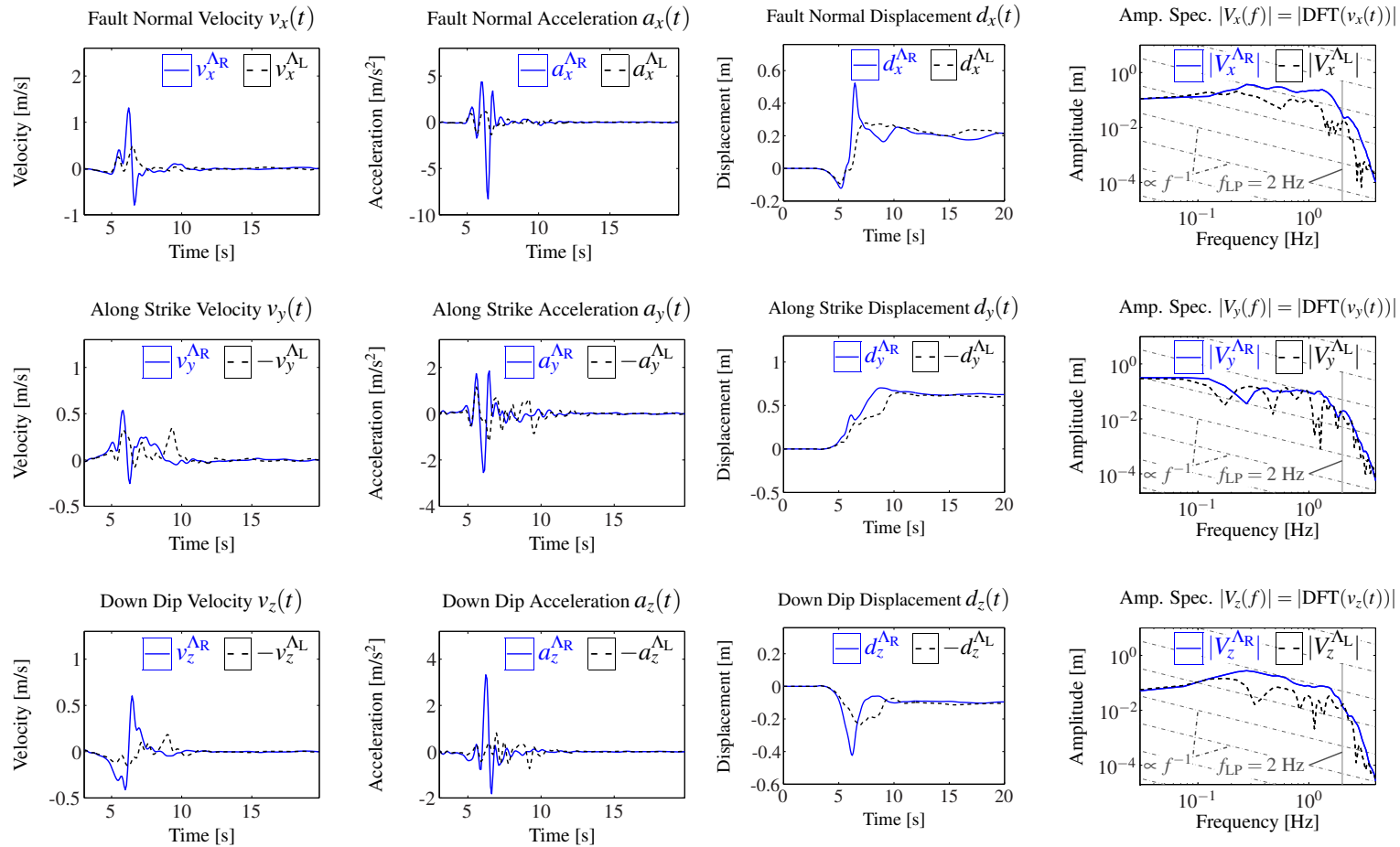


FIGURE 5.7: Seismograms and velocity amplitude spectra of example 1 at stations S_1 for both material contrast orientations (Λ_R , Λ_L). The seismograms are low-pass filtered at 2 Hz. One can see a considerable difference in ground motion when switching materials. The difference is especially large for the fault normal component of velocity (factor of 3) and acceleration (factor of 6) at this station: $\max[v_x^{\Lambda_R}] \approx 3\max[v_x^{\Lambda_L}]$ and $\max[a_x^{\Lambda_R}] \approx 6\max[a_x^{\Lambda_L}]$, while the difference in final displacement is negligible for all three components (d_x , d_y , d_z).

The resulting peak ground motion of example 1 is shown in Figure 5.6. While the Λ_L case shows a large directivity in PGV as well as in PGA, the directivity is less obvious and not simply reversed for the Λ_R case. In the Λ_L case the area of large PGV and PGA is left of the epicenter at about 24 km along strike, while in the Λ_R -case the relevant ground motion is spread over larger portions along the fault. The maximum peak value of ground motion appears in the Λ_L -case and is about 2.3 m/s peak velocity. One can identify its origin with an area of high initial shear traction just below this area (see Figure 5.2). This patch of the fault produces also large ground motion in the Λ_R -case, but less pronounced due to its dynamically unfavored direction. Additionally there is significant ground motion to the right of the epicenter in the Λ_R -case. The area of highest relative difference of peak ground motion is close to the fault at 36 km along strike with values of $\delta\text{PGV} \approx 110\%$ and $\delta\text{PGA} \approx 140\%$.

In Figure 5.7 we show seismograms and velocity amplitude spectra at station S_1 (see Figure 5.6) located at 36 km along strike, 2 km off fault on the slow sides, for both material contrast orientations (Λ_R, Λ_L). The seismograms are low-pass filtered at 2 Hz. As it can be seen in Figure 5.6 this station is located where $\delta\text{PGV} \approx 100\%$ and $\delta\text{PGA} \approx 130\%$. For both orientations the signals exhibit a duration of about 10 s where most shaking takes place within a time-window of about 3-13 s. This time window resembles basically the duration time of the whole event (≈ 10 s). However, a larger amplification of the signal can be seen in the Λ_R -case within a time-window of 3-8 s than for the Λ_L -case. Therefore the seismograms exhibit a considerable change in ground motion amplitudes for the reversed orientations of the material contrast. The difference is especially large for the fault normal component of velocity (factor of 3) and acceleration (factor of 6) at station S_1 : $\max[v_x^{\Lambda_R}] \approx 3\max[v_x^{\Lambda_L}]$ and $\max[a_x^{\Lambda_R}] \approx 6\max[a_x^{\Lambda_L}]$, while the difference in final displacement is negligible for all three components (d_x, d_y, d_z).

Final slip of example 1 ($D = D(y, z)$) is not enough to characterize the wavefield ($v(x, y, z, t), \sigma(x, y, z, t)$) which emanates during the rupture propagation since it contains no information on the time-dependent evolution of the fault. A better fingerprint appears to be peak slip velocity V_{\max} since it contains some information on the time-evolution of slip as a function of the time-derivative of slip: $V_{\max} = V_{\max}(\dot{D}(y, z, t))$. In Figure 5.5 distributions of peak slip velocity for a pair of simulations with switched material contrast orientation (top, Λ_L & bottom, Λ_R) of example 1 were shown. The large differences in V_{\max} account for the large differences in the resulting ground motion. In Figure 5.8 we show the propagation velocities, v_r , calculated from the smoothed gradient of peak arrival times (time when maximum slip velocity arrives) of the rupture. For both cases (Λ_L, Λ_R) significant areas are blue. In these areas the propagation velocity is close the generalized Rayleigh velocity ($v_r = [v_{\text{gr}} - 6\%, v_{\text{gr}}]$). The differences in rupture propagation velocity is another illustration that the slip history on the fault is significantly altered when switching the material contrast orientation.

We ascertain that the seismic radiation differs substantially between both orientations of the material contrast even though slip on the fault is in general very similar. This possibility was

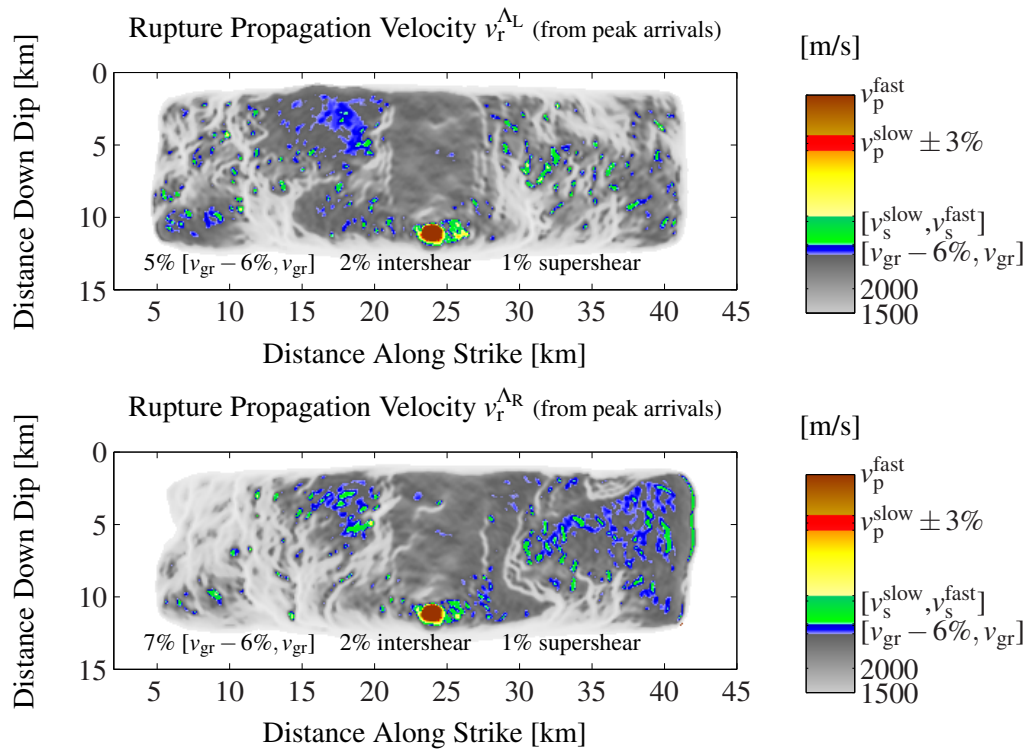


FIGURE 5.8: Rupture propagation velocity calculated from the smoothed gradient of peak arrival times for both material orientations (top, Λ_L & bottom, Λ_R) of example 1. Blue shading highlights areas with a propagation velocity that is close the generalized Rayleigh velocity ($v_r = [v_{gr} - 6\%, v_{gr}]$).

mentioned previously by Andrews and Harris (2005). The large differences in strong ground motion are due to very different slip histories on the fault. Since in our model those can only be different due to the presence of the material discontinuity, this suggests the bimaterial effect to be important for earthquake hazard.

5.3.2 Example 2

We proceed to an example in which final slip on the fault and moment magnitude differ considerably between both orientations of the simulation pair (Λ_L , Λ_R), resulting in very large differences in ground motion.

The parameters are summarized in table 5.1, with specific parameters of $L = 0.2$ m, $D_c = 0.3$ m, $f_s = 0.8$, $f_d = 0.56$, $\Delta x = 100$ m, the range of initial shear stress $\tau_0 = 40 \dots 80$ MPa (tapered to zero towards the edges), with a resulting inverse strength excess $S^{-1} = 0.39$.

In Figure 5.9 we show the distribution of initial shear stress for example 2. The initial shear stress is the same for both simulations with reversed orientation of the material contrast. The rupture is nucleated at about 7 km down dip and 31.5 km along strike by an instantaneously overstressed patch ($\varnothing_{\text{nuc}} = 2$ km around the peak value of initial stress) visible in dark-red color.

In Figure 5.10 we show the distribution of final slip D for the pair of simulations with switched material orientation (top, Λ_L & bottom, Λ_R).

The correlation coefficient of final slip $C_{D^{\Lambda_R}, D^{\Lambda_L}} = 0.38$, the slip dissimilarity value $\delta D = 139\%$ (equation (5.4)), and the moment magnitudes for both events are $M_W^{\Lambda_R} = 6.32$ and $M_W^{\Lambda_L} = 6.82$. The distributions of final slip in this example are thus very different.

In Figure 5.11 we compare the evolution of slip velocity on the fault for the Λ_L - and Λ_R -case at four instances in time. One can see that at $t = 2$ s rupture has a slightly higher amplitude

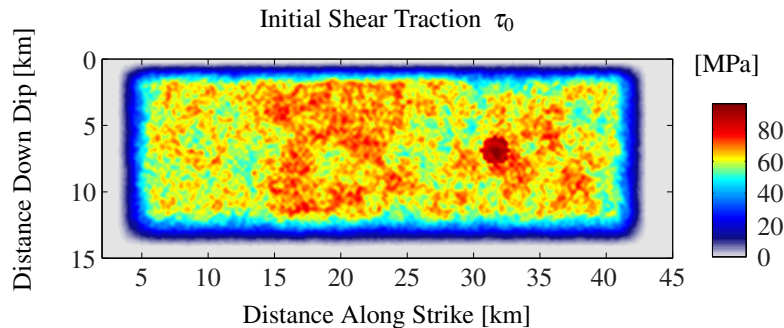


FIGURE 5.9: Initial shear stress for example 2. The shear stress distribution is identical for the two simulations with reversed bimaterial orientations $\tau_0^{\Lambda_R} = \tau_0^{\Lambda_L} = \tau_0$. The overstressed patch is visible at about 7 km down dip and 31.5 km along strike.

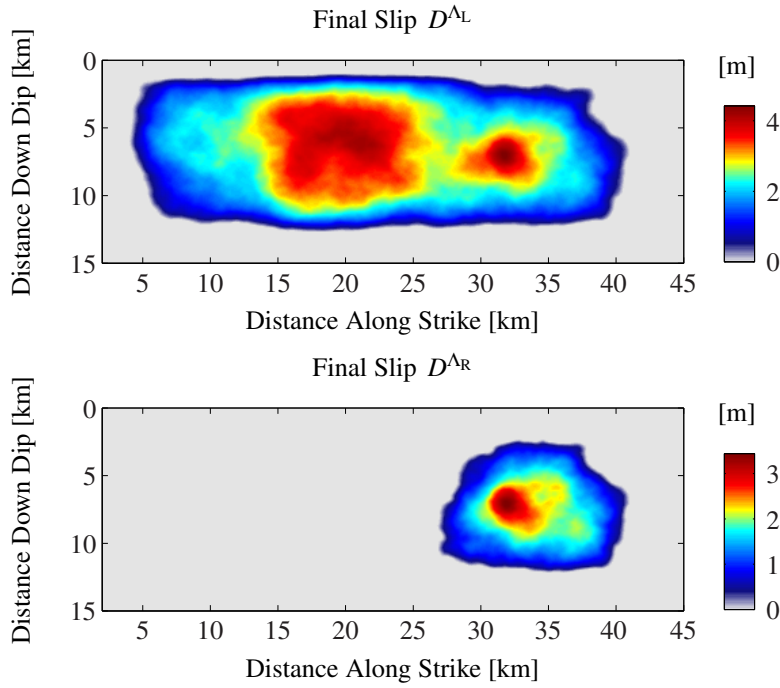


FIGURE 5.10: Distributions of final slip for both material orientations (top, Λ_L & bottom, Λ_R) of example 2. The correlation coefficient for both distributions of slip $C_{D^{\Lambda_R}, D^{\Lambda_L}} = 0.38$, the slip dissimilarity is $\delta D = 139\%$, and the moment magnitudes differ by half a unit: $M_W^{\Lambda_R} = 6.32$, $M_W^{\Lambda_L} = 6.82$.

and larger propagation velocity in its preferred direction for the Λ_R -case when comparing to the Λ_L -case. At $t = 8$ s and $t = 14$ s there are only tiny slipping patches remaining for the Λ_R -case while in the Λ_L -case considerable slipping patches can be recognized. In the Λ_R -case rupture dies out and no slip is remaining at $t = 20$ s. Figure 5.12 shows a detail of slip velocity at the moment of minimal slip velocity of the Λ_L -case with additional contours showing the propagation velocity as contour lines. The snapshot is taken at the moment when in the Λ_L -case rupture slowly overcomes a region of relatively low initial shear stress around 5-10 km down dip and 24-28 km along strike and then speeds up and amplifies in the region of large initial shear stress around 14-24 km along strike (see Figure 5.9), and it finally ruptures the entire fault in its preferred direction (Λ_L).

Thus, the bimaterial mechanism helps to overcome an asperity of low initial shear stress initiating a secondary event along the fault in its preferred direction, while in the case of reversed material contrast orientation (Λ_R -case) it cannot. In Figure 5.13 we show distributions of peak slip velocity V_{\max} on the fault of example 2 (top, Λ_L & bottom, Λ_R). The correlation coefficient for both distributions of peak slip velocity $C_{V_{\max}^{\Lambda_R}, V_{\max}^{\Lambda_L}} = 0.07$, and the dissimilarity value of the peak slip velocity distributions $\delta V_{\max} = 41\%$ (equation (5.4)). A region with a comparatively small peak slip velocity ($V_{\max}^{\Lambda_L} \leq 1$ m/s) can be identified at around 25-26 km along strike in the Λ_L -case. This region has low initial shear stress (see Figure 5.9). As mentioned before, rupture stops at this obstacle in the Λ_R -case. In the Λ_L -case the region with low initial shear stress can

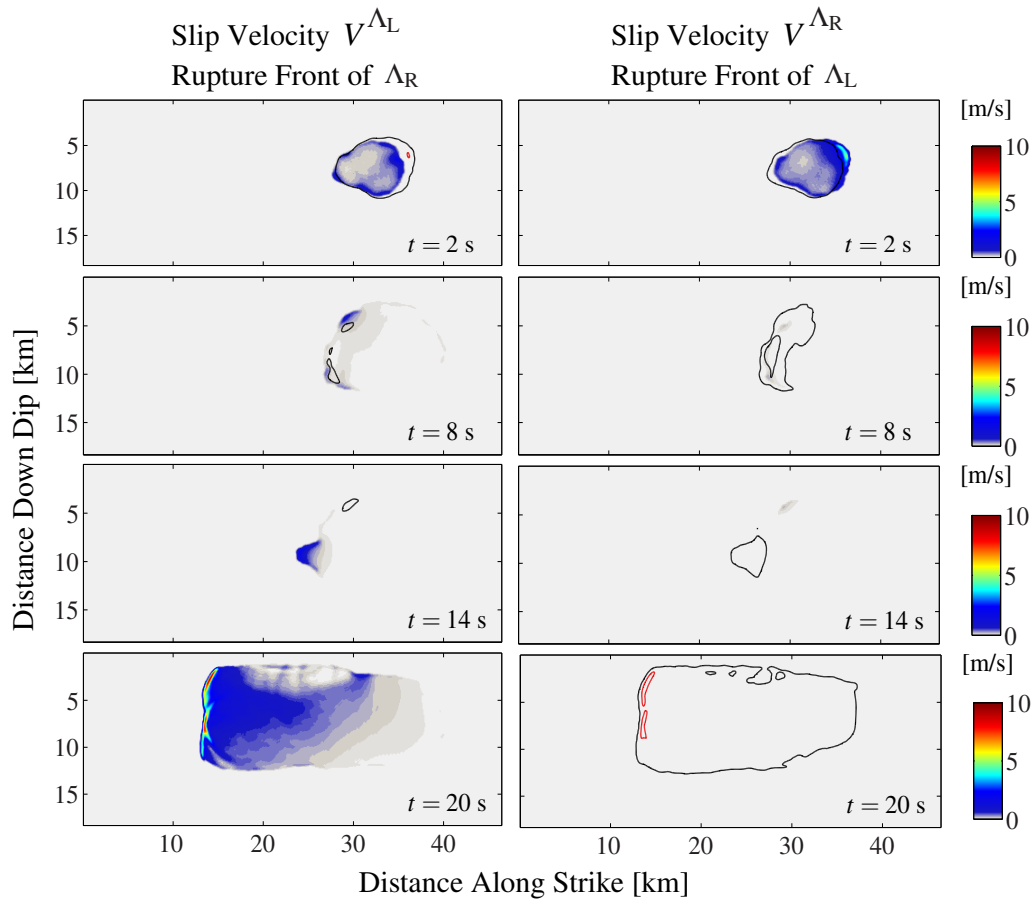


FIGURE 5.11: Time evolution of the rupture for example 2, showing snapshots of slip velocity for four instances in time for both material orientations (left panel, Λ_L , and right panel, Λ_R). The black contour marks the rupture front of the reversed orientation, the red one shows regions of high slip velocity of the reversed orientation.

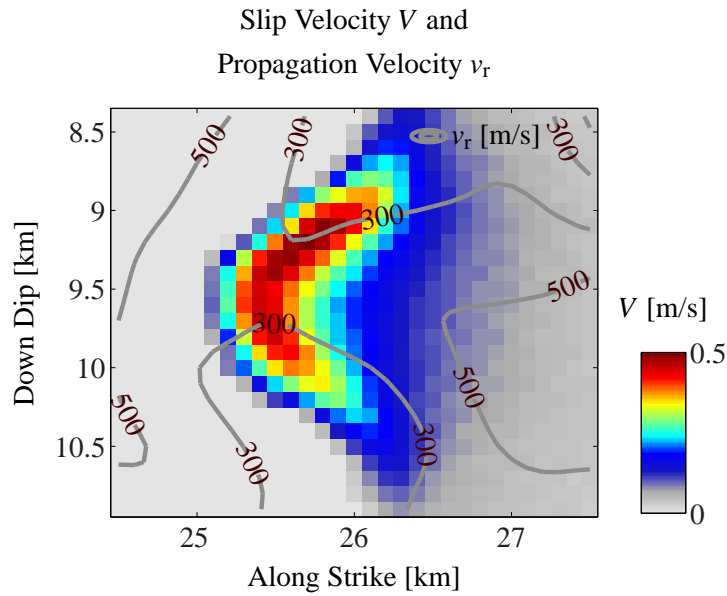


FIGURE 5.12: Slip velocity (color-coded) and propagation velocity calculated from first arrival times (contour) of example 2 at $t = 14$ s (detail of Figure 5.11 Λ_L -case, 3rd panel from top).

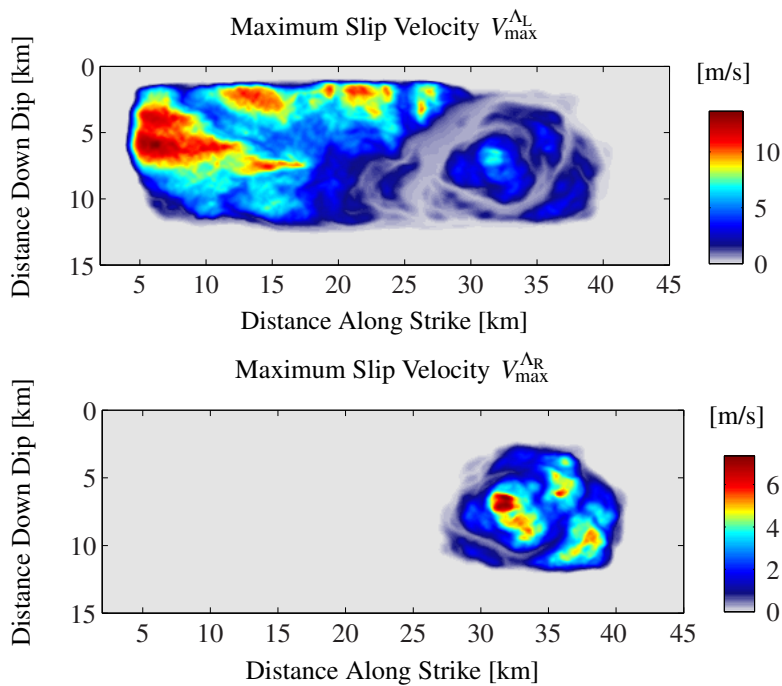


FIGURE 5.13: Distributions of peak slip velocity for both material orientations (top, Λ_L & bottom, Λ_R) of example 2. A region with a comparatively small peak slip velocity ($V_{\max}^{\Lambda_L} \leq 1$ m/s) can be identified at around 25-26 km along strike, which corresponds to the asperity of low initial shear stress mentioned in the text. The event for the Λ_R -case stops at this obstacle.

be overcome although slip velocity is less than 1 m/s and propagation velocity (calculated from arrival times) reaches a minimum value of $v_r^{\min} \approx 315$ m/s (see Figure 5.12).

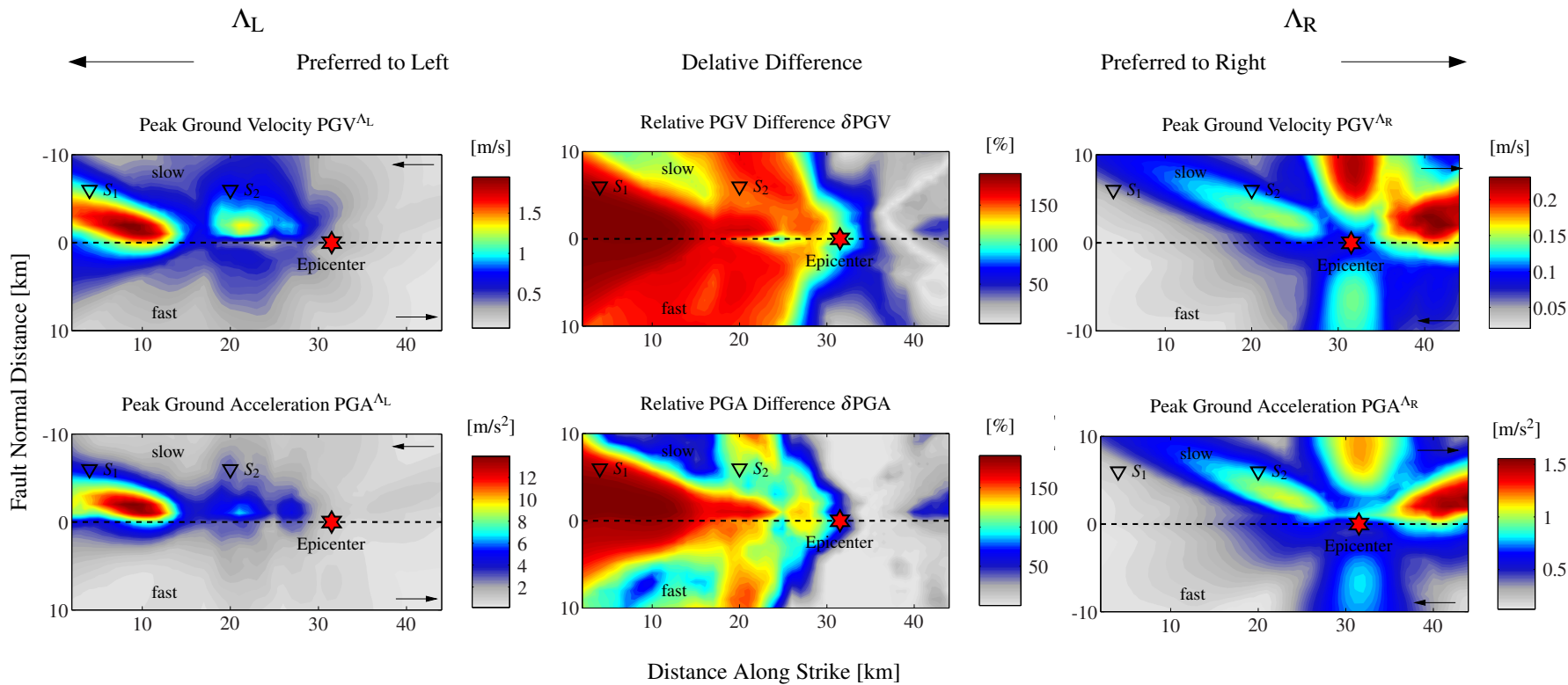


FIGURE 5.14: Peak ground motion maps of example 2 for both material contrast orientations (Λ_L , Λ_R). The epicenter is marked by the red star, the locations of two virtual seismometers S_1 , S_2 are marked by black triangles, their seismograms being shown in Figures 5.15 and 5.16.

Obviously the resulting peak ground motion shows huge differences between the two material contrast orientations (Λ_L , Λ_R). In Figure 5.14 we show PGV^{Λ_L} and PGA^{Λ_L} (left side), PGV^{Λ_R} and PGA^{Λ_R} (right side), and δPGV , δPGA (center). The maximum relative difference in PGV and PGA is almost 190%, the highest possible values being 200% (see equation (5.5)). One can recognize a slight directivity effect to the right in the Λ_R -case (Figure 5.14 left side). As mentioned earlier, in the Λ_L -case we discovered the initiation of a secondary event. This secondary event makes the peak ground motion an order of magnitude of amplitude different (remember the difference in moment magnitude M_W is half a magnitude). The secondary event propagates only in the Λ_L -direction and hence has a very strong directivity to the Λ_L -direction.

We show in Figures 5.15 and 5.16 the waveforms generated at stations S_1 and S_2 , respectively (see their locations in Figure 5.14). S_1 is located within a region of large difference in peak ground motion while S_2 is in a region of moderate difference in PGA, but already large differences in PGV.

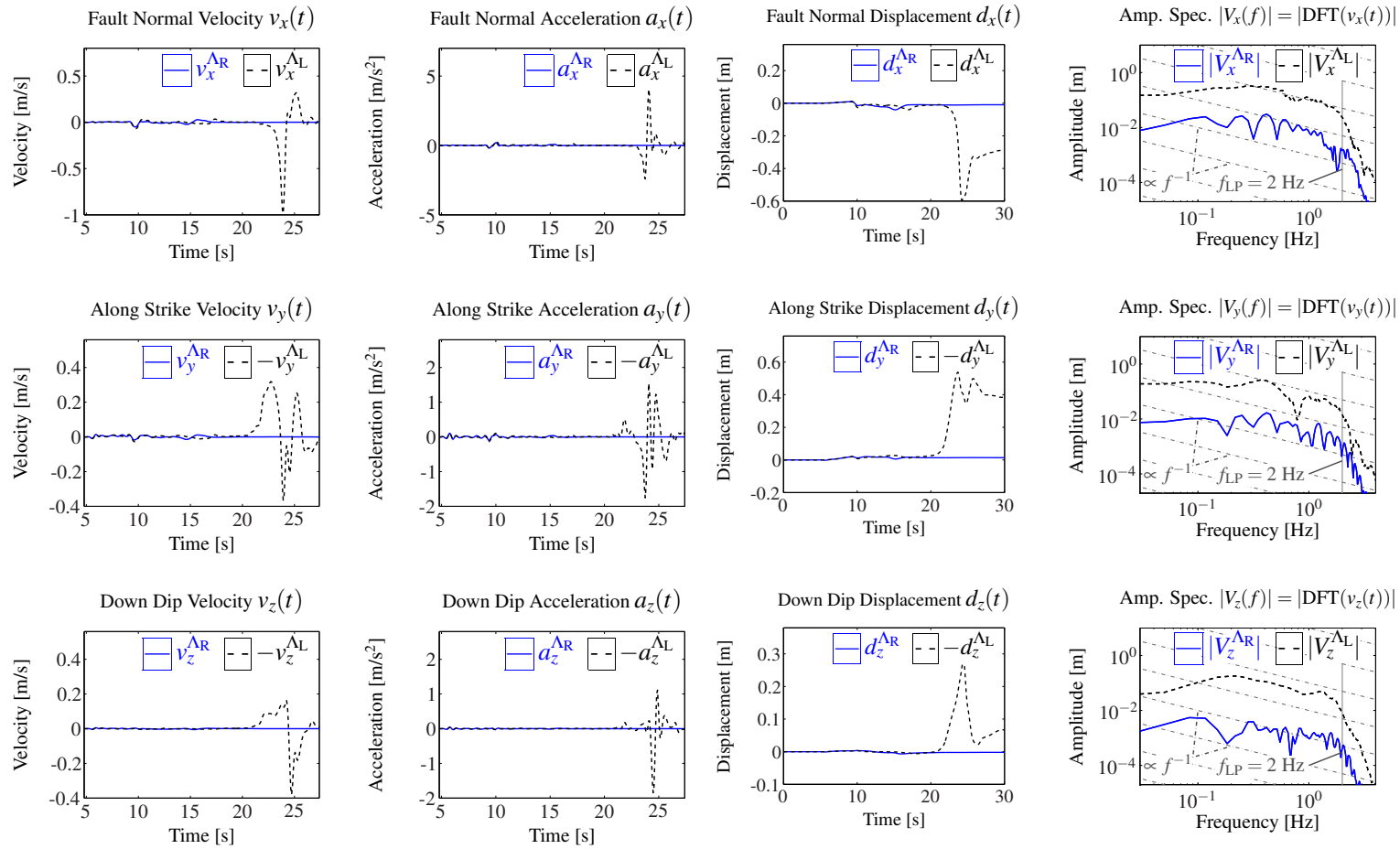


FIGURE 5.15: Seismograms and velocity amplitude spectra of example 2 at station S_1 for a pair of simulations with reversed bimaterial orientations (see also Figure 5.14 for station location). The seismograms are low-pass filtered at 2 Hz. As it can be seen in Figure 5.14 this is a station located within a region of very large difference in peak ground motion (both δPGV and $\delta\text{PGA} > 160\%$). The difference is huge for all components (v_x , v_y , v_z , a_x , a_y , a_z , d_x , d_y , d_z) for the entire frequency band of all Fourier components (V_x , V_y , V_z). The early phase in the seismograms are similar.

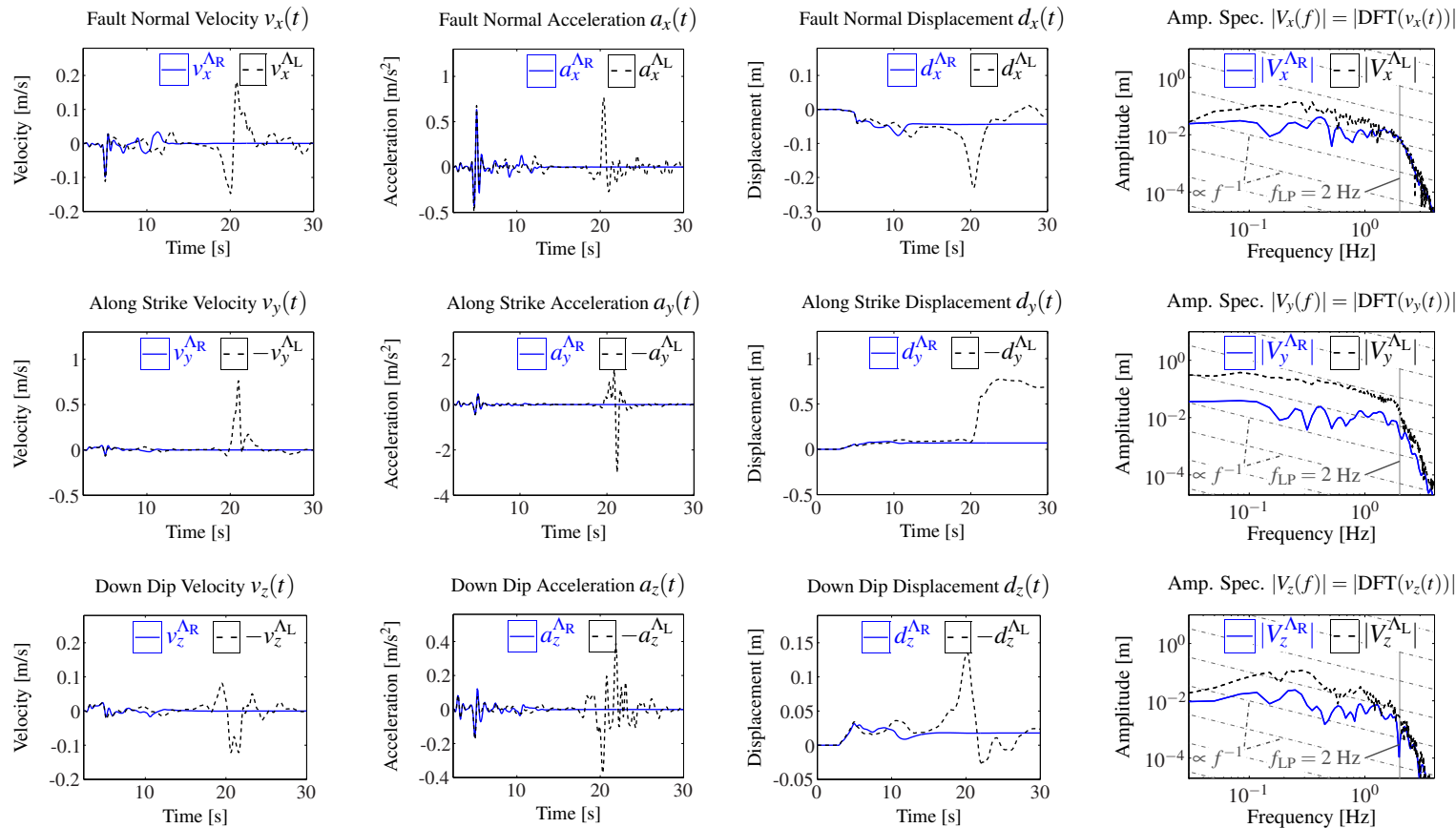


FIGURE 5.16: Seismograms and velocity amplitude spectra of example 2 at station S_2 for a pair of simulations with reversed bimaterial orientations (see also Figure 5.14 for station location). The seismograms are low-pass filtered at 2 Hz. As it can be seen in Figure 5.14 this is a station with a large difference in peak ground velocity ($\delta\text{PGV} \approx 150\%$) but moderate difference in peak ground acceleration ($\delta\text{PGA} \approx 100\%$). For the fault normal component one can see a difference of peak amplitude of velocity of about a factor of 2, while the peak acceleration is very similar. The early phase in the seismograms are similar.

Since we already investigated the large differences of the fault rupture and peak ground motion, it is not surprising we also see large differences in the individual seismograms. One can easily identify an early phase which belongs to the initial event in both cases (Λ_L and Λ_R) and a clearly separated signal which stems from a secondary event, present only in the Λ_L -case. The signals of the early phase ($t \leq 12$ s) have a large similarity (shape and amplitudes) at stations S_1 and S_2 . Consistent with the slip history on the fault shown before, the secondary event, which is present only in the Λ_L -case, produces the much larger ground motion, with a difference of up to a factor of 9 for PGV as well as for PGA. This is due to much larger slip velocities (factor of 2, see Figure 5.13) on the fault area which ruptures only in the Λ_L -case, especially those areas close to the free surface.

A characteristic of a Weertman pulse travelling along a bimaterial interface is its propagation velocity $v_r \approx v_{gr}$, the generalized Rayleigh velocity. Figure 5.17 shows the rupture propagation velocity for example 2. For the Λ_L case (top panel of Figure 5.17) the rupture propagation velocity v_r is, in 9% of the total slipping area, close to the generalized Rayleigh velocity ($v_r = [v_{gr} - 6\%, v_{gr}]$). These areas show up in blue color shading and are an indicator for the Weertman pulse significantly contributing to the rupture dynamics. In both cases most of the fault ruptured with a velocity slower than the generalized Rayleigh velocity, as indicated by the gray shaded regions (94% for Λ_R and 83% for Λ_L). We find there is indication for a superimposed Weertman pulse in example 2 for the Λ_L -case.

The shown example demonstrates the bimaterial effect to be important in the entire subshear velocity range. First, the bimaterial mechanism being efficient in a range of very slow propagation velocities, giving the ability to overcome asperities of low initial shear stress. Second, there is indication that for an appropriate state of initial shear stress, as in the the Λ_L -case of the given example, and after a sufficiently large propagation distance, features typical for the Weertman pulse (e.g. sharpening behavior at the rupture front with large slip velocities, and a propagation velocity close to the generalized Rayleigh velocity), nucleate naturally from the initially slow event as a superimposed part of the rupture. The large macroscopic difference in this example suggests that the fault is close to a critical state at key parts of the fault where rupture propagation is on the verge of dying or propagating, the bimaterial mechanism being the incident that tips the scale. The resulting peak ground motion is orders of magnitude different for the Λ_R and Λ_R cases. Thus we can infer that the bimaterial mechanism is important for earthquake dynamics, strong ground motion and earthquake hazard.

5.3.3 Example 3

In this example we show that even a distinct Weertman pulse can nucleate naturally in the presence of heterogeneous stress and slip-weakening friction. Once such a pulse is generated it can more efficiently overcome low-stress regions while propagating more or less constantly close to the generalized Rayleigh velocity. The pulse is generating large amplitudes in the

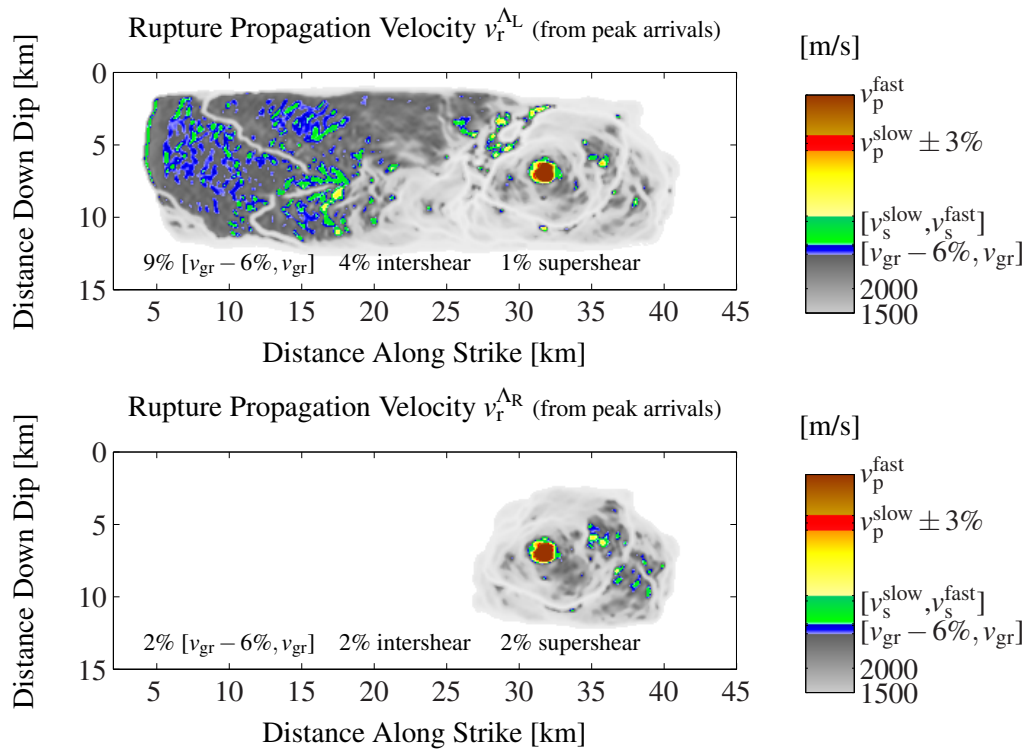


FIGURE 5.17: Rupture propagation velocity calculated from the smoothed gradient of peak arrival times for both material orientations of example 2. For the Λ_R case (bottom panel) the rupture propagation velocity v_r is, within 9% of the total slipping area, close to the generalized Rayleigh velocity ($v_r = [v_{gr} - 6\%, v_{gr}]$). These areas show up in blue color shading and are an indicator for the bimaterial mechanism significantly contributing to the rupture dynamics. The instantaneous nucleation patch shows up as a dark red region.

emanated wavefield at relatively high frequencies.

The parameters are summarized in table 5.1, with specific parameters of $L = 0.2$ m, $D_c = 0.3$ m, $f_s = 0.8$, $f_d = 0.48$, initial shear stress varies randomly between 26 and 80 MPa (tapered to zero towards the edges), inverse of strength excess $S^{-1} = 0.27$, $\Delta x = 100$ m. In Figure 5.18 the initial distribution of shear stress on the fault plane is shown for example 3. The nucleation patch with 2 km diameter can be seen at about 5 km down dip and 12.5 km along strike. The resulting distributions of final slip are shown in Figure 5.19. The largest differences between D^{Λ_L} and D^{Λ_R} can be seen by the additional area of slip of D^{Λ_R} on the right side at 35-42 km along strike which is absent in the Λ_L -case. In comparison with the total slip on the fault the additional slip in the Λ_R -case is small.

In Figure 5.20 we compare the evolution of slip velocity on the fault for the Λ_L - and Λ_R -case at four instances in time. In the early stage of the rupture ($t = 2$ s) the rupture propagates in a crack-like manner. Then, stopping phases are initiated at the tapered regions at the boundaries (top side first, then bottom and left side) ($t = 4.5$ s). After that, rupture propagates in both cases (Λ_R , Λ_L) to the right side, essentially as a pulse ($t \geq 7$ s). The rupture front of the Λ_L -case propagates much slower than in the Λ_R -case. At time-steps $t = 7$ s and $t = 9.5$ s rupture develops towards a distinct pulse in the Λ_R -case with large slip velocity, while in the Λ_L -case it is slowly getting smaller.

The resulting distributions of peak slip velocity are shown in Figure 5.21. The distributions of peak slip velocity are very different. The correlation coefficient for both distributions of peak slip velocity is $C_{V_{\max}^{\Lambda_R}, V_{\max}^{\Lambda_L}} = 0.47$, the dissimilarity value of the peak slip velocity distributions $\delta V_{\max} = 27\%$ (equation (5.4)). One can see that in the Λ_L -case peak slip velocity stays below 10 m/s over most of the slipping fault, with two exceptions which can be related to highly stressed regions close the lower boundary of the fault (see Figure 5.18). In the Λ_R -case peak slip velocity looks very different. Here a large portion of the fault (approximately at 22-42 km along strike and 4-12 km down dip) ruptures at high slip velocities ($V_{\max}^{\Lambda_R} \approx 12...19$ m/s). Most

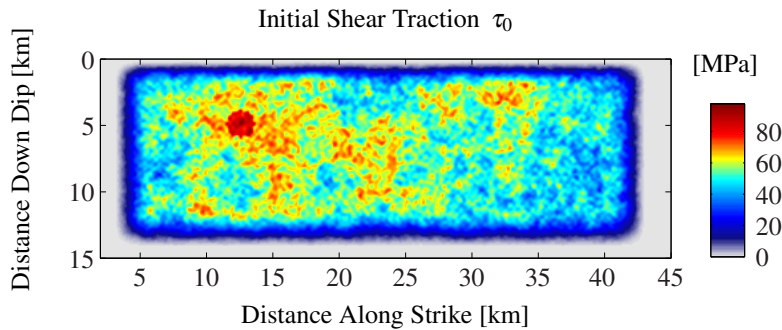


FIGURE 5.18: Initial shear stress for example 3. The overstressed patch is clearly visible at about 5 km down dip and 12.5 km along strike. The shear stress distribution is identical for the two simulations with reversed bimaterial orientations $\tau_0^{\Lambda_R} = \tau_0^{\Lambda_L} = \tau_0$.

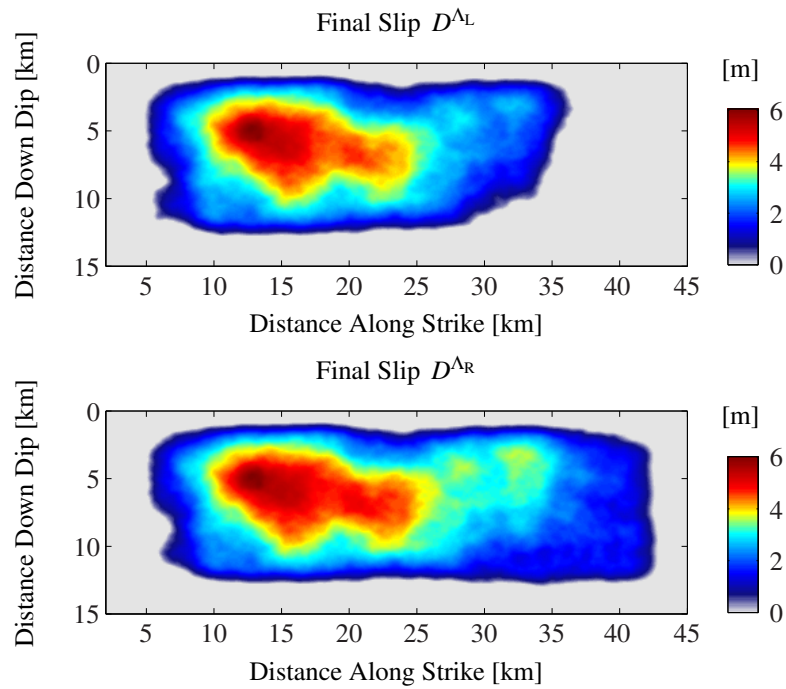


FIGURE 5.19: Distributions of final slip for both material orientations (top, Λ_L & bottom, Λ_R) of example 3. The correlation coefficient for both distributions of slip is $C_{D^{\Lambda_R}, D^{\Lambda_L}} = 0.94$, the slip dissimilarity is $\delta D = 28\%$, and the moment magnitudes differ slightly: $M_W^{\Lambda_R} = 6.90$, $M_W^{\Lambda_L} = 6.82$.

of this area is not in a very highly prestressed condition (see Figure 5.18). In Figure 5.22 the rupture propagation velocity is shown for both material contrast orientations.

In the Λ_R -case (bottom panel of Figure 5.22) the rupture propagation velocity v_r is, within 23% of the total slipping area, close to the generalized rayleigh velocity ($v_r = [v_{gr} - 6\%, v_{gr}]$). The colormap is constructed such that these areas show up in blue. The predominantly blue-shaded portion of the fault suggests that the Weertman-type of slip pulse is part of the solution. In the Λ_R -case we gather the evidence that there is a superimposed wrinkle-like pulse between 18-30 km distance along strike and a more or less distinct wrinkle-like pulse from 30-41 km distance along strike. In the Λ_L -case the rupture propagation velocity reaches intershear velocity but stays sub-Rayleigh in 91% of the slipping fault area.

The large differences in peak slip velocity distributions in Figure 5.21 suggest a large difference in ground motion at the surface for example 3. Maps of peak ground motion and their differences of example 3 are displayed in Figure 5.23.

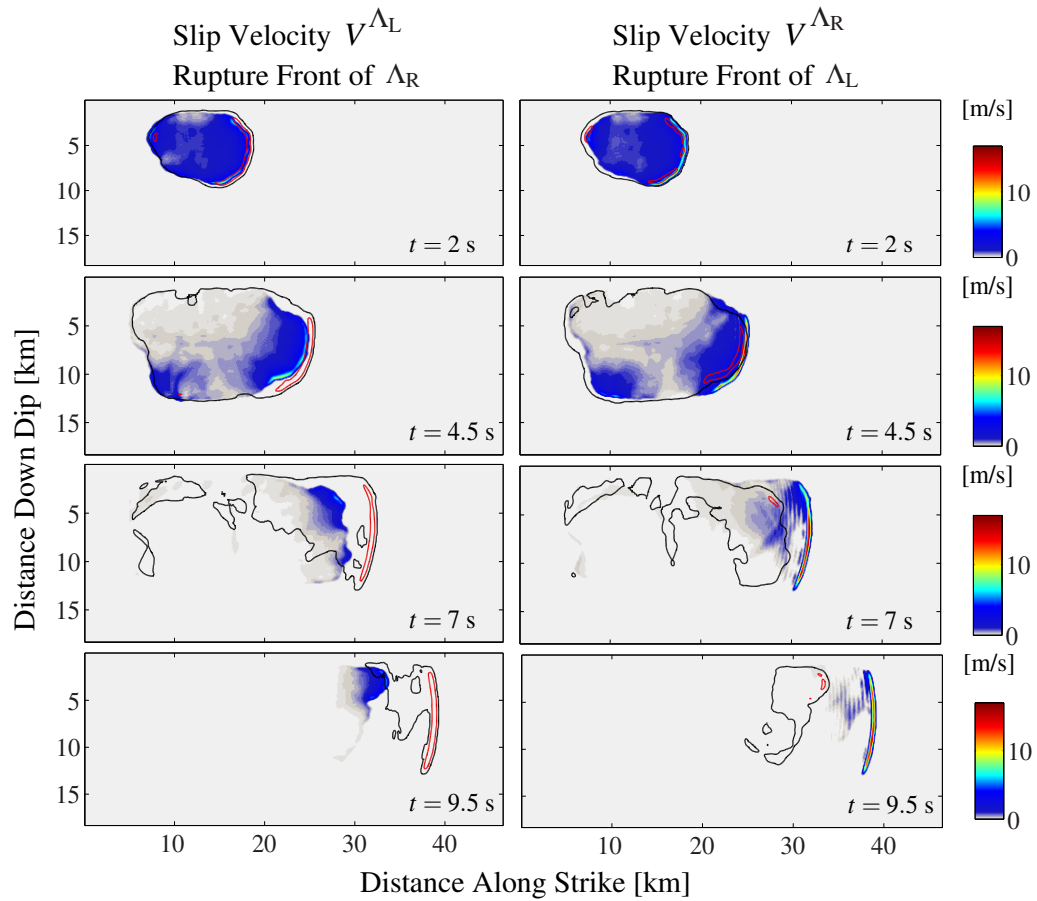


FIGURE 5.20: Time evolution of the rupture for example 3, showing snapshots of slip velocity for four instances in time for both material orientations (left panel, Λ_L , and right panel, Λ_R). The black contour marks the rupture front of the reversed orientation, the red one shows regions of high slip velocity of the reversed orientation. The Λ_R -case features a sharp and distinct pulse.

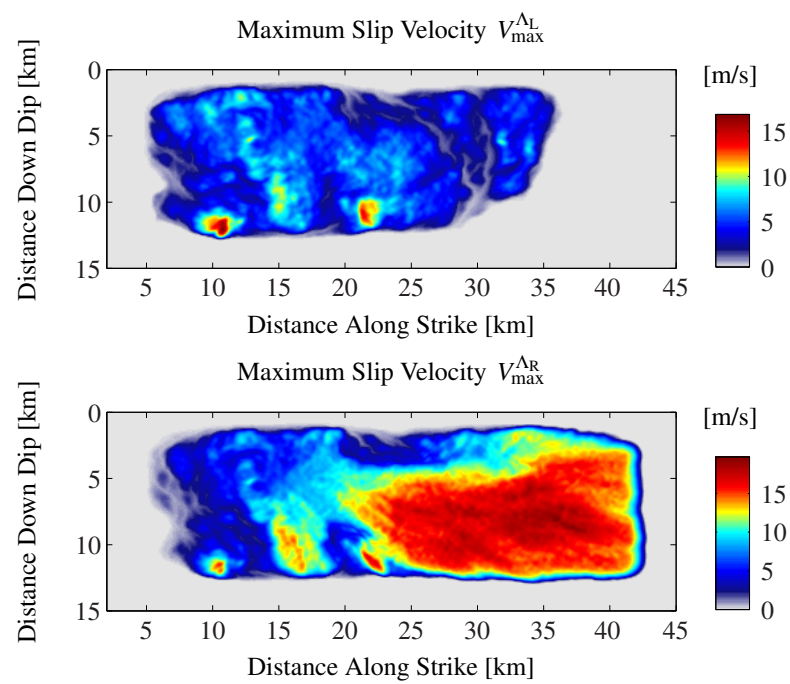


FIGURE 5.21: Distributions of peak slip velocity of example 3, a pair of simulation with switched material orientation (top, Λ_L & bottom, Λ_R).

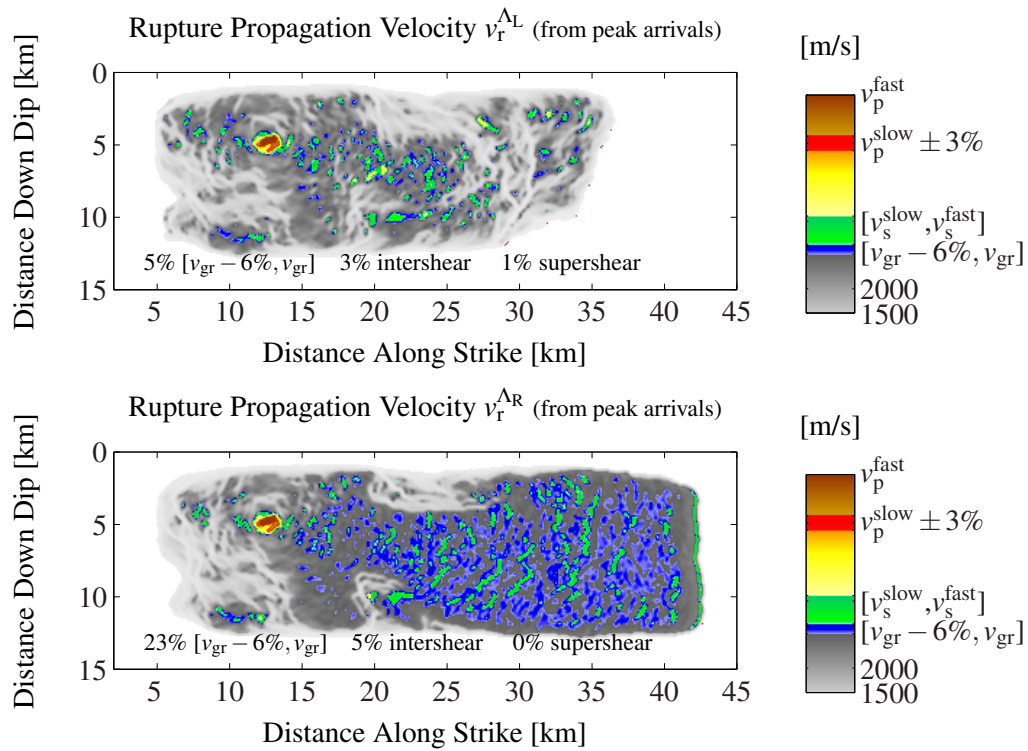


FIGURE 5.22: Rupture propagation velocity of example 3 calculated from the smoothed gradient of peak arrival times of the rupture. The instantaneous nucleation patch shows up as a dark red region with an unrealistically high propagation velocity. For the Λ_R case (bottom panel) the rupture propagation velocity, v_r , is, within 23% of the total slipping area, close to the generalized Rayleigh velocity ($v_r = [v_{gr} - 6\%, v_{gr}]$). These areas show up in blue color shading and are an indicator that the Weertman-type of slip pulse is part of the solution.

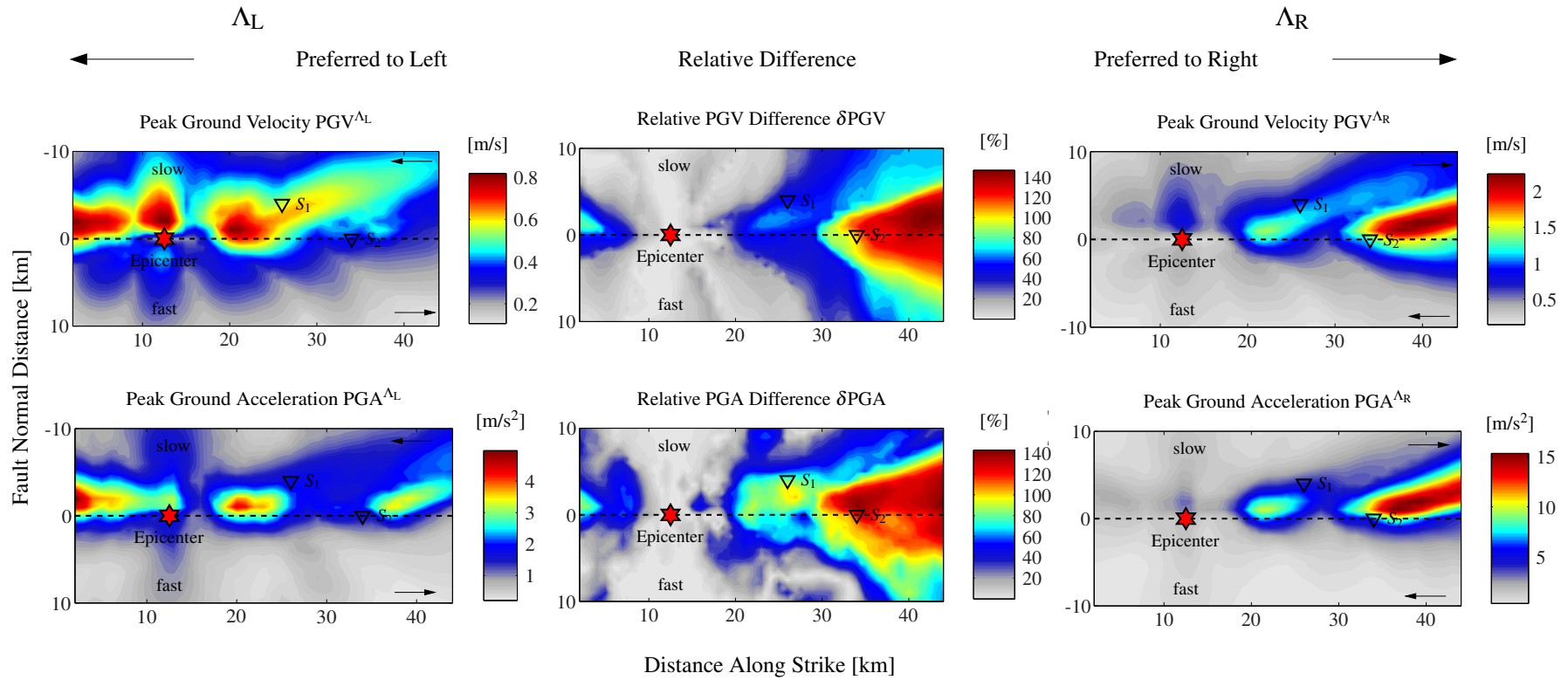


FIGURE 5.23: Peak ground motion maps of example 3 for both material contrast orientations (Λ_L , Λ_R). The epicenter is marked by the red star, the locations of two virtual seismometers S_1 and S_2 are marked by black triangles, their seismograms being shown in Figures 5.24 and 5.25. As expected from the large differences in peak slip velocity (Figure 5.21) and propagation velocity (Figure 5.22) one can see that maximum PGV^{Λ_L} and maximum PGV^{Λ_R} differ by almost a factor of 3 and maximum PGA^{Λ_L} and maximum PGA^{Λ_R} differ by more than a factor of 3. While PGV^{Λ_R} and PGA^{Λ_R} provide a very strong directivity to the right, ground motion in the Λ_L -case is distributed with less directivity.

The relative difference values of ground motion (as defined in equations (5.5)) are slightly above 140% for PGV as well as for PGA. The setup of initial shear stress of example 3 lets the rupture propagate mainly to the right for both material contrast orientations (Λ_L , Λ_R). Therefore a setup induced directivity might be expected in the maps of peak ground motion (Figure 5.23) for both cases. In fact in the Λ_R -case we can notice a huge directivity. For the Λ_L -case, on the contrary, the potential directivity does not really show up. Here the preferred direction of the bimaterial interface (Λ_L) is opposing the favoring due to the setup, and the ground motion looks much more symmetric than in the Λ_R -case.

We show seismograms and spectra at two stations (S_1 and S_2) for example 3 in Figure 5.24. The location of the two stations can be seen in Figure 5.23. Station S_1 is located on the slow sides 4 km off fault and 26 km distance along strike, which is a point with $\delta\text{PGV} \approx 50\%$ and $\delta\text{PGA} \approx 90\%$. Station S_2 is located directly on the fault at 34 km along strike distance which is a point with larger relative differences: $\delta\text{PGV} \approx 110\%$ and $\delta\text{PGA} \approx 125\%$.

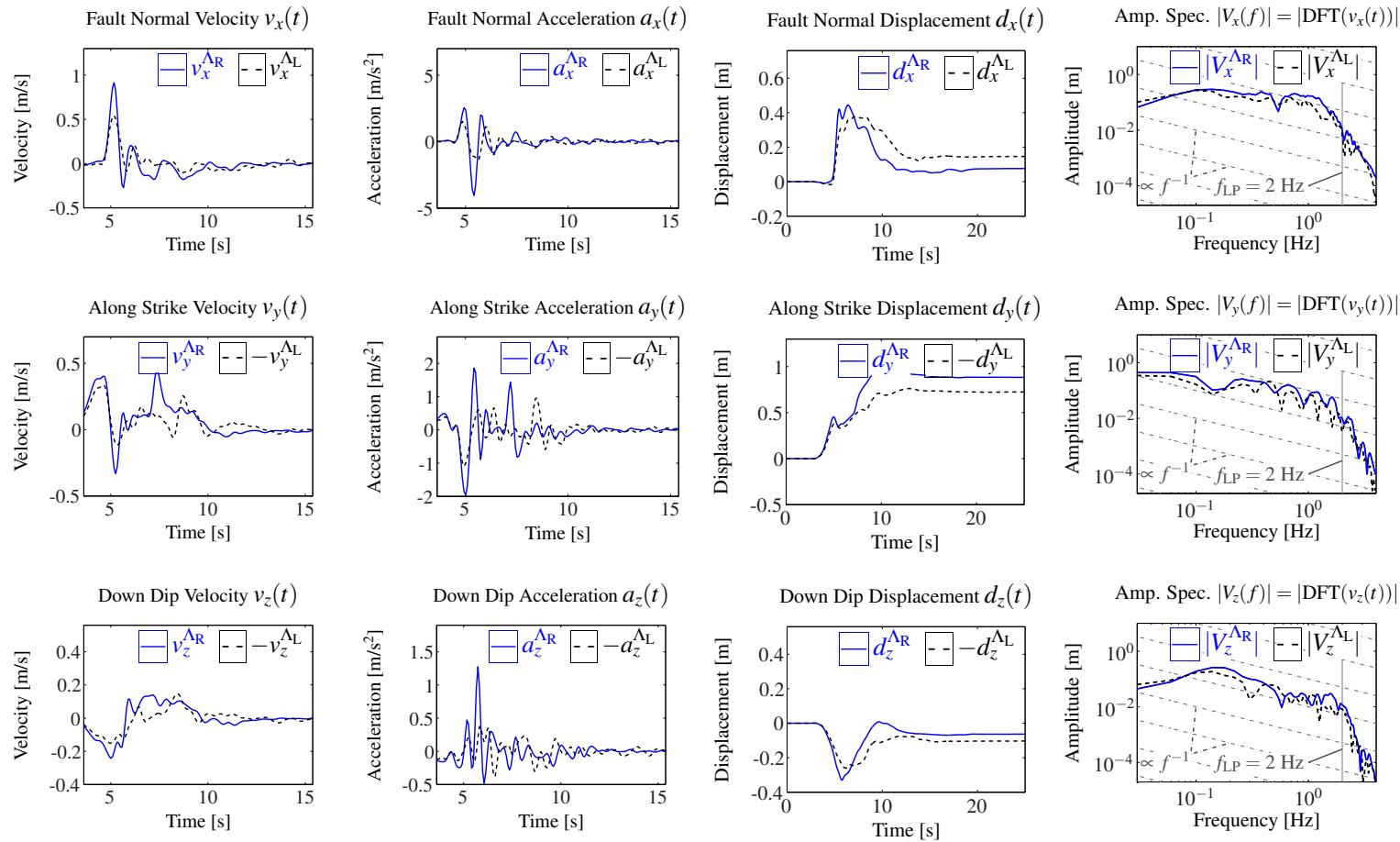


FIGURE 5.24: Seismograms and velocity amplitude spectra station S_1 of example 3 at station S_1 for a pair of simulations with reversed bimaterial orientations (Λ_R , Λ_L). The seismograms are low-pass filtered at 2 Hz. As it can be seen in Figure 5.23, this is a point with $\delta\text{PGV} \approx 50\%$ and $\delta\text{PGV} \approx 90\%$. Large amplitude differences can be seen especially in all three acceleration components (\approx factor of 2 or greater). For the fault-normal component one can remark smaller displacement for the Λ_R -case than for the Λ_L -case although acceleration and velocity are both larger in the Λ_R -case. The spectra show in both cases a decay of amplitude that meets $V(f) \propto f^{-1}$ over a wide frequency band.

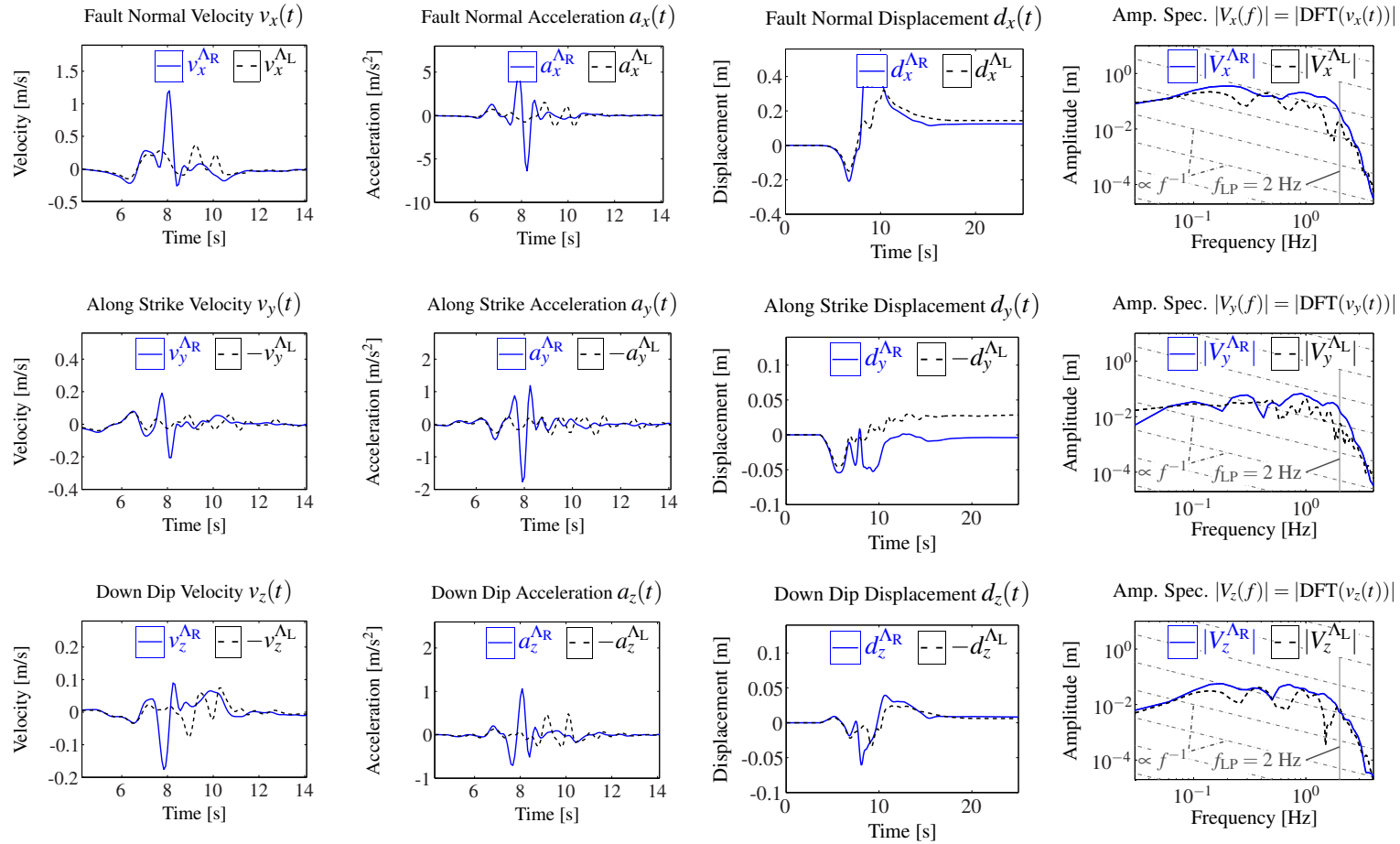


FIGURE 5.25: Seismograms and velocity amplitude spectra at station S_2 of example 3 which is located directly on the fault for the Λ_R and Λ_L case. The seismograms are low-pass filtered at 2 Hz. As can be seen in Figure 5.23, this is a station with relative differences: $\delta\text{PGV} \approx 110\%$ and $\delta\text{PGV} \approx 125\%$. The seismograms show a similar shaking duration of about 5 s, but the signals in the Λ_R -case are more concentrated in a small time-window around $t = 8$ s than in the Λ_L -case. The decay of the amplitudes are less close to a $V(f) \propto f^{-1}$ relation, especially for the y -component (strike component).

Although not in the region of highest relative differences, both stations exhibit considerable differences in the wavefield generated by the two reversed material configurations. The wrinkle-like slip pulse generates large peak velocities and accelerations with a strong directivity. The large accelerations of the fault normal components are especially remarkable (see Figure 5.25). The example demonstrates that the phenomenon of the Weertman pulse can become important in earthquake dynamics as well as strong ground motion.

5.3.4 Example 4

Under the conditions of relatively high initial shear stress, hence cases where inverse of strength excess S^{-1} is relatively large, we have some cases where rupture becomes supershear. In some cases the bimaterial inhibits the development of supershear rupture in the preferred direction, while it supports supershear rupture in the opposite propagation direction. Here we discuss an example in which the rupture propagation velocity becomes supershear over a large portion of the fault.

The parameters are summarized in table 5.1, with specific frictional parameters of $L = 0.2$ m, $D_c = 0.2$ m, $f_s = 0.8$, $f_d = 0.52$, $S^{-1} = 0.62$, initial shear stress varies randomly between 26 and 80 MPa, $\Delta x = 100$ m. The initial distribution of shear stress on the fault plane for example 4 is shown in Figure 5.26. The overstressed nucleation patch can be seen at about 7 km down dip and 32 km along strike distance.

In Figure 5.27 distributions of final slip of example 4 for both material orientations are shown. For both cases (Λ_R and Λ_L) rupture breaks the entire fault. The correlation coefficient of final slip $C_{D^{\Lambda_R}, D^{\Lambda_L}} = 0.98$, the slip dissimilarity value $\delta D = 11\%$ (equation (5.4)) and the moment magnitudes M_W for both events are $M_W^{\Lambda_R} = 6.99$ and $M_W^{\Lambda_L} = 7.01$. The distributions of final slip in this example are thus very similar although one can recognize that there is more slip in the tapered region at the edge of the fault on the left side in the Λ_L -case.

As we did in the previous examples, we illustrate slip history on the fault with distributions of slip velocity at four instances in time for both material contrast orientations (Λ_L , Λ_R) of example 4 in Figure 5.28 .

For this case as well, rupture initially propagates as an enlarging crack-like rupture mostly slower than the generalized Rayleigh velocity. One can recognize that in each case rupture propagates slightly faster to their preferred direction in the early phase of the rupture (until $t \approx 4$ s). Afterwards, the rupture front heading to the left quickly becomes supershear in both cases. The region where supershear propagation is triggered can be related to a large region of relatively high initial shear stress (at about 14-25 km along strike distance, see Figure 5.26). Although rupture becomes supershear in the Λ_L -case, the propagation phase that holds the peak value of slip velocity ($V_{\max}^{\Lambda_L}$) remains mostly at the generalized Rayleigh velocity or the intershear-range. In the Λ_R -case peak slip velocity travels essentially just behind the first arrival of the rupture. The distribution of peak slip velocity is shown in Figure 5.29. The correlation coefficient for

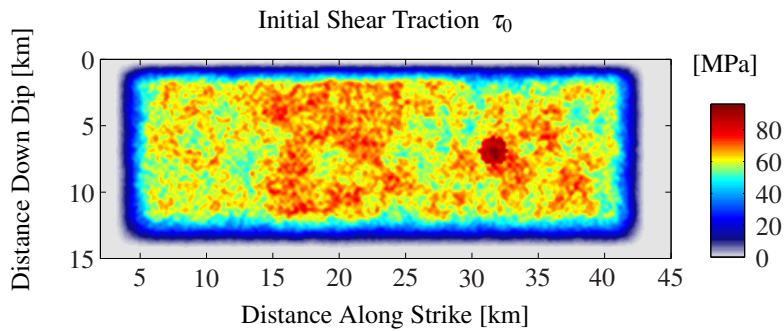


FIGURE 5.26: Initial shear stress for example 4. The overstressed nucleation patch is clearly visible at about 7 km down dip and 32 km along strike. The shear stress distribution is identical for the two simulations with reversed bimaterial orientations $\tau_0^{\Lambda_R} = \tau_0^{\Lambda_L} = \tau_0$.

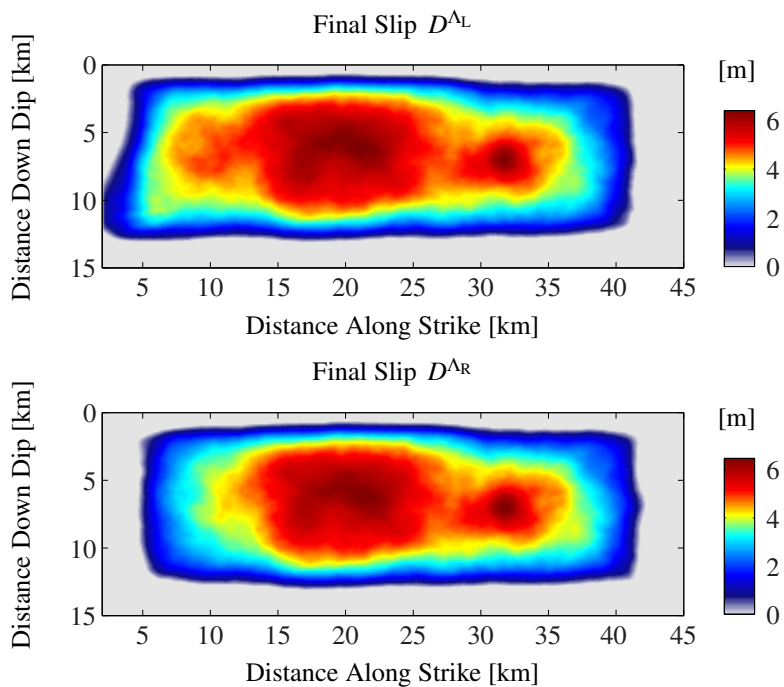


FIGURE 5.27: Distributions of final slip for both material orientations (top, Λ_L & bottom, Λ_R) of example 4. The correlation coefficient for both distributions of slip is $C_{D^{\Lambda_R}, D^{\Lambda_L}} = 0.98$, the slip dissimilarity is $\delta D = 11\%$, and the moment magnitudes are almost identical: $M_W^{\Lambda_R} = 6.99$, $M_W^{\Lambda_L} = 7.01$.

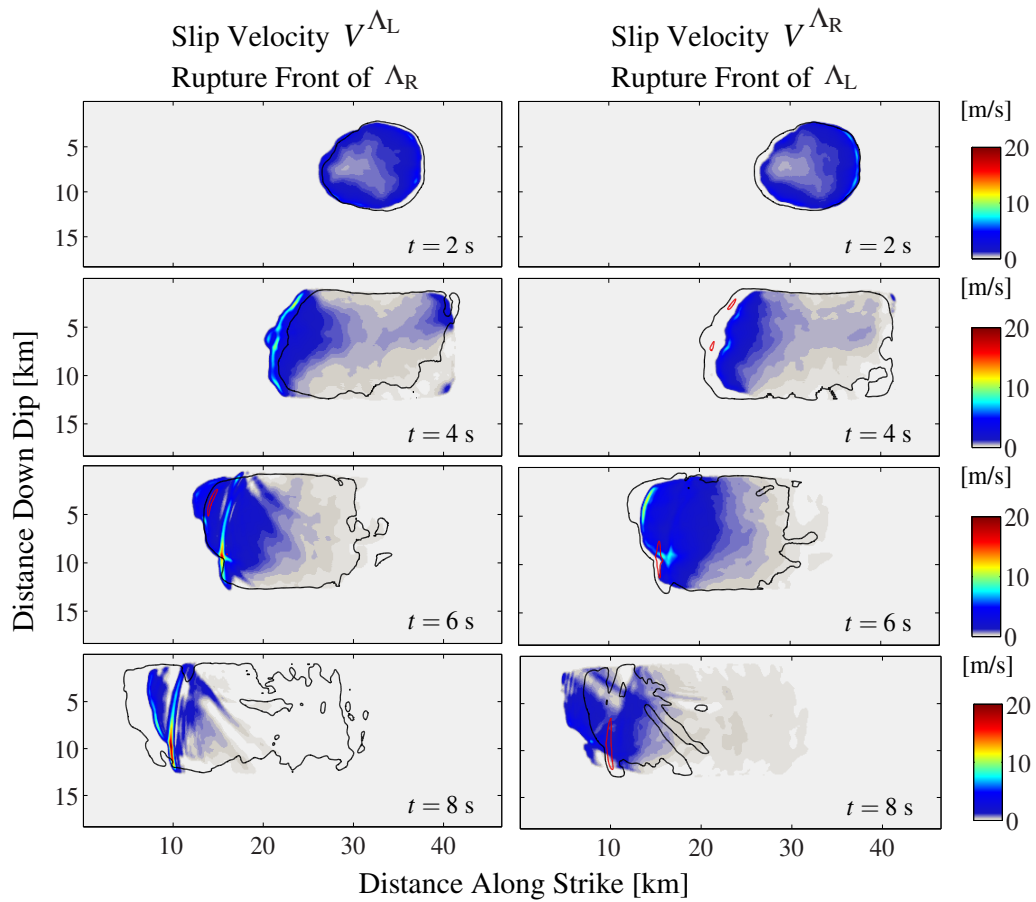


FIGURE 5.28: Time evolution of the rupture for example 4, showing snapshots of slip velocity for four instances in time for both material orientations (left panel, Λ_L , and right panel, Λ_R). The black contour marks the rupture front of the reversed orientation, the red one shows regions of high slip velocity of the reversed orientation. Both cases (Λ_L and Λ_R) become supershear. But unlike the Λ_R -case, in the Λ_L -case the peak amplitude travels far behind the supershear first arrival (left panel).

both distributions of peak slip velocity is $C_{V_{\max}^{\wedge R}, V_{\max}^{\wedge L}} = 0.56$, the dissimilarity value of the peak slip velocity distributions $\delta V_{\max} = 17\%$ (equation (5.4)).

Figures 5.26, 5.29, 5.28 demonstrate that the rupture history on the fault can be considerably influenced by the bimaterial mechanism also under high-stress condition (small strength excess parameter S). In the previous examples (1-3) we noted that the bimaterial mechanism potentially speeds up rupture propagation in the preferred direction. Here we can remark that when the conditions on the fault are such that rupture can become supershear, the bimaterial mechanism may delay the arrival of peak slip velocity such that a secondary rupture propagation phase behind a supershear rupture tip holds the peak values, or it can even suppress supershear propagation. In Figure 5.30 we show rupture propagation velocities of example 4 calculated from peak arrival times as well as propagation velocity calculated from first arrival times.

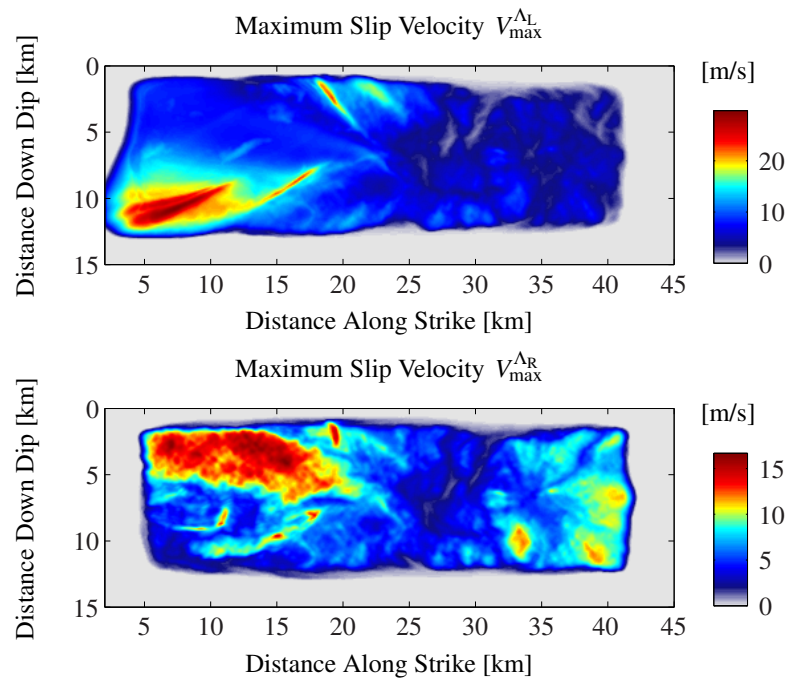


FIGURE 5.29: Distributions of peak slip velocity for both material orientations (top, Λ_L & bottom, Λ_R) of example 4. In the Λ_R -case the area of large peak slip velocity with values up to 15 m/s is related to the area of supershear propagation velocity and close to the surface (around 6-19 km along strike and 2-6 km down dip). In the Λ_L -case peak slip velocity becomes very high (up to 29 m/s) in a zone with a propagation velocity predominantly in the range of the generalized Rayleigh and intershear velocity and no fast supershear propagation (around 4-15 km along strike and 9-12 km down dip).

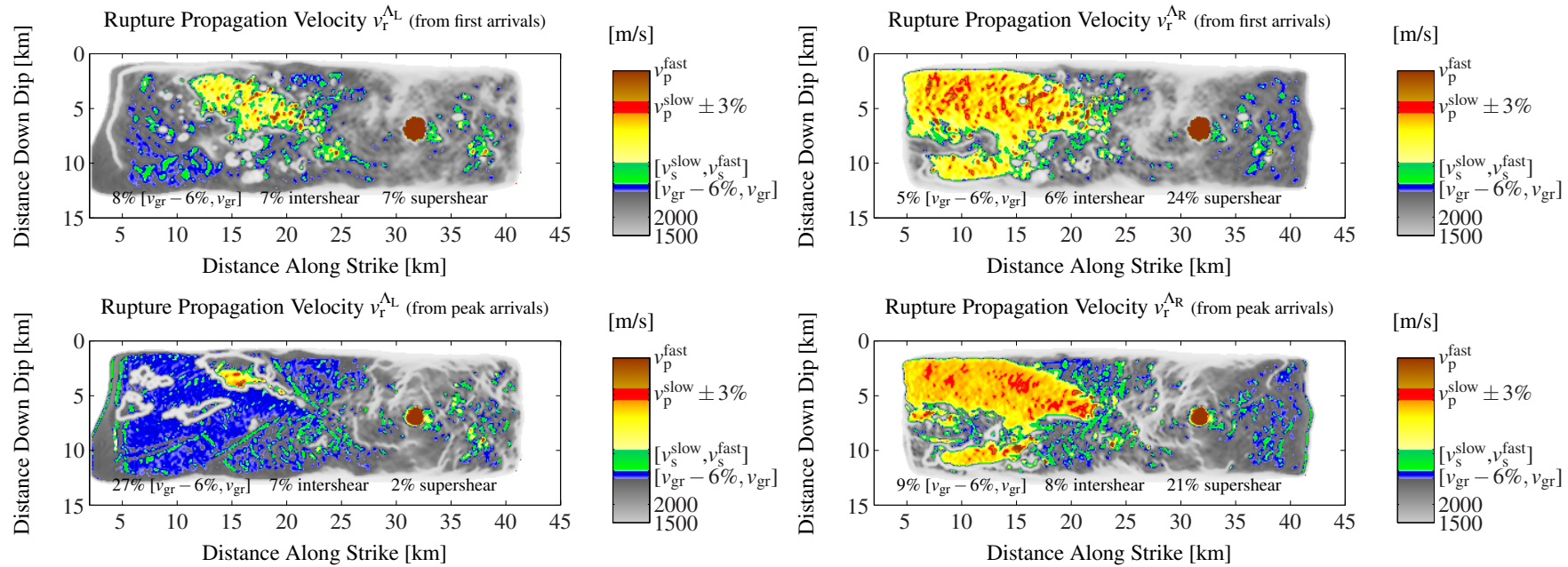


FIGURE 5.30: Rupture propagation velocity of example 4. For the Λ_L -case (left side) and for the Λ_R -case (right side) rupture propagation velocity calculated from the smoothed gradient of first arrival times (top) and calculated from the smoothed gradient of peak arrival times (bottom). The two cases with reversed material contrast show significant difference in propagation velocities. The differences between propagation velocities calculated from first (top) and peak arrivals (bottom) are larger for the Λ_L -case (left side).

The slip history on the fault discussed earlier and shown in Figure 5.28 also becomes evident in the plots of the rupture propagation velocity. In the Λ_L -case the peak travels close to the generalized Rayleigh velocity over 27% of the fault (Figure 5.30 bottom left), while also supershear propagation is initiated for 7% of the fault area (Figure 5.30 top left). However, the difference in the propagation velocities from first arrivals and from peak arrivals (compare Figure 5.30 top left with bottom left) show that despite the supershear propagation at the rupture tip a secondary rupture phase with higher slip velocity propagates behind the rupture tip. In the Λ_R -case the propagation velocities calculated from first arrival times and from peak arrival times agree much more than in the Λ_L -case, which reveals the fact that no considerable secondary rupture phase travels behind the rupture front. In the Λ_R -case more than 20% of the fault rupture at a propagation velocity in the supershear range (see Figure 5.30 right side). However there is only little indication (red color) for a rupture phase travelling at the velocity of the slower p-wave velocity v_p^{slow} .

In Figure 5.31 peak ground motion on the surface for example 4 is shown. The peak amplitudes of velocity and acceleration are unrealistically high in this example ($\text{PGV}_{\text{max}}^{\Lambda_L} \approx 5 \text{ m/s}$, $\text{PGA}_{\text{max}}^{\Lambda_L} > 30 \text{ m/s}^2$). However, this is mostly due to a small patch with very high slip velocities just below the surface at about 18-19 km along strike distance in both cases (Λ_L , Λ_R).

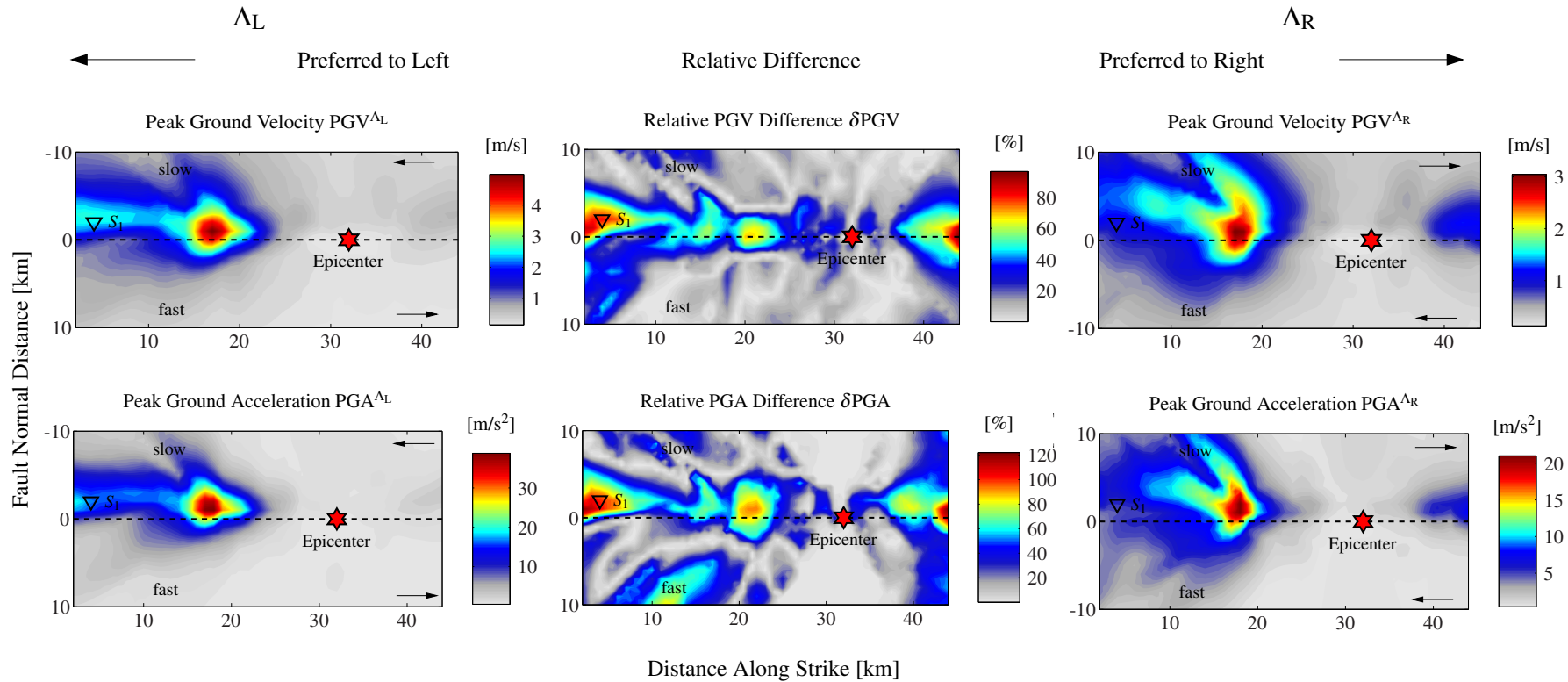


FIGURE 5.31: Peak ground motion maps of example 4 for both material contrast orientations (Λ_L , Λ_R). The epicenter is marked by the red star, the location of a virtual seismometer S_1 is marked by a black triangle, its seismograms being shown in Figure 5.32. In this example peak amplitudes of velocity and acceleration are unrealistically high close to 2 km off fault distance, 4 km along strike distance ($\text{PGV}_{\max}^{\Lambda_L} \approx 5$ m/s, $\text{PGA}_{\max}^{\Lambda_L} > 30$ m/s). The largest relative difference shows up above the left vicinity of the fault around station S_1 .

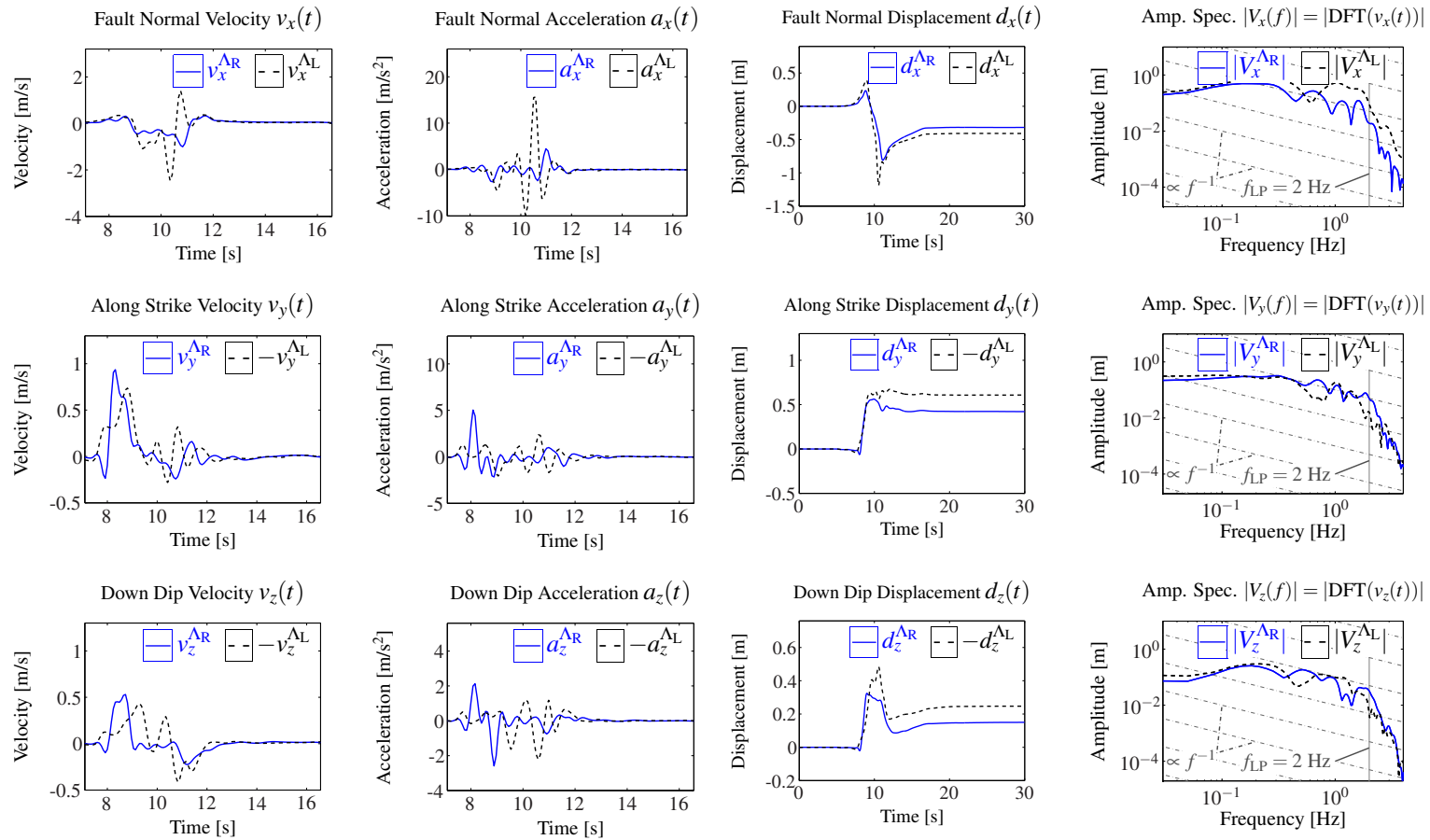


FIGURE 5.32: Seismograms and velocity amplitude spectra at station S_1 for example 4. The seismograms are low-pass filtered at 2 Hz. As can be seen in Figure 5.31, this is a station with relative differences: $\delta\text{PGV} \approx 95\%$ and $\delta\text{PGV} \approx 100\%$. For the Λ_L -case the seismograms nicely show two separated arrival times. The first one is mainly visible in the along strike component of velocity v_y lasting from $t = 8 - 10$ s, although obviously this part of the signal does not provide much acceleration. A second signal can mainly be seen in the fault normal velocity component v_x lasting from $t = 10 - 11$ s which provides very large accelerations in the fault normal direction (a_x). The Λ_R -case provides a signal lasting mainly from $t = 8 - 12$ s with no signal splitting as in the Λ_L -case, its main amplitude between $t = 8 - 9$ s.

In Figure 5.32 we plot the seismograms and spectra at station S_1 (see location in Figure 5.31). The differences between the simulations with reversed orientation are remarkable.

5.3.5 General Stable Features

Just after triggering the instantaneous nucleation patch, rupture starts propagating as essentially classical crack-like ruptures in the sub-Rayleigh velocity range. In many cases with a small inverse strength excess S^{-1} the initial shear stress does not allow for large propagation distances and large propagation velocity. In these cases rupture stays in the sub-Rayleigh propagation mode over the entire event duration. In other cases the inverse of strength excess S^{-1} is larger and initial shear stress allows for larger propagation velocities. In those cases the rupture often develops superimposed wrinkle-like pulses as part of the rupture or, after larger propagation distances, even exhibit predominant wrinkle-like pulses of slip. Although slip can be very similar when comparing the simulations with reversed material contrast orientation, ground motion differ substantially even when both cases (Λ_L and Λ_R) are sub-Rayleigh. On average, the differences in peak ground motion within a pair of simulations with reversed material contrast are larger in the cases when a superimposed or distinct wrinkle-like pulse of slip is present. For very large S^{-1} we find cases where propagation velocity becomes supershear. We find that the material contrast supports supershear propagation in the unfavored propagation direction, while it shows the tendency of preventing ruptures from becoming supershear in the preferred direction. This may be related to the existence of an additionally favored mode, that is antipodal to the preferred direction of the Weertman pulse (Λ -direction) and travelling at the velocity of the slower p-wave (see Cochard and Rice (2000) for details). However, only a few cases exist within the tested parameter range for which the supershear propagation is in a significant area percentage ($\geq 5\%$) close to the velocity of the slower p-wave v_p^{slow} . In our simulations we have cases with differences of moment magnitudes of up to $\Delta M_W = 1$ within one pair of simulations with reversed material contrast orientation but same parameters.

5.3.6 Results of 300 Simulation Pairs

The four examples in sections 5.3.1, 5.3.2, 5.3.3, and 5.3.4 show that a heterogeneous initial shear stress on a bimaterial frictional interface governed by regularized slip-weakening friction can produce a wide range of rupture propagation modes within the tested parameter space. We first visually inspected more than 300 simulation pairs, then defined objective criterion for the occurrence of the following modes of rupture propagation:

- i sub-Rayleigh propagation,
- ii superimposed wrinkle-like slip pulse propagating into the preferred direction,
- iii predominant or distinct wrinkle-like pulse of slip propagating into the preferred direction,

- iv intershear propagation,
- v supershear propagation,
- vi supershear propagation close to the p-wave velocity of the slower medium propagating to the non-preferred direction.

We summarize the results of all simulations in the diagrams shown in Figure 5.33. The aim is to show that the features presented in sections 5.3.1, 5.3.2, 5.3.3, 5.3.4, and 5.3.5 are stable over ranges of parameters and random realizations. In the left panels of Figure 5.33 the x -axis is the inverse of strength excess $1/S$, which is representative of the state of shear stress load of the fault, with large $1/S$ values meaning high relative stress. The x -axis of the right panels is the dissimilarity of peak slip velocity distributions δV_{\max} (equation (5.4)) as a measure of the difference in slip history introduced by the material contrast. The y -axis of the top panels shows the relative difference in PGV, which is the analogous measure concerning the ground motion, while the y -axis for the bottom panels, the moment magnitude M_W , shows the total slip for each event for each pair of simulations. Each colored triangle represents the occurrence of one of the six modes listed above. The direction of the triangles point into the preferred direction of each simulation. Hence, each triangle pointing to the left represents the occurrence of a specific propagation mode for a Λ_L -simulation, while each triangle pointing to the right represents the occurrence of this specific propagation mode for a Λ_R -simulation. The simulations for a given pair with reversed orientations (Λ_L , Λ_R) have in general different moment magnitudes, hence the symbols for the two orientations split up spatially and a simulation pair is connected with a gray line. Otherwise, the symbols appear on top of each other. Since for all of our simulated cases rupture starts propagating spontaneously in the sub-Rayleigh range (mode i) we do not display the corresponding symbol (black triangle) when at least one of the other modes (ii-vi) shows up in addition.

The examples discussed in sections 5.3.1, 5.3.2, 5.3.3, 5.3.4 are highlighted and isolated by the magenta circles in Figure 5.33. Of course the rest of the 300 simulation pairs also comprise other combinations of effects and/or propagation modes than the ones in the four examples, hence there are symbol combinations which we do not explicitly discuss as for the examples in the previous sections. Yet, all propagation modes are nicely shown in those four examples. The only exception is the mode which is represented by a red triangle, which stands for propagation close to the p-wave velocity of the softer medium in the non-preferred direction. In example 4 (section 5.3.4) there is actually some small area (red shaded area in Figure 5.30) which indicates such propagation, though it is below our chosen threshold. Simulations which showed slightly larger area percentage with $v_r = v_p^{\text{slow}} \pm 3\%$ existed only in very few cases. When supershear propagation occurred it stayed mostly below the velocity of the slow p-wave v_p^{slow} .

The plots in Figure 5.33 provide several tendencies in the results of our parameter space study, though clear systematic trends remain difficult to retrieve. Here we discuss some general

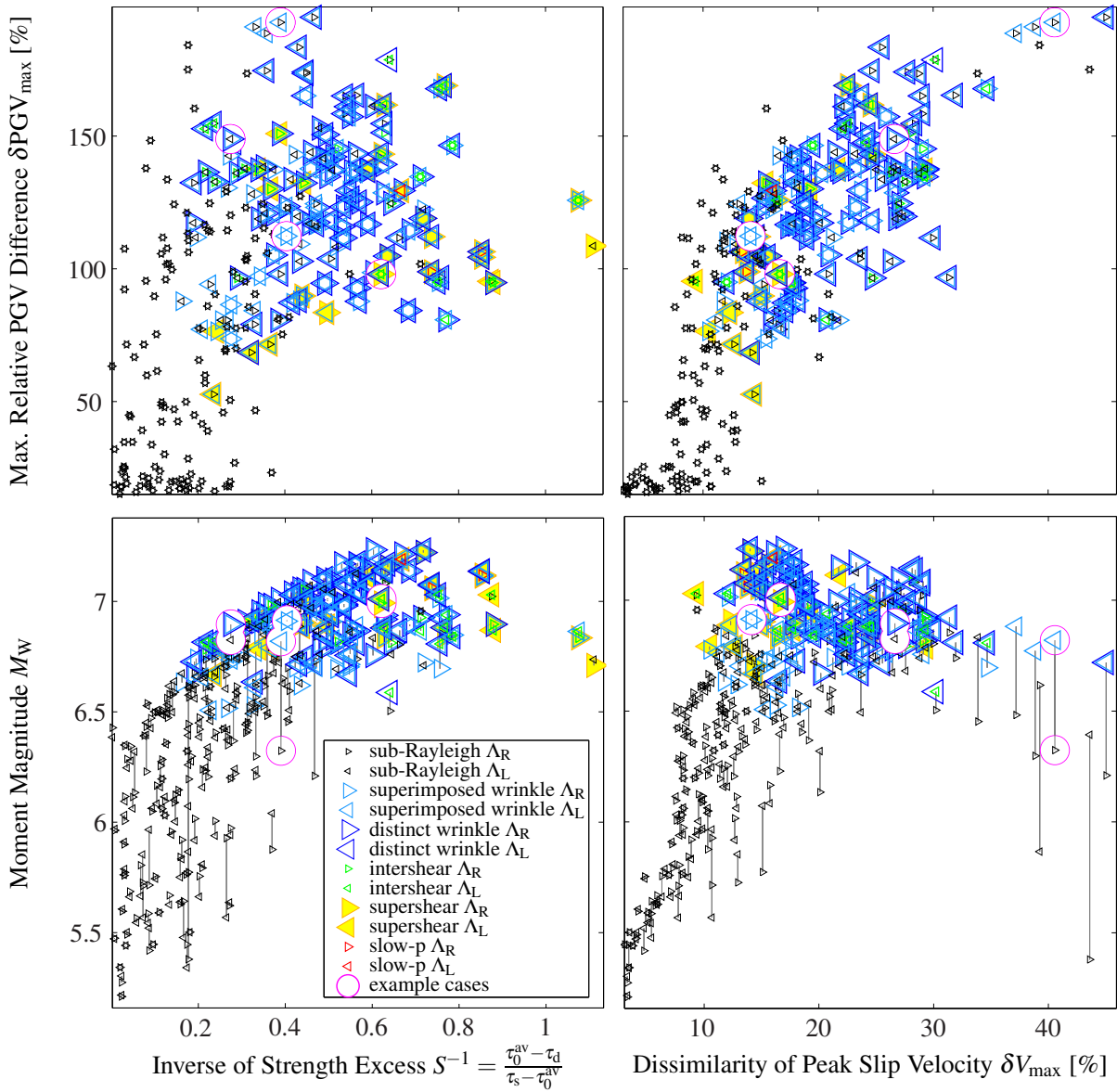


FIGURE 5.33: Summary showing the occurrence of the six possible propagation modes, as a function of inverse of strength excess, dissimilarity of peak slip velocity, moment magnitude, and maximum relative PGV difference for more than 300 simulation pairs.

findings that exist within the tested model and parameter limits.

Superimposed wrinkle-like slip pulses travelling in the preferred direction close to the generalized Rayleigh velocity nucleate naturally for a large number of events. Very often the ruptures become even predominant wrinkle-like pulses. There are events which become supershear for one orientation, while staying sub-Rayleigh in the reversed configuration. Also there are several cases similar to example 4 (section 5.3.4), where two rupture phases, a supershear and a wrinkle-like pulse, propagate for one material contrast orientation, while there is mainly supershear propagation in the simulation with reversed situation.

Inside the parameter-space tested here, small events ($M_W \approx 5.3 - 6.5$) never develop wrinkle-like pulses (no blue triangle in the lower half of the plots, see Figure 5.33 bottom panels). We think that this has its origin in too small propagation distances from the instantaneous nucleation patch. In other words, we believe that those events which developed a wrinkle-pulse are not large because of the wrinkle-like pulse, but that they could develop the wrinkle-like phenomenon because of a large enough propagation distance. The situation might change if the nucleation procedure would include dynamic bimaterial effects, which would be more realistic.

Supershear rupture occurs only in cases of relatively large moment magnitude $M_W \gtrsim 6.7$ (see Figure 5.33 bottom panels, yellow triangles). In contrast to the wrinkle-like propagation mode, supershear often occurs in the early stage of a rupture (which can thus be used as a prediction for a large event in our model). Whether supershear rupture is initiated around the nucleation zone or further away, it generally involves an area where initial shear stress is relatively high even though its average might be rather low (inverse of strength excess small: $1/S \approx 0.25$).

In Figure 5.33 one can notice that for the majority of simulation pairs which have not developed wrinkle-like propagation modes for at least one of the orientations (Λ_L, Λ_R), the relative difference in ground motion is, on average, smaller than for the couples for which at least one orientation developed the wrinkle-pulse (see top panels: more points with two black triangles – which appear as a star – are in the lower half with $\delta PGV_{\max} < 110\%$ than in the upper half $\delta PGV_{\max} > 110\%$). Nevertheless Figure 5.33 exhibits many examples with no wrinkle-mode or supershear-mode of propagation throughout the entire range of δPGV , and there are also many examples which exhibit a large difference in propagation mode (e.g. superimposed and/or distinct Weertman pulse for Λ_L and sub-Rayleigh for Λ_R) but a medium difference in ground motion ($70\% < \delta PGV_{\max} < 110\%$). Even very large differences in peak-ground motion ($\delta PGV, \delta PGA$) are possible when the dominant propagation mode is sub-Rayleigh (cases with two black triangles in the range of high $\delta PGV \geq 150\%$).

In most of the simulation pairs with a large dissimilarity of peak slip velocity, $\delta V_{\max} \gtrsim 20\%$, a wrinkle-like pulse of slip is involved for one orientation of the material contrast, while it is not in the reversed configuration (see Figure 5.33 right panels, the cases with a blue triangle in one direction only). There are few cases with large dissimilarity of peak slip velocity although both simulations of a pair are essentially in the sub-Rayleigh range of propagation velocity (see Fig-

ure 5.33 right bottom panel, simulation pairs represented by two black triangles). However, in those cases the difference in moment magnitudes is also large and hence these are cases where rupture could slowly overcome asperities of low initial shear stress and renucleate large additional portions of the fault in one material configuration only, like in example 2 (section 5.3.2), but staying sub-Rayleigh here.

As mentioned earlier, our model has a lower limit of event size due to the nucleation patch ($M_W^{\min} \approx 5.3$) and an upper limit ($M_W^{\max} \approx 7.2$) due to the size of the fault. We demonstrated in example 3 that the wrinkle-mode can be very efficient in overcoming larger distances of relatively low initial shear stress once such a mode of propagation is initiated. Contrary to the usual modes of ruptures, these wrinkle pulses are not easily stopped by the artificially low initial stresses of the tapering regions near the boundaries; often such still well developed pulses reached the unbreakable barrier. Hence those ruptures appear to be potential candidates for large earthquakes ($M_W > 7.2$) in a spatially extended fault model of the same kind. However, we do not accomplish such an extension in the study presented here.

5.3.7 Summary of Results

We found a range of realistic parameters for which nucleated earthquakes essentially develop as classical cracks with no development of a superimposed or distinct wrinkle-like pulse Weertman pulse or supershear rupture propagation and with no large differences in final slip, as in Andrews and Harris (2005). Nevertheless the seismic radiation differs substantially for many of those cases between the bimaterial orientations, leading to differences in strong ground motion due to different slip histories (this possibility has been mentioned by Andrews and Harris (2005)).

For another range of realistic parameters we found a transformation of rupture during propagation from an initially crack-like propagation into an enlarging crack with a superimposed wrinkle-like pulse. Although seismic radiation differs for the switched bimaterial orientations, final slip does not change significantly in this case. On average these cases show larger differences in ground motion than the previous cases.

For yet other sets of realistic parameters we found that ruptures start like classical cracks, then slowly break stress barriers (areas of lower stress) only in the preferred direction (Λ), then trigger a secondary event at an area of high stress. This leads to differences of earthquake magnitudes and a strong directivity. In these cases only early phases of the ground motion are comparable between the two bimaterial orientations. The secondary events have the potential to develop wrinkle-like propagation modes since they start already unilaterally in the preferred direction, although a limiting factor is the size of the fault. Peak ground motions are orders of magnitude different. We therefore presume that the bimaterial mechanism is important for

earthquake dynamics as well as for earthquake hazard and damage.

We also found sets of realistic parameters where rupture transforms to a mainly wrinkle-like pulse. Seismic radiation can be very different in these cases when switching materials. These pulses often overcome additional areas of low initial shear stress. Thus it provides a potential mechanism to trigger additional ruptures further along strike in the preferred direction beyond the limited fault size used in this study, where these ruptures are always stopped ultimately at the model boundary.

We finally found situations where supershear propagation occurred. In many cases the bimaterial mechanism prevents rupture from becoming supershear in the preferred direction, while supporting it in the opposite direction. Also, there are cases with a supershear propagation at the rupture tip and a superimposed wrinkle-like slip pulse travelling behind the rupture tip at the generalized Rayleigh velocity in the favored direction. In these cases peak amplitudes of ground motion can split up in time, thus feigning effects which might be misinterpreted as shear wave splitting originated by anisotropy in the surrounding medium.

5.4 Discussion

Geological fault zone structures are thought to be complex systems on all scales, and realistic models of earthquake rupture are thought to involve a large number of physical mechanisms, e.g. off-fault energy dissipation due to plastic strain (Andrews, 2005), visco-elasticity, melt lubrication (Di Toro et al., 2006), thermal pressurization (Bizzarri and Cocco, 2006a,b), flash heating (Rice, 2006), poroelasticity (Dunham and Rice, 2008), and others. We exclude all those effects and use a simple planar frictional interface governed by slip-weakening friction and a heterogeneous initial shear stress. In such a model all physical processes on the fault are projected into the friction laws and/or into the heterogeneous stress, which together might mimic realistic macroscopic behavior of the fault. Therefore, there is the possibility that many different effects, not considered in this work, may counterbalance (or enhance) the bimaterial mechanism and therefore hinder (or support) the generation of propagation modes we found.

For instance, Rudnicki and Rice (2006) developed a poroelastic fault-zone model which has been explored by Dunham and Rice (2008). A mismatch in poroelastic properties across faults may lead to a similar response as a mismatch of elastic parameters across the fault (normal stress reductions/increases). The elastic and the poroelastic effects enhance each other for the case that the compliant side is more permeable, while they oppose each other for the case that the stiff side is more permeable. In the range of representative contrasts of natural faults (10% contrast of elastic parameters, and a factor-of-ten contrast of permeability) both effects have

comparable magnitudes (Dunham and Rice, 2008).

Rice (2006) argues that there should exist some additional weakening mechanism(s). Otherwise, in view of the small thickness of the shear zone, melting would essentially always occur for typical slip velocities and rise times, which is not observed on exhumed faults. But note that most earthquake simulations performed so far fall into this unrealistic category.

However, in the context of modeling earthquake scenarios with dynamic source models and a simple weakening mechanism of the frictional interface (e.g., slip-weakening friction) between elastic half-spaces, our study shows that the presence of a material contrast can significantly alter slip history on the fault, hence can diversify resulting wave-effects at the free surface. These should be taken into account in estimates of peak ground motion. In fact, kinematic features specific of bimaterial dynamics (like strong directivity related to the Weertman pulse preferred direction, as shown here) might need to be incorporated into earthquake scenario simulations with kinematic source models.

In all our simulations we found that the rupture had to propagate a certain distance before it could develop characteristics of the Weertman pulse (e.g., $v_r = v_{gr}$, self-sharpening, self-amplifying behavior). This suggests that the wrinkle-modes of rupture on bimaterial interfaces is more significant for large earthquakes after large propagation distances. However, in our instantaneous nucleation procedure, dynamic bimaterial effects are not accounted for. This introduces a lower limit for earthquake sizes which are affected by the bimaterial mechanism. Hence its contribution might be underestimated for small earthquakes in our study.

We noted that in cases where the rupture propagation velocity is not close to the generalized Rayleigh velocity, the slip history is altered significantly, leading to large differences in ground motion, when switching materials. Thus it is not necessary to nucleate Weertman-like pulses to alter the dynamic behavior on the fault.

Once a Weertman pulse is nucleated, it shows self-sharpening and self-amplifying behavior. This makes it difficult to come to grid-independent solutions for all involved field variables on a detailed scale. However, the goal of this study is not a detailed investigation of the wrinkle-like pulse itself, but to qualitatively estimate rupture histories on a bimaterial strike-slip fault and the resulting ground motion. Higher numerical resolutions are of course desirable, but we are nevertheless confident that the various tendencies showing up in our limited parameter sets would also be present in simulations with higher resolutions, leaving the overall picture of results unchanged.

The tapering of shear stress to the fault edges and the unbreakable boundary at the fault edge cause every rupture to ultimately stop. As for real ruptures this results in a very strong seismic radiation at the fault edges for the case of a rupture front with large amplitude hitting the tapered region (or even the unbreakable boundary). This enhances peak ground motion at the vicinities of the fault. However, the tapering region can be seen as another stress heterogeneity present in both material configurations (Λ_L, Λ_R).

A common feature for many individual model realizations tested in this study is a non-symmetric propagation velocity, with generalized Rayleigh velocity into the preferred direction and supershear propagation in the unfavored direction. Such propagation is also observed in laboratory experiments by Xia et al. (2005), as well as in other numerical studies (e.g. Shi and Ben-Zion, 2006). In the case of a constant friction coefficient (Coulomb friction) the non-symmetric propagation is restricted to the two explicit propagation modes: (1) the Weertman pulse in the preferred direction with $v_r = v_{gr}$, and (2) the slow-p pulse associated $v_r = v_p^{slow}$ (Cochard and Rice, 2000). It has been discussed by Xia et al. (2005) that the 1999 $M_W = 7.4$ Izmit earthquake and the 1999 $M_W = 7.2$ Düzce earthquake are potential candidates for such a bimaterial-typical propagation behavior, with supershear propagation in one direction only, that is towards the east (Bouchon et al., 2001). Both these events happened along the northern branch of the North Anatolian Fault (NNAF). In order to explain the asymmetric propagation of the two events with the bimaterial favoring, the southern side of the NNAF must have slower seismic velocities than the northern side of the NNAF. We are not aware of any detailed model of seismic velocities in that region, but there is evidence that the south side of the NNAF has slower seismic velocities: deformation inferred from coseismic and early postseismic SAR interferometry (Cakir et al., 2003) as well as from GPS data (Flerit et al., 2003) both indicate larger deformation on the south side. Therefore, a velocity contrast across the NNAF, its slower side being the south side, is very likely. And our results are consistent with the laboratory experiments of Xia et al. (2005) and with the observations of asymmetric rupture propagation at the Izmit and Düzce earthquakes. However, a refracted arrival recorded close to the eastern edge of the 1999 Izmit rupture gives evidence the material on the northern side might be the slower side, and the supershear propagation to the east has been misinterpreted by Bouchon et al. (2001) assuming that a material contrast with smaller seismic velocities on the northern side promotes supershear rupture to the east. This misinterpretation has been clarified by Andrews (2002).

Another fault that has often been mentioned in connection with bimaterial rupture propagation is the Parkfield section of the San Andreas fault. There, the velocity structure is well known to have a moderate velocity contrast across the fault, its slow side being the continental side. Hence the preferred rupture direction in the subshear range at Parkfield is to the southeast. Nevertheless, while the 1966 earthquake indeed propagated to the southeast, the recent 2004 $M_W = 6$ event ruptured mainly in the dynamically unpreferred northwest direction. Some authors take this as evidence that material contrast is not relevant for earthquake source dynamics, and that the propagation direction cannot be predicted (e.g. Andrews and Harris, 2005; Harris and Day, 2005). However, it seems clear that material contrast is not the only factor that influences rupture dynamics, and we agree with Ben-Zion (2006a,b) that the propagation direction can only be predicted in a statistical sense. For example, if the nucleation zone is close to a barrier, there is only one direction for the earthquake to rupture, whether it be the favored or the

unfavored direction!

Custódio and Archuleta (2007) compare the 1966 and 2004 Parkfield earthquakes. The hypocenters of both events are in different locations; also, the large difference in aftershock locations of the 1966 (Eaton et al., 1970) and the 2004 (Thurber et al., 2006) Parkfield events show that the events did not only rupture in different directions, but ruptured different areas of the fault. Such variability is to be expected within an area of heterogeneous stress, which is thought to be the rule rather than the exception, and we would need to know the state of stress more precisely in order to be able to quantitatively estimate the relative contribution of the various factors. The results of our simulations also show considerable variability, all of which being due to the heterogeneity in the initial stress field, and they are certainly consistent with the two Parkfield events.

Besides, even if the rupture extent and direction of the 2004 event is not controlled by the material contrast, the radiated ground motion may still have been considerably influenced by the bimaterial dynamics, similar to what we show in our study (e.g., example 1, Figure 5.6). Also, even though the 2004 rupture mainly propagated to the northwest, there were some propagation to the southeast; there were accelerometer stations close to the south eastern edge of the fault which recorded large amplitudes in ground motion, especially for the fault normal component (see for example Shakal et al. (2006); Liu et al. (2006)), which is a characteristic feature of bimaterial rupture.

Earthquakes on a bimaterial interface are also suspect of causing non-symmetric aftershock distributions. Rubín and Ampuero (2007) simulated bimaterial 2D in-plane ruptures with regularized slip-weakening friction and force them to stop at stress barriers after some propagation distance along the fault. They find different behaviors of stopping for the dynamically favored and unfavored directions that can explain asymmetric aftershock distributions of bimaterial faults as has been observed by Rubín and Gillard (2000); Rubín (2002). As in our simulations, Rubín and Ampuero (2007) observe that under certain conditions bimaterial slip pulses propagate into stress barriers much further than regular rupture modes. This is due to the tensile perturbation of normal stress which carries the bimaterial pulse of slip. Rubín and Ampuero (2007) showed that this effect smoothes the stress concentrations at the edge of the fault in the dynamically preferred direction. Our results verify the estimation that generation of pulses is not inhibited in the 3D case with a heterogeneous stress distribution (Rubín and Ampuero, 2007). We found that also in our 3D-model with heterogeneous shear stress, pulses of slip are generated and travel far into stress barriers, smoothing out and significantly reducing amplitudes of stress concentration at the fault edges.

Ampuero and Ben-Zion (2008) studied in-plane ruptures on a bimaterial fault governed by a regularized strongly velocity-weakening friction. They showed that for a wide range of parameters large scale pulses travelling into the preferred direction are also possible, and small scale pulses (scale of the process zone) can detach from the rupture front also travelling into

the preferred direction, the latter being dependent on the relaxation scale of the regularization. They also found asymmetric bilateral crack-like propagation within another range of parameters and tried to analyze the asymmetry in seismic potency of their events in a statistical sense. In our study, we do not have a velocity-weakening model and no large scale pulses are generated (aside from ruptures becoming pulse-like events due to stopping phases radiating from the fault boundaries in our 3D model setup). However, all our results are consistent with the results of Ampuero and Ben-Zion (2008). We agree with Ampuero and Ben-Zion (2008) that it is important to clarify effects of the bimaterial mechanism on earthquake rupture propagation with additional theoretical studies, and test the associated predictions with detailed field and laboratory observations.

5.5 Conclusion

We performed a numerical investigation of dynamic ruptures on a bimaterial interface in 3D with regularized slip-weakening friction and a heterogeneous initial shear stress and discussed the resulting strong ground motion. We showed that for many parameter sets the dynamics of rupture propagation are significantly influenced by the broken symmetry due to the material discontinuity during rupture propagation. Large differences in peak ground motion (PGV & PGA) are possible when changing the orientation of the material contrast even when slip-distribution of the individual events are very similar.

Wrinkle-like slip pulse specific to the bimaterial mechanism nucleates naturally from initially crack-like propagation of rupture when the involved parameters allowed for large propagation distances. Once such a pulse is generated it appears to have high potential to overcome large distances within areas of relatively low initial shear stress. It also appears that the existence of a wrinkle-like slip pulse impedes the initiation of supershear propagation in the preferred direction. For those cases where supershear is nevertheless initiated, a secondary superimposed wrinkle pulse propagating at the generalized Rayleigh velocity is often nucleated behind the rupture front. By contrast, supershear propagation seems to be promoted in the unfavored direction.

The dynamic weakening of the fault due to the normal stress alteration during slip is also efficient in the range of small propagation velocities. In such cases, secondary events are triggered and the orientation of the material contrast determines rupture extent and the size of the earthquake, potentially by orders of magnitude.

The variety of propagation modes investigated in this study is consistent with laboratory experiments, thorough numerical investigation, as well as with crustal earthquake observations.

Therefore our main conclusions are:

1. The influence of a material contrast on final slip may be small, nevertheless – as shown

in this study and envisioned by Andrews and Harris (2005) – the effect on the surface ground motion and earthquake hazard can be substantial.

2. Our simulations contradict the conclusion of previous studies (‘The wrinkle-like slip pulse is not important in earthquake dynamics’ Andrews and Harris, 2005). We find that for a broad range of realistic parameters the wrinkle-mode of propagation is an attractive propagation mode of rupture. When such pulses are generated, earthquake rupture dynamics is strongly influenced by the wrinkle-like slip pulse characteristic of bimaterial interfaces. The resulting effect on ground motion may be very large.

3. It is not necessary that a wrinkle-like pulse (or Weertman pulse) be generated to significantly alter slip history. The bimaterial mechanism can affect rupture dynamics throughout the entire range of seismic propagation velocity (from sub-Rayleigh to supershear) and might even support very slow modes of propagation, the latter obviously needing deeper investigation.

Chapter 6

Discussion, Conclusion and Future Work

6.1 Discussion and Conclusion

The results presented here may have important implications to a number of issues of earthquake and fault physics and ground motion associated with large geological structures that have well-developed material interfaces.

Plate boundaries and other major faults, the sites of the large earthquakes, often have prominent bimaterial interfaces that separate different media. Such media contrasts are generated progressively by the creation of damage during the faulting process and the juxtaposition of different rocks across large displacement faults. Large faults also tend to nucleate and grow along pre-existing geological sutures that separate different blocks.

The numerical investigations of dynamic ruptures on bimaterial interfaces in this study demonstrate, that in the presence of material discontinuity over significant ranges of parameter sets, the dynamics of rupture propagation on individual faults, and rupture migration patterns in systems of multiple faults are significantly influenced by the broken symmetry of stress during rupture propagation. The bimaterial interfaces are mechanically favored surfaces for rupture propagation, introducing directionality of dynamic fault rupture propagation and seismic radiation. Changing the orientation of shearing on a heterogeneously loaded bimaterial fault can lead to large differences in peak values of ground motion even when the distribution of slip remains essentially unaffected.

The findings presented in chapters 3, 4, and 5 and other complementary studies (e.g., Shi and Ben-Zion, 2006; Dalguer and Day, 2007b; Ampuero and Ben-Zion, 2008) show that ruptures on a bimaterial interface tend to evolve during propagation from initial symmetric cracks with relatively low mechanical efficiency to slip pulses with preferred propagation direction and high mechanical efficiency, for significant ranges of parameters. Such pulses can overcome large areas of relatively low initial shear stress, or (at high stress level) impede supershear propagation in the favored direction, support supershear propagation in the unfavored direction. The generality of bimaterial specific modes of rupture propagation (chapter 4), the large variety

of propagation modes emerging (chapter 5), as well as the patterns of localization of fault slip in structures with velocity contrasts (chapter 3) is consistent with laboratory experiments (e.g., Xia et al., 2005), with thorough numerical investigation (e.g., Ampuero and Ben-Zion, 2008; Dunham and Rice, 2008), with crustal earthquake observations (e.g., Lewis et al., 2005, 2007; Rubin and Ampuero, 2007), as well as with geological studies (e.g., Dor et al., 2006b, 2008).

Main Conclusions The results provided in chapter 3, chapter 4, and chapter 5 and the foregoing discussion supports the following as the main conclusions of this study:

- 1 For comparatively broad ranges of realistic parameters the wrinkle-mode of propagation is an attractive propagation mode of rupture, the earthquake rupture dynamics is strongly influenced by the wrinkle-like slip pulse characteristic of bimaterial interfaces.
- 2 The bimaterial mechanism can affect rupture dynamics throughout the entire range of seismic propagation velocity (from very slow, over sub-Rayleigh, to supershear).
- 3 Spontaneous migration of ruptures to the material interfaces implies that the dynamic phenomena associated with the wrinkle-like pulses are not limited to the set of hypocenters located directly on the material interfaces. Hence, material interfaces provide a mechanism for a positive feedback between structure and rupture properties that can lead to progressive regularization of geometrical heterogeneities with cumulative slip and potentially suppression of dynamic branching from large fault zone structures.
- 4 The influence of a material contrast across a fault on the ground motion and its directivity and earthquake hazard can be substantial.

Contradictory but fragile conclusions exist in the literature ('The wrinkle-like slip pulse is not important in earthquake dynamics' Andrews and Harris, 2005), ('Material contrast does not predict earthquake rupture propagation direction' Harris and Day, 2005). Placing such rigorous statements may be a catalyzing style of research since they provoked a considerable debate recently. Yet they hold the risk of losing unbiasedness and are likely misleading since those studies involve models that incorporate simultaneously multiple ingredients letting the models appear "realistic". However, the number of simulations provided by Andrews and Harris (2005) and Harris and Day (2005) does not suit the high dimensionality (less than 5 simulations in both studies altogether). By contrast, the parameter studies presented here (chapters 3 and 5) contain several hundreds of simulations for comparatively few degrees of freedom (in the sense of few parameters specific to dynamic rupture). Different potential key ingredients should be the target of separate detailed parameter-space studies. Published results on the problem at hand indicate that properties of ruptures on material interfaces in cases incorporating slip-weakening friction (e.g., chapter 5) and mixed-mode rupture (e.g., chapter 4) evolve for wide ranges of conditions toward results of cases without these ingredients (e.g., Andrews and Ben-Zion, 1997; Harris

and Day, 1997; Shi and Ben-Zion, 2006; Brietzke and Ben-Zion, 2006; Brietzke et al., 2007; Rubin and Ampuero, 2007; Ampuero and Ben-Zion, 2008; Brietzke et al., 2009).

However, the physical basis for many additional observed phenomena remain to be explored in future times, making it challenging to coming to definitive conclusions (compare chapter 2). Therefore discussions on the problems at hand should be conducted in an unprepossessed candid way.

6.2 Future Work

Theoretical studies on earthquake source dynamics are a challenging task. The essence of such studies is the effort to clarify the possible effects of a small number of ingredients (e.g., material contrast, fluid pressurization, melting, gel formation, plastic deformation, etc.) on the process of spontaneous rupture propagation. Simulations that incorporate many ingredients simultaneously may appear superficially better, but are often not useful because it is not possible to obtain clear quantitative knowledge (i.e., specific ranges of parameters that lead to different dynamic regimes) from such simulations as long as the multi-dimensional parameter-space associated with a more realistic model becomes essentially too large to be efficiently explored.

Due to the high complexity and multi-dimensionality of the non-linear physical processes involved in earthquake source dynamics (as discussed in chapter 2) and the large diversity of propagation phenomena associated with even relatively simple models (e.g., Coulomb or slip-weakening friction on a planar bimaterial fault) with relatively small degrees of freedom (as discussed in chapters 3 & 5) additional new and intensified measurements need to be accomplished in the laboratory, as well as in the field, to better constrain parameters of existing physical models. Besides, new theoretical concepts need to be developed in the long run, aiming a better understanding of what controls earthquake fault rupture.

In matters of the study presented, several future lines of investigations are arising.

For instance, the generality of the tendencies of rupture migration in fault zone typical structures (as studied in chapter 3) should be tested in future simulations incorporating additional levels of realism in the assumed structure (e.g., dimensionality) and rheology (e.g., slip- and rate-dependent friction). The observed localization of slip at material discontinuities (Chester and Chester, 1998) are certainly compatible with the simulations performed in chapter 3 of this study.

The example in section 5.3.2 of chapter 5 demonstrated the potential of relatively slow rupture propagation phases being supported in the dynamically favored direction. Hence, the role of material contrasts on the nucleation phase, which was neglected here using an instantaneous overstressed patch on the fault, is a potentially fruitful line of future research. Yamashita (2007) showed that postseismic quasi-static fault slip due to pore pressure change on a bimaterial interface can advance postseismic slip. This suggests that the influence of the bimaterial mechanism

on the nucleation might be significant. Therefore it may also become interesting to study how much the behavior of earthquake cycles is diversified assuming bimaterial faults. Is the switching between seismologically quiet and active times different in bimaterial fault systems?

As mentioned before, local permeability contrast across the fault can also produce asymmetric rupture (Rudnicki and Rice, 2006) as well as asymmetry of aseismic slip (Yamashita, 2007). The effect of poroelastic material can principally enhance or inhibit elastic bimaterial effects. More precisely, the two effects enhance each other if the compliant side is more permeable, and oppose each other if the stiff side is more permeable. The two effects have comparable magnitudes for parameters representative of natural faults (a wave-speed contrast of about 5 – 10% and a factor-of-ten permeability contrast)(Dunham and Rice, 2008). Certainly such results should be accounted for when interpreting observations as well as synthetics.

Wrinkle-like pulses generate high off-fault yielding stresses that should trigger anelastic deformation close to the source (Andrews, 2005). Such off-fault yielding reduces the amplitudes of the emanating wavefield. Pure elasticity maximizes the impact of the wrinkle-like pulse. In order to upgrade the robustness of the results presented in this study, additional non-elastic off-fault rheology should be incorporated for the cases of very high off-fault stress.

Another issue that arises is the possibility of fault opening, the implied loss of shear resistance to slip, and its quantification for events with large rupture propagation distances. Which mechanisms prevents opening (e.g., plastic deformation)? How likely is tensile crack propagation and which are the geological indications (e.g., pulverization of rocks (Dor et al., 2006a))?

The robustness of the mechanism generating wrinkle-like pulses with respect to regularization parameters should also be addressed in future studies. The values of regularization parameters for natural faulting remain uncertain. In chapter 5 the regularization parameter L is of the same order as the range of critical slip distances D_c . A raising L reduces the instability associated with the material contrast (bimaterial effect), while raising D_c reduces frictional instability. A more thorough exploration of L/D_c -ratio in future studies needs to be done. Since the L and D_c are rather empirical parameters, physical constraints on these parameters or even a physical replacement of these parameters are desired.

For large earthquakes there exists deviations from the approximate scale-invariant scaling relations associated with relatively small earthquakes (Ben-Zion, 2008). A potential future investigation could also reveal the contribution of bimaterial faults on such deviations from scale invariant scaling relations.

The study presented here has the aim of highlighting the importance of material discontinuities and its diversifying effect on comparatively simple physical models. For this the widely exemplary approach of this study is suitable. However, efforts on trying to make parameters studies more systematic need to be done. Possibly this requires the incorporation of scaling relations and discussions on the basis of non-dimensional characteristic values instead of potentially scale dependent values.

Appendix A

Finite Difference Approximations

A.1 Elastic Wave Propagation

The system of elastodynamic equations (equations 2.4, 2.6) can be approximated numerically using finite-differences schemes as described by various authors (e.g., Levander, 1988; Igel et al., 1995; Graves, 1996). The finite-difference approximation scheme for the wave-propagation part is briefly recapitulated in this section.

A.1.1 Time Derivatives

The finite-difference approximations of the time derivatives are second-order central differences,

$$\partial_t \mathbf{v}(t) \approx \frac{\mathbf{v}(t + \Delta t/2) - \mathbf{v}(t - \Delta t/2)}{\Delta t}, \quad (\text{A.1})$$

$$\partial_t \boldsymbol{\sigma}(t + \Delta t/2) \approx \frac{\boldsymbol{\sigma}(t + \Delta t) - \boldsymbol{\sigma}(t)}{\Delta t}. \quad (\text{A.2})$$

The evolution of velocities and stresses is staggered in time.

A.1.2 Space Derivatives

The staggering of field variables of the elastic wave-equation in the velocity-stress formulation is illustrated in Figure A.1. We introduce $D_\xi^{(2)}$ for the discrete centered two-point finite-differences (2nd-order approximation), and $D_\xi^{(4)}$ for the centered four-point finite-difference (4th-order approximation) with $\xi = x, y, z$. Using the indexing as shown in Figure A.1, and letting ϕ represent an arbitrary stress or velocity component, the spatial finite-differences can

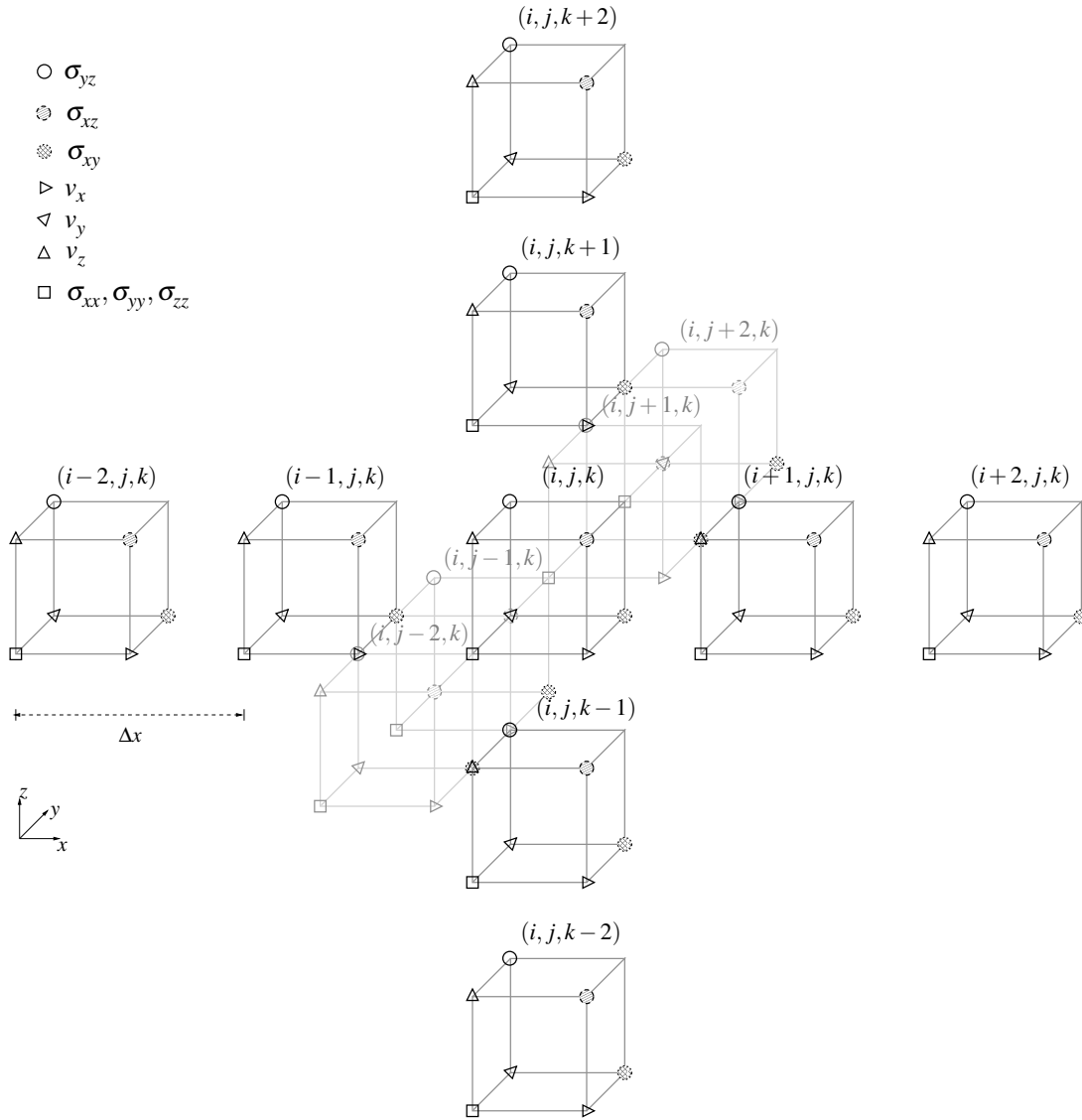


FIGURE A.1: Staggered velocity-stress grid.

be written as follows:

$$\begin{aligned}
 \left[D_x^{(2)-} \phi \right]_{i,j,k} &= (\phi_{i,j,k} - \phi_{i-1,j,k}) \\
 \left[D_x^{(2)+} \phi \right]_{i,j,k} &= (\phi_{i+1,j,k} - \phi_{i,j,k}) \\
 \left[D_y^{(2)-} \phi \right]_{i,j,k} &= (\phi_{i,j,k} - \phi_{i,j-1,k}) \\
 \left[D_y^{(2)+} \phi \right]_{i,j,k} &= (\phi_{i,j+1,k} - \phi_{i,j,k}) \\
 \left[D_z^{(2)-} \phi \right]_{i,j,k} &= (\phi_{i,j,k} - \phi_{i,j,k-1}) \\
 \left[D_z^{(2)+} \phi \right]_{i,j,k} &= (\phi_{i,j,k+1} - \phi_{i,j,k})
 \end{aligned} \tag{A.3}$$

$$\begin{aligned}
\left[D_x^{(4)-} \phi \right]_{i,j,k} &= \left(\frac{9}{8} (\phi_{i,j,k} - \phi_{i-1,j,k}) - \frac{1}{24} (\phi_{i+1,j,k} - \phi_{i-2,j,k}) \right) \\
\left[D_x^{(4)+} \phi \right]_{i,j,k} &= \left(\frac{9}{8} (\phi_{i+1,j,k} - \phi_{i,j,k}) - \frac{1}{24} (\phi_{i+2,j,k} - \phi_{i-1,j,k}) \right) \\
\left[D_y^{(4)-} \phi \right]_{i,j,k} &= \left(\frac{9}{8} (\phi_{i,j,k} - \phi_{i,j-1,k}) - \frac{1}{24} (\phi_{i,j+1,k} - \phi_{i,j-2,k}) \right) \\
\left[D_y^{(4)+} \phi \right]_{i,j,k} &= \left(\frac{9}{8} (\phi_{i,j+1,k} - \phi_{i,j,k}) - \frac{1}{24} (\phi_{i,j+2,k} - \phi_{i,j-1,k}) \right) \\
\left[D_z^{(4)-} \phi \right]_{i,j,k} &= \left(\frac{9}{8} (\phi_{i,j,k} - \phi_{i,j,k-1}) - \frac{1}{24} (\phi_{i,j,k+1} - \phi_{i,j,k-2}) \right) \\
\left[D_z^{(4)+} \phi \right]_{i,j,k} &= \left(\frac{9}{8} (\phi_{i,j,k+1} - \phi_{i,j,k}) - \frac{1}{24} (\phi_{i,j,k+2} - \phi_{i,j,k-1}) \right)
\end{aligned} \tag{A.4}$$

A.1.3 Wave Equations

Using the approximations introduced in the previous sections (A.1.1,A.1.3) the 2nd-order and 4th-order approximate versions of the wave-equations (equations 2.4, 2.6) can be written as:

$$\begin{aligned}
\sigma_{xx}(t + \Delta t) &= \sigma_{xx}(t) + \frac{\Delta t}{\Delta x} \left((\lambda + 2\mu) D_x^{(o)+} v_x + \lambda (D_y^{(o)+} v_y + D_z^{(o)+} v_z) \right) \\
\sigma_{yy}(t + \Delta t) &= \sigma_{yy}(t) + \frac{\Delta t}{\Delta x} \left((\lambda + 2\mu) D_y^{(o)+} v_y + \lambda (D_x^{(o)+} v_x + D_z^{(o)+} v_z) \right) \\
\sigma_{zz}(t + \Delta t) &= \sigma_{zz}(t) + \frac{\Delta t}{\Delta x} \left((\lambda + 2\mu) D_z^{(o)+} v_z + \lambda (D_x^{(o)+} v_x + D_y^{(o)+} v_y) \right) \\
\sigma_{xy}(t + \Delta t) &= \sigma_{xy}(t) + \frac{\mu \Delta t}{\Delta x} (D_y^{(o)-} v_x + D_x^{(o)-} v_y) \\
\sigma_{xz}(t + \Delta t) &= \sigma_{xz}(t) + \frac{\mu \Delta t}{\Delta x} (D_z^{(o)-} v_x + D_x^{(o)-} v_z) \\
\sigma_{yz}(t + \Delta t) &= \sigma_{yz}(t) + \frac{\mu \Delta t}{\Delta x} (D_z^{(o)-} v_y + D_y^{(o)-} v_z),
\end{aligned} \tag{A.5}$$

for the stress, and

$$\begin{aligned}
v_x(t + \Delta t/2) &= v_x(t - \Delta t/2) + \frac{\Delta t}{\rho \Delta x} (D_x^{(o)-} \sigma_{xx} + D_y^{(o)+} \sigma_{xy} + D_z^{(o)+} \sigma_{xz}) \\
v_y(t + \Delta t/2) &= v_y(t - \Delta t/2) + \frac{\Delta t}{\rho \Delta x} (D_x^{(o)+} \sigma_{xy} + D_y^{(o)-} \sigma_{yy} + D_z^{(o)+} \sigma_{yz}) \\
v_z(t + \Delta t/2) &= v_z(t - \Delta t/2) + \frac{\Delta t}{\rho \Delta x} (D_x^{(o)+} \sigma_{xz} + D_y^{(o)+} \sigma_{yz} + D_z^{(o)-} \sigma_{zz}),
\end{aligned} \tag{A.6}$$

for the velocities, with o denoting the order ($o = \{2, 4\}$), the sign in the index (\pm) denoting the orientation of the operator with respect to the indexing (see Figure A.1 and equation A.3 & A.4) of the finite-difference operators $D_{\xi}^{(o)\pm}$.

The 4-point operator can be used for any point located at a distance of at least $2\Delta x$ away from a frictional interface with some of the field variables being potentially discontinuous. The position of the fault inside a staggered-grid cell depends on the implementations of the fault (e.g., traction-at-split-node as in section A.2, or stress-glut method as in section A.3).

A.2 Traction-at-Split-Nodes (TSN) Implementation of a Fault in Staggered-Grid Finite-Differences

A.2.1 Fault Plane Slip Velocity and Shear Traction

At points on the fault plane second-order difference approximations to equations 2.4, 2.6 have to be used, and a partitioning into new, separate equations for the plus- and minus-side values of the split-node variables has to be introduced. In Figure A.2 one can see, that of the nine independent velocity and stress components, six have their grid locations on the fault-plane, which are, in the case of a fault-normal that is parallel to the x -direction, the tangential velocities v_y and v_z and the stress components σ_{yz} , σ_{xx} , σ_{yy} , and σ_{zz} . While σ_{xx} stays continuous, the other five components become discontinuous across the fault plane when slip-velocity is non-zero. On the fault-plane, these five variables are therefore split into plus-side and minus-side parts (v_y^\pm , v_z^\pm , σ_{yz}^\pm , σ_{yy}^\pm , and σ_{zz}^\pm). The index i_{FP} is used to specify the grid cell containing the fault plane (note that the index i_{FP} also involves grid points located at $+\Delta x/2$ -distance from the actual splitting fault plane). As mentioned in section A.1.3, finite-difference operators located

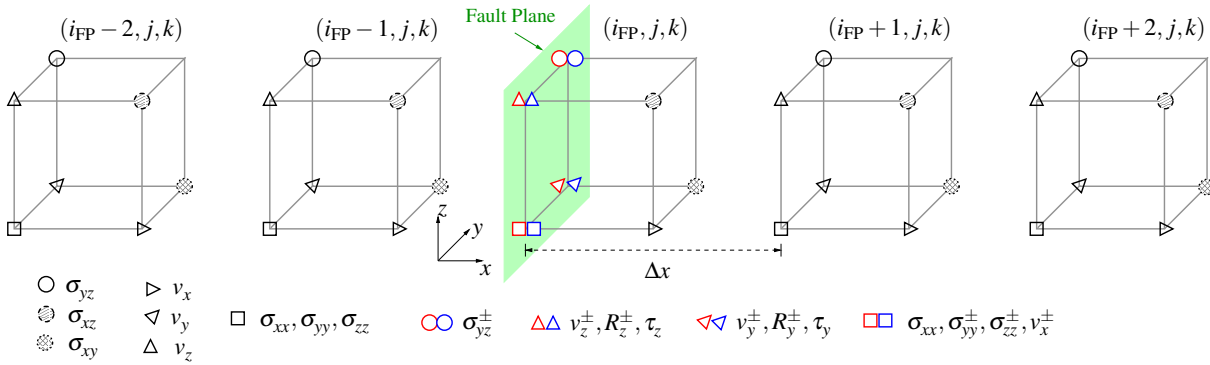


FIGURE A.2: Traction-at-split-node implementation in a staggered finite-difference grid.

at $2\Delta x$ -distance or more away from a frictional interface remain untouched also in the case of discontinuity of velocity (slip). At any point located at a distance of exactly $3\Delta x/2$ from the fault plane, each spatial derivative can be approximated with the same fourth-order spatial difference operator as before, but now the difference approximation to the derivative with respect to the x -coordinate involves a value of the field variable on the fault plane. For that fault plane value, the corresponding half of the fault plane split node for that variable has to be used. That is, x -difference operators $D_x^{(4)}$ centered on the plus sides of the fault at $x_{FP} + 3\Delta x/2$ use the plus-side split-node variable, x -difference operators $D_x^{(4)}$ centered on the minus sides of the fault at $x_{FP} - 3\Delta x/2$ use the plus-side split-node variable. At points $x_{FP} \pm \Delta x$ and $x_{FP} \pm \Delta x/2$, 2nd-order operators have to be used, with using the corresponding sides of split-node components at $x_{FP} \pm \Delta x/2$.

A Special treatment is introduced at points on the fault plane in the following. The finite-difference operators $D_{\xi}^{(o)\pm} = D_{\xi}^{(o)}$ (equation A.3) introduced in section A.1.3 are used with the orientation index of the centered operators (\pm) being dropped here for reasons of simplicity. The appropriate operator centered at the desired point has to be chosen accordingly (see equations A.5 & A.6). Introducing one-sided difference approximations for $\partial_x \sigma_{xy}$ and $\partial_x \sigma_{xz}$ applicable to the plus and minus sides of the fault as

$$[\partial \sigma_{xy}]_{jk}^{\pm} \approx \pm \frac{[\sigma_{xy}]_{iFP,j,k} - [\tau_y(t) - \tau_y^0]_{j,k}}{\Delta x/2}, \quad (\text{A.7})$$

$$[\partial \sigma_{xz}]_{jk}^{\pm} \approx \pm \frac{[\sigma_{xz}]_{iFP,j,k} - [\tau_z(t) - \tau_z^0]_{j,k}}{\Delta x/2}, \quad (\text{A.8})$$

the velocity components on the plus and minus sides can be written as

$$[v_y^{\pm}(t + \Delta t/2)]_{j,k} = [v_y^{\pm}(t - \Delta t/2)]_{j,k} + \frac{\Delta t}{M_{j,k}^{\pm}} \left([R_y^{\pm}]_{j,k}(t) \mp \Delta x^2 [\tau_y(t) - \tau_y^0]_{j,k} \right), \quad (\text{A.9})$$

$$[v_z^{\pm}(t + \Delta t/2)]_{j,k} = [v_z^{\pm}(t - \Delta t/2)]_{j,k} + \frac{\Delta t}{M_{j,k}^{\pm}} \left([R_z^{\pm}]_{j,k}(t) \mp \Delta x^2 [\tau_z(t) - \tau_z^0]_{j,k} \right), \quad (\text{A.10})$$

where

$$M_{j,k}^{\pm} = \frac{\Delta x^3}{4} \rho_{j,k}^{\pm} \quad (\text{A.11})$$

$$[R_y^{\pm}]_{j,k} = \frac{\Delta x^2}{2} \left(\pm 2 [\sigma_{xy}]_{iFP,j,k} + [D_y^{(2)} \sigma_{yy}^{\pm}]_{j,k} + [D_z^{(2)} \sigma_{yz}^{\pm}]_{j,k} \right) \quad (\text{A.12})$$

$$[R_z^{\pm}]_{j,k} = \frac{\Delta x^2}{2} \left(\pm 2 [\sigma_{xz}]_{iFP,j,k} + [D_y^{(2)} \sigma_{yz}^{\pm}]_{j,k} + [D_z^{(2)} \sigma_{zz}^{\pm}]_{j,k} \right) \quad (\text{A.13})$$

Slip velocity components V_y and V_z can be calculated as the differential velocity of the split-nodes:

$$V_y(t + \Delta t/2) = v_y^+(t + \Delta t/2) - v_y^-(t + \Delta t/2), \quad (\text{A.14})$$

$$V_z(t + \Delta t/2) = v_z^+(t + \Delta t/2) - v_z^-(t + \Delta t/2). \quad (\text{A.15})$$

Slip can be obtained by simple integration:

$$D_y(t + \Delta t) = D_y(t) + \Delta t V_y(t + \Delta t/2), \quad (\text{A.16})$$

$$D_z(t + \Delta t) = D_z(t) + \Delta t V_z(t + \Delta t/2). \quad (\text{A.17})$$

To evaluate slip and slip velocity, the traction at split-nodes has to be evaluated first. Defining a trial value for the traction $\tilde{\tau}$ the required shear traction vector to enforce continuity of tangential velocity is:

$$\tilde{\tau}_y(t) = \frac{\Delta t^{-1} M^+ M^- V_y(t - \Delta t/2) + M^- R_y^+(t) - M^+ R_y^-(t)}{\Delta x^2 (M^+ + M^-)} + \tau_y^0 \quad (\text{A.18})$$

$$\tilde{\tau}_z(t) = \frac{\Delta t^{-1} M^+ M^- V_z(t - \Delta t/2) + M^- R_z^+(t) - M^+ R_z^-(t)}{\Delta x^2 (M^+ + M^-)} + \tau_z^0 \quad (\text{A.19})$$

$$\sigma_{xy} = \begin{cases} \tilde{\tau}_y & \text{for } \tilde{\tau} \leq \tau^s \\ \tau^s \frac{\tilde{\tau}_y}{\tilde{\tau}} & \text{for } \tilde{\tau} > \tau^s \end{cases}, \quad \sigma_{xz} = \begin{cases} \tilde{\tau}_z & \text{for } \tilde{\tau} \leq \tau^s \\ \tau^s \frac{\tilde{\tau}_z}{\tilde{\tau}} & \text{for } \tilde{\tau} > \tau^s \end{cases} \quad (\text{A.20})$$

where $\tilde{\tau}$ is the magnitude of the trial traction vector defined in (19) $\tilde{\tau} = \sqrt{\tilde{\tau}_y^2 + \tilde{\tau}_z^2}$. Since the y - and z -components of the velocity v_y , v_z , and therefore of the trial traction $\tilde{\tau}_y$ and $\tilde{\tau}_z$, are defined at different grid points, the evaluation of $\tilde{\tau}$ requires interpolation.

A.2.2 Split Stress Components

Three of the stresses components that lie on the fault plane are discontinuous (σ_{yz} , σ_{yy} , and σ_{zz}) (see Figure A.2), and are therefore partitioned into plus-side and minus-side stresses. Increments to the σ_{yz} stress component involve only differentiations of velocity components taken in the y - and z -directions, i.e., parallel to the fault plane, so the plus- and minus-side values of this stress component can be calculated from the regular (second-order) formulas, applied separately to the plus- and minus-side velocities.

$$[\sigma_{yz}^\pm]_{j,k} = \frac{\mu_{j,k}^\pm}{\Delta x} \left[D_z^{(2)} v_y^\pm + D_y^{(2)} v_z^\pm \right]_{j,k} \quad (\text{A.21})$$

which can be time-integrated to obtain $\sigma_{yz}(t)$. The normal stresses σ_{yy} and σ_{zz} involve also the fault-normal derivative $\partial_x v_x$. To overcome this problem plus- and minus-side fault-normal velocities are introduced v_x^\pm at grid-points where normal stress is defined. The finite-difference approximation becomes:

$$[\partial_x v_x]_{j,k}^+ \approx \frac{[v_x]_{i_{FP},j,k} - [v_x^+]_{i_{FP},j,k}}{\Delta x/2} \quad (\text{A.22})$$

$$[\partial_x v_x]_{j,k}^- \approx \frac{[v_x^-]_{i_{FP},j,k} - [v_x]_{i_{FP}-1,j,k}}{\Delta x/2} \quad (\text{A.23})$$

assuming continuous normal traction ($\sigma_{xx}^+ = \sigma_{xx}^-$) and allowing no opening ($v_x^+ = v_x^-$) the split-node fault-normal velocity v_x^\pm can be obtained:

$$[v_x]_{j,k}^+ = [v_x]_{j,k}^- = \frac{A^+ [v_z]_{i_{FP},j,k} + A^- [v_z]_{i_{FP}-1,j,k} - B^- + B^+}{A^+ + A^-} \quad (\text{A.24})$$

with,

$$A^\pm = \frac{2}{\Delta x} \left(\lambda_{j,k}^\pm + 2\mu_{j,k}^\pm \right), \quad (\text{A.25})$$

$$B^\pm = \frac{\lambda_{j,k}^\pm}{\Delta x} \left(D_y^{(2)} v_y^\pm + D_z^{(2)} v_z^\pm \right)_{j,k}. \quad (\text{A.26})$$

For the split-node normal-stress components follows:

$$[\sigma_{yy}^+]_{j,k} = \frac{[\lambda^+ + 2\mu^+]_{j,k} [D_y^{(2)} v_y^+]_{j,k}}{\Delta x} + \frac{\lambda_{j,k}^+ \left([D_z^{(2)} v_z^+]_{j,k} + 2[v_x]_{i_{FP},j,k} - 2[v_x^+]_{i_{FP},j,k} \right)}{\Delta x} \quad (\text{A.27})$$

$$[\sigma_{yy}^-]_{j,k} = \frac{[\lambda^- + 2\mu^-]_{j,k} [D_y^{(2)} v_y^-]_{j,k}}{\Delta x} + \frac{\lambda_{j,k}^- \left([D_z^{(2)} v_z^-]_{j,k} - 2[v_x]_{i_{FP}-1,j,k} + 2[v_x^-]_{i_{FP},j,k} \right)}{\Delta x} \quad (\text{A.28})$$

$$[\sigma_{zz}^+]_{j,k} = \frac{[\lambda^+ + 2\mu^+]_{j,k} [D_z^{(2)} v_z^+]_{j,k}}{\Delta x} + \frac{\lambda_{j,k}^+ \left([D_y^{(2)} v_y^+]_{j,k} + 2[v_x]_{i_{FP},j,k} - 2[v_x^+]_{i_{FP},j,k} \right)}{\Delta x} \quad (\text{A.29})$$

$$[\sigma_{zz}^-]_{j,k} = \frac{[\lambda^- + 2\mu^-]_{j,k} [D_z^{(2)} v_z^-]_{j,k}}{\Delta x} + \frac{\lambda_{j,k}^- \left([D_y^{(2)} v_y^-]_{j,k} - 2[v_x]_{i_{FP}-1,j,k} + 2[v_x^-]_{i_{FP},j,k} \right)}{\Delta x} \quad (\text{A.30})$$

A characteristic of low-order difference approximations is the generation of short-wavelength oscillations (e.g., Day, 1982b; Day et al., 2005). In order suppress these oscillations, an artificial viscous damping of Kelvin-Voigt type can in principle introduced into the equations of motion. Such a damping is artificial, and is intended to stabilize the numerical solution of the elasto-dynamic problem, rather than to represent a physical damping.

A.2.3 Verification of TSN-implementation

Accuracy tests for the TSN-method in a staggered-grid finite-difference scheme have been performed by Dalguer and Day (2007a) and are not duplicated in this work. In order to demonstrate the functionality of the implementation used in this study a few tests were undertaken.

SCEC 2D In-Plane Slip-Weakening Testcase

In this test for the in-plane case described by Otilio et al. (2008) solutions obtained by using a finite-difference code with triangular mesh (Andrews, 1973) is compared with the solutions of a TSN implementation assembled into a 3D finite-difference code developed in this study (see sections A.2, A.1.1, A.1.3 for details). A sketch of the model setup is shown in Figure A.3. The parameters for the model are as follows: initial shear stress $\tau_0 = 81.6$ MPa inside the

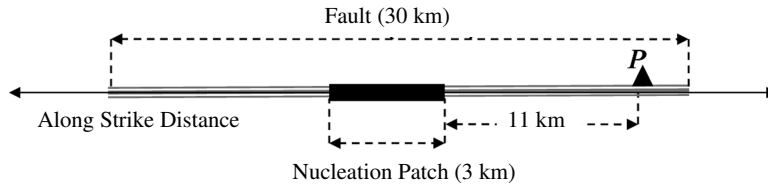


FIGURE A.3: Model setup for the in-plane SCEC test with slip-weakening friction on the fault (modified after Otilio et al. (2008)). Seismograms are compared at point P , situated at 11 km distance from the nucleation region. The seismograms for a specific set of parameters (see values given in the text) are shown in Figure A.4.

nucleation region, and $\tau_0 = 70$ MPa outside the nucleation region on the fault, the initial normal stress $\sigma_{n_0} = 120$ MPa, the static friction coefficient $f_s = 0.677$, the dynamic friction coefficient $f_d = 0.525$, critical slip distance $D_c = 0.4$ m. In Figure A.4 the retrieved seismograms at a point P on the fault (as it is described by Otilio et al. (2008), see Figure A.3) are shown. We find that within this graphical comparison both implementations converge essentially to the same numerical solution. A more systematic test aiming to obtain quantitative accuracy values and convergence rate is not part of this study.

A Bimaterial Slip-Weakening Testcase

Results of a simple testcase with a bimaterial slip-weakening setup is presented here. The model and its parameters is described in Figure A.5. The model parameters are as specified in Figure A.5. The elastic constants are $v_p^{\text{slow}} = 5000$ m/s $v_p^{\text{fast}} = 6000$ m/s $v_s^{\text{slow}} = 2917$ m/s $v_s^{\text{fast}} = 3500$ m/s $\rho^{\text{slow}} = 2417$ m/s $\rho^{\text{fast}} = 2900$ m/s. In Figure A.6 two profiles centered around the hypocenter along the in- & anti-plane direction on the fault for a bimaterial slip-weakening testcase are presented. Solutions of two different methods are compared here: (1) an implemen-

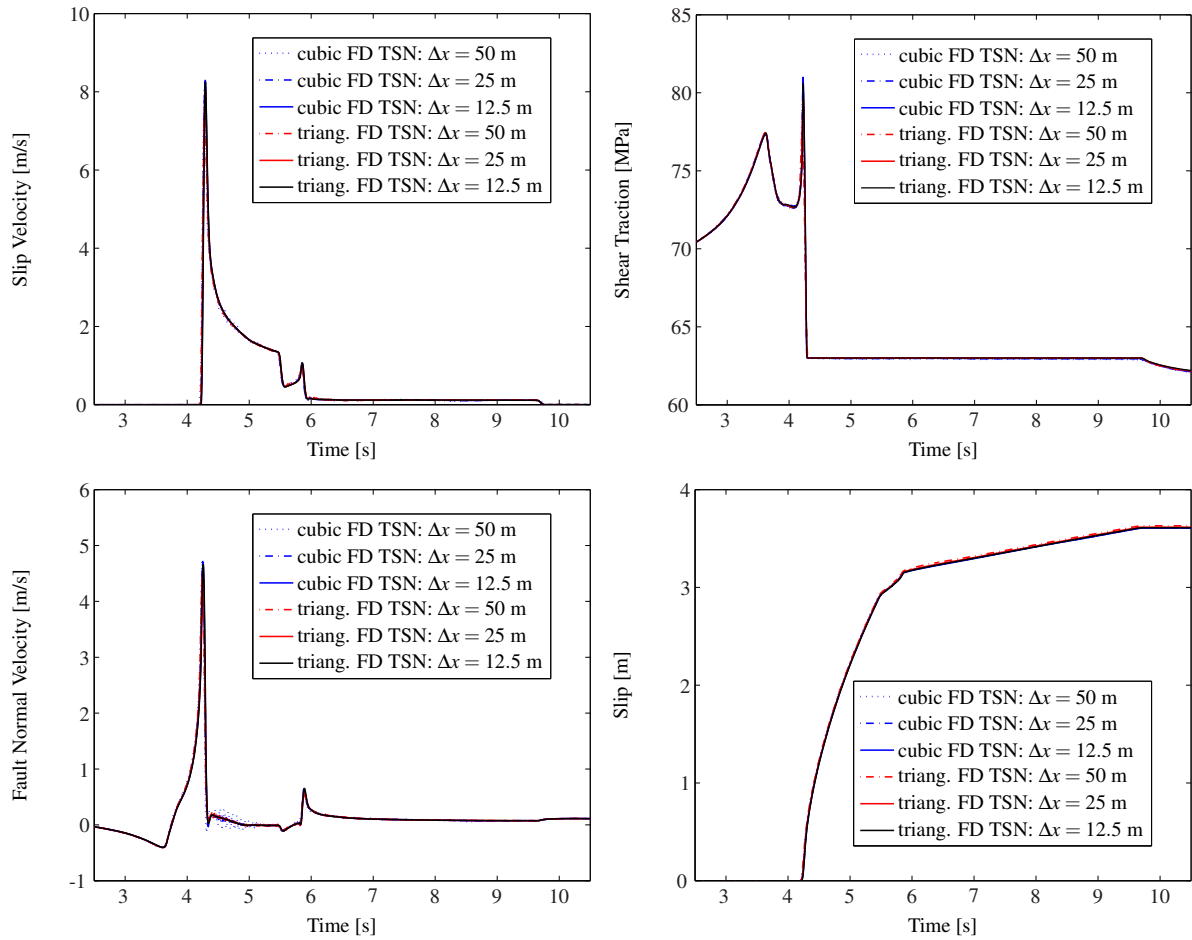


FIGURE A.4: Seismograms at a point on the fault for the SCEC testcase as described by Otilio et al. (2008), model setup displayed in Figure A.3, retrieved from two independent finite-differences TSN implementations, one with a triangular grid, the other with a cubed grid.

tation of TSN for staggered-grid finite-differences as introduced by Dalguer and Day (2007a) assembled into a 3D finite-difference code developed in this study (see sections A.2, A.1.1, A.1.3 for details), and (2) a spectral boundary integral method (Dunham, 2007). Like in the previous testcase, this test has to be seen as a qualitative rather than quantitative test of our implementation. A more explicit test of the numerical scheme has been accomplished by Dalguer and Day (2007a).

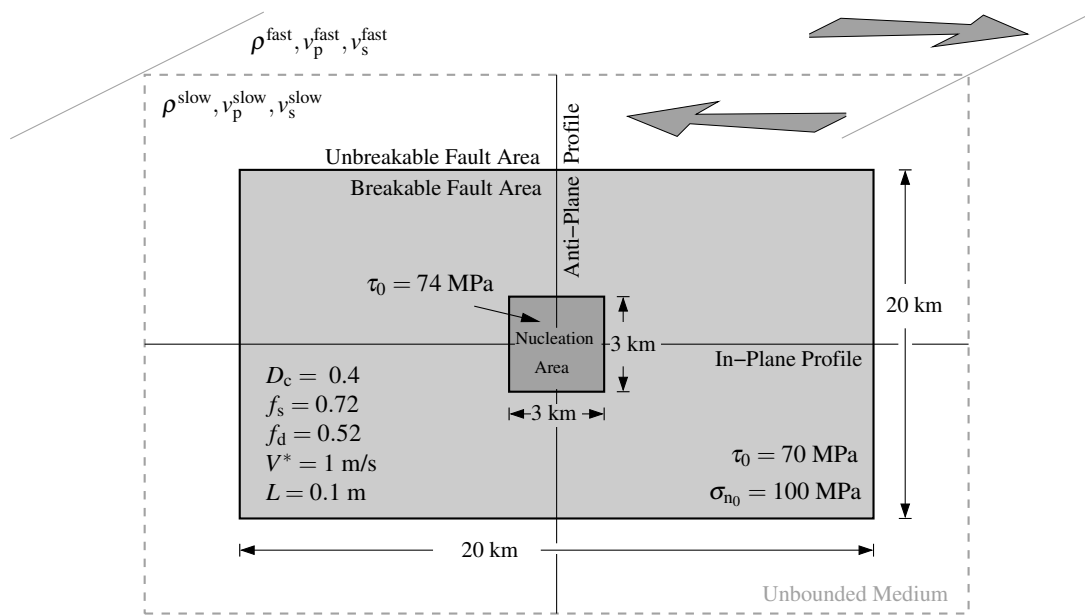


FIGURE A.5: Model setup and parameters for a bimaterial test case with regularized slip-weakening on the fault.

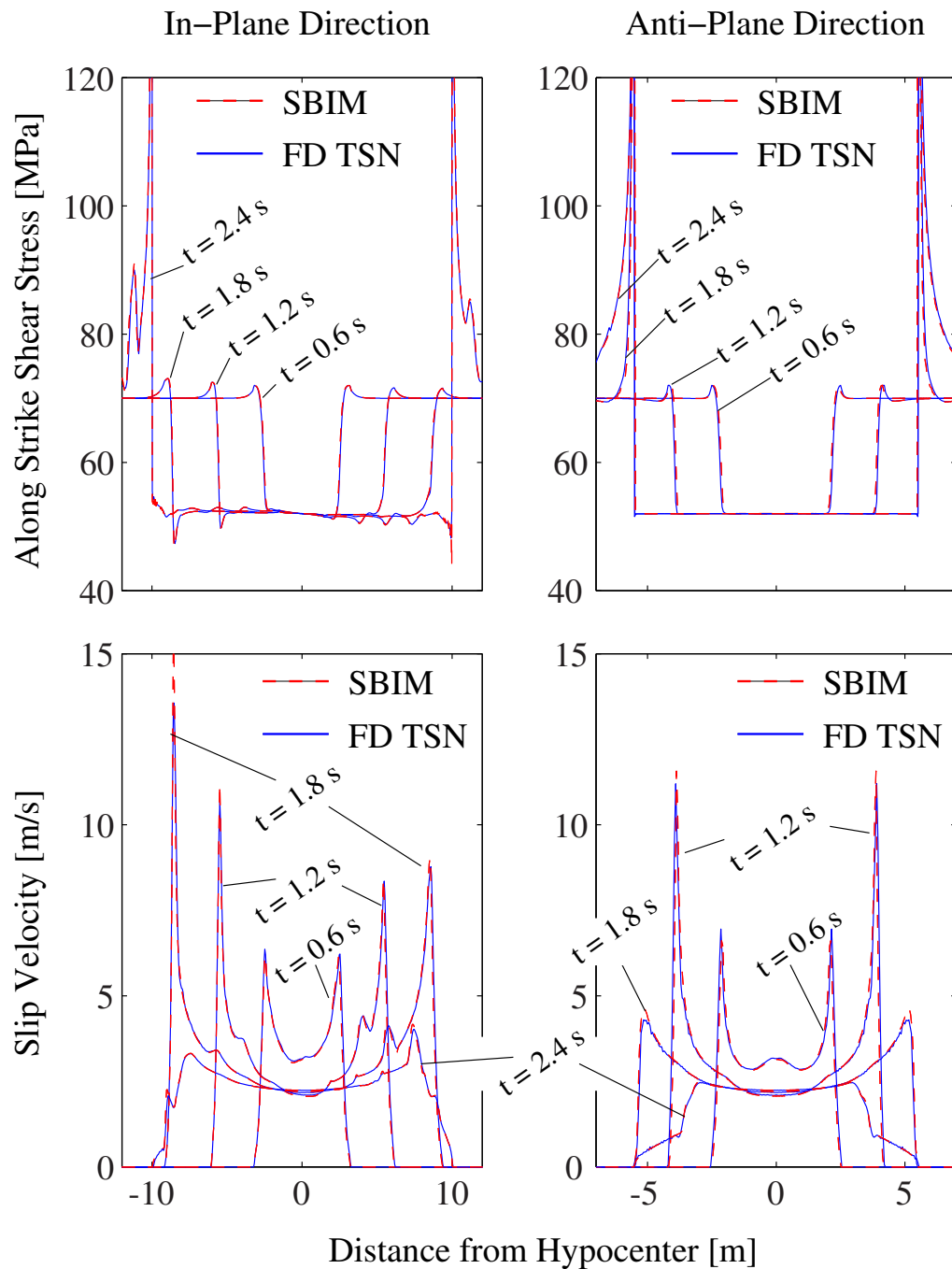


FIGURE A.6: Solutions of two different methods are compared here: (1) an implementation of TSN for staggered-grid finite-difference (Dalguer and Day, 2007a) assembled into a 3D-FD code developed in this study (see sections A.2, A.1.1, A.1.3 for details), and (2) a spectral boundary integral method (Dunham, 2007). The plots show snapshots of slip velocity and shear traction of two profiles centered around the hypocenter along the in-plane direction (left side) and the anti-plane direction (right side) on the fault for a bimaterial slip-weakening testcase.

A.3 The Stress Glut Method (SGM) Implementation of a Fault in Staggered-Grid Finite-Differences

A.3.1 Description of the Stress Glut Method & Implementation

A fault in a finite-difference grid can be represented either as a surface with an explicit displacement discontinuity (e.g., TSN (section A.2)) or as an inelastic zone that may be only one grid interval thick. This section describes an implementation after Andrews (1999) of the latter choice, which is the stress glut method. Backus and Mulcahy (1976) show that any offset from linear elastic behavior is a source of the elastodynamic field. Inelastic strain is the density of seismic potency, and the offset in stress, termed stress glut by Backus and Mulcahy, is seismic moment density. A finite-difference formulation in terms of velocity and stress, in which stress gradients are used to update velocity and velocity gradients are used to update stress, can easily accommodate inelastic strain. All that is required is that stress is changed in accordance with any constitutive law. An element with stress altered from its elastic value will affect its neighbors as an Eshelby inclusion.

The calculation can proceed as follows. In each time step at each point in the fault zone, stress is first incremented by the ordinary equations, as if the current inelastic strain rate was zero. Then shear stress is compared to frictional shear strength. If it is larger, it is reduced to be equal to frictional shear strength. The adjustment is an increment of seismic moment density.

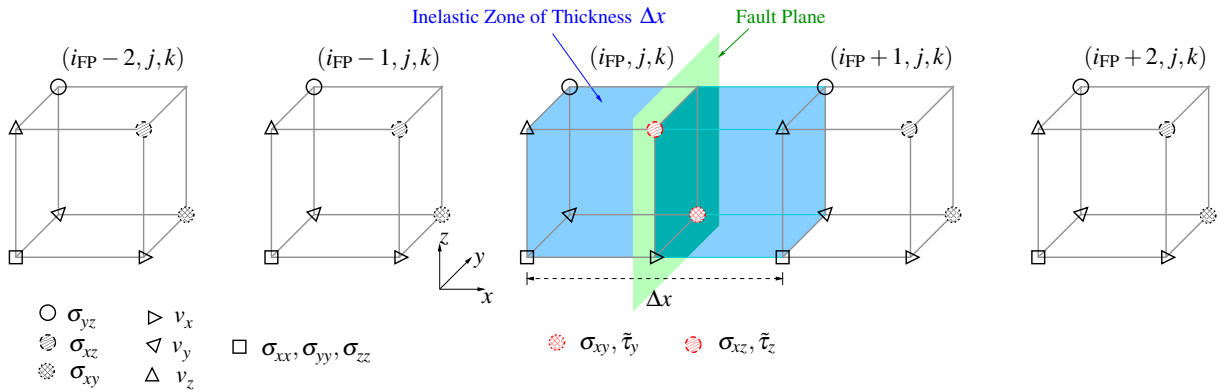


FIGURE A.7: Stress-glut method implementation in a staggered finite-difference grid.

In the following description the fault-normal direction is assumed to be the x -direction. The fault zone is therefore a slab of one grid interval thickness, centered on a y - z -plane containing points where σ_{xy} and σ_{xz} are defined. The shear strength of the fault is $\tau^s = f \max(0, -\sigma_{xx})$, with f the coefficient of friction. In the fault zone, shear stress components σ_{xy} and σ_{xz} may be altered. Trial values of these components, found by adding elastic increments to previous

values, are denoted by $\tilde{\tau}_y$ and $\tilde{\tau}_z$. The trial magnitude of shear traction is $\tilde{\tau} = \sqrt{\tilde{\tau}_y^2 + \tilde{\tau}_z^2}$

$$\sigma_{xy} = \begin{cases} \tilde{\tau}_y & \text{for } \tilde{\tau} \leq \tau^s \\ \tau^s \frac{\tilde{\tau}_y}{\tilde{\tau}} & \text{for } \tilde{\tau} > \tau^s \end{cases}, \quad \sigma_{xz} = \begin{cases} \tilde{\tau}_z & \text{for } \tilde{\tau} \leq \tau^s \\ \tau^s \frac{\tilde{\tau}_z}{\tilde{\tau}} & \text{for } \tilde{\tau} > \tau^s \end{cases} \quad (\text{A.31})$$

Each component is reduced by the same factor so that the adjustment is collinear with the traction vector. Since the shear stresses σ_{xy} and σ_{xz} and normal stress σ_{xx} are defined at different grid locations, interpolations for the stress-adjustment is necessary. The stress adjustment is equivalent to an increment of the seismic moment tensor in the finite-difference cell centered on the stress point,

$$\Delta M_{xy}(t) = (\tilde{\tau}_y(t) - \sigma_{xy}(t))(\Delta x)^3 \quad (\text{A.32})$$

$$\Delta M_{xz}(t) = (\tilde{\tau}_z(t) - \sigma_{xz}(t))(\Delta x)^3 \quad (\text{A.33})$$

the inelastic strain is principally distributed through a thickness of one grid interval. However, the seismic moment increment can be reinterpreted as an increment of slip $\Delta v \Delta t$ on the midplane of the inelastic zone (the plane going through the adjusted stress points),

$$\Delta M_{xy}(t) = \mu \Delta v_y(t) \Delta t (\Delta x)^2 \quad (\text{A.34})$$

$$\Delta M_{xz}(t) = \mu \Delta v_z(t) \Delta t (\Delta x)^2 \quad (\text{A.35})$$

therefore the slip velocity $V_i = \Delta v_i$, can be obtained from:

$$V_y(t) = \Delta v_y(t) = \frac{\tilde{\tau}_y(t) - \sigma_{xy}(t)}{\mu} \frac{\Delta x}{\Delta t} \quad (\text{A.36})$$

$$V_z(t) = \Delta v_z(t) = \frac{\tilde{\tau}_z(t) - \sigma_{xz}(t)}{\mu} \frac{\Delta x}{\Delta t} \quad (\text{A.37})$$

The stress-glut method does not need any further feedback of adjustment of velocities at neighboring grid-points, the adjustment of stress has already accomplished the coupling to the rest of the calculation. There is no inertia in this procedure, and stopping of slip needs no special consideration. Slip velocity is defined at the same space-time point as the stress component that was adjusted, and are therefore displaced by half a time step and a half spatial step from the points where ordinary grid velocity is defined. If the coefficient of friction is dependent only on slip, then slip from a half time step earlier may be used to evaluate shear strength to get an updated slip value with first-order accuracy. The first-order midstep value of slip may be used to repeat the procedure and achieve second-order accuracy. However, if friction depends on slip

velocity, a pair of simultaneous equations for the current value of slip velocity and frictional stress has to be solved. The solution of the pair of equations must be coded explicitly for each particular friction law.

When allowing no rake rotation there is only one component of slip, and the antiplane component of traction is zero (pure strike-slip case, $\tau_z = 0$). As mentioned before, if one wants to incorporate rake rotation, then the traction components must be interpolated at common points, and any adjustment has to be redistributed to the staggered-grid. In this case yielding is nonlocal, and slip velocity is slightly diffused. This smoothing can be interpreted as a small artificial viscosity. For the implementation of the stress-glut method in a fourth-order finite-difference scheme, all 4-point differences have to be replaced by 2-point operators where the 4-point operator would cross the fault. Spatial derivatives located directly on the fault also have to be 2-point operators. In the case that the fault is a bimaterial interface, the density ρ for the evaluation of the fault-normal velocity (here v_x) on the fault-plane is best taken to be the arithmetic mean of both sides $\rho_{FP} = (\rho^+ + \rho^-)/2$ while the elastic constants μ & λ for the evaluation of the shear traction on the fault (here τ_y & τ_z) and the slip velocity V are best taken to be the harmonic mean, e.g. $\mu_{FP} = (2\mu^+\mu^-)/(\mu^+ + \mu^-)$ (Moczo et al., 2007).

A.3.2 Verification of the SGM-Implementation

The implementation of the stress glut Method in the 3D finite-difference code with staggered grid has been tested by Brietzke (2003) for a prescribed rupture at constant velocity as explained and performed before by Andrews (1999).

Circular Expanding Crack Testcase

A circular crack prescribed to grow from a point at a constant rupture velocity v_r that is less than the Rayleigh velocity has a radially symmetric slip function, $V(r,t) = C(v_r)(v_s/v_r)(\Delta\tau/\mu)\sqrt{(v_r t)^2 - r^2}$ (Dahlen, 1974, equations 27, 28, and 44). For $v_r/v_s = 0.8$ the coefficient is $C(v_r)(v_s/v_r) = 0.938$. To remove the singularity in the solution the analytical solution can be smeared out in time. In a realistic earthquake simulation, $\Delta\tau/\mu$ is small. Then the elastodynamic problem is linear apart from the fault boundary condition, and amplitudes can be scaled arbitrarily. In the following non-dimensional units are chosen identical to the ones of Andrews (1999). With shear modulus $\mu = 1$, $v_s = 1$, rupture propagation velocity $v_r = 0.8$, and stress drop $\Delta\tau = 0.2$, dynamic friction level τ_d . Time histories are examined at $r = 20$. Results are calculated for discretization intervals $\Delta x = 1$, $\Delta x = 0.5$, and $\Delta x = 0.25$, corresponding to propagation distances of 20, 40, and 80 elements, respectively. Boundaries of the finite-difference grid are located far enough away that there are no reflections in the plotted results. The calculation is constrained to have only one component of slip. The rupture propagation is prescribed using a frictional shear strength that is prescribed as a function of space

and time, $\tau^s = \max[\tau_d, \tau_0 + (\tau_0 - \tau_k)(r - v_r t)/D]$. No fixed upper shear strength is defined, and slip starts wherever elastic stress first meets the function τ^s , which will be at some radius larger than $r = v_r t$. The distance in which τ^s falls from τ_0 to τ_k is chosen to be $D = 1.2$. The solution in a continuum with the prescribed τ^s used here, assuming $D = 0$ would be a sharp-tipped crack solution. Since finite-difference methods converge only for smooth solutions, D is chosen somewhat larger than the largest grid-spacing of $\Delta x = 1$ used for this test. Therefore the crack tip is smeared out over a cohesive zone extending from $r = v_r t - D$ to some radius greater than $v_r t$ where stress first equals τ^s . The analytical solution for the slip velocity (shown in Figure A.8) is smeared out with $D = 1.2$ as well: $V(r, t) = (V_a(r, t + D/v_r) - V_a(r, t - D/v_r))/(2D/v_r)$. Inside the cohesive zone this is very approximate. Figure A.8 shows the results calculated at two points

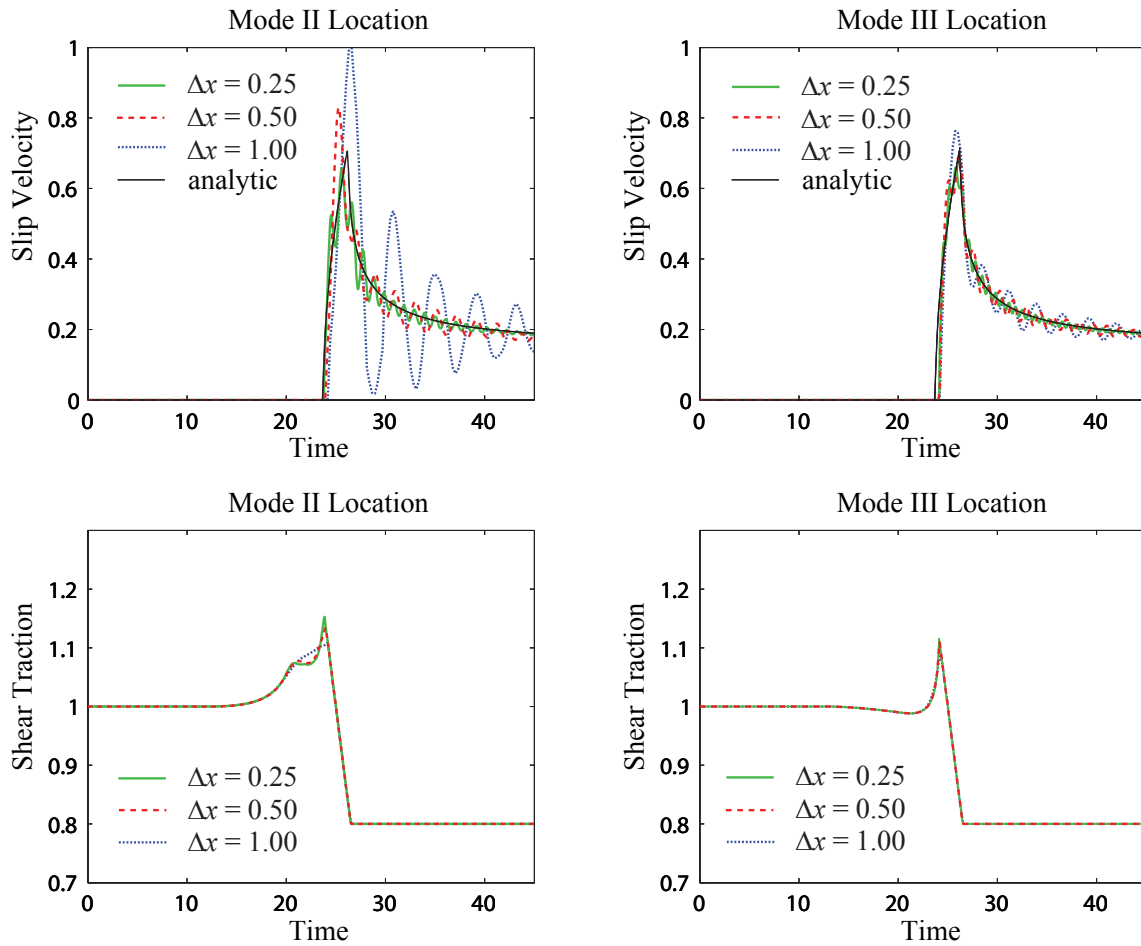


FIGURE A.8: Test for the frictional boundary response of the SGM-method for a circularly expanding rupture at constant rupture propagation velocity. Top panels show the slip velocity for three grid-spacings in comparison with the smeared out analytical solution for a point along the in-plane direction (mode II) and anti-plane direction (mode III). Bottom panels show the corresponding evolutions of the shear traction.

(in-plane direction and anti-plane direction). The top panels show slip velocity calculated with three different discretizations compared with the smeared-out analytic solution. The bottom panels show the shear traction calculated with the three discretizations. Shear traction is unconstrained while slip velocity remains zero, and then it follows the prescribed function of τ^s . The results in Figure A.8 demonstrate that the numerical method converges with grid-refinement to the analytical solution.

Bimaterial Wrinkle Pulse Testcase

In this study the stress glut method has been applied in order to study the wrinkle-like slip pulse specific to bimaterial interfaces. Therefore we tested the convergence of the method in a bimaterial setup with regularized Coulomb friction with a spontaneously propagating rupture with grid-refinements. As discussed in section 2.3.3, in the case that the frictional interface separates dissimilar elastic materials, the problem of frictional sliding is mathematically ill-posed under certain circumstances due to the Adams instability (Adams, 1995). The ill-posedness can be regularized, but even in the regularized case a fine numerical mesh can become necessary to resolve the feature of the wrinkle-like slip pulse, or the Weertman pulse (Weertman, 1980), due to the highly instable divergent behavior of the such a pulse. Therefore the parameter case studied by Cochard and Rice (2000) can be seen as a useful benchmark of the numerical method. In Figure A.9 the results of this setup are shown as seismograms of slip velocity, shear stress, friction, and normal stress at two points on the fault. The parameters used are as follows: elastic parameters $\rho^{\text{fast}} = 3333.3 \text{ kg/m}^3$, $v_s^{\text{fast}} = 3000.0 \text{ m/s}$, $v_p^{\text{fast}} = 5196.2 \text{ m/s}$, $\rho^{\text{slow}} = 2777.7 \text{ kg/m}^3$, $v_s^{\text{slow}} = 2500.0 \text{ m/s}$, and $v_p^{\text{slow}} = 4330.1 \text{ m/s}$, friction coefficient $f_c = 0.75$, characteristic slip velocity $V^* = 1 \text{ m/s}$, characteristic length $L = 8.5 \text{ mm}$, initial shear stress $\tau_0 = 70 \text{ MPa}$, initial normal stress $\sigma_0 = 100 \text{ MPa}$. The nucleation procedure and parameters are the same as used by Cochard and Rice (2000). Figure A.9 provides that with a grid-spacing of $\Delta x = 0.25 \text{ m}$ a sufficient convergence is achieved at a propagation distance of up to 300 m.

Like in the case of TSN, the graphical verifications of SGM performed here have to be seen as a qualitative rather than quantitative test of our implementation. More explicit tests of the numerical scheme have been accomplished by various authors, (e.g, Dalguer and Day, 2006, , and references therein). Those studies provide indication that the stress glut method fails to provide good convergence for several testcases in comparison to other methods, e.g. the traction-at-split-node (TSN) scheme. However, as can be seen in Figure A.9, in the specific case of a bimaterial interface with regularized Coulomb friction we get satisfyingly converging results for the study presented in chapter 4.

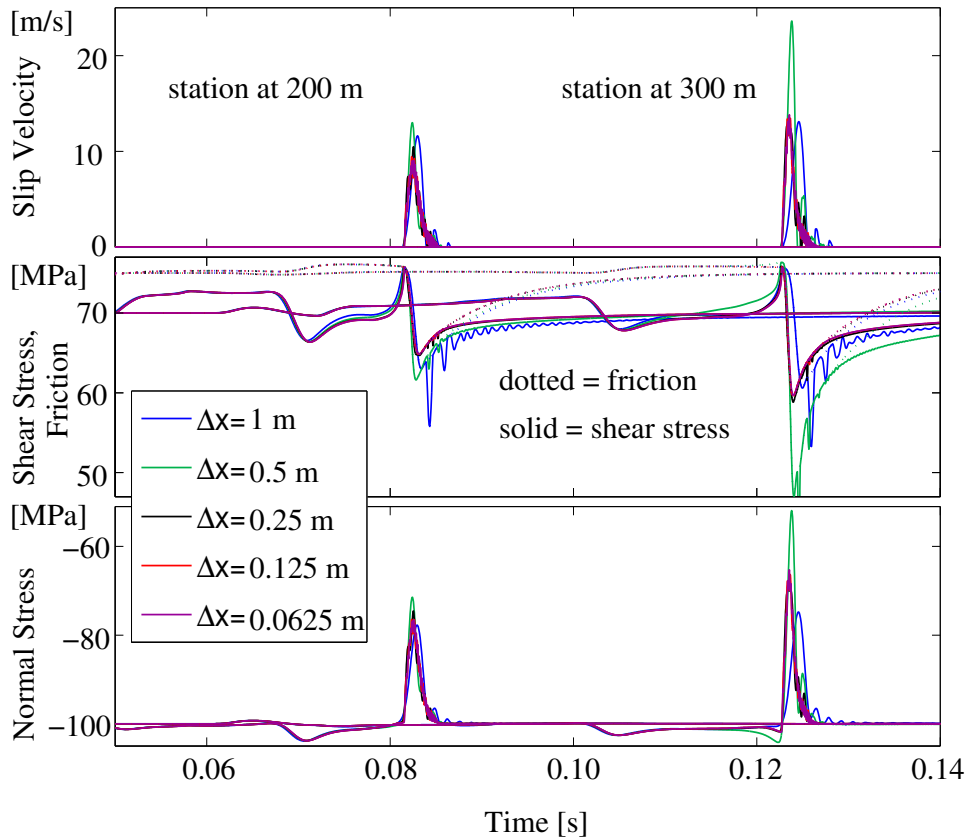


FIGURE A.9: Testcase for the bimaterial wrinkle-like pulse of slip with regularized Coulomb friction. Slip velocity, shear stress, friction, and normal stress at two stations at 200 m and 300 m propagation distance in-plane direction for the parameter case of Cochard and Rice (2000). For the shown propagation distances a resolution of $\Delta x = 0.25$ m appears to be sufficient since the results of $\Delta x = 0.25$ m, $\Delta x = 0.125$ m, and $\Delta x = 0.0625$ m basically collapse to the same solution.

Appendix B

Definitions

B.1 Slip, Slip Velocity, Peak Slip Velocity

The definition of slip velocity V in this study is the differential velocity across the fault,

$$\mathbf{V} = \begin{pmatrix} V_y \\ V_z \end{pmatrix} = \begin{pmatrix} v_y^+ \\ v_z^+ \end{pmatrix} - \begin{pmatrix} v_y^- \\ v_z^- \end{pmatrix}, \quad (\text{B.1})$$

its absolute value $V = |\mathbf{V}|$. Its peak slip velocity (or maximum slip velocity) is the maximum over time of the absolute value of slip velocity:

$$V_{\max} = \max_t (|\mathbf{V}(y, z, t)|). \quad (\text{B.2})$$

and slip is then the integral of slip velocity over time:

$$\mathbf{D} = \int_{t_0}^T \mathbf{V} dt. \quad (\text{B.3})$$

B.2 Rupture Propagation Velocity

The rupture propagation velocity is normally referred to as the propagation velocity of the tip of the advancing rupture (propagation velocity calculated from first arrival times, see figure B.1). However, in this study we use the term rupture propagation velocity also for propagation velocity values inferred from the arrival times of peak slip velocity, which mostly is nearby the crack tip (see Figure B.1).

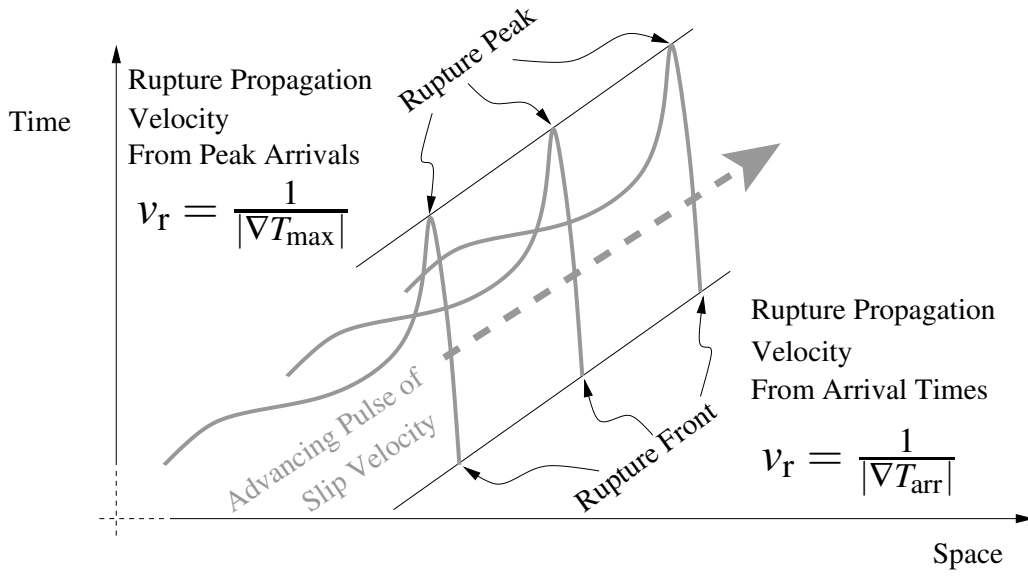


FIGURE B.1: The velocity with which a rupture spreads across the fault (rupture propagation velocity) can be inferred from first arrivals (onset of slip) or the peak arrivals (maximum slip velocity).

B.3 Seismic Moment and Moment Magnitude

Assuming the existence of discontinuous differential displacement on a fault plane, the scalar seismic moment of a slipping patch (see Figure B.2) is defined as:

$$M_0 = \mu AD \tag{B.4}$$

The moment magnitude as a dimensionless number M_W is then defined by:

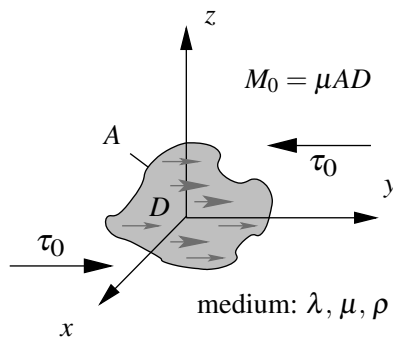


FIGURE B.2: A patch of slip invokes a scalar seismic moment M_0 .

$$M_W = \frac{2}{3} \left(\log_{10} \frac{M_0}{\text{N} \cdot \text{m}} - 9.1 \right) = \frac{2}{3} \left(\log_{10} \frac{M_0}{\text{dyn} \cdot \text{cm}} - 16.1 \right) \tag{B.5}$$

with $1 \text{ dyn} \cdot \text{cm} = 1 \text{ N} \cdot \text{m} \cdot 10^{-7}$.

B.4 Peak Ground Velocity and Peak Ground Acceleration

The definition of peak ground velocity (PGV) and peak ground acceleration (PGA), as used in this study, is the maximum over time of the absolute value of velocity $|\mathbf{v}|$ and absolute value of acceleration $|\mathbf{a}|$ at a point on the surface (x, y, z_0)

$$\text{PGV}(x, y) = \max_t(|\mathbf{v}(x, y, z_0, t)|), \quad \text{PGA}(x, y) = \max_t(|\mathbf{a}(x, y, z_0, t)|), \quad (\text{B.6})$$

with;

$$|\mathbf{v}| = \sqrt{v_x^2 + v_y^2 + v_z^2}, \quad |\mathbf{a}| = \sqrt{a_x^2 + a_y^2 + a_z^2} \quad (\text{B.7})$$

unless stated otherwise.

B.5 Weertman Pulse or Adams' Steady State Pulse

In the case of a constant friction coefficient and an existing generalized Rayleigh wave speed, there exists a steady state propagating slip pulse solution (Adams, 1998). The existence of such a pulse has been suggested before by Weertman (1980), who didn't work out the exact solution. The solution of Adams (1998) can easily be deduced from Weertman's developments (Weertman, 1980) as it has been mentioned by Rice (1997). In that solution the shear stress is uniform and equal to the initial stress, i.e. smaller than the shear strength $\tau_0 < f\sigma_{n_0}$. The compressive normal stress is equal to initial normal stress $|\sigma_0|$ everywhere except within the pulse zone, in which it is uniform and equal to $|\tau_0|/f$. Therefore the reduction in normal stress is the driving mechanism. The apparent coefficient of friction (which would be measured in a friction experiment) is $f^* = |\tau_0|/|\sigma| < f$. In particular, one can have $f^* = 0$, corresponding to a complete drop in normal stress. Hence, one can have sliding with an arbitrarily low initial shear stress and an arbitrarily high coefficient of friction but, e.g., without any generation of heat. This pulse travels at the generalized Rayleigh velocity into the direction of slip of the softer side of the bimaterial configuration. The slip velocity is uniform and given by:

$$V = \frac{(f|\sigma_{n_0}| - \tau_0)v_{\text{gr}}}{f\mu^*}, \quad (\text{B.8})$$

$\mu^*(v_s, v_p)$ being a complicated function of the wave speeds v_s and v_p and material properties (Weertman, 1980) (misprint corrected by Cochard and Rice (2000)):

$$\mu^* = \frac{2\mu_1\mu_2}{\Delta} [\mu_1(\gamma_1\beta_1 - \alpha_1^4)(\gamma_2\beta_2 - \alpha_2^2) - \mu_2(\gamma_2\beta_2 - \alpha_2^4)(\gamma_1\beta_1 - \alpha_1^2)] \quad (\text{B.9})$$

$$\Delta = \mu_1^2 (1 - \gamma_2 \beta_2) (\gamma_1 \beta_1 - \alpha_1^4) + \mu_2^2 (1 - \gamma_1 \beta_1) (\gamma_2 \beta_2 - \alpha_2^4) + \mu_1 \mu_2 [(1 - \alpha_1^2) (1 - \alpha_2^2) (\gamma_1 \beta_2 + \gamma_2 \beta_1) + 2 (\gamma_1 \beta_1 - \alpha_1^2) (\gamma_2 \beta_2 - \alpha_2^2)] \quad (\text{B.10})$$

$$\alpha_i = \sqrt{1 - v_r / 2v_{s_i}^2}, \quad \beta_i = \sqrt{1 - v_r / v_{s_i}^2}, \quad \gamma_i = \sqrt{1 - v_r / v_{p_i}^2} \quad (\text{B.11})$$

B.6 Generalized Rayleigh Velocity

The generalized Rayleigh velocity is the root of $\bar{\mu}$ in the subshear velocity range, $\bar{\mu}$ being a complicated function of the propagation velocity v_r and material properties:

$$\bar{\mu} (v_{\text{gr}}) = 0 \quad (\text{B.12})$$

$$\bar{\mu} = \frac{2\mu_1\mu_2}{\Delta} [\mu_1\gamma_2 (1 - \alpha_2^2) (\gamma_1\beta_1 - \alpha_1^4) + \mu_2\gamma_1 (1 - \alpha_1^2) (\gamma_2\beta_2 - \alpha_2^4)] \quad (\text{B.13})$$

with Δ as defined in equation B.10, and α , β , γ as defined in equations B.11.

Acknowledgment

I would like to thank Heiner Igel for providing me the opportunity to do a doctorate in the seismology group at the LMU Munich. Invaluable thanks go to Alain Cochard for his great staying power in scientific remote guidance and advice, exemplary persuasive idealism, his interest also in details, his indispensable humor and matchless style, and all the yogurts he dispensed. I thank Yehuda Ben-Zion for kicking off my PhD with a first project and useful comments during the final stage of my thesis.

I thank Marcus Mohr for being an always available, extremely helpful expert on latex, emacs, mathematics, debugging, linux, programming language standards and many other things. I thank Jens Öser for having done a great job on progressively pimping my PC for about 5 years, and for assuring data security of the huge amount of data produced during the work of this thesis. I thank Martin Käser for his sportive team spirit, both, on the job and while cycling. I thank Josep de la Puente for bequeathing me his old notebook that enabled a more efficient work in the last six months of my thesis. I thank Michael Ewald for being a funny office made during the first half of this thesis, for sharing the contents of his “Quatsch”-folder from time to time, and for being a skillful colleague especially in the fields of finite-differences, coding, matlab, nutrition, as well as Rotz- und Schweinerock, also for recalling the essential rules for success, and finally for always clarifying the question of guilt! I thank František Gallovič for sharing expertise on the FFT, and for being a knowledgeable conversationalist in many fields (from physics to food). I thank Michael Winklhofer for being a cooperative colleague, with an encouraging humor. I thank Moritz Beyreuther for many hints on latex and linux related stuff. I thank Toni Kraft for his noble courtesy as an aristocratic benefactor and for convincing me that “der Graf immer Rech hat”, in fact! I also thank my fellow sufferers Susanne Lehndorfer and Jan Hautmann for being humorous colleagues, lightening up the frustrating stages of this thesis.

I acknowledge the helpfulness of Eva Szabo, Carsten Glasenapp, Tine Chab, Michael Ewald, Anke Lindmeier, Heiner Igel, Jens Öser, Jana Holupirek, Carmen Marti-Pastor, Verena Pressler, Josep de la Puente, Agnes Wasik, Stefanie Rieger, Christina Plattner, Giampiero Iaffaldano, Ernst Brandt and my family during my cervical collar times in 2006. A special thank goes to Enzo Schneider and his brother Mark Schneider who established the contact to a renowned neurosurgeon with a special experience in the desired kind of surgery, giving me a second birthday in August’06.

I thank the Leibniz-Rechenzentrum (LRZ) for providing the parallel super-computing facilities used in this study. I acknowledge financial support from the KONWIHR project, the Munich Reinsurance, the Department for Earth and Environmental Sciences. This work also benefitted from comments from many researchers world wide, thanks to all of you! Correspondingly I would like to thank the financial backers (aforementioned and SPICE) financing the participation and presentation my work in progress at diverse meetings within Europe and the US from time to time. I would like to thank Peter Moczo for organizing two very nice Workshops in Smolenice (NMESD 2003 and NMESD 2007), the courtyard party night running 2003 became legendary!

Additional thanks go to Eva Szabo, Oliver Borchers, Virginia Souza-Egipsy, Teresa Reinwald, Peter Danecek, Carmen Marti-Pastor, Alex Hornung, Gunnar Jahnke, Carsten Glasenapp, Verena Hermann, Anke Lindmeier, Josep de la Puente, Tobias Metz, Joachim Wassermann, Frederic Flerit, Christoph Moder, Kurt Grubbe, Andreas Fichtner, Erika Vye, Nguyen Pham, Cristóbal Castro, Haijiang Wang, Wiwit Suryanto, Markus Tremml, Marion Bachhäubl, Yvonne Neßler, Amanda Steininger, Veronika Strachwitz, and last but not least my family, all for very various reasons.

Bibliography

- R. E. Abercrombie and J. R. Rice. Can observations of earthquake scaling constrain slip weakening? Geophys. J. Int., 162(2):406–424, 2005. doi: 10.1111/j.1365-246X.2005.02579.x. URL <http://dx.doi.org/10.1111/j.1365-246X.2005.02579.x>.
- J. D. Achenbach and H. I. Epstein. Dynamic interaction of a layer and a half-space. J. Eng. Mech. Div., EM5:27–42, 1967.
- G. G. Adams. Self-excited oscillations of two elastic half-spaces sliding with a constant coefficient of friction. ASME Journal of Applied Mechanics, 62:867–872, 1995.
- G. G. Adams. Steady sliding of two elastic half-spaces with friction reduction due to interface stick-slip. ASME Journal of Applied Mechanics, 65:470–475, 1998.
- G. G. Adams. An intersonic slippulse at a frictional interface between dissimilar solids. ASME Journal of Applied Mechanics, 86:81–86, 2001.
- M. Adda-Bedia and M. Ben Amar. Self-sustained slip pulses of finite size between dissimilar materials. J. Mach. Phys. Solids, 51:1849–1861, 2003.
- J.-P. Ampuero and Y. Ben-Zion. Cracks, pulses and macroscopic asymmetry of dynamic rupture on a bi-material interface with velocity-weakening friction. Geophys. J. Int., 173(2):674–692, May 2008. doi: 10.1111/j.1365-246X.2008.03736.x. URL <http://dx.doi.org/10.1111/j.1365-246X.2008.03736.x>.
- J. P. Ampuero and F. A. Dahlen. Ambiguity of the Moment Tensor. Bull. Seism. Soc. Am., 95(2):390–400, 2005. doi: 10.1785/0120040103. URL <http://dx.doi.org/10.1785/0120040103>.
- D. J. Andrews. A numerical study of tectonic stress release by underground explosions. Bull. Seism. Soc. Am., 63(4):1375–1391, 1973. URL <http://bssa.geoscienceworld.org/cgi/content/abstract/63/4/1375>.
- D. J. Andrews. Rupture propagation with finite stress in antiplane strain. J. Geophys. Res., 81(20):3575–3582, 1976a. URL <http://www.agu.org/journals/jb/v081/i020/JB081i020p03575/>.
- D. J. Andrews. Rupture velocity of plane strain shear cracks. J. Geophys. Res., 81(32):5679–5689, 1976b. URL <http://www.agu.org/journals/jb/v081/i032/JB081i032p05679/>.

- D. J. Andrews. Test of two methods for faulting in finite difference calculations. Bull. Seism. Soc. Am., 89(4):931–937, 1999. URL <http://bssa.geoscienceworld.org/cgi/content/abstract/89/4/931>.
- D. J. Andrews. Rupture dynamics with energy loss outside the slip zone. J. Geophys. Res., 110: B01307, January 2005. doi: 10.1029/2004JB003191. URL <http://dx.doi.org/10.1029/2004JB003191>.
- D. J. Andrews. Comment on “how fast is rupture during an earthquake? new insights from the 1999 turkey earthquake”. Geophys. Res. Lett., 29(15):1714, 2002. doi: 10.1029/2001gl014126. URL <http://dx.doi.org/10.1029/2001gl014126>.
- D. J. Andrews and Y. Ben-Zion. Wrinkle-like slip pulse on a fault between different materials. J. Geophys. Res., 102:553–572, 1997. doi: 10.1029/96JB02856. URL <http://dx.doi.org/10.1029/96JB02856>.
- D. J. Andrews and R. A. Harris. The wrinkle-like slip pulse is not important in earthquake dynamics. Geophys. Res. Lett., 32:L23303, December 2005. doi: 10.1029/2005GL023996. URL <http://dx.doi.org/10.1029/2005GL023996>.
- G. Backus and M. Mulcahy. Moment tensors and other phenomenological descriptions of seismic sources. I. Continuous displacements. Geophys. J. Int., 46:341–361, 1976. doi: 10.1111/j.1365-246X.1976.tb04162.x. URL <http://dx.doi.org/10.1111/j.1365-246X.1976.tb04162.x>.
- G. I. Barenblatt. The formation of brittle cracks during brittle fracture. general ideas and hypotheses. axially-symmetric cracks. Appl. Math. Mech., 23:1273–1282, 1959.
- N. M. Beeler and T. E. Tullis. Self-healing slip pulses in dynamic rupture models due to velocity-dependent strength. Bull. Seism. Soc. Am., 86:1130–1148, 1996. URL <http://bssa.geoscienceworld.org/cgi/content/abstract/86/4/1130>.
- Y. Ben-Zion. A comment on “The wrinkle-like slip pulse is not important in earthquake dynamics” by Andrews and Harris. Geophys. Res. Lett., 33:L06310, 2006a. doi: 10.1029/2005GL025372. URL <http://dx.doi.org/10.1029/2005GL025372>.
- Y. Ben-Zion. A comment on “Material contrast does not predict earthquake rupture propagation direction” by Harris and Day. Geophys. Res. Lett., 33:L13310, 2006b. doi: 10.1029/2005GL025652. URL <http://dx.doi.org/10.1029/2005GL025652>.
- Y. Ben-Zion. Dynamic ruptures in recent models of earthquake faults. J. Mach. Phys. Solids, 49:2209–2244, 2001. doi: 10.1016/S0022-5096(01)00036-9. URL [http://dx.doi.org/10.1016/S0022-5096\(01\)00036-9](http://dx.doi.org/10.1016/S0022-5096(01)00036-9).
- Y. Ben-Zion. Collective behavior of earthquakes and faults: Continuum-discrete transitions, progressive evolutionary changes and different dynamic regimes. Rev. Geophys., in press:1–122, 2008. doi: 10.1029/2008RG000260. URL <http://dx.doi.org/10.1029/2008RG000260>.

- Y. Ben-Zion. Key Formulas in Earthquake Seismology, volume 81B of International Handbook of Earthquake and Engineering Seismology, chapter Appendix 2, pages 1857–1875. Academic Press, 2003. URL http://earth.usc.edu/~ybz/pubs_recent/IASPEI03/App-2_IASPEI_03.pdf.
- Y. Ben-Zion and D. J. Andrews. Properties and implications of dynamic rupture along a material interface. Bull. Seism. Soc. Am., 88(4):1085–1094, 1998. URL <http://bssa.geoscienceworld.org/cgi/content/abstract/88/4/1085>.
- Y. Ben-Zion and Y. Huang. Dynamic rupture on an interface between a compliant fault zone layer and a stiffer surrounding solid. J. Geophys. Res., 107:2042, February 2002. doi: 10.1029/2001JB000254. URL <http://dx.doi.org/10.1029/2001JB000254>.
- Y. Ben-Zion and P. Malin. San Andreas fault zone head waves near Parkfield, California. Science, 251: 1592–1594, 1991.
- Y. Ben-Zion and C. G. Sammis. Characterization of fault zones. Pure Appl. Geophys., 190:677–715, 2003. doi: 10.1007/PL00012554. URL <http://dx.doi.org/10.1007/PL00012554>.
- Y. Ben-Zion and Z. Shi. Dynamic rupture on a material interface with spontaneous generation of plastic strain in the bulk. Earth Planet. Sci. Lett., 236:486–496, July 2005. doi: 10.1016/j.epsl.2005.03.025. URL <http://dx.doi.org/10.1016/j.epsl.2005.03.025>.
- Y. Ben-Zion, S. Katz, and P. Leary. Joint inversion of fault zone head waves and direct p arrivals for crustal structure near major faults. J. Geophys. Res., 97(2):1943–1951, 1992.
- Y. Ben-Zion, Z. Peng, D. Okaya, L. Seeber, J. G. Armbruster, N. Ozer, A. J. Michael, S. Baris, and M. Aktar. A shallow fault-zone structure illuminated by trapped waves in the Karadere-Duzce branch of the North Anatolian Fault, western Turkey. Geophys. J. Int., 152:699–717, March 2003. doi: 10.1046/j.1365-246X.2003.01870.x. URL <http://dx.doi.org/10.1046/j.1365-246X.2003.01870.x>.
- G. Beroza and T. Mikumo. Short slip duration in dynamic rupture in the presence of heterogeneous fault properties. J. Geophys. Res., 101(B10):22,449–22,460, 1996. URL <http://www.agu.org/journals/jb/v101/iB10/96JB02291/>.
- R. L. Biegel and C. G. Sammis. Relating fault mechanics to fault zone structure. Adv. Geophys., 47: 65–111, 2004.
- A. Bizzarri and M. Cocco. Slip-weakening behavior during the propagation of dynamic ruptures obeying rate- and state-dependent friction laws. 108(B8):2373, 2003. doi: 10.1029/2002JB002198. URL <http://dx.doi.org/10.1029/2002JB002198>.
- A. Bizzarri and M. Cocco. A thermal pressurization model for the spontaneous dynamic rupture propagation on a three-dimensional fault: 1. methodological approach. J. Geophys. Res., 111:B05303, 2006a. doi: 10.1029/2005JB003862. URL <http://dx.doi.org/10.1029/2005JB003862>.

- A. Bizzarri and M. Cocco. A thermal pressurization model for the spontaneous dynamic rupture propagation on a three-dimensional fault: 2. traction evolution and dynamic parameters. *J. Geophys. Res.*, 111:B05304, 2006b. doi: 10.1029/2005JB003864. URL <http://dx.doi.org/10.1029/2005JB003864>.
- A. Bizzarri, M. Cocco, D. J. Andrews, and E. Boschi. Solving the dynamic rupture problem with different numerical approaches and constitutive laws. *Geophys. J. Int.*, 144:656–678, March 2001. doi: 10.1046/j.1365-246X.2001.01363.x. URL <http://dx.doi.org/10.1046/j.1365-246X.2001.01363.x>.
- M. S. Boettcher and C. Marone. Effects of normal stress variation on the strength and stability of creeping faults, *J. Geophys. Res.*, 109, b03406, doi:10.1029/2003jb002824. *J. Geophys. Res.*, 109:B03406, 2004. doi: 10.1029/2003JB002824. URL <http://dx.doi.org/10.1029/2003JB002824>.
- M. Bouchon, M.-P. Bouin, H. Karabulut, M. N. Toksöz, M. Dietrich, and A. J. Rosakis. How fast is rupture during an earthquake ? new insights from the 1999 turkey earthquakes. *Geophys. Res. Lett.*, 28(14):2723–2726, 2001. URL <http://www.agu.org/journals/gl/v028/i014/2001GL013112/>.
- F. Brace and J. D. Byerlee. Stick-slip as a mechanism for earthquakes. *Science*, 153(3739):990–992, 1966. doi: 10.1126/science.153.3739.990. URL <http://dx.doi.org/10.1126/science.153.3739.990>.
- G. Brietzke, H. Igel, G. Jahnke, M. Treml, M. Ewald, H. Wang, A. Cochard, and G. Wang. *Computational Elastic Wave Propagation: Advances in Global and Regional Seismology*, volume XIV of *High Performance Computing in Science and Engineering*, Munich 2004, pages 445–458. Springer-Verlag Berlin Heidelberg Germany, 2004. URL <http://www.springer.com/math/cse/book/978-3-540-44326-1>.
- G. B. Brietzke. Numerical simulation of kinematic and dynamic ruptures in anisotropic media. Master's thesis, Ludwig-Maximilians Universität München, 2003.
- G. B. Brietzke and Y. Ben-Zion. Examining tendencies of in-plane rupture to migrate to material interfaces. *Geophys. J. Int.*, 167(2):807–819, 2006. doi: 10.1111/j.1365-246X.2006.03137.x. URL <http://dx.doi.org/10.1111/j.1365-246X.2006.03137.x>.
- G. B. Brietzke, A. Cochard, and H. Igel. Dynamic rupture along bimaterial interfaces in 3D. *Geophys. Res. Lett.*, 34:L11305, 2007. doi: 10.1029/2007GL029908. URL <http://dx.doi.org/10.1029/2007GL029908>.
- G. B. Brietzke, A. Cochard, and H. Igel. Importance of bimaterial interfaces for earthquake dynamics and strong ground motion. *Geophys. J. Int.*, in press:1–18, 2009. doi: 10.1111/j.1365-246X.2009.04209.x. URL <http://dx.doi.org/10.1111/j.1365-246X.2009.04209.x>.

- E. E. Brodsky and H. Kanamori. Elastohydrodynamic lubrication of faults. *J. Geophys. Res.*, 106:16,357–16,374, 2001. URL <http://www.agu.org/journals/jb/v106/iB08/2001JB000430/>.
- Z. Cakir, J.-B. de Chabali er, R. Armijo, B. Meyer, A. Barka, and G. Peltzer. Coseismic and early post-seismic slip associated with the 1999 Izmit earthquake (Turkey), from SAR interferometry and tectonic field observations. *Geophys. J. Int.*, 155:93–110, 2003. doi: 10.1046/j.1365-246X.2003.02001.x. URL <http://dx.doi.org/10.1046/j.1365-246X.2003.02001.x>.
- F. M. Chester and J. S. Chester. Ultracataclasite structure and friction processes of the Punchbowl fault, San Andreas system, California. *Tectonophysics*, 295:199–221, 1998. doi: 10.1016/S0040-1951(98)00121-8. URL [http://dx.doi.org/10.1016/S0040-1951\(98\)00121-8](http://dx.doi.org/10.1016/S0040-1951(98)00121-8).
- F. M. Chester, J. P. Evans, and R. L. Biegel. Internal structure and weakening mechanisms of the San Andreas fault. *J. Geophys. Res.*, 98(B1):771–786, 1993. URL <http://www.agu.org/journals/jb/v098/iB01/92JB01866/>.
- M. Cocco and A. Bizzarri. On the slip-weakening behavior of rate- and state-dependent constitutive laws. *Geophys. Res. Lett.*, 29(11):1516, 2002. doi: 10.1029/2001GL013999. URL <http://dx.doi.org/10.1029/2001GL013999>.
- M. Cocco, A. Bizzarri, and E. Tinti. Physical interpretation of the breakdown process using a rate- and state-dependent friction law. *Tectonophysics*, 378:241–262, 2004. doi: 10.1016/j.tecto.2003.09.015. URL <http://dx.doi.org/10.1016/j.tecto.2003.09.015>.
- A. Cochard and R. Madariaga. Complexity of seismicity due to highly rate-dependent friction. *J. Geophys. Res.*, 101(B11):25,321–25,336, 1996. URL <http://www.agu.org/journals/jb/v101/iB11/96JB02095/>.
- A. Cochard and J. R. Rice. Fault rupture between dissimilar materials: Ill-posedness, regularization, and slip-pulse response. *J. Geophys. Res.*, 105:25891–25908, 2000. doi: 10.1029/2000JB900230. URL <http://dx.doi.org/10.1029/2000JB900230>.
- F. Collino and C. Tsogka. Application of the perfectly matched absorbing layer model to the linear elastodynamic problem in anisotropic heterogeneous media. *Geophysics*, 66(1):294–307, 2001. URL <http://www.math.uchicago.edu/~tsogka/publications.html>.
- S. Cust odio and R. J. Archuleta. Parkfield earthquakes: Characteristic or complementary? *J. Geophys. Res.*, 112:B05310, 2007. doi: 10.1029/2006JB004617. URL <http://dx.doi.org/10.1029/2006JB004617>.
- F. A. Dahlen. On the ratio of P-wave to S-wave corner frequencies for shallow earthquake sources. *Bull. Seism. Soc. Am.*, 64(4):1159–1180, 1974. URL <http://bssa.geoscienceworld.org/cgi/content/abstract/64/4/1159>.

- L. A. Dalguer and S. M. Day. Comparison of fault representation methods in finite difference simulations of dynamic rupture. *Bull. Seism. Soc. Am.*, 96(5):1764–1778, October 2006. doi: 10.1785/0120060024. URL <http://bssa.geoscienceworld.org/cgi/reprint/96/5/1764>.
- L. A. Dalguer and S. M. Day. Staggered-grid split-node method for spontaneous rupture simulation. *J. Geophys. Res.*, 112:B02302, 2007a. doi: 10.1029/2006JB004467. URL <http://dx.doi.org/10.1029/2006JB004467>.
- L. A. Dalguer and S. M. Day. Asymmetric pulse-like rupture at bimaterial interface with slip-weakening friction model. *EOS Trans. AGU, Fall Meet. Suppl.*, 88(52):Abstract S14B–03, 2007b.
- L. D. Dalguer, K. Irikura, J. D. Riera, and H. C. Chiu. The importance of the dynamic source effects on strong ground motion during the 1999 chi-chi, taiwan, earthquake: Brief interpretation of the damage distribution on buildings. *Bull. Seism. Soc. Am.*, 91:1112–1127, 2001. doi: 10.1785/0120000705. URL <http://dx.doi.org/10.1785/0120000705>.
- S. Das and K. Aki. A numerical study of two-dimensional spontaneous rupture propagation. *Geophys. J. Int.*, 50:643–668, 1977. doi: 10.1111/j.1365-246X.1977.tb01339.x. URL <http://dx.doi.org/10.1111/j.1365-246X.1977.tb01339.x>.
- S. M. Day. Three-dimensional finite difference simulation of fault dynamics: Rectangular faults with fixed rupture velocity. *Bull. Seism. Soc. Am.*, 72(3):705–727, 1982a. URL <http://bssa.geoscienceworld.org/cgi/content/abstract/72/3/705>.
- S. M. Day. Three-dimensional simulation of spontaneous rupture: the effect of nonuniform prestress. *Bull. Seism. Soc. Am.*, 72:1881–1902, 1982b. URL <http://bssa.geoscienceworld.org/cgi/content/abstract/72/6A/1881>.
- S. M. Day, G. Yu, and D. J. Wald. Dynamic stress changes during earthquake rupture. *Bull. Seism. Soc. Am.*, 88(2):512–522, 1998. URL <http://bssa.geoscienceworld.org/cgi/content/abstract/88/2/512>.
- S. M. Day, L. A. Dalguer, N. Lapusta, and Y. Liu. Comparison of finite difference and boundary integral solutions to three-dimensional spontaneous rupture. *J. Geophys. Res.*, 110:B12307, 2005. doi: 10.1029/2005JB003813. URL <http://dx.doi.org/10.1029/2005JB003813>.
- G. Di Toro, D. L. Golbsby, and T. E. Tullis. Friction falls toward zero in quartz rock as slip velocity approaches seismic rates. *Nature*, 427:436–439, 2004. doi: 10.1038/nature02249. URL <http://dx.doi.org/10.1038/nature02249>.
- G. Di Toro, T. Hirose, S. Nielsen, and S. Pennacchioni, G. Shimamoto. Natural and experimental evidence of melt lubrication of faults during earthquakes. *Science*, 311:647–649, February 2006. doi: 10.1126/science.1121012. URL <http://dx.doi.org/10.1126/science.1121012>.

- J. H. Dieterich. Modeling of rock friction. 1. experimental results and constitutive equations. *J. Geophys. Res.*, 84(B5):2161–2168, 1979. URL <http://www.agu.org/journals/jb/v084/iB05/JB084iB05p02161/>.
- O. Dor, Y. Ben-Zion, T. K. Rockwell, and J. Brune. Pulverized rocks in the Mojave section of the San Andreas fault zone. *Earth Planet. Sci. Lett.*, 245:642–654, 2006a. doi: 10.1016/j.epsl.2006.03.034. URL <http://dx.doi.org/10.1016/j.epsl.2006.03.034>.
- O. Dor, T. K. Rockwell, and Y. Ben-Zion. Geologic observations of damage asymmetry in the structure of the San Jacinto, San Andreas and Punchbowl faults in southern California: A possible indicator for preferred rupture propagation direction. *Pure Appl. Geophys.*, 163:301–349, 2006b. doi: 10.1007/s00024-005-0023-9. URL <http://dx.doi.org/10.1007/s00024-005-0023-9>.
- O. Dor, C. Yildirim, T. K. Rockwell, Y. Ben-Zion, O. Emre, M. Sisk, and T. Y. Duman. Geologic and geomorphologic asymmetry of the 1943 and 1944 earthquakes on the North Anatolian Fault: possible signals for preferred earthquake propagation direction. *Geophys. J. Int.*, 173:483–504, 2008. doi: 10.1111/j.1365-246X.2008.03709.x. URL <http://dx.doi.org/10.1111/j.1365-246X.2008.03709.x>.
- E. M. Dunham. Conditions governing the occurrence of supershear ruptures under slip-weakening friction. *J. Geophys. Res.*, 112:B07302, 2007. doi: 10.1029/2006JB004717. URL <http://dx.doi.org/10.1029/2006JB004717>.
- E. M. Dunham and J. R. Rice. Earthquake slip between dissimilar poroelastic materials. *J. Geophys. Res.*, 113:B09304, 2008. doi: 10.1029/2007JB005405. URL <http://dx.doi.org/10.1029/2007JB005405>.
- J. P. Eaton, M. E. O’Neil, and J. N. Murdock. Aftershocks of the 1966 Parkfield-Cholame, California, earthquake: a detailed study. *Bull. Seism. Soc. Am.*, 60:1151–1197, 1970. URL <http://bssa.geoscienceworld.org/cgi/content/abstract/60/4/1151>.
- D. Eberhart-Phillips and A. J. Michael. Seismotectonics of the Loma Prieta, California, region determined from three-dimensional v_p , v_p/v_s , and seismicity. *J. Geophys. Res.*, 103:21,009–21,120, 1998. URL http://www.agu.org/journals/jb/jb9809/jb103_9.html.
- R. Feng and T. V. McEvilly. Interpretation of seismic reflection profiling data for the structure of the San Andreas fault zone. *Bull. Seism. Soc. Am.*, 73:1701–1720, 1983. URL <http://bssa.geoscienceworld.org/cgi/content/abstract/73/6A/1701>.
- F. Flerit, R. Armijo, G. C. P. King, B. Meyer, and A. Barka. Slip partitioning in the Sea of Marmara pull-apart determined from GPS velocity vectors. *Geophys. J. Int.*, 154:1–7, 2003. doi: 10.1046/j.1365-246X.2003.01899.x. URL <http://dx.doi.org/10.1046/j.1365-246X.2003.01899.x>.

- M. Fohrmann, H. Igel, G. Jahnke, and Y. Ben-Zion. Guided Waves from Sources Outside Faults: An Indication for Shallow Fault Zone Structure? *Pure Appl. Geophys.*, 161:2125–2137, December 2004. doi: 10.1007/s00024-004-2553-y. URL <http://dx.doi.org/10.1007/s00024-004-2553-y>.
- G. S. Fuis, T. Ryberg, N. Godfrey, D. A. Okaya, and J.M. Murphy. Crustal structure and tectonics from the Los Angeles basin to the Mojave desert, southern ca. *Geology*, 29:15–18, 2001. doi: 10.1130/0091-7613(2001)029<0015:CSATFT>2.0.CO;2. URL [http://dx.doi.org/10.1130/0091-7613\(2001\)029<0015:CSATFT>2.0.CO;2](http://dx.doi.org/10.1130/0091-7613(2001)029<0015:CSATFT>2.0.CO;2).
- G. S. Fuis, R. W. Clayton, P. M. Davis, W. J. Ryberg, T. Lutter, D. A. Okaya, E. Hauksson, C. Prodehl, J. M. Murphy, M. L. Benthien, S. A. Baher, M. D. Kohler, K. Thygesen, G. Simila, and G. R. Keller. Fault systems of the 1971 San Fernando and 1994 Northridge earthquakes, southern California: Relocated aftershocks and seismic images from LARSE II. *Geology*, 31:171–174, 2003. doi: 10.1130/0091-7613(2003)031<0171:FSOTSF>2.0.CO;2. URL [http://dx.doi.org/10.1130/0091-7613\(2003\)031<0171:FSOTSF>2.0.CO;2](http://dx.doi.org/10.1130/0091-7613(2003)031<0171:FSOTSF>2.0.CO;2).
- E. Fukuyama and R. Madariaga. Rupture dynamics of a planar fault in a 3D elastic medium: Rate- and slip-weakening friction. *Bull. Seism. Soc. Am.*, 88(1):1–17, 1998. URL <http://bssa.geoscienceworld.org/cgi/content/abstract/88/1/1>.
- E. Fukuyama and T. Mikumo. Slip-weakening distance estimated at near-fault stations. *Geophys. Res. Lett.*, 34:L09302, 2007. doi: 10.1029/2006GL029203. URL <http://dx.doi.org/10.1029/2006GL029203>.
- R. W. Graves. Simulating seismic wave propagation in 3D elastic media using staggered-grid finite differences. *Bull. Seism. Soc. Am.*, 86(4):1091–1106, 1996. URL <http://bssa.geoscienceworld.org/cgi/content/abstract/86/4/1091>.
- R. A. Harris and S. M. Day. Effect of a low-velocity zone on a dynamic rupture. *Bull. Seism. Soc. Am.*, 87:1267–1280, 1997. URL <http://bssa.geoscienceworld.org/cgi/content/abstract/87/5/1267>.
- R. A. Harris and S. M. Day. Material contrast does not predict earthquake rupture propagation direction. *Geophys. Res. Lett.*, Vol. 32:L23301, 2005. doi: 10.1029/2005GL023941. URL <http://dx.doi.org/10.1029/2005GL023941>.
- R. A. Harris and S. M. Day. Dynamic 3D simulations of earthquakes on en echelon faults. *Geophys. Res. Lett.*, 26(14):2089–2092, 1999. URL <http://www.agu.org/journals/gl/v026/i014/1999GL900377/>.
- T. H. Heaton. Evidence for and implications of self-healing pulses of slip in earthquake rupture. 64: 1–20, November 1990. doi: 10.1016/0031-9201(90)90002-F. URL [http://dx.doi.org/10.1016/0031-9201\(90\)90002-F](http://dx.doi.org/10.1016/0031-9201(90)90002-F).

- T. Hirose and T. Shimamoto. Growth of molten zone as a mechanism of slip weakening of simulated faults in gabbro during frictional melting. *J. Geophys. Res.*, 110:B05202, 2005. doi: 10.1029/2004JB003207. URL <http://dx.doi.org/10.1029/2004JB003207>.
- T. Hong and C. Marone. Effects of normal stress perturbations on the frictional properties of simulated faults. 6:Q03012, 2005. doi: 10.1029/2004GC000821. URL <http://dx.doi.org/10.1029/2004GC000821>.
- T. Hori, N. Kato, K. Hirahara, B. Baba, and Y. Kaneda. A numerical simulation of earthquake cycles along the Nankai Trough in southwest Japan: lateral variation in frictional property due to the slab geometry controls the nucleation position. *Earth Planet. Sci. Lett.*, 228:215–226, 2004. doi: 10.1016/j.epsl.2004.09.033. URL <http://dx.doi.org/10.1016/j.epsl.2004.09.033>.
- Y. Ida. Cohesive force across the tip of a longitudinal-shear crack and griffith's specific surface energy. *J. Geophys. Res.*, 77:3796–3805, 1972. URL <http://www.agu.org/journals/jb/v077/i020/JB077i020p03796/>.
- H. Igel, P. Mora, and B. Riollet. Anisotropic wave propagation through finite-difference grids. *Geophysics*, 60(4):1203–1216, 1995. doi: 10.1190/1.1443849. URL <http://dx.doi.org/10.1190/1.1443849>.
- H. Kanamori and E. E. Brodsky. The physics of earthquakes. *Physics Today*, 54:34–39, 2001. URL http://ptonline.aip.org/journals/doc/PHTOAD-ft/vol_54/iss_6/34_1.shtml.
- B. V. Kostrov. Self-similar problems of propagation of shear cracks. *J. Appl. Math. Mech.*, 28:1077–1087, 1964.
- B. V. Kostrov. Unsteady propagation of longitudinal shear cracks. *J. Appl. Math. Mech.*, 30:1241–1248, 1966.
- Rice J. R. Ben-Zion Y. Lapusta, N. and G. Zheng. Elastodynamic analysis for slow tectonic loading with spontaneous rupture episodes on faults with rate- and state-dependent friction. *J. Geophys. Res.*, 105(B10):23,765–23,789, 2000. URL <http://www.agu.org/journals/jb/v105/iB10/2000JB900250/>.
- X. Le Pichon, C. Kreemer, and N. Chamot-Rooke. Asymmetry in elastic properties and the evolution of large continental strike-slip faults. *Journal of Geophysical Research (Solid Earth)*, 110:B03405, March 2005. doi: 10.1029/2004JB003343. URL <http://dx.doi.org/10.1029/2004JB003343>.
- A. R. Levander. Fourth-order finite-difference P-SV seismograms. *Geophysics*, 53(11):1425–1436, 1988. doi: 10.1190/1.1442422. URL <http://dx.doi.org/10.1190/1.1442422>.
- M. A. Lewis, Z. Peng, Y. Ben-Zion, and F. L. Vernon. Shallow seismic trapping structure in the San Jacinto fault zone near Anza, California. *Geophys. J. Int.*, 162:867–881, July 2005. doi:

- 10.1111/j.1365-246X.2005.02684.x. URL <http://dx.doi.org/10.1111/j.1365-246X.2005.02684.x>.
- M. A. Lewis, Y. Ben-Zion, and J. J. McGuire. Imaging the deep structure of the San Andreas fault south of Hollister with joint analysis of fault zone head and direct P arrivals. *Geophys. J. Int.*, 169:1028–1042, 2007. doi: 10.1111/j.1365-246X.2006.03319.x. URL <http://dx.doi.org/10.1111/j.1365-246X.2006.03319.x>.
- V. C. Li. *Mechanics of Shear Rupture Applied to Earthquake Zones*. In: *Fracture Mechanics of Rock*. Academic Press, 1987.
- M. F. Linker and J. H. Dieterich. Effects of variable normal stress on rock friction: Observations and constitutive equations. *J. Geophys. Res.*, 97(B4):4923–4940, 1992. URL <http://www.agu.org/journals/jb/v097/iB04/92JB00017/>.
- P. Liu, S. Custodio, and R. J. Archuleta. Kinematic inversion of the 2004 m 6.0 parkfield earthquake including an approximation to site effects. *Bull. Seism. Soc. Am.*, 96:S143–S158, 2006. doi: 10.1785/0120050826. URL <http://dx.doi.org/10.1785/0120050826>.
- D. Lockner, H. Naka, H. Tanaka, Ito, H., and R. Ikeda. Permeability and strength of core samples from the Nojima fault of the 1995 Kobe earthquake. In *Proceedings of the International Workshop on the Nojima Fault Core and Borehole Data Analysis, Tsukuba, Japan, Nov 22-23, 1999*, pages 147–152, Menlo Park, CA., 1999. U.S. Geological Survey. URL <http://earthquake.usgs.gov/research/physics/lab/technical.php#L>.
- W. J. Lutter, G. S. Fuis, T. Ryberg, D. A. Okaya, R. W. Clayton, P. M. Davis, C. Prodehl, J. M. Murphy, V. E. Langenheim, M. L. Benthien, N. J. Godfrey, N. I. Christensen, K. Thygesen, C. H. Thurber, G. Simila, and G. R. Keller. Upper crustal structure from the Santa Monica mountains to the Sierra Nevada, southern California: tomographic results from the Los Angeles regional seismic experiment, phase ii (LARSE). *Bull. Seism. Soc. Am.*, 94(2):619–632, April 2004. doi: 10.1785/0120030058. URL <http://dx.doi.org/10.1785/0120030058>.
- R. Madariaga, K. Olsen, and R. Archuleta. Modeling dynamic rupture in a 3D earthquake fault model. *Bull. Seism. Soc. Am.*, 88(5):1182–1197, 1998. URL <http://bssa.geoscienceworld.org/cgi/content/abstract/88/5/1182>.
- H. Magistrale and C. Sanders. P-wave image of the Peninsular Ranges batholith, southern California. *Geophys. Res. Lett.*, 22:2549–2552, 1995. URL <http://www.agu.org/journals/gl/v022/i018/95GL02241/>.
- P. M. Mai and G. C. Beroza. A spatial random-field model to characterize complexity in earthquake slip, *J. geophys. res.*, 107(b11), 2308, doi:10.1029/2001jb000588, 2002. *J. Geophys. Res.*, 107(B11):2308, 2002. doi: 10.1029/2001JB000588. URL <http://dx.doi.org/10.1029/2001JB000588>.

- C. Marcinkovich and K. Olsen. On the implementation of perfectly matched layers in a three-dimensional fourth-order velocity-stress finite difference scheme. *J. Geophys. Res.*, 108(B5):2276, 2003. doi: 10.1029/2002JB002235. URL <http://dx.doi.org/10.1029/2002JB002235>.
- C. Marone. Laboratory-Derived Friction Laws and Their Application to Seismic Faulting. *Annu. Rev. Earth Planet. Sci.*, 26:643–696, 1998. doi: 10.1146/annurev.earth.26.1.643. URL <http://dx.doi.org/10.1146/annurev.earth.26.1.643>.
- J. A. C. Martins and F. M. F. Simões. On some sources of instability/ill-posedness in elasticity problems with Coulomb's friction, pages 95–106. Contact mechanics. Plenum, New York, 1995.
- J. McGuire. Estimating the finite source properties of small earthquake ruptures. *Bull. Seism. Soc. Am.*, 94:377–393, 2004. doi: 10.1785/0120030091. URL <http://dx.doi.org/10.1785/0120030091>.
- J. McGuire and Y. Ben-Zion. High-resolution imaging of the Bear Valley section of the San Andreas Fault at seismogenic depths with fault-zone head waves and relocated seismicity. *Geophys. J. Int.*, 163:152–164, 2005. doi: 10.1111/j.1365-246X.2005.02703.x. URL <http://dx.doi.org/10.1111/j.1365-246X.2005.02703.x>.
- T. Mikumo, K. B. Olsen, E. Fukuyama, and Y. Yagi. Stress-breakdown time and slip-weakening distance inferred from slip-velocity functions on earthquake faults. *Bull. Seism. Soc. Am.*, 93:264–282, 2003. doi: 10.1785/0120020082. URL <http://dx.doi.org/10.1785/0120020082>.
- P. Moczo, J. Kristek, M. Galis, P. Pazak, and M. Balazovjeh. The finite-difference and finite-element modelling of seismic wave propagation and earthquake motion. *acta physica slovacica*, 57:1–406, 2007. URL <http://www.physics.sk/aps/pubs/2007/aps-07-02/aps-07-02.pdf>.
- S. B. Nielsen and J. M. Carlson. Rupture pulse characterization: Self-healing, self-similar, expanding solutions in a continuum model of fault dynamics. *Bull. Seism. Soc. Am.*, 90(6):1480–1497, 2000. doi: 10.1785/0120000021. URL <http://dx.doi.org/10.1785/0120000021>.
- M. Ohnaka. Nonuniformity of the constitutive law parameters for shear rupture and quasistatic nucleation to dynamic rupture: a physical model of earthquake generation processes. *Proc. Natl. Acad. Sci. USA*, 93(9):3795–3802, 1996. URL <http://www.pnas.org/cgi/content/abstract/93/9/3795>.
- M. Ohnaka. A constitutive scaling law and a unified comprehension for frictional slip failure, shear fracture of intact rock, and earthquake rupture. *J. Geophys. Res.*, 108(B2):2080, 2003. doi: 10.1029/2000JB000123. URL <http://dx.doi.org/10.1029/2000JB000123>.
- M. Ohnaka and T. Yamashita. A cohesive zone model for dynamic shear faulting based on experimentally inferred constitutive relation and strong motion source parameters. *J. Geophys. Res.*, 94(B5):4089–4104, 1989. URL <http://www.agu.org/journals/jb/v094/iB04/JB094iB04p04089/>.

- R. Otilio, S Day, J. Castillo, and L. A. Dalguer. Modelling of rupture propagation using high-order mimetic finite differences. *Geophys. J. Int.*, 172:631–650, 2008. doi: 10.1111/j.1365-246X.2007.03651.x. URL <http://dx.doi.org/10.1111/j.1365-246X.2007.03651.x>.
- A. C. Palmer and J. R. Rice. The growth of slip surfaces in the progressive failure of overconsolidated clay. *Proceedings of the Royal Society of London, A* 332:527–548, 1973. URL <http://www.jstor.org/pss/78279>.
- T. Pearson. PGPLOT Graphics Subroutine Library, California Institute of Technology, 1995-2002. URL <http://www.astro.caltech.edu/~tjp/pgplot/>.
- Z. Peng and Y Ben-Zion. Systematic analysis of crustal anisotropy along the Karadere-Duzce branch of the north Anatolian fault. *Geophys. J. Int.*, 159:253–274, 2004. doi: 10.1111/j.1365-246X.2004.02379.x. URL <http://dx.doi.org/10.1111/j.1365-246X.2004.02379.x>.
- Z. Peng, Y. Ben-Zion, L. Zhu, and A.J. Michael. Inference of a shallow fault zone layer in the rupture zone of the 1992 Landers, California earthquake from locations of events generating trapped waves and travel time analysis. *Geophys. J. Int.*, 155:1021–1041, 2003. doi: 10.1111/j.1365-246X.2003.02109.x. URL <http://dx.doi.org/10.1111/j.1365-246X.2003.02109.x>.
- V. Prakash. Frictional response of sliding interfaces subjected to time varying normal pressures. *J. of Tribol.*, 120:97–102, 1998. doi: 10.1115/1.2834197. URL <http://dx.doi.org/10.1115/1.2834197>.
- V. Prakash and R. J. Clifton. *Time resolved dynamic friction measurements in pressure-shear*, volume 165 of *Appl. Mech. Div.*, pages 33–48. ASME, New York, 1993.
- K. Ranjith and J. Rice. Slip dynamics at an interface between dissimilar materials. *J. Mach. Phys. Solids*, 49:341–361, 2001. doi: 10.1016/S0022-5096(00)00029-6. URL [http://dx.doi.org/10.1016/S0022-5096\(00\)00029-6](http://dx.doi.org/10.1016/S0022-5096(00)00029-6).
- M. Renardy. Ill-posedness at the boundary for elastic solids sliding under coulomb friction,. *J. Elast.*, 27(3):281–287, 1992. URL <http://www.springerlink.com/content/g63597g001472373/>.
- J. R. Rice. Slip pulse at low driving stress along a frictional fault between dissimilar media. *Eos Trans. AGU*, 78:F464, 1997.
- J. R. Rice. Heating and weakening of faults during earthquake slip. *J. Geophys. Res.*, 111:B05311, 2006. doi: 10.1029/2005JB004006. URL <http://dx.doi.org/10.1029/2005JB004006>.
- J. R. Rice and M. Cocco. *The Dynamics of Fault Zones*, volume 95 of *Dahlem Workshop Reports*, chapter Seismic fault rheology and earthquake dynamics, pages 1–36. The MIT Press, Cambridge, MA, USA, 2006. URL http://esag.harvard.edu/rice/216_RiceCocco_DahlemWrkshp05.pdf.

- J. R. Rice, C. G. Charles G. Sammis, and R. Parsons. Off-fault secondary failure induced by a dynamic slip pulse. *Bull. Seism. Soc. Am.*, 95(1):109–134, 2005. doi: 10.1785/0120030166. URL <http://dx.doi.org/10.1785/0120030166>.
- E. Richardson and C. Marone. Effects of normal stress vibrations on frictional healing. *J. Geophys. Res.*, 104(B12):28,859–28,878, 1999. URL <http://www.agu.org/journals/jb/v104/iB12/1999JB900320/>.
- A. M. Rubin. Aftershocks of microearthquakes as probes of the mechanics of rupture. *J. Geophys. Res.*, 107(B7):2142, July 2002. doi: 10.1029/2001JB000496. URL <http://dx.doi.org/10.1029/2001JB000496>.
- A. M. Rubin and J. P. Ampuero. Aftershock asymmetry on a bimaterial interface. *J. Geophys. Res.*, 112:B05307, 2007. doi: 10.1029/2006JB004337. URL <http://dx.doi.org/10.1029/2006JB004337>.
- A. M. Rubin and D. Gillard. Aftershock asymmetry/rupture directivity among central San Andreas fault microearthquakes. *J. Geophys. Res.*, 105(B8):19,095–19,109, 2000. URL <http://www.agu.org/journals/jb/v105/iB08/2000JB900129/>.
- J. W. Rudnicki and J. R. Rice. Effective normal stress alteration due to pore pressure changes induced by dynamic slip propagation on a plane between dissimilar materials. *J. Geophys. Res.*, 111:B10308, 2006. doi: 10.1029/2006JB004396. URL <http://dx.doi.org/10.1029/2006JB004396>.
- A. Runia. Slip instability and state variable friction laws. *J. Geophys. Res.*, 88(B12):10,359–10,370, 1983. URL <http://www.agu.org/journals/jb/v088/iB12/JB088iB12p10359/>.
- M. J. Rymer, J. C. Tinsley, J. A. Treiman, J. R. Arrowsmith, K. B. Clahan, A. M. Rosinskim, W. A. Bryant, G. S. Snyder, H. A. Fuis, N. Toké, and G. W. Bawden. Surface fault slip associated with the 2004 parkfield, california, earthquake. *Bull. Seism. Soc. Am.*, 96(4B):S11–S27, 2006. doi: 10.1785/0120050830. URL <http://dx.doi.org/10.1785/0120050830>.
- C. H. Scholz. Earthquakes and friction laws. *Nature*, 391:37–42, 1998. doi: doi:10.1038/34097.
- A. Shakal, V. Graizer, M. Huang, R. Borchardt, H. Haddadi, K. Lin, C. Stephens, and P. Roffers. Preliminary analysis of strong-motion recordings from the 28 September 2004 Parkfield, California earthquake. *Seism. Res. Lett.*, 76(1):27–39, 2005.
- A. Shakal, H. Haddadi, V. Graizer, K. Lin, and M. Huang. Some Key Features of the Strong-Motion Data from the M 6.0 Parkfield, California, Earthquake of 28 September 2004. *Bull. Seism. Soc. Am.*, 96(4b):90–118, September 2006. doi: 10.1785/0120050817. URL <http://dx.doi.org/10.1785/0120050817>.
- N. M. Shapiro, M. Campillo, L. Stehly, and M. H. Ritzwoller. High resolution surface wave tomography from ambient seismic noise. *Science*, 307:1615–1618, 2005. doi: 10.1126/science.1108339. URL <http://dx.doi.org/10.1126/science.1108339>.

- Z. Shi and Y Ben-Zion. Dynamic rupture on a bimaterial interface governed by slip-weakening friction. Geophys. J. Int., 165:469–484, 2006. doi: 10.1111/j.1365-246X.2006.02853.x. URL <http://dx.doi.org/10.1111/j.1365-246X.2006.02853.x>.
- Z. K. Shipton, J. P. Evans, R. E. Abercrombie, and E. E. Brodsky. Earthquakes: Radiated Energy and the Physics of Faulting, chapter The Missing Sinks: Slip Localization in Faults, Damage Zones, and the Seismic Energy Budget, pages 217–222. Geophysical Monograph Series. American Geophysical Union, 2006.
- R. H. Sibson. Interaction between temperature and pore-fluid pressure during earthquake faulting - a mechanism for partial or total stress relief. Nature, 243:66–68, 1973.
- R. H. Sibson. Generation of pseudotachylite by ancient seismic faulting. Geophys. J. Int., 43:775–794, 1975. doi: 10.1111/j.1365-246X.1975.tb06195.x. URL <http://dx.doi.org/10.1111/j.1365-246X.1975.tb06195.x>.
- R. H. Sibson. Thickness of the seismic slip zone. Bull. Seism. Soc. Am., 93(3):1169–1178, 2003. doi: 10.1785/0120020061. URL <http://dx.doi.org/10.1785/0120020061>.
- J. G. Spray. Viscosity determinations of some frictionally generated silicate melts: Implications for fault zone rheology at high strain rates. J. Geophys. Res., 98(B5):8053–8068, 1993. URL <http://www.agu.org/journals/jb/v098/iB05/93JB00020/>.
- T. Tanimoto and K. Prindle Sheldrake. Three-dimensional s-wave velocity structure in southern California. Geophys. Res. Lett., 29(8):1223, 2002. doi: 10.1029/2001GL013486. URL <http://dx.doi.org/10.1029/2001GL013486>.
- C. Thurber, H. Zhang, F. Waldhauser, J. Hardebeck, A. Michael, and D. Eberhart-Phillips. Three-dimensional compressional wavespeed model, earthquake relocations, and focal mechanisms for the Parkfield, California, region. Bull. Seism. Soc. Am., 96:S38–S49, 2006. doi: 10.1785/0120050825. URL <http://dx.doi.org/10.1785/0120050825>.
- E. Tinti, E. Fukuyama, A. Piatanesi, and M. Cocco. A kinematic source-time function compatible with earthquake dynamics. Bull. Seism. Soc. Am., 95(4):1211–1223, 2005. doi: 10.1785/0120040177. URL <http://dx.doi.org/10.1785/0120040177>.
- A. Tsutsumi and T. Shimamoto. High-velocity frictional properties of gabbro. Geophys. Res. Lett., 24:699–702, 1997. doi: 10.1029/97GL00503. URL <http://dx.doi.org/10.1029/97GL00503>.
- J. J. Weertman. Dislocations moving uniformly on the interface between isotropic media of different elastic properties. J. Mach. Phys. Solids, 11:197–204, 1963. doi: 10.1016/0022-5096(63)90052-8. URL [http://dx.doi.org/10.1016/0022-5096\(63\)90052-8](http://dx.doi.org/10.1016/0022-5096(63)90052-8).

- J. J. Weertman. Unstable slippage across a fault that separates elastic media of different elastic constants. J. Geophys. Res., 85:1455–1461, March 1980. URL <http://www.agu.org/journals/jb/v085/iB03/JB085iB03p01455/>.
- C. A. J. Wibberley and T. Shimamoto. Internal structure and permeability of major strike-slip fault zones: the Median Tectonic Line in Mie Prefecture, Southwest Japan. Journal of Structural Geology, 25:59–78, 2002. doi: 10.1016/S0191-8141(02)00014-7. URL [http://dx.doi.org/10.1016/S0191-8141\(02\)00014-7](http://dx.doi.org/10.1016/S0191-8141(02)00014-7).
- Z. L. Wu and Y. T. Chen. Definition of Seismic Moment at a Discontinuity Interface. Bull. Seism. Soc. Am., 93(4):1832–1834, 2003. doi: 10.1785/0120020234. URL <http://dx.doi.org/10.1785/0120020234>.
- K. Xia, A. J. Rosakis, H. Kanamori, and J. R. Rice. Laboratory earthquakes along inhomogeneous faults: Directionality and supershear. Science, 308:681–684, 2005. doi: 10.1126/science.1108193. URL <http://dx.doi.org/10.1126/science.1108193>.
- T. Yamashita. Postseismic quasi-static fault slip due to pore pressure change on a bimaterial interface. J. Geophys. Res., 112:B05304, 2007. doi: <http://dx.doi.org/10.1029/2006JB004667>. URL 10.1029/2006JB004667.
- Z. Zhang and S. Y. Schwartz. Seismic anisotropy in the shallow crust of the Loma Prieta segment of the San Andreas fault system. J. Geophys. Res., 99(B5):9651–9661, 1994. URL <http://www.agu.org/journals/jb/v099/iB05/94JB00241/>.
- G. Zheng and J. R. Rice. Conditions under which velocity-weakening friction allows a self-healing versus a cracklike mode of rupture. Bull. Seism. Soc. Am., 88(6):1466–1483, 1998. URL <http://bssa.geoscienceworld.org/cgi/content/abstract/88/6/1466>.

Gilbert Björn Brietzke

Zeno-Diemer-Str. 2
80638 München

curriculum vitae

born 16th December 1973 in Bremen

School Education

- 1980—1984 Primary School, *Grundschule Iprump*, Delmenhorst
- 1984—1986 5th and 6th Grade, *Pestalozzi-Schulzentrum*, Delmenhorst
- 1986—1994 Grammar School, *Gymnasium an der Willmsstraße*, Delmenhorst

Civilian Service

- 08.1994—11.1994 **Delivery man**, *Hospital St. Josef Stift*, Delmenhorst.
- 12.1994—11.1995 **Adviser**, *Blindenverein Bremen e.V.*, Bremen.

University Education

- 10.1995—03.2003 **Studies of Geophysics**, *Westfälische Wilhelms-Universität*, Münster.
- 10.1997 **Intermediate Diploma**, *Westfälische Wilhelms-Universität*, Münster.
- 09.1998—03.1999 **Semester Abroad**, *University of Salford*, Greater Manchester, England.
- 10.2000 **Diploma Examination**, *Westfälische Wilhelms-Universität*, Münster.
- 10.2001—01.2003 **Diploma Thesis**, *Ludwig-Maximilians-Universität*, München.
- 03.2003 **Diploma in Geophysics**, *Westfälische Wilhelms-Universität*, Münster.
- 02.2003—06.2003 **Research Fellowship**, *University of Southern California*, Los Angeles, USA.
- since 07.2003 **Ph.D.-Student**, *Ludwig-Maximilians-Universität*, München.

Industry

- 04.2005—09.2006 **Scholarship**, *Munich Reinsurrance*, München.
- 01.2001—10.2001 **Student Trainee**, *MTU Aero Engines (DaimlerChrysler)*, München.
- 08.1998—08.1999 **Student Trainee**, *DMT-GmbH, GeoTec division*, Essen.
- 06.1998—09.1999 **Student Trainee**, *GeoHiRes International Ltd.*, Borken.
- 02.1998—04.1998 **Student Trainee**, *NFS GmbH (Daimler-Benz Aerospace)*, Ulm.

Gilbert Brietzke, München, September 15th 2008

